Energetic electron precipitation of pulsating aurorae and their mesospheric effects

Fasil Tesema Kebede

Thesis for the degree of Philosophiae Doctor (PhD)
University of Bergen, Norway
2021

UNIVERSITY OF BERGEN

Energetic electron precipitation of pulsating aurorae and their mesospheric effects

Fasil Tesema Kebede

Thesis for the degree of Philosophiae Doctor (PhD)
at the University of Bergen

Date of defense: 17.06.2021

Year: 2021

Title: Energetic electron precipitation of pulsating aurorae and their mesospheric effects

Name: Fasil Tesema Kebede

Print: Skipnes Kommunikasjon / University of Bergen

Scientific environment

This dissertation has been fully funded by Birkeland Center for Space Science (BCSS) from the Norwegian Research Council (NRC) project number 223252 in Energetic Particle Precipitation group targeting the question "what are the effects of particle precipitation on the atmosphere?" The study is carried out at the Department of Arctic Geophysics in University Centre in Svalbard (UNIS) and at the Department of Physics and technology in University of Bergen.

Acknowledgements

My three years at UNIS could have been impossible without the help of my supervisor Dr. Noora Partamies. Thank you for believing in me and giving me this opportunity, and made my transition from "horizontal B" to "vertical B" very smooth. Thank you for teaching me to talk to a problem rather than talking about it and for the guidance, support, enthusiasm, and encouragement. I would also like to thank my co-supervisor, Dr. Hilde Nesse Tyssøy, for all the supports and encouragement throughout my Ph.D. study. Thank you for the science discussions in the CAS meetings.

Many thanks to all members of the Department of Arctic Geophysics at UNIS for making the working environment enjoyable. The coffe4science crew, Erkka Heino and Emma Bland, thank you for the scientific discussions. My UNIS B322 officemates, Katie, Kjersti, and Nina, thank you for all the discussions and let me brag about the Ethiopian coffee. Katie and Kjersti, thank you for allowing me to shout, scream, and listening to my life complaints, and most of all, encourage and teach me the culture in this part of the world; that is what best friends are for.

I would also like to thank UNIS, the Norwegian Research Council, and Birkeland Centre for Space Science for funding my PhD. I acknowledge the data providers, editors, and reviewers of my publications for the suggestions and help that made this work possible.

My special thanks to my family, my Moms (Enat and Alemye) for always being helpful, encouraging, and supportive; without your support, I would not have pursued an academic career at all. And most importantly, I would like to thank my wife Zebiba for being the most fantastic person I know and, of course, the unconditional support and love she gave me all these years. Samuel and Benyas, thank you for cheering me up and always asking me, "Hvordan gikk det på jobb i dag, pappa?" every day after work.

Thank you all!

Fasil Tesema
Longyearbyen, March 2021

"As long as there are games to play it is not over."

Sir Alex Ferguson

Abstract

Pulsating aurorae (PsAs) are low-intensity diffuse type aurora, which switches on and off with a quasi-periodic oscillation period from a few seconds to $\sim$ 10 seconds. They are predominantly observed after midnight magnetic local time, during the recovery phase of substorms, and at the equatorward boundary of the auroral oval. Pulsating aurorae are caused by precipitating energetic electrons, which span a wide range of energies between 10s of keV to 100s of keV electrons. The origin of PsA electrons is mainly from the plasma sheet and occasionally from the outer radiation belt. The stoppage altitude of these precipitating electrons can reach down to the mid-mesosphere (70 km), a region where increased ionization can impact the ozone balance. The pulsating aurora altitude range consists of a transition between neutral dominating and plasma dominating regions. This makes the energy deposition associated with pulsating aurora very important in the magnetosphere-atmosphere-ionosphere dynamics.

To understand the contribution of the PsA electrons in ionizing the atmosphere and changing its chemistry, the energy of the electrons should be characterized. A general way of providing energy information about the precipitating electrons is constructing energy spectra from possible satellite and ground-based measurements. To investigate the atmospheric chemistry effects of PsA electrons, the spectra can be used as an input in atmospheric models. In addition, from the spatio-temporal characteristics of PsA a realistic input for the atmospheric models can also be constructed.

In this thesis, satellite measurements of precipitating electrons during PsA events identified using optical observations are used to construct the energy spectrum. The energy spectrum is used in a one-dimensional ion chemistry model to study the effects of the electrons in the middle atmosphere. Radar measurements of electron density and HF radio wave attenuation during PsA are used to characterize the ionization level and the spatio-temporal extent of PsA. The ionization level of different types of PsA is also studied using electron density measurements and ion chemistry model outputs.

Outline

This thesis consists of an introductory part and four scientific papers. Chapter 1 gives an introduction to the thesis. In Chapter 2, the Sun-Earth environment will be introduced and an overview of regions of the magnetosphere, the Earth's atmosphere, and relevant processes related to the topic of the thesis will be provided. In Chapter 3, the instruments and data used in the publications will be discussed. Chapter 4 will mainly discuss PsA related literature together with the findings of this thesis. In Chapter 5, a summary of the four papers used in the thesis will be presented. Finally, Chapter 6 will outline conclusions and future prospects.

The papers included in this thesis are:

Paper I **Tesema, F.**, Partamies, N., Tyssøy, H. N., Kero, A., & Smith-Johnsen, C.: Observations of electron precipitation during pulsating aurora and its chemical impact. Journal of Geophysical Research: Space Physics, 125, e2019JA027713. https://doi.org/10.1029/2019JA027713, 2020.

Paper II **Tesema, F.**, Partamies, N., Nesse Tyssøy, H., and McKay, D.: Observations of precipitation energies during different types of pulsating aurora, Annales Geophysicae, 38, 1191–1202, https://doi.org/10.5194/angeo-38-1191-2020, 2020.

Paper III Bland, E., **Tesema, F.**, and Partamies, N.: D-region impact area of energetic electron precipitation during pulsating aurora, Annales Geophysicae, 39, 135–149, https://doi.org/10.5194/angeo-39-135-2021, 2021.

Paper IV **Tesema, F.**, Partamies N., Whiter D. K., Ogawa, Y., Types of pulsating aurora: Comparison of model and EISCAT electron density observations, submitted to Annales Geophysicae, March 2021.

I have also contributed to the following papers, but, they are not part of this work:

Paper A Partamies, N., **Tesema, F.**, Bland, E., Heino, E., Nesse Tyssøy, H., and Kallelid, E.: Electron precipitation characteristics during isolated, compound, and multi-night substorm events, Annales Geophysicae, 39, 69–83, https://doi.org/10.5194/angeo-39-69-2021, 2021.

Paper B **Tesema, F.** Meriwether, J., Damtie, B., Nigussie, M.: Nighttime equatorial 630-nm emission variability over Ethiopia. Advances in Space research, https://doi.org/10.1016/j.asr.2020.06.007, 2020.

Contents

Chapter 1

Introduction

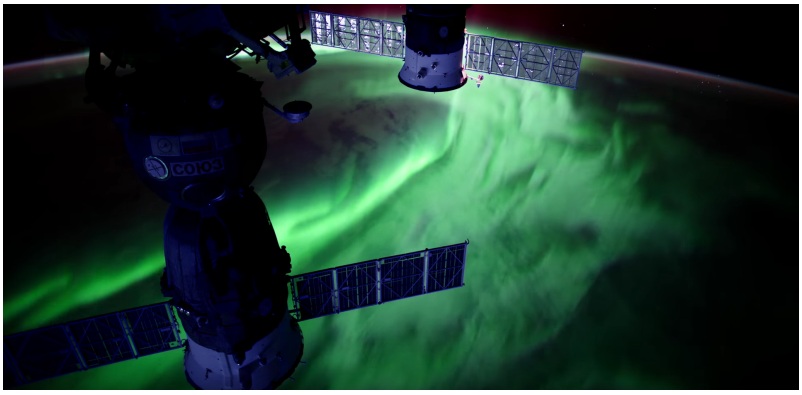

Figure 1.1: An auroral image taken from the International space station, pulsating aurora is seen to the right of the bright arc. (https://www.nasa.gov/image-feature/goddard/2016/stunning-aurora-from-space). Credit:NASA

The Sun, the nearest star and energy source for our home planet Earth, sustains life by emitting light and heat in the form of electromagnetic radiation. Besides, the Sun emits a continuous stream of particles, mainly electrons and protons, in the form of solar wind that could destroy the Earth's environment. However, we are mostly protected by the Earth's magnetic field, deflecting the solar wind particles and shielding us in a region called the magnetosphere. This shielding is not perfect and depends on the magnetic field's direction. The magnetic field which is embedded (frozen) into the solar wind is called the interplanetary magnetic field (IMF). When the IMF direction is anti-parallel to the geomagnetic field, the magnetosphere opens up through merging of the two fields in a process called magnetic reconnection. This allows the solar wind particles to enter the magnetosphere and slide down along geomagnetic field lines to collide with the Earth's atmosphere over the polar regions and creates a magnificent display called the aurora. The aurora color and structure can differ depending on the energy of the particles.

Most of the auroral displays we see are caused by the electrons. As the electrons precipitate down to the atmosphere, they create different colors of the aurora, mainly red, green, and blue. The green and blue auroral emissions occur deep into the at-

mosphere, around 100 km, and are caused by relatively energetic electrons compare to the red aurora, which occurs above 200 km. The nightside aurora we can see with our naked eye, is formed as spirals, curls, and curtains rapidly moving around in the midnight sky, after which a diffuse type, low intensity aurora appears. Within the diffuse aurora, features start to blink on and off. This display is called pulsating aurora (PsA).

PsA is known as the highest energy aurora. It is mainly caused by the precipitation of energetic electrons originated from the modulation of magnetospheric electrons by wave-particle interactions (*Kasahara et al.*, 2018; *Nishimura et al.*, 2010, 2011a). It is mostly sub-visual to human eyes but manifests as blinking patches and arcs in photographs. The horizontal size of the aurora ranges from 10 to 200 km and the pulsation period is of the order of a few seconds. The atmospheric ionization due to the PsA electrons occurs below 110 km, sometimes down to 70 km altitude. This broad range of altitudes, which includes the mesosphere and lower thermosphere, indicates a large range of electron energies during a PsA. The energetic PsA electrons in the middle atmosphere produce odd hydrogen ($HO_x = H + OH + HO_2$) and odd nitrogen ($NO_x = N + NO + NO_2$) gases (*Sinnhuber et al.*, 2012). The middle atmospheric ozone, which is known to regulate the heating balance in the middle atmosphere, can be depleted by the HO_x and NO_x gases through catalytic reactions. This creates an imbalance in the middle atmospheric heating and cooling rates, and the effect can propagate to the lower atmosphere contributing to climate variability (*Seppälä et al.*, 2009).

In recent years, the role of energetic particle precipitation in the middle atmospheric chemistry and further down to the regional surface temperature and pressure variability has been acknowledged (*Rozanov et al.*, 2012). However, most of the studies related to the energetic particle precipitation focused on substorm-related precipitation and short-term precipitation like solar proton events (*Seppälä*, 2004; *Seppälä et al.*, 2007a; *Sinnhuber et al.*, 2016; *Turunen et al.*, 2009). The contribution of PsA electron precipitation, which could be in the relativistic energy range, has been given even less attention. Global models often use magnetic indices to quantify the energy deposition to the atmosphere, which can work to some level in the active geomagnetic periods (*Tyssøy et al.*, 2019). However, the energy deposition associated with PsA is likely overlooked in energetic particle precipitation (EPP) proxies based on magnetic indices. This is due to the fact that PsA is often a substorm recovery phase phenomenon, and magnetic indices cannot capture the energy deposition associated with it (*Partamies et al.*, 2017). In order to provide realistic inputs for global models, there is a need to characterize the spatio-temporal variations of PsA and the energy of the electrons causing it. In general, the characteristics, morphology, and occurrence rate of PsA have been well documented. However, the spatial coverage and statistical information about PsA electrons' energy and their effects in the middle atmospheric chemistry have been very limited.

This thesis work has mainly focused on characterizing energetic particle precipitation during PsA and its effect on atmospheric chemistry. The results fill the above-mentioned knowledge gap by providing the statistical energy spectrum of PsA electrons, the magnetic local time extent, and latitude coverage of PsA. The middle atmospheric effects of PsA electrons are studied by implementing the 1D ion and neutral chemistry model. The results presented in this thesis further strengthen the characteristics and morphology of PsA reported in previous studies and provide additional information about the electron precipitation during different categories of PsA.

Chapter 2

The Sun-Earth environment

In this chapter, the background material needed to understand the Sun-Earth interaction is discussed. It begins with a quick overview of the Sun and solar wind, followed by examining the magnetosphere's basic structure and regions. Section 3, highlights the magnetospheric substorm, a plasma source for the inner magnetosphere and a process responsible for most of the nightside aurora displays over the polar region. The motion of charged particles inside the magnetosphere and a short introduction to radiation belts will be presented in section 4 and 5, respectively. Finally, a brief description of the Earth's atmosphere focusing on the ionosphere, aurora, and middle atmosphere dynamics and chemistry will be presented.

2.1 The Sun and solar wind

The Sun, our nearest star and the center of our solar system, is located 150 million kilometers away from the Earth. The light and heat from the Sun are essential to sustain life on Earth. The Sun is made of 92.1% Hydrogen, 7.8% Helium, and 0.1% of heavier atoms such as oxygen and carbon. These gases are held together by the Sun's gravitational attraction. This attraction creates a region of high pressure at the center of the Sun, called the core. In the core, the pressure is so high that four hydrogen atoms fuse together, by a process called nuclear fusion, to create a helium atom. This process releases staggering amounts of energy that powers the Sun. The energy will heat the gases and break apart atoms into charged particles to create a super-hot mix of electrons and ions called plasma. The plasma is continuously rotating and convecting, which results in a complex solar magnetic field topology (*Babcock*, 1961). This solar magnetic field is the primary driver of a wide variety of solar phenomena, ranging from slowly varying features, such as sunspot, solar prominences, and coronal holes, to highly dynamic features such as solar flares and coronal mass ejections. At the outermost surface of the Sun, the corona, high temperatures result in a pressure force that exceeds the Sun's gravity, allowing the plasma to escape the Sun. The escaped plasma streaming out to space is called the solar wind (*Parker*, 1959, 1958a).

The solar wind mainly consists of protons and electrons together with small fraction of Helium and trace gases such as carbon, nitrogen, oxygen, and Neon. It flows continuously away from the Sun and fills the interplanetary space. There are two solar wind categories: a fast, uniform, and quasi-steady wind blowing at a velocity >

400 km/s as well as a slow, gusty, and highly varying wind with < 400 km/s. The origin of the fast and slow solar wind is different (*Abbo et al.*, 2016, and references therein). The fast solar wind originates from open solar magnetic field regions of the Sun called coronal holes (*Cranmer*, 2009; *Feldman et al.*, 2005). Such open field lines dominate solar magnetic poles during solar minimum and low latitudes during solar maximum (*Cranmer*, 2009). However, the origin of the slow solar wind is still unclear (*Abbo et al.*, 2016) and it might be associated with small coronal holes, open field regions around the boundaries of large coronal holes, and closed coronal loops (*Schwadron et al.*, 2005).

Because solar wind is a highly conducting fluid, it also drags the solar magnetic field away from the Sun. This plasma motion with the interplanetary magnetic field lines is termed as the frozen-in field concept (*Alfvén*, 1942). The plasma embedded within the solar magnetic field in the interplanetary space is called IMF. Thus, the solar wind plasma follows the IMF that is still tied to the Sun. The combination of the radially flowing solar wind (red arrows in Figure 2.1) and the Sun's rotation causes the spiral structure often called the Parker spiral (*Parker*, 1958b). At the Earth's orbit, the angle between the IMF and the sunward direction is mostly 45° (*Jackel et al.*, 2013). The solar wind parameters, magnetic field strength and orientation, velocity, temperature, and density vary throughout the 11-year solar cycle and during transient structures such as corotating interaction regions, and coronal mass ejections. On average, the solar wind density is about 5 cm^{-3}, a temperature of 10^5 K, and field strength 5 nT.

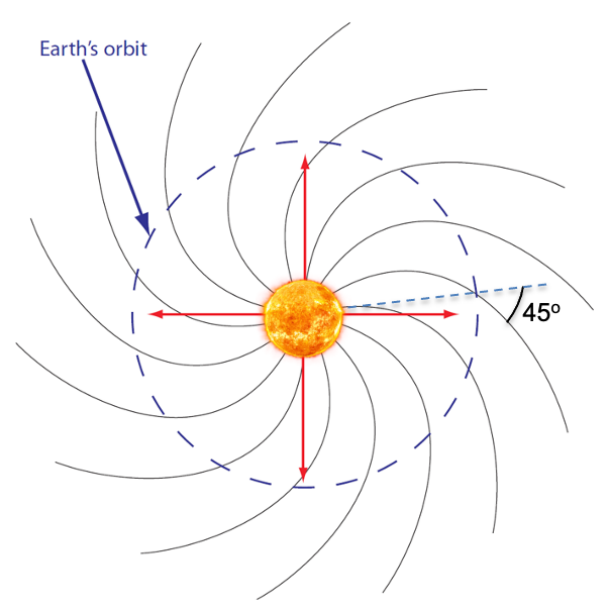

Figure 2.1: Schematic diagram of Parker spiral.

2.2 Earth's magnetosphere

The Earth has its own magnetic field, believed to originate from the electric currents produced by the convective motion of conductive material (mainly molten iron) far below the surface in the Earth's outer core (*Elsasser*, 1939). It can be approximated as a dipole field titled 11° away from Earth's rotation axis. It acts as an obstacle to the solar wind flow and protects the Earth's atmosphere from being stripped away by solar wind particles. Thus, this field is an important shield for the Earth. The effect of this field extends far out into space to create a region called the magnetosphere (*Gold*, 1959). It is shaped when the solar wind interacts with the Earth's magnetic field. Therefore, the solar wind is responsible for the form of the magnetosphere.

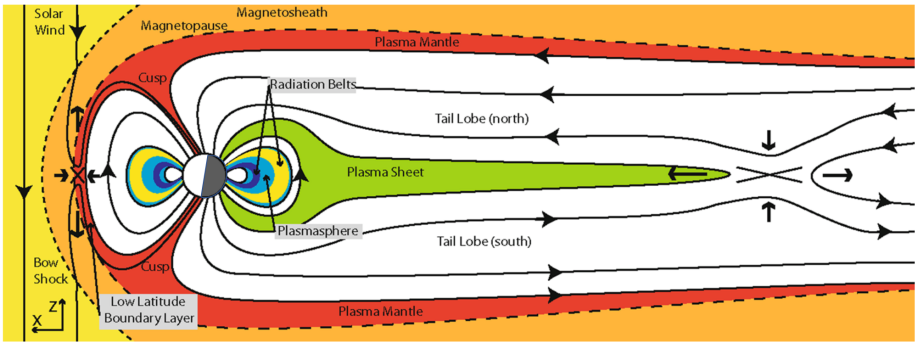

Figure 2.2: Structure and regions of the Earth's magnetosphere (Eastwood et al., 2015).

On the sunward side of the Earth, the solar wind compresses the magnetosphere and diverts along the flanks towards the nightside. On the nightside, the diverted solar wind sweeps the magnetic field and stretches it far out to form the magnetotail as shown in Figure 2.2. Since the solar wind is a supersonic wind, it creates a shock boundary outside the magnetosphere known as the bow shock (denoted with the outer dashed line in the figure). This slows down the solar wind and forms a region of thermalized subsonic hot and dense plasma with strong field called the magnetosheath (*Retinò et al.*, 2007, and references therein). This region is colored orange in Figure 2.2. The magnetosphere's general shape is controlled by the balance between the pressure exerted by the magnetosheath and the magnetosphere creating a boundary called magnetopause. Assuming the main solar dynamic pressure is coming from the ions, the pressure balance at the magnetopause can be written as

$$n_{sw} m_i v_{sw}^2 = \frac{B^2}{2\mu_0}, \tag{2.1}$$

where n_{sw}, m_i, and v_{sw} are the number density, mass and flow speed of the solar wind, respectively, B is the geomagnetic field strength and μ_o is the magnetic permittivity of the vacuum.

Inside the magnetosheath, the solar wind plasma and the geomagnetic field interact at the magnetopause. The location of this boundary is typically at a distance of ~10 Earth radii (R_E) from the Earth, where one R_E is 6371 km. The interaction between

the two fields largely depends on the IMF orientation. The most efficient interaction happens when the two magnetic fields are directed antiparallel, as shown in Figure 2.2. This enables the two fields to merge through a process called magnetic reconnection. In this process, the frozen-in field concept breaks down, allowing the plasma and the field to move separately. The magnetic field lines reconfigure and change their magnetic topology. The highly kinked and newly formed open magnetic field lines retreat and move away from the reconnection region, and the field and the plasma start to move together again. This process allows the solar wind plasma to diffuse through the open field lines and precipitate in the cusps, a region where solar wind plasma has a direct acess to the magnetosphere. The solar wind then drags the open field lines from the dayside over the polar cap (region of open field lines) onto the nightside, where the open field lines once again will reconnect to form closed field lines. The closed magnetic field lines convect into the inner magnetotail along the dawn and dusk flanks and then back to the dayside to complete the cycle. The entire cyclic process is known as the Dungey cycle (*Dungey*, 1961).

On the nightside, the magnetic field lines connected to the Earth tend to stretch far out, as shown on the right-hand side of Figure 2.2. Next to the magnetosheath, the major part of the magnetotail is covered by tail lobes, which consists of low-density cold plasma of predominantly ionospheric origin (*Haaland et al.*, 2017). The solar wind and the tails lobes' field lines are connected and form a plasma mantle boundary. The plasma mantle consists of cool magnetosheath plasma that moves in antisunward direction. Inside the lobes is the plasma sheet. It is a reservoir of hot and relatively dense plasma at the center of the magnetotail. It typically has a thickness of 4–8 R_E with 0.1–1 cm^{-3} electron density, 1 keV electron temperature, and 5 keV protons. In this region, the magnetic field pressure is dominated by plasma pressure. The magnetic field is relatively weak, especially around the magnetotail reconnection point. The plasma in the plasma sheet is primarily tied to the closed magnetic field lines and is responsible for a large fraction of the geomagnetic activity, in particular disturbances associated with magnetospheric substorms.

2.3 Magnetospheric substorm

In the open magnetosphere model proposed by Dungey (*Dungey*, 1961), the magnetopause and magnetotail reconnections are considered to be balanced. Hence, the magnetosphere is in a steady-state. However, the reality is different. For example, variations of solar wind parameters, such as changes in the direction of the IMF, will create an imbalance between magnetic flux loading and unloading between the dayside and nightside reconnection. The net amount of magnetic flux transported from the dayside reconnection will pile up in the magnetotail. This makes the magnetotail unstable, and the surplus magnetic energy stored in the magnetotail suddenly ejected in the form of particle thermal and kinetic energy through reconnection (*Angelopoulos et al.*, 2008). The events related to the explosive release of energy are commonly referred to as substorms (*Akasofu and Chapman*, 1961).

Satellites around geosynchronous orbit (6.6 R_E) observe magnetospheric changes during substorms (*Turner et al.*, 2017, and references therein). The main signatures of substorms in the magnetosphere are plasma sheet thinning and expansion, magnetic

field dipolarization, fast plasma flows (Bursty Bulk flows (BBFs)), energetic particle injection and intensified field-aligned currents, which can be associated with different phases of the substorm (*Angelopoulos et al.*, 1992; *McPherron*, 1970, 1972; *McPherron et al.*, 1973). During the growth phase, the magnetic flux from the dayside reconnection is transported over the poles and increases the open flux in the magnetotail lobes. If the loading of this flux is quicker than the unloading through nightside reconnection, pressure develops in the magnetotail and changes the magnetic field topology from a dipole-like to tail-like configuration. This increases the stress on the tail and results in thinning of the plasma sheet (*Nakamura et al.*, 2002). This is followed by a substorm onset, where the magnetic field suddenly relaxes from the stressed tail-like to a dipolar configuration due to the disruption of the cross-tail current. This reconfiguration is called dipolarization. Following the dipolarization occurs an earthward expansion of the heated plasma sheet. At this point, a sudden inward transport of energetic electrons and ions (tens to hundreds of keV) from the plasma sheet into the inner magnetosphere can be observed (*Dai et al.*, 2014; *Sandhu et al.*, 2018; *Turner et al.*, 2017). This sudden enhancement of the flux of energetic particles (2 or 3 orders of magnitude larger than the quiet time), called particle injections, contributes to the ring current's build-up (*Sandhu et al.*, 2018), resulting in geomagnetic storms and variability in the inner magnetospheric regions, such as radiation belts and plasmasphere (*He et al.*, 2016; *Millan and Baker*, 2012; *Pierrard and Cabrera*, 2006; *Zhang et al.*, 2017).

2.4 Particle motion in the magnetosphere

Once the solar wind particles find pathways to the magnetosphere, their motion is governed by the well known Lorentz force, which can be written as:

$$\mathbf{F} = q(\mathbf{E} + \mathbf{V} \times \mathbf{B}), \tag{2.2}$$

Where q is the particle's charge, $\mathbf{E}$ is the electric field, $\mathbf{B}$ is the geomagnetic field, and $\mathbf{V}$ is the particle's velocity. In the absence of an electric field, the particle will gyrate around the magnetic field with a frequency (called gyro or cyclotron-frequency, ω_g) given by:

$$\omega_g = \frac{\|q\|\|B\|}{m}, \tag{2.3}$$

where m is the mass of the particle. The radius with which the particle gyrates (called gyro radius, r) is given by:

$$r = \frac{mv_\perp}{\|q\|\|B\|}, \tag{2.4}$$

where $v_\perp$ is the perpendicular component of the particle's velocity. If we introduce a uniform electric field, the particle will experience a drift called electrodynamic drift v_E given by:

$$v_E = \frac{\mathbf{E} \times \mathbf{B}}{B^2}. \tag{2.5}$$

The above equations consider a uniform magnetic field, but often this is not the case in the magnetosphere. The geomagnetic field has gradients and curvatures, as illustrated

in Figure 2.3, which results in magnetic drifts. The gradient drift, v_{grad}, of particles can be written as:

$$v_{grad} = \frac{m{v_\perp}^2}{2qB^3}(\mathbf{B} \times \nabla \mathbf{B}), \tag{2.6}$$

where $v_\perp$ is the particle's perpendicular velocity, and $\nabla \mathbf{B}$ is the gradient of the magnetic field. Similarly the curvature drift, v_{curv} is given by:

$$v_{curv} = \frac{m{v_\parallel}^2}{q}\frac{\mathbf{R}_c \times \mathbf{B}}{{R_c}^2 B^2}, \tag{2.7}$$

where R_c is the radius of curvature and $v_\parallel$ is the particle's parallel velocity.

Suppose the Earth's magnetic field changes very slowly (or 'adiabatically') compared with the typical particle motion periodicities. These physical quantities are called adiabatic invariants. The three magnetic adiabatic invariants (the magnetic moment, longitudinal invariant, and drift (flux) invariant) can describe the main features of the motion of charged particles trapped in a slowly varying magnetic field in the magnetosphere.

The first adiabatic invariant, the magnetic moment μ is associated with the gyro motion of the particle, can be written as (*Baumjohann and Treumann*, 1996):

$$\mu = \frac{m{v_\perp}^2}{2B}. \tag{2.8}$$

μ is conserved as long as the variation of magnetic field B is small compared to the gyro period (equation 2.3), and the gyroradius (equation 2.4) is much larger than the magnetic field line curvature.

The second invariant, longitudinal invariant, is associated with the particle's bounce (mirror) motion. It is defined as the bouncing motion period of the trapped particles between two mirror points (i.e., the northern and southern hemispheres) on a magnetic field line, as illustrated in Figure 2.3(a). It can be expressed as:

$$J = \oint p_\parallel ds, \tag{2.9}$$

where $p_\parallel$ is the particle's momentum parallel to the geomagnetic field and ds is a distance element along the field line. J is invariant as long as the magnetic field varies in a time longer than the bounce period.

The third invariant, Φ, is the drift motion around the Earth as shown in Figure 2.3(b). This drift is due to the magnetic gradient and the curvature of the geomagnetic field. The combination of the two drifts can be described as:

$$v_{both} = ({v_\parallel}^2 + \frac{1}{2}{v_\perp}^2)\frac{\mathbf{B} \times \nabla \mathbf{B}}{\omega_g B^2}. \tag{2.10}$$

The particle's charge is involved in this equation, electrons drift eastward, and ions drift westward as shown in Figure 2.3 (a). Φ is defined as the total magnetic flux enclosed by the periodic orbit of a trapped particle. It can take the form of:

$$\Phi = \frac{2\pi m}{q^2}\mu, \tag{2.11}$$

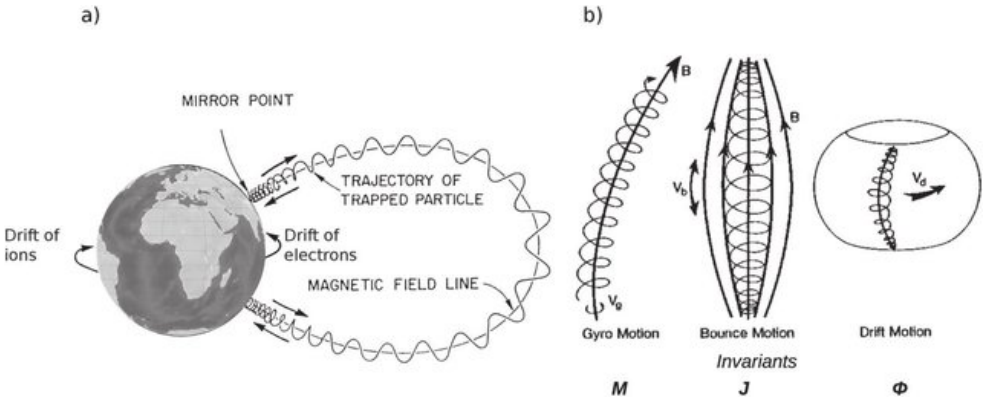

Figure 2.3: Particle motion in the magnetosphere (a) and associated constants of motion in an ideal magnetic field (adiabatic invariants) (b).

Φ is invariant whenever the frequency of the electromagnetic fields is much smaller than the drift frequency.

In the inner magnetosphere, it is possible that a charged particle keeps gyrating, bouncing, and drifting. This, for example, creates magnetospheric regions such as ring current, plasmasphere, and radiation belts. However, the mirror point where the particle is bouncing back depends on the angle between the local magnetic field and the particle's velocity when it enters the inner magnetosphere at the magnetic equator. This angle is known as the pitch angle. If the pitch angle at the entrance point corresponds to a mirror altitude less than 100 km, the particle will be lost (precipitate) in the neutral atmosphere instead of bouncing back. The set of angles where the particle will precipitate is called the loss cone.

The adiabatic invariants discussed above hold in quiet geomagnetic conditions and quasi-dipolar magnetic field configuration. However, during geomagnetic disturbance periods, the adiabatic invariants can be violated. If either one or two of the adiabatic invariants is violated, a particle can be accelerated through gyro-resonant interaction with plasma waves, diffused across the magnetic field, or pitch angle scattered and precipitated into the atmosphere. Such violation related processes are essential in the dynamics of inner magnetospheric regions, such as the radiation belt (*Baker et al.*, 2018; *Millan and Baker*, 2012; *Turner et al.*, 2012).

Various types of plasma waves, which can be electromagnetic, electrostatic or magnetosonic, are generated in the magnetosphere through the conversion of plasma and energetic particles' kinetic energy into wave energy. These plasma waves interact with the particles to accelerate and pitch angle scatter the particles themselves. Such wave-particle interactions in the magnetosphere are an essential component in the inner magnetosphere dynamics. Among numerous waves in the magnetosphere, chorus and electron cyclotron harmonic (ECH) waves' interactions with magnetospheric electrons are the dominant causes of pulsating aurora, which will be discussed in detail in Chapter 4.

ECH waves are electrostatic emissions with frequencies between the harmonics of the local electron cyclotron frequency dominantly around the odd integral half-harmonics. The loss cone instability of the ambient, hot plasma sheet electron distribution with a low-density cold component is thought to be the main driver of ECH

waves (*Horne*, 2003). These waves are localized to a few degrees of the magnetic equatorial zone of the magnetosphere and are observed most frequently in the night and dawn sectors (21–06 MLT) between 5 R_E and 10 R_E regions (*Ni et al.*, 2011; *Zhang et al.*, 2014). They are capable of scattering plasma sheet electrons at farthest distances (>8 R_E) in the non-dipolar magnetic field region of the outer magnetosphere.

Chorus wave emissions are intense electromagnetic and right-handed polarized whistler mode waves that are excited naturally in the low density region outside the plasmasphere and near the geomagnetic equatorial region of the magnetosphere (*Li et al.*, 2011). They are observed in two distinct frequency bands: lower and upper band. The lower band chorus (LBC) waves have frequencies between 0.1 f_{ce} and 0.5 f_{ce}, and the upper band waves have frequencies between 0.5 f_{ce} and f_{ce}, where f_{ce} is the equatorial electron gyro-frequency. The amplitude of both bands are generally higher during the geomagnetic active periods (*Li et al.*, 2011). They exist both in the nighttime (22–06 MLT) confined to magnetic equator and daytime (06-13 MLT) propagating to a much higher latitudes. They can also persist on the dayside at a distance above 7 R_E during low geomagnetic activity (*Li et al.*, 2009). The high amplitude chorus waves are mainly confined in the region from the premidnight to postdawn sector and inside 8 R_E. On average, the upper band chorus waves are stronger in the nightime than in the daytime and are restricted to regions within 7 R_E.

2.5 Radiation Belts

The discovery of radiation belts is dated back to the start of the space age. Van Allen discovered the radiation belts using the Geiger-Muller counter onboard Explorer 1, the first US satellite, in 1958 (*Van Allen et al.*, 1958). The radiation belts are doughnut-shaped regions comprised of trapped electrons and protons (Figure 2.3) that drift around the Earth. There are two separate radiation belts (Figure 2.4), the inner radiation belt located close to the Earth, at about 1–2 R_E, and the outer radiation belt, located at about 3–7 R_E (*Van Allen*, 1959; *Van Allen and Frank*, 1959). Protons and electrons form the inner radiation belt; however, the outer radiation belt is dominated by electrons. While the inner belt is usually stable, the outer belt is highly dynamic and variable, especially during active geomagnetic periods (*Reeves et al.*, 2003). Several competing processes control the dynamics of the outer radiation belt (for example see *Baker et al.*, 2016). Inward radial diffusion and local acceleration due to the transfer of energy from whistler-mode plasma waves to radiation belt electrons are the sources of the dynamics (*Baker et al.*, 2014). Electrons are removed continuously from the radiation belts through outward radial diffusion, magnetopause shadowing, and precipitation (*Shprits et al.*, 2006; *Turner et al.*, 2012; *Ukhorskiy et al.*, 2006).

The outer belt consists of trapped energetic electrons (from 0.1 up to 10 MeV) injected from the geomagnetic tail during substorms and are subsequently energized through wave-particle interactions (*Baker et al.*, 2018; *Millan and Baker*, 2012; *Shklyar*, 2017). The inner belt mostly contains energetic protons with energies up to 100 MeV and electrons in the range of hundreds of keV trapped by a stronger magnetic field compared to the outer belt (*Baker et al.*, 2018, and references therein). Electron and proton fluxes vary dramatically due to substorm-related injections and acceleration of particles from the magnetotail reconnection. Much is known about the

radiation belts from a suite of satellite observations in the magnetosphere such as Magnetospheric multiscale, Van Allen probes, Cluster, and GOES (*Li and Hudson*, 2019; *Ripoll et al.*, 2020). For example, new reports from Van Allen probes observations unravel the existence of a persistent intermediate/remnant electron belt that leads to three belt configurations (*Pinto et al.*, 2018) and significant achievements in understanding the ultrarelativistic electrons which are accelerated due to various wave-particle interactions (*Baker et al.*, 2014; *Kanekal et al.*, 2015). As shown in Figure 2.4 radiation belts host many technological infrastructures in space that most of us rely on. Therefore, modeling and predicting the behavior of radiation belts is very important (*Baker et al.*, 2018). Although there are significant efforts in modelling radiation belts' variations (*Tu et al.*, 2019, and references therein), there are still open questions about the dynamics and processes we do not fully understand (*Kessel*, 2016; *Ripoll et al.*, 2020; *Ukhorskiy and Sitnov*, 2013).

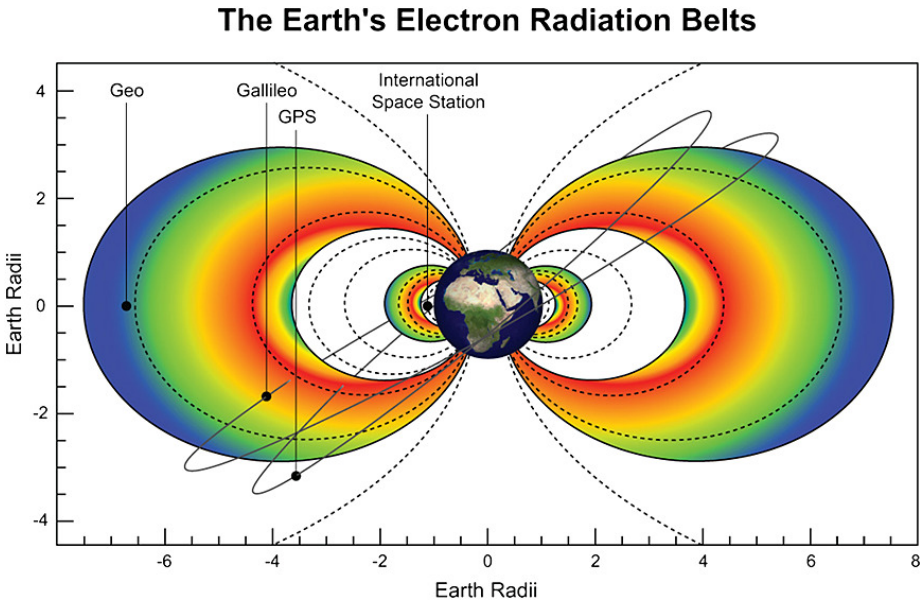

Figure 2.4: Schematic diagram of electron radiation belts and space-based technological infrastructures (Horne et al., 2013).

2.6 Earth's atmosphere

Earth's atmosphere is a gaseous region surrounding the Earth, which is retained by the Earth's gravity and extends from the surface up to about one thousand kilometers. It absorbs solar radiation and warms the surface. This region can be divided into different subregions based on different physical properties such as temperature, density, and composition. Based on temperature, the Earth's atmosphere can be divided into five subregions: troposphere, stratosphere, mesosphere, thermosphere, and exosphere (see Figure 2.5). From the Earth's surface up to around 10 km is called the troposphere, where the air is warmer near the Earth's surface and becomes colder higher up. The

troposphere is highly turbulent and hosts most of the terrestrial weather. Above the troposphere is a stable region, the stratosphere. In the stratosphere, temperature increases steadily due to the absorption of solar ultraviolet radiation by the ozone layer and reaches a maximum of around 50 km. The region above the stratosphere up to about 90 km is called the mesosphere. It has a decreasing temperature profile because of less gas molecules to absorb the solar radiation. Troposphere, stratosphere, and mesosphere account for 99% of the atmospheric mass with nitrogen (N_2) and oxygen (O_2). The region above the mesosphere is called the thermosphere. In the thermosphere, the temperature rises exponentially because of the absorption of higher energy parts of solar radiation until it reaches a steady value. The region beyond 600 km is called the exosphere, where the atmosphere gradually fades away into the interplanetary space. The mesosphere, stratosphere and lower thermosphere regions are also grouped as the middle atmosphere. The region above the middle atmosphere is called the upper atmosphere, where solar radiation and particle precipitation ionize the neutrals forming a plasma of ions and electrons. This partially ionized region extending from the mesosphere to the thermosphere is called the ionosphere.

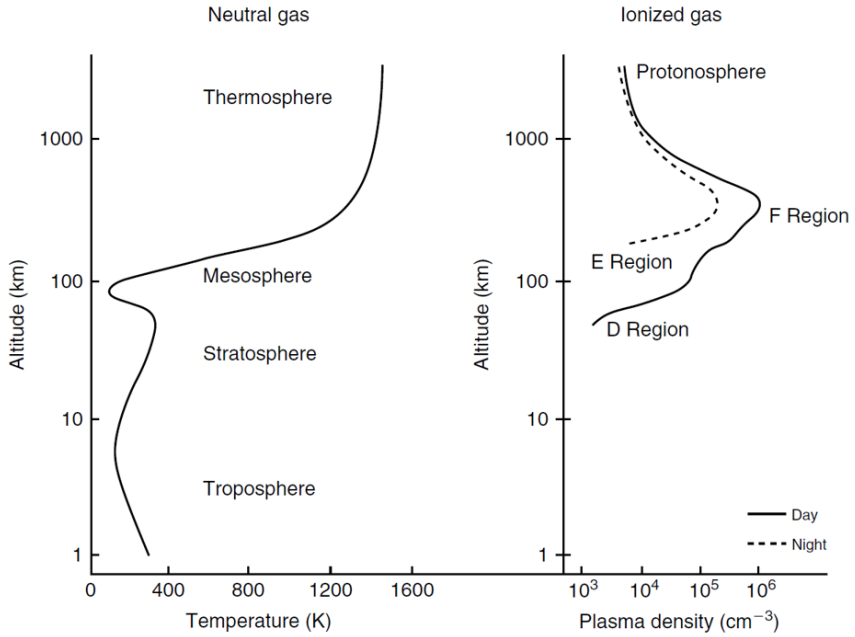

Figure 2.5: Altitude profiles of neutral atmospheric temperature (left) and ionospheric plasma density during the day and night (right) (Kelley, 2009).

2.6.1 Polar ionosphere

The ionosphere is a region of the Earth's atmosphere roughly located between 60 to 1000 km (see Figure 2.5), consisting of a relatively large number of free electrons and ions. The polar ionosphere is formed by photoionizations of neutrals with extreme

ultraviolet and X-ray wavelengths and particle precipitation from the magnetosphere. Galactic cosmic rays, Lyman-alpha scattering, and meteors can also contribute to the ionization process (*Hunsucker and Hargreaves*, 2002). Because the atmospheric compositions, densities, and ion production rates change with altitude, the balance between ionization and recombination processes leads to several distinct electron density peaks. Based on the peaks, the ionosphere can be divided into three subregions (D, E, and F). The D region is the lowest region of the ionosphere below 90 km, the E region is between 90 and 140 km, and the F region is above the E region with its peak around 300km. Most of the ionosphere is covered by F region which ranges from 140 km to 500 km. In the absence of sunlight, particle precipitation is the main source to maintain the electron density in both the D and E region.

The polar ionosphere is coupled with the magnetosphere through electric fields, field-aligned currents, and particle exchange (precipitation and outflow) and is highly dynamic (*Heelis*, 1982). Perhaps, the most complex region of the polar ionosphere is the D region. Many complicated and heavy/cluster positive and negative ions are formed in the D region due to frequent ion chemical reactions (*Brasseur and Solomon*, 2005). The primary ionization sources for the D region are the Lyman-alpha, solar X-rays, and secondary cosmic rays. D region is most effective in attenuating high-frequency (HF) radio waves (*Hunsucker and Hargreaves*, 2002) and increasing cosmic noise absorption (CNA). It can severely interfere with HF radio wave transmissions if its electron density is enhanced by energetic electron precipitation and solar proton events.

2.6.2 Discrete and diffuse aurora

Aurora, officially called aurora borealis in the northern polar region and aurora australis in the southern polar region, is the most known and easily identifiable space weather phenomena in the Sun-Earth connection. It is an emission of light caused by the collisions between the solar wind and magnetospheric plasma particles and the neutrals in the Earth's polar atmosphere. The spectrum of auroral emissions cover the X-ray to the infrared depending on the atmospheric gas and the precipitating particles' energy. The neutral constituents and molecular ions involved in the dominant auroral emissions are N, O, N_2, N_2^+, O_2, O_2^+. They have specific emission lines. The aurora's dominant emissions are from the 557.7 nm green atomic oxygen line and blue emission at 427.8 nm from molecular nitrogen around 100 km altitude (*Brekke*, 2015). Red line atomic emission at 630 nm is dominant in the ionosphere's F region, altitudes between 150 and 300 km. A continuous band of aurora around the polar regions, called the auroral oval, can be found on average extending from 68° to 78° geomagnetic latitudes in both hemispheres. In the auroral oval, the aurora is seen in different structures and colors, indicating different categories. Typically, a division is made into two broad categories of the aurora, which are diffuse and discrete aurora.

Discrete aurora is highly structured and dynamic, usually seen as an intensification of oxygen green and red line emissions. It often dominates the nightside aurora around the magnetic midnight and near local magnetic noon. The field-aligned acceleration is the primary mechanism behind the nighttime discrete aurora types, such as the auroral arcs, spirals, curls, folds, and auroral bulge (*Borovsky et al.*, 2020). The local noon

discrete auroras are caused by magnetosheath particles precipitating along the open field lines (*Frey et al.*, 2019). In general, there are two mechanisms behind discrete aurora, the quasi-static electric field producing inverted V-type (monoenergetic) aurora and the dispersive Alfven waves producing the broadband aurora (*Newell et al.*, 2009).

Diffuse aurorae appear as relatively homogenous, weak emission located at the auroral oval's equatorward part. They occur predominantly in the post-midnight sector and can also be observed in the daytime (*Ni et al.*, 2016). The emission and ionization of diffuse aurora occur in the E region, around 100 km altitude (*Nishimura et al.*, 2020). The sources of the diffuse aurora electrons are predominantly in the central plasma sheet ($> 8\,R_E$) and occasionally in the outer radiation belt (around $5\,R_E$) (*Ni et al.*, 2016). The electrons are scattered into the loss cone by the electron cyclotron harmonic (ECH) waves and the whistler-mode waves (*Ni et al.*, 2008, 2016; *Nishimura et al.*, 2013; *Thorne et al.*, 2010). The energy of diffuse aurora electrons lies below 20 keV. Furthermore, diffuse aurorae provide the largest contribution to the global energy deposition in the magnetosphere-atmosphere coupled system (*Newell et al.*, 2009).

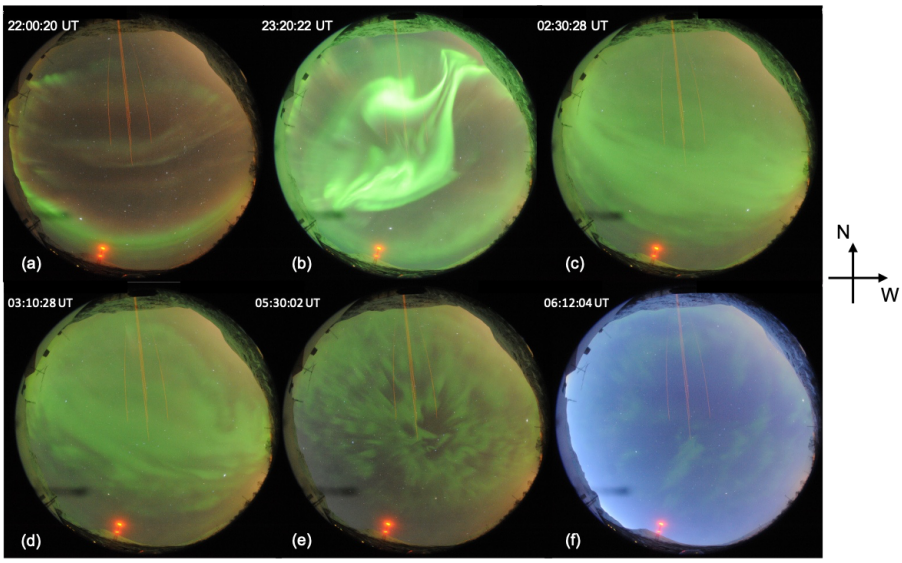

Figure 2.6: Nighttime all-sky camera observations of aurora on January 21-22, 2015 at Tromsø (69.58°N, 19.21°E). An example of substorm related auroral structures: growth phase (a), expansion phase (b), and recovery phase (c-f). Source: `http://polaris.nipr.ac.jp/~acaurora/aurora/Tromso/`

Nighttime auroral structures are also a signature of substorms, collectively referred to as auroral substorms and are the ionospheric counterparts of the magnetospheric substorms discussed in section 2.3 (*Akasofu*, 1964). The growth phase of a substorm usually starts when the southward IMF is coupled with the dayside magnetosphere through reconnection. This can be identified as an auroral arc moving equatorward attributed to magnetic flux buildup in the stretched magnetic field topology on the nightside. Immediately before the breakup and at the substorm onset, the auroral arc brightens. Within a few minutes, a sudden and intense increase in brightness and poleward motion of different dynamic and fast-moving auroral structures (Figure 2.6 (b)), such as streamers,

spirals, and westward traveling surge. During the recovery phase, the poleward moving aurora intensity will fade away, and diffuse aurora become dominant, as shown in Figure 2.6 (c). Within the diffuse aurora, there is a relatively structured diffuse aurora in the post-midnight to morning sector, called pulsating aurora, as illustrated in Figure 2.6 (d-f). For example, during the recovery phase of the substorm shown in Figure 2.6 (d), pulsating aurora emerges on the equatorward side of the all-sky camera and continues to extend the whole field of view until late morning (Figure 2.6 (f)).

The energy deposition varies correspondingly along the substorm evolution. Immediately after the substorm onset, usually between 22 and 00 MLT, a sharp increase up to four-fold in the auroral power can be observed (*Newell et al.*, 2001). In the post-midnight period, the auroral power starts to recover very slowly. The diffuse and pulsating aurora, which often lies in the post-midnight sector are known to be associated with higher electron energies and lower fluxes. Diffuse aurora is the dominant aurora, which constitutes most of the energy flux deposited in the atmosphere (*Newell et al.*, 2009).

2.6.3 Middle atmosphere

The middle atmosphere includes the stratosphere, mesosphere, and lower thermosphere. It includes the ozone layer, the coldest part of the atmosphere (summer mesopause), polar mesospheric clouds, and overlaps with the ionosphere. It is where meteors ablate, and where airglow and aurora are emitted in a wide range of wavelengths. Its structure and composition are determined by the interplay between radiative and dynamical processes as well as photochemical reactions. Ozone, which is found between 15 and 100 km altitude as shown in Figure 2.7, is an essential constituent of the middle atmosphere in determining the chemical and radiative budget (*Brasseur and Solomon*, 2005). The changes in the ozone balance in this region can also propagate to the troposphere and affect the polar climate variability (*Brasseur and Solomon*, 2005; *Seppälä et al.*, 2009). As the stratosphere is too low for in-situ satellite observations and too high for balloon measurements, the only direct observation of the region is by sounding rockets, which are quite expensive. This makes the middle atmosphere studies challenging.

In general, atmospheric dynamics is typically driven by the heat differences induced by the inhomogeneous insolation. There exists an upward cross-tropopause transport in the tropics and downward in the extratropics as part of a global mass circulation in the stratosphere (yellow arrows in Figure 2.7). This occurs as an indirect response to zonal (westward) forcing in the stratosphere, caused by the breaking of large-scale waves, for example, planetary waves (green arrows), propagating from the troposphere as shown in Figure 2.7. This large-scale circulation in the stratosphere is referred to as Brewer-Dobson circulation (BDC), which systematically transports ozone poleward and downward. Due to the asymmetric distribution of land-sea thermal contrasts and topography between northern and southern hemispheres, planetary waves are stronger in the northern hemisphere. Thus, the Arctic stratosphere is more dynamic than the Antarctic. In addition, BDC circulation is more substantial in the wintertime because stratospheric winds in the summertime filter planetary waves. Pole to pole extended wave-driven circulation (residual circulation) exists in the mesosphere primarily due to

gravity waves (pink arrows) propagating up from the troposphere.

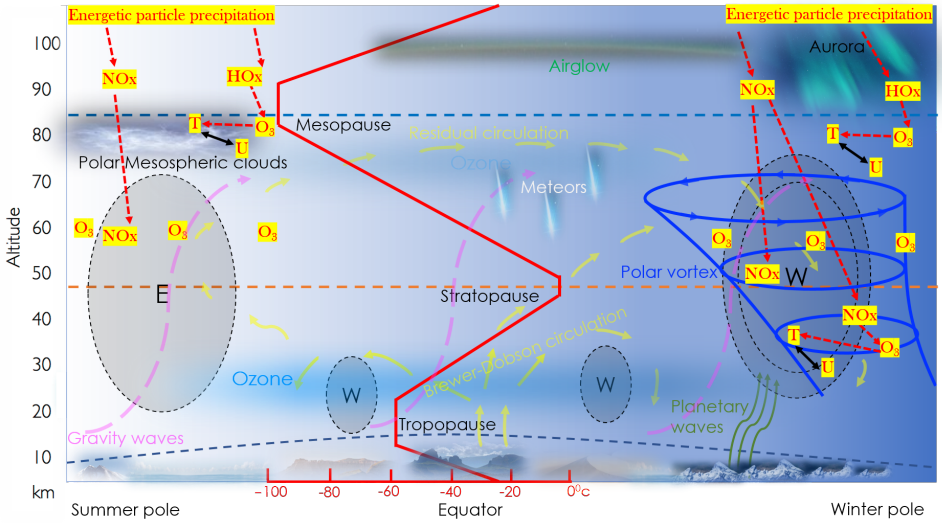

Figure 2.7: Low and middle atmospheric circulation, winds, waves, altitude profile of temperature, phenomena and processes. T denotes temperature and U denotes the zonal wind.

During winter, the polar region is not heated in absence of solar radiation, this forms a meridional temperature gradient. Temperature imbalance causes meridional winds which then turn right due to the coriolis force on Northern Hemisphere (NH) and form west-east directed winds (blue arrows in Figure 2.7). The circumpolar cyclone created by the winds is called the polar vortex. It forms in September and persists until April (*Kidston et al.*, 2015). Vertically, it extends from tropopause to mesosphere as illustrated in Figure 2.7. However, when the jet (the strong wind following the edge of the vortex) is weak, planetary waves can propagate upward and dissipate momentum, which starts to decelerate the jet or, in some extreme cases, reverses its direction and induces an increase of temperature and weakening of the vortex. This reversal of jet to westward is followed by the polar vortex displacement or split into two cells. This phenomenon is observed in NH due to the presence of planetary wave activity originated through the land-sea contrast and the Earth's topography in this hemisphere.

2.6.4 Mesospheric ozone chemistry

As discussed in the previous section, ozone is an important constituent in the stratospheric and mesospheric regions. The principal reaction that leads to the production of ozone (O_3) is a three body reaction:

$$O + O_2 + M \longrightarrow O_3 + M, \tag{2.12}$$

where M is the number density of air molecules. The main reactions producing oxygen atom and molecular oxygen for the above reaction involve photodissociation by the sunlight are:

$$O_2 + h\nu \longrightarrow 2O, \tag{2.13}$$

and

$$O_3 + h\nu \longrightarrow O_2 + O, \tag{2.14}$$

Locally, three-body reactions can also produce oxygen molecules

$$O + O + M \longrightarrow O_2 + M, \tag{2.15}$$

and

$$O_3 + O + M \longrightarrow 2O_2 + M, \tag{2.16}$$

Reactions (2.15) and (2.16) are highly dependent on altitude. In the stratosphere, atmospheric density and pressure are so high that the loss of ozone through reaction (2.14) is instantaneously followed by the production of oxygen molecule by reactions (2.15) and (2.16) and oxygen atom by reaction (2.13). The net reaction leads to ozone production through reaction (2.12). The decrease in pressure in the mesosphere and lower thermosphere makes the three body reactions (2.15) and (2.16) slow and gives a longer lifetime for oxygen atom which becomes abundant. In the nighttime, there is no production through (2.13) and (2.14), thus, reaction (2.12) dominates the production of ozone.

Apart from the solar radiation coming from the Sun, in polar regions, the precipitation of energetic particles deposit their energy and change the atmospheric chemistry. Energetic particle precipitation (EPP) result in the production of odd Hydrogen ($HO_x = H + OH + HO_2$) and odd Nitrogen ($NO_x = N + NO + NO_2$) at the mesospheric or lower thermospheric region. Due to the positive ion chemistry in the middle atmosphere (*Brasseur and Solomon*, 2005), the energetic particle precipitation produces HO_x from water vapour (H_2O). Above 60 km, HO_x triggers a catalytic reaction:

$$\begin{aligned} H + O_3 &\longrightarrow OH + O_2 \\ OH + O &\longrightarrow H + O_2. \end{aligned} \tag{2.17}$$

The net reaction efficiently removes O_x as:

$$O + O_3 \longrightarrow 2O_2, \tag{2.18}$$

Photodissociation of N_2 by solar EUV and X-rays is the main source of mesospheric and thermospheric NO_x. However, energetic particle precipitation can also produce NO_x. The abundant neutral molecules, O, O_2, and N_2, in the atmosphere can be ionized or dissociated by the EPP to produce ions (N_2^+, N^+, O^+, and O_2^+), electrons and N. These ions will further react with O, O_2, N_2 to produce N. Then, at the mesosphere NO will be formed by a reaction:

$$N + O_2 \longrightarrow NO + O, \tag{2.19}$$

NO can produce NO_2 through many reactions, but the dominant one is the reaction with ozone.

$$NO + O_3 \longrightarrow NO_2 + O. \tag{2.20}$$

During sunlit conditions, NO_2 can quickly be converted back to NO through photodissociation and oxidation (*Rusch et al.*, 1981). NO can also be destroyed by photolysis and cannibalistic reactions (*Brasseur and Solomon*, 2005). The above-mentioned more

complicated sets of reactions are more efficient than the production of NO through the oxidation of nitrous oxide (i.e., $N_2O + O^1D \longrightarrow 2NO$). During the polar winter months, the mesospheric NO_x will survive many hours, even months and can be transported downwards, as shown in Figure 2.7) (*Seppälä et al.*, 2007b). This leads to ozone depletion through the following catalytic reaction:

$$\begin{aligned} NO + O_3 &\longrightarrow NO_2 + O_2 \\ NO_2 + O &\longrightarrow NO + O_2 \end{aligned} \tag{2.21}$$

The net reaction becomes:

$$O + O_3 \longrightarrow 2O_2, \tag{2.22}$$

For the instantaneous ozone loss in the mesosphere, HO_x is more important than NO_x. In the absence of sunlight during winter and spring NO_x, which has a longer life span, can be transported down to the stratosphere, especially during winter inside the polar vortex (right-hand side of Figure 2.7), and deplete ozone through the catalytic reactions. Such a depletion of ozone will affect the stratosphere's radiation budget and ultimately global circulation. EPP's impact on the middle atmospheric ozone may influence the local temperature gradient to drive a zonal wind and affect the polar vortex variability, and eventually, climate variability.

Chapter 3

Measurements and methods

The results presented in this work are based on ground-based and satellite observations as well as ion chemistry model results. All-sky camera data from Magnetometers Ionospheric Radars All-sky Cameras Large Experiment (MIRACLE) network and from National institute of polar research (NIPR) in the both hemispheres were used to identify pulsating aurora events. EISCAT radars at Tromsø, SuperDARN radars in the southern hemisphere, KAIRA riometry in Kilipisjärvi, Northern Finland, low altitude satellites, and Southampton electron transport and ion chemistry model were used to characterize the energetic electron precipitation during pulsating aurora. The middle atmospheric chemistry effects of the PsA energetic electrons were studied using the one dimensional Sodankylä ion chemistry (SIC) model developed by the Sodankylä Geophysical observatory. In this chapter, we briefly introduce all these instruments and the models used in this thesis.

3.1 All-sky cameras

FMI-MIRACLE ASC stations

All-sky Camera (ASC) is an important optical device used to study ionospheric phenomena and upper atmospheric disturbances, such as aurora, airglow, and travelling atmospheric (ionospheric) disturbances. Since mid 1900s ASC have been a common tool and a huge data source to study auroral dynamics in relation to the coupling processes within the magnetosphere-atmosphere system. A typical ASC consists of a fish-eye lens, filter wheel, optics, and a detector (shown in Figure 3.1 (a) and (b)) and has a 180-degree of field of view. The Finnish meteorological institute (FMI) auroral imaging started during the international geophysical year (IGY) 1957–58. Since then, the cameras have been upgraded in three phases. The first generation of cameras used a black and white films and were operated until 1973. They were replaced by the color film cameras operated until 1997. In 1996, FMI replaced the colored film cameras with digital cameras (*Syrjäsuo*, 2001). After 2007, some of the camera detectors are upgraded from intensified charge coupled device (ICCD)(Figure 3.1 (a)) to electron multiplying CCD (EMCCD) (Figure 3.1(b)) (*Sangalli et al.*, 2011).

ASC observations of aurora require dark and clear skies with no light contamination. This makes the imaging season limited in the winter time at polar regions. The imaging season in the NH auroral region starts in September and ends in April. In paper

I and II we used FMI-ASC from MIRACLE network which are located in the auroral region (ABK, KEV, KIL, MUO, and SOD stations) as shown in Figure 3.1. The ASC data used in these papers span the years between 1997 and 2020, therefore all the data are from ASC with ICCD and EMCCD detectors. One ASC image covers a circular area with a diameter of about 600 km at 110 km altitude. Keograms are often used to quickly analyze auroral evolution throughout the night. They are created by extracting north-south pixel columns of consecutive individual all-sky images and stacking them in time. For further analysis an ewogram, an east-west counterpart of a keogram can be developed, this will be discussed in Chapter 3. The ASC filter wheel shown in Figure 3.1(a) and (b) hold 3 inch filters at wavelengths of 427.8 nm, 438.0 nm, 540.0 nm, 557.7 nm, 620.0 nm, 630.0 nm with a bandwidth of 2 nm. Most of our event identification is through 557.7 nm filter, however, for a few occasions we used the 427.8 nm filter as a substitute. An example of a keogram at 557.7 nm filter provided at FMI-MIRACLE database on February 18 2017 is shown in Figure 3.2.

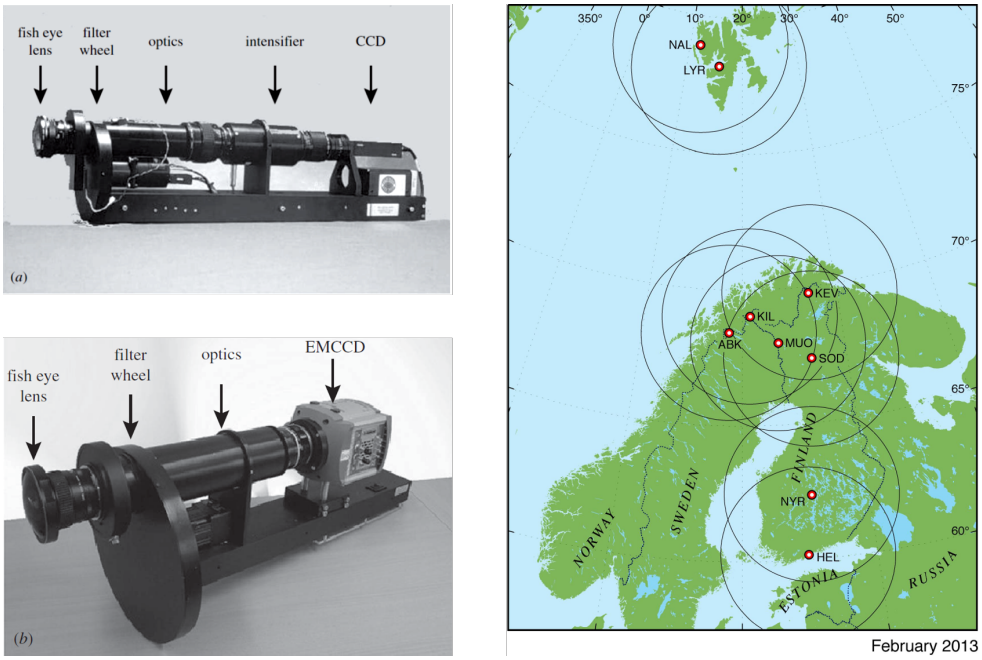

Figure 3.1: Setup of MIRACLE ASC with ICCD (a) and with EMCCD (b). FOV of 9 ASCs in the MIRACLE network, six of which belong to FMI, two are operated by SGO, and one by Italian space institute in Rome. In this study we used the five ASCs located in the auroral oval region (ABK, KEV, KIL, MUO, SOD). Source: https://space.fmi.fi/MIRACLE/ASC/?page=locations.

Figure 3.2 shows two clear substorms, where the first started after 17:30 UT and the second one after 22 UT. Both substorms showed growth, expansion and recovery phases. During the recovery phases, pulsating aurora which is identified as vertical stripes in the keogram is evident. Pulsating aurorae occurred in this keogram between 20 and 21:30 UT and after 23:30, however, between 2 UT and 4 UT pulsating aurora was visible in the far North location and started to cover more area of the FOV of the camera after 4 UT. At 5 UT the camera stopped operating due to sunlight.

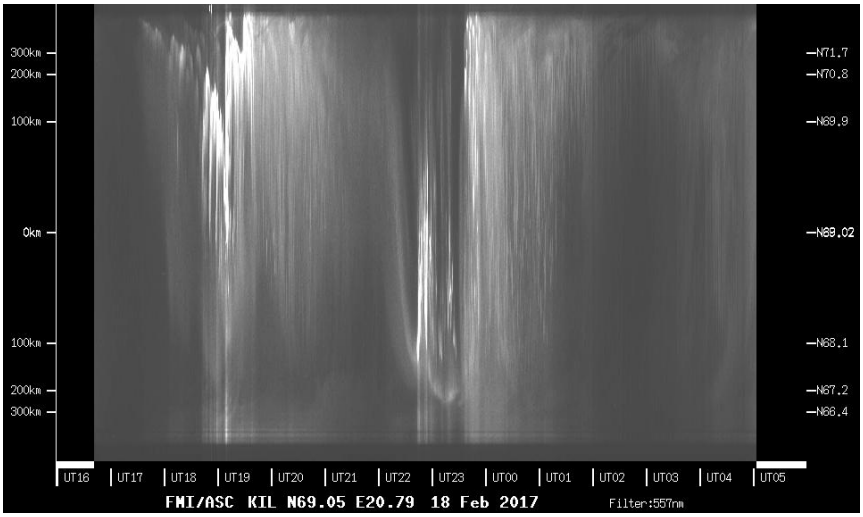

Figure 3.2: Example of keogram available at the FMI-MIRACLE database for PsA event identification. The horizontal axis is time in UT, and the vertical axis is distance from the ASC location to the north and south (right hand side of the vertical axis). In this particular case 3 PsA events were observed: between 20 and 21:30 UT, 00 and 02:30, and after 4 UT until the camera stopped operating due to sunlight. Source: https://space.fmi.fi/MIRACLE/ASC/?page=keograms.

National institute of polar research (NIPR) ASC stations

In Paper III, we used auroral images from fisheye Nikon 8 mm/F2.8 color digital camera located at Syowa station in the Antarctica. The camera is operated by the National institute of Polar research (NIPR) in Japan. It is programmed to capture images with exposure time of few seconds and image cadence between 6 and 30 seconds. The imaging season in the southern hemisphere is between March and October. A sample keogram available in NIPR database is displayed in Figure 3.3. Two PsA events are marked with yellow rectangles. The second PsA was interrupted by termination of ASC operation due to sunlight. The auroral quicklook viewer of NIPR ground-based network [1] was used to classify PsA into different categories.

In paper IV, we used data from Watec monochromatic Imager (WMI) located at Tromsø and operated by NIPR. It consists of a highly sensitive Watec camera, a fish-eye lens and optical band-pass filters at 428 nm, 558 nm, and 630 nm with bandwidth of 10 nm. The system is capable of obtaining images with the time resolution of 1 second, which is suitable to study the high spatio-temporal variations of substorms and pulsating aurora. A detail description of the WMI system is available at *Ogawa et al.* (2020). In this thesis, we used data from the green line emission (at 558 nm). The same approaches explained above and the quicklook viewer at NIPR network were used to identify PsA events and classify them into different types.

[1] http://pc115.seg20.nipr.ac.jp/www/AQVN/evs1.html

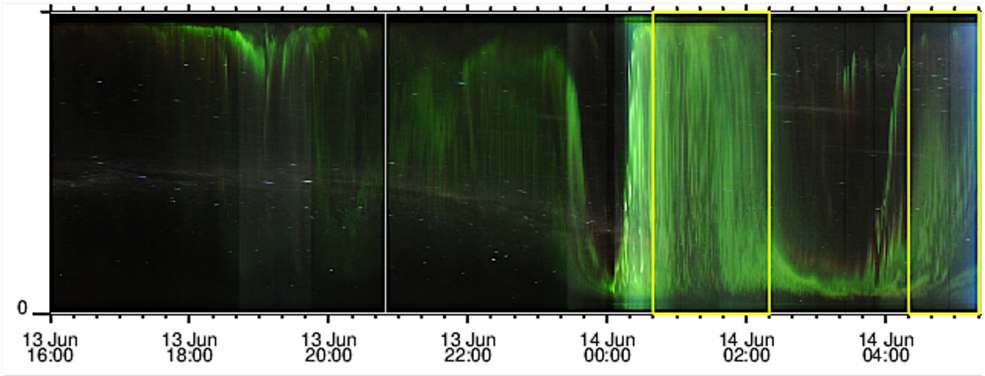

Figure 3.3: Example of keogram on June 13–14 2015 available at Syowa station. PsA events are marked with yellow rectangles (Bland et al., 2019).

3.2 Low altitude satellites

Low altitude (low Earth) orbit satellites have a nearly circular orbit at a height between 250 to 2000 km from the Earth's surface. The orbital speed mainly depends on the altitude, where at low altitude they have to move fast to overcome the Earth's gravity. They make 12–16 orbits per day and at a given location they can be observed above the horizon for about 5 to 20 minutes duration. Low altitude satellites can be inclined between 0° and 90° above the equatorial plane. The orbit can be at low inclination to study equatorial and low latitude regions only, or high inclination to pass over the polar region. A particular type of polar orbiting satellite is the sun-synchronous orbit which is fixed relative to the Sun making the satellite pass over the same location at the same local time. This makes them ideal for monitoring, for example, weather patterns and study how the weather evolve over the years. A satellite in a sun-synchronous orbit would usually be at an altitude of between 600 and 900 km making it to travel at a speed of approximately 7.5 km/sec. Satellites at the low Earth orbit have a typical lifetime of 7–10 years due to the effect of the atmospheric drag on their orbit. The satellites also encounter protons, electrons, heavy ions and neutrons, and through time the particle detectors onboard will degrade.

DMSP

The Defense Meteorological Satellite Program (DMSP) maintains a constellation of Sun-synchronous, near-polar orbiting satellites, at 98° inclination and an altitude of approximately 830 km. They have orbital periods of roughly 101 minutes, so they would orbit the Earth 14.3 times in 24 hours. DMSP satellites carry different instruments that have been providing important environmental and space weather information since mid-1960s. Among the instruments, the special sensor electron and ion spectrometers (SSJ4 and SSJ5) monitor the energy flux of electrons and ions that precipitate from the Earth's magnetosphere.

The SSJ4 detectors are flown in the DMSP series from Flight 6 (F6) to F15 and measure the flux of precipitating electrons and ions in the range of 30 keV to 30 eV. They consists of an array of four cylindrical, curved plate, electrostatic analyzers which are

grouped into high and low energy measurements for each of ions and electrons. Each particle detector has 20 channels spaced at equal intervals in energy on a logarithmic scale. The two low energy detectors consist of 10 channels measuring particle energies at 30, 44, 65, 95, 139, 204, 300, 440, 646 and 949 eV. The high energy detector measures particles in 10 channels at 0.949, 1.392, 2.04, 3.0, 4.4, 6.46, 9.45, 13.9, 20.4 and 30 keV. The measurements are centered on a local vertical within a solid angle of 4° by 5°, and 2° by 5° for the low and high energy detectors, respectively. A complete description of SSJ4 is found in (*Hardy et al.*, 1984).

The SSJ5 detectors are flown in the DMSP flight F16 to F19. They consist of a pair of nested triquadrispherical (270°) electrostatic analyzers with a field of view of 4° by 90° fan for electrons and ions. The 90° field of view is divided into six 15° sectors. The electron and ion counts from all the six sectors are summed once per second to provide the same output as the SSJ4 detectors. One of the data sources we used in this thesis is from SSJ4/5 sensors. Onboard DMSP flights from F13 to F19 where F13 to F15 have SSJ4 detectors and the rest SSJ5 detectors. Data from these detectors have been very important in characterizing auroral electron and ion precipitation (*Hardy et al.*, 2008, 1989). In Paper I, precipitating electrons measured by SSJ4/5 detectors were used to characterize the energy flux spectrum of pulsating aurora electrons. SSJ4/5 data set is available at different scientific organizations covering different subsets of the data. We used the data from Cedar Madrigal database. Details about the sensors and particle flux construction is available at (*Redmon et al.*, 2017).

POES

The Polar orbiting environmental satellites (POES) are polar orbiting Sun-synchronous satellites at an altitude of approximately 850 km with orbital period around 100 minutes. They have continuously monitoring the near-Earth environment since 1978. Like DMSP, they carry various instruments to monitor meteorological, oceanographic and space weather activities. The space environment monitor 1 (SEM-1) before 1998 and space environment monitor 2 (SEM-2) after 1998 are being flown with the satellites to measure the influx of energetic ions and electrons into the atmosphere. In this study, we used the SEM-2 that has two detectors: Total electron detector (TED) and the medium energy proton and electron detector (MEPED) which measure protons and electrons at different energies. TED consists of eight electrostatic analyzers that are grouped into two of four channels and oriented differently with respect to the local magnetic field. One group of four channels is oriented 0° and the other group 30° as shown in the schematic diagram on Figure 3.5. Among the four channels in the specific orientation, two of them measure electrons and the other two measure protons. The two electron detectors measure the energy range 50 eV to 1 keV, and 1 keV to 20 keV. The data are available as differential fluxes at the four channels on both 0° and 30° telescopes with energy bands of 0.15–0.22 keV, 0.69–1 keV, 2.12–3.08 keV, and 6.50–9.46 keV. In this work, we only used the 0° telescope fluxes to account for the lower limit of precipitating electrons.

MEPED includes eight separate solid-state energetic particle detectors that measure electrons and protons from 30 keV to 200 MeV. Four of the detectors measure electrons and protons in the energy range between 30 keV and 6.9 MeV. The remaining four omni-directional detector systems used to measure energetic protons incident on

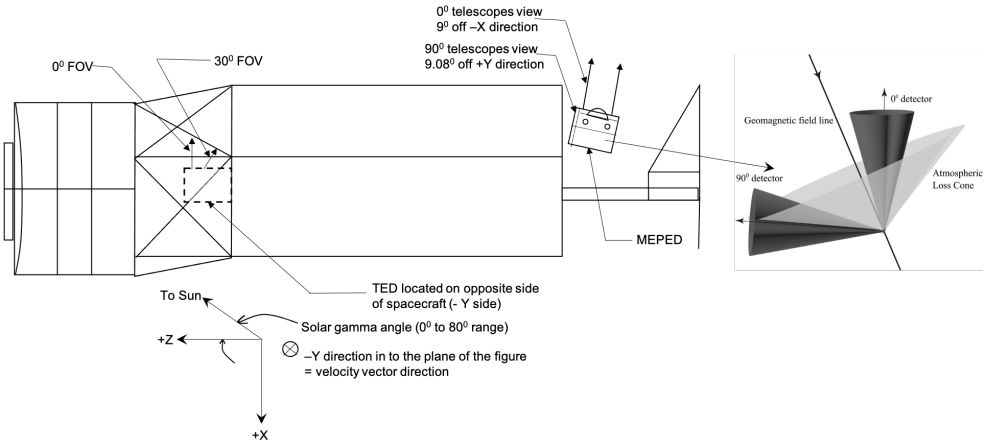

Figure 3.4: Schematic of POES satellite with MEPED and TED detectors (Green, 2013), and detectors' orientation with respect to the geomagnetic field line, modified from Nesse Tyssøy et al. (2016).

the solid-state detectors over a wide range of angles (*Evans and Greer*, 2000). Among the four energetic particle detectors, two are measuring the electrons with energies in the range between 30 keV and 2.5 MeV, and the other two measuring protons in the range between 30 keV and 6.9 MeV. For each particle type the detectors are grouped into two as 0° and 90° detectors as shown on the right hand side of Figure 3.5. As illustrated in this Figure, the 0° detectors at high latitudes measure precipitating particles in the atmospheric loss cone, while the 90° detectors measure a mixture of trapped and precipitating particles depending on their location. This indicated that the 0° detectors will underestimate and the 90° detectors will overestimate the flux of precipitating particles. To make use of both detectors and mitigate the overestimation from the 90° detectors, *Nesse Tyssøy et al.* (2016) estimated the precipitating fluxes in the atmospheric loss cone by fitting fluxes from both detectors on to the Fokker-Planck equation of particles. Low energy proton contamination in the electron detectors were corrected. In addition, cross contamination of relativistic electrons in the proton detector provides an extra energy channel. This provides us four energy channels at $>$ 43 keV, $>$ 114 keV,$>$ 292 keV, and $>$ 756 keV. Further details about correction of contamination and construction of energy channels can be found in *Nesse Tyssøy et al.* (2016); *Ødegaard et al.* (2017); *Sandanger et al.* (2015). The integral fluxes obtained in the four channels are converted to differential fluxes and fitted with power law function to extrapolate data points in the process of constructing the spectrum by combining with the TED differential flux measurements.

FAST

Fast auroral snapshot explorer (FAST) was designed and built by NASA's Goddard space flight center and was launched in the year 1996 to 83° inclination elliptical orbit of 350 km by 4175 km (*Carlson et al.*, 1998). Its orbital motion evolves throughout the year making the satellite cross the auroral zones four times per orbit over a wide range of altitudes, local times, and seasons. The orbital period is 133 minutes and it spins

around an axis normal to the orbital plane every 5 seconds. It has fluxgate and search coil magnetometers to measure magnetic field, electric field and Langmuir probes to measure electric field, ion mass spectrograph to measure major ion distributions, and quadrispherical electrostatic analyzers to measure electrons and ions pitch angle distributions (*Pfaff et al.*, 2001). The electrostatic analyzers onboard FAST is designed to measure auroral electrons and ions with a wide dynamics range and a high sensitivity, energy, time and angular resolutions. It can measure full pitch angle electron and ions flux distributions 48 energy bins at different angles in 1 second time resolution. The measured energy range for electrons is between 4 eV and 30 keV, and for ions between 3 eV and 25 keV (*Carlson et al.*, 2001). Electron measurements from the electrostatic analyzers at low pitch angles ($< 3^{\circ}$) were used in Paper I.

3.3 Ion and neutral chemistry models

Sodankylä ion and neutral chemistry model

The Sodankylä Ion Chemistry model (SIC) was first introduced and used to interpret incoherent radar measurements by *Burns et al.* (1991) including 35 ion chemistry in the D and lower E regions for geomagnetic quiet conditions. In addition to the quiet time external ionization sources, photoionization and galactic cosmic rays, *Turunen et al.* (1996) included proton and electron precipitation as additional ionization sources. Later, *Verronen et al.* (2002) and *Verronen et al.* (2005) extended the model to include neutral chemistry and vertical transport that takes molecular and eddy diffusion into account. The latest version of the model introduced by *Verronen et al.* (2016) consists of hundreds of reactions involving 70 ions (41 positive and 29 negative) and 34 neutrals. The background neutral atmosphere and temperatures are taken from MSIS-00 model and for daily changing solar spectrum it uses SOLAR2000 model. It can be run in either steady-state or time-dependent mode between 20 and 150 km altitudes with 1 km resolution and chemical step of 15 minutes. The model has been used to study the particle precipitation effects on the middle atmosphere. The chemical reaction part of the model is now included in the whole atmosphere community climate model with ion chemistry extension (WACCM-D). This global model is used extensively in the scientific community. For extensive details of SIC model see (*Verronen et al.*, 2016, and references therein). In Paper I, we used the spectrum of precipitating electrons during pulsating aurora as an external forcing in this 1D model to study the chemical change in the atmosphere.

Southampton electron transport and ion chemistry model

The auroral model used in this study combines the electron transport code (*Lummerzheim and Lilensten*, 1994) and ion chemistry and energetics model (*Lanchester et al.*, 2001; *Palmer*, 1995). It incorporates the principal positive ions and minor neutrals species between 80 and 500 km altitude and solves the coupled continuity equations for them. The main inputs to the transport code are the energy flux and distribution of electrons. In addition, the solar activity parameters, AP, daily F10.7, and 81-day average F10.7 are used as inputs. In Paper IV, we used spectra constructed from direct measurement of precipitating electrons from an overpassing POES satellites as an en-

ergy input to the model. The outputs of the model are the time evolution of ion and neutral density, electron and ion temperature, and selected optical emission rates. Assuming equal ion and electron pairs during ionization due to particle precipitation, the ion density can also be considered as electron density. In Paper IV, we compared this electron density with the EISCAT electron density measurements during different types of pulsating aurora.

3.4 Radar measurements

3.4.1 EISCAT radars at Tromsø

EISCAT scientific association hosts six radars at four sites, at Kiruna in Sweden, at Sodankylä in Finland, at Tromsø and Longyearbyen in Norway. The EISCAT radars at Tromsø consists of two independent radar systems operating at Very High Frequency (VHF) and Ultra High Frequency (UHF) frequencies. The UHF antenna is a fully steerable parabolic dish (shown in Figure 3.5) with diameter of 32 m, antenna gain of 48.1 dBi, and transmitted frequency of 930 MHz with a peak power of 2 MW. The VHF radar operates at a frequency of 224 MHz with peak transmitter power of 3 MW. The antenna is a parabolic cylinder with 120 m by 40 m aperture. It is a steerable antenna in the meridional plane between -30° and 60° zenith angle.

A number of commonly used radar programs are available to observe region of interest which includes D, E and F regions of the ionosphere. However, in this study we used Common Programme One (CP1), CP2, and CP6. The experiments used when running these programs are *manda* and *beata* modes for both field-aligned and zenith, and are suitable to observe D and E region ionization. Details about these radar experiment modes are found in the EISCAT database [2].

EISCAT radars provide height resolved measurements of electron density, electron and ion temperatures, and line-of-sight ion velocities. From these measurements it is also possible to derive ionospheric parameters such as the electric field, conductivity, and current. In Paper II, we utilized the electron density measurements in the D and E regions of the atmosphere to characterize the precipitating electrons ionization level during different categories of PsA. In Paper IV, we also used the EISCAT electron densities to test the ion chemistry and energetics model introduced in section 3.3.

3.4.2 SuperDARN

Super Dual Auroral Radar Network (SuperDARN) is a network of ground-based coherent scatter and high frequency (HF) radars designed to study the Earth's upper atmosphere and ionosphere (*Greenwald et al.*, 1995). SuperDARN radars are monostatic phased-array radars with main array and interferometer array. The interferometer array is used to measure the elevation angles of the signals. SuperDARN radars operate in the HF frequency band between 8 and 20 MHz, however, most radars use the lower end of this range (8–18 MHz). Since the first radar installed at Goose Bay, Labrador (*Greenwald et al.*, 1985), the network has been expanding in both longitudinal and latitudinal

[2] https://eiscat.se/scientist/document/experiments/

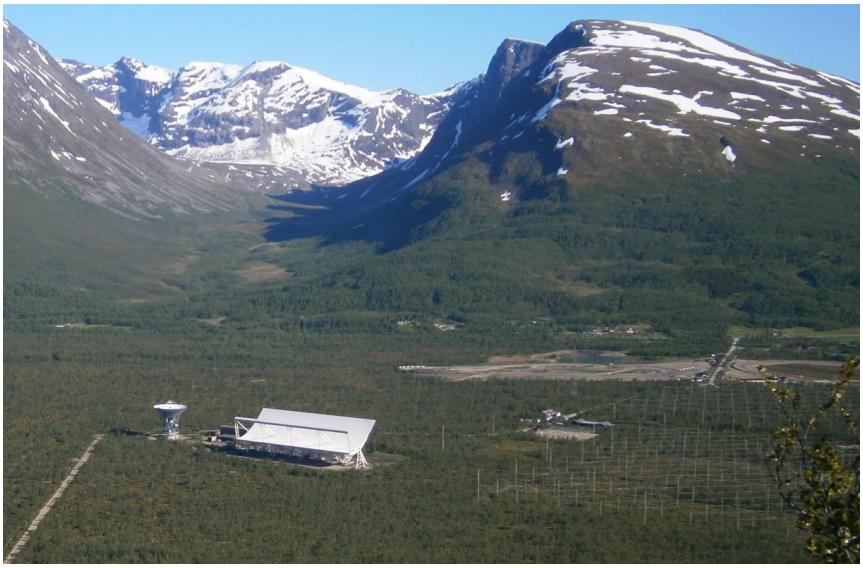

Figure 3.5: EISCAT facility at Tromsø. VHF (parabolic cylinder) and UHF (parabolic dish) radars are located in the lower left part of the photo. Photo taken from mountain Storforsaksla (North of the radar site), my first visit to Norway on July 06 2012.

extent. Currently, the network consists of 36 nearly-identical radars (23 in the Northern Hemisphere and 13 in the Southern Hemisphere) with the same software and data products (*Nishitani et al.*, 2019). At the beginning, the radars were designed to measure and study ionospheric convection and ionospheric irregularities but have became a versatile instrument to study many processes in the near-Earth environment, such as meteor ionization trails, sea ice cover, and polar mesospheric clouds (*Hosokawa et al.*, 2005; *Hussey et al.*, 2000; *Thomas et al.*, 2014).

A single SuperDARN radar consists of two parallel arrays of antennas 16 electronically phased array antennas that can be steered in 16 beam directions. The azimuth separation between the beams is 3.24° and spanning a total of 52°. The range resolution depends on the pulse length of the transmitted signal. The normal (common) operating mode has a pulse length of 300 μs corresponding to a range resolution of 45 km. A full scan through all the 16 beams takes 1 or 2 minutes, with a dwell time of 3 or 6 seconds for each position, respectively.

The standard data products from SuperDARN radars are Doppler velocity, spectral width and power (signal-to-noise ratio) of the received backscatter. These data products are extensively exploited to study the structure and dynamics of various ionospheric phenomena in the mid to high latitude regions. However, recently *Bland et al.* (2018) made use of the raw echo power and the background radio noise level (sky noise) from each scan in all the 75 range gates along the beam to identify HF wave attenuation caused by energetic particle precipitation in the D region. In paper III, we apply this approach to 10 SuperDARN radars in the Southern hemisphere to study the D region impact area of electron precipitation associated with pulsating aurora.

3.5 KAIRA

The Kilpisjärvi Atmospheric Imaging Receiver Array (KAIRA) is a dual array of omni-directional HF-VHF radio antennas located near Kilpisjärvi, Finland. It is a versatile instrument which can be used for scientific studies ranging from geoscience applications such as riometer imaging and ionospheric scintillation to deep space in radio astronomy (*McKay-Bukowski et al.*, 2015). The observational technique used in this study is the interferometric riometry imaging. KAIRA has low and high band antenna array. For riometric imaging the low band with frequency of 38.1 MHz was used. All-sky images were formed by applying 2D Fourier transforms on the cross-correlated signals sampled in 1 second from 48 low-band inverted-V dipole antennas as shown in Figure 3.4. From the riometry it is possible to produce a cosmic noise absorption (CNA) image of the sky, similar to ASC, and a riogram as a counterpart of keogram. KAIRA data has been used in significant number of studies related to precipitating electrons effect in the atmosphere (*Grandin et al.*, 2017; *McKay et al.*, 2018). In Paper II, we utilized these riograms to study CNA induced by the precipitating electrons during PsA.

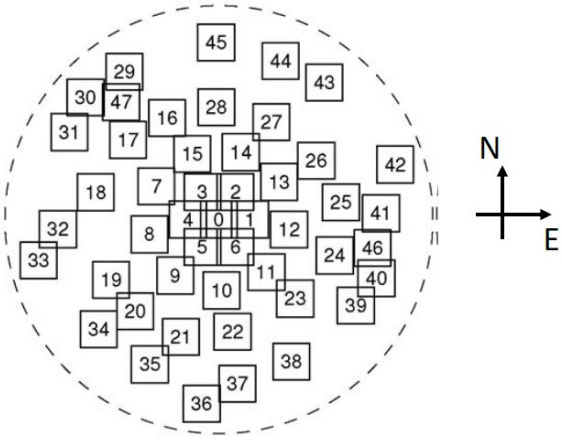

Figure 3.6: KAIRA low-band antenna array (McKay-Bukowski et al., 2015).

Chapter 4

Pulsating aurora

Pulsating aurora (PsA), a type of diffuse aurora usually observed in the recovery phase of a substorm and the post-midnight to morning sector, is the main focus of this thesis. It is caused by energetic electrons originated from the magnetosphere that can reach the middle atmosphere and deplete the ozone layer. The sources of electrons are the plasma sheet and the outer radiation belt, making PsA an integral element of the magnetosphere-ionosphere coupled system. Statistical studies from many years of optical data and recent advances in high-speed optical instruments combined with satellite measurements have revealed many interesting structures, sources and characteristics of PsA. In the first section of this chapter an up-to-date introduction to the morphology and characteristics of PsA will be presented. Then, the source and energy of electrons associated with PsA will be presented in section 2. This will be followed by a discussion about the atmospheric effects of the PsA electrons. The recent extensive reviews of PsA by *Lessard* (2012) and *Nishimura et al.* (2020) have provided a good basis for the following sections.

4.1 Morphology and characteristics of pulsating aurora

PsA is a relatively distinctive and structured diffuse aurora blinking on and off with recurrence periods up to tens of seconds (*Johnstone*, 1978; *Royrvik and Davis*, 1977; *Yamamoto*, 1988). Despite its low emission intensity compared to the usual midnight fast-moving aurora displays, PsA is mainly sub-visual to a naked eye. Its luminous intensity is in the range of a few hundred to few kilo Rayleighs at green (557.7 nm) and blue (428 nm) line emissions, and usually occurs over a diffuse background (*Davis*, 1978; *McEwen et al.*, 1981; *Royrvik and Davis*, 1977). PsA is known to have two distinct periodicities, primary oscillation in the order of seconds and the 3-Hz frequency internal modulation (*Nishiyama et al.*, 2014; *Sandahl et al.*, 1980). However, higher internal modulations up to 10 Hz to 15 Hz have also been observed superposed on top of slower (few second period) pulsations (*Samara and Michell*, 2010). Using state of the art high speed cameras, an extremely fast modulation up to 54 Hz has also reported by *Kataoka et al.* (2012). Furthermore, these fast modulations are reported to be well correlated with bright and small PsA structures (*Nishiyama et al.*, 2012, 2014).

As illustrated in the previous chapter in Figure 2.6, PsA can be related to substorms. It is often observed in a substorm recovery phase and the post-midnight to morning sec-

tor (*Jones et al.*, 2011; *Partamies et al.*, 2017). However, few studies have indicated that it can also be observed during substorm expansion and growth phases and in the afternoon sector (*Berkey*, 1978; *McKay et al.*, 2018). *Oguti et al.* (1981) reported that PsA is a common component of auroral displays with occurrence probability of 30% at the magnetic midnight and 100% after 4 MLT. They showed that the occurrence in the morning sector was also possible for quiet periods of time. An extensive statistical study by *Jones et al.* (2011) in the Canadian sector using Time History of Events and Macroscale Interactions during Substorms (THEMIS) ground-based auroral camera data also showed that PsA is quite common with the occurrence rate of 60% in the morning hours. They suggested that PsA is not only restricted in the substorm recovery phase but a persistent and long-lived phenomenon that can be disrupted by auroral substorms. All the previous ASC-based studies are limited to nighttime. A SuperDARN radar detection technique by *Bland et al.* (2019) showed that the PsA occurrence rate is about 50% during the winter and 15% during the summer months. In Paper I, a total of 840 events suggested that 86% of the events occurred in the after midnight with a maximum occurrence between 2 and 7 MLT.

The most likely duration of the PsA is reported to be about 1.5 hrs (*Jones et al.*, 2011; *Partamies et al.*, 2017). *Partamies et al.* (2017) used 400 PsA events in the years between 1997 and 2007 from the MIRACLE network of ASC (*Sangalli et al.*, 2011) and showed that the median duration of PsA is 1.4 hrs. They indicated that this duration is a conservative value due to limitation on either the aurora drifting away from the camera field of view or termination of imaging due to the dawn. In Paper I, we extended *Partamies et al.* (2017) PsA event list by an additional 12 years, and found a slightly longer duration of about 2 hrs. Using SuperDARN radar at Syowa station, Antarctica *Bland et al.* (2019) showed an even longer duration of 2.25 hrs. An extremely persistent PsA event which lasted for 15 hrs and covered a wide range of longitudes (10 hrs of local time) have also been reported by *Jones et al.* (2013). Therefore, PsA is clearly a common phenomenon which may have a significant contribution to the energy deposition in the atmosphere.

The altitude of emission and ionization associated with PsA occurs in the lower E region at 90–120 km with a peak around 110 km (*Hosokawa and Ogawa*, 2015; *Kawamura et al.*, 2020). The emission peak height is also reported to be dependent on magnetic local time with a tendency to decrease after 6 MLT (*Hosokawa and Ogawa*, 2015; *Kawamura et al.*, 2020; *Partamies et al.*, 2017). From 21 PsA events *Hosokawa and Ogawa* (2015) showed that the altitude of the peak ionization during the on phase of PsA is systematically lower by 10 km than the off phase. *Kataoka et al.* (2016) used auroral stereoscopy technique to determine the emission altitude and found that a pulsating patch lies between 85–95 km with a gradual variation of altitude (10 km increase over 5 s) compared to streaming discrete arc above 100 km. Using similar technique *Partamies et al.* (2017) revealed a decrease in peak emission height by 8 km at the onset of PsA.

Figure 4.1 shows the electron density maximum (bottom) and its height (top) as a function of MLT from EISCAT radars during 92 PsA events (as in Paper II). The EISCAT electron density observations showed that the altitude of maximum electron density lies between 90 and 120 km and follows a normal distribution centred at 107 km as illustrated in Figure 4.1 (c). This distribution is slightly different from *Hosokawa and Ogawa* (2015) results from 21 PsA events. Figure 7 (c) of their results showed

that the height of the maximum electron density is centred around 110 km. Our results agree well with the indirect approaches, auroral stereoscopy results from *Kataoka et al.* (2016) and *Partamies et al.* (2017), and results based on lifetime of the excited oxygen atom by *Kawamura et al.* (2020). This supports the feasibility of both approaches in characterizing PsA. From Figure 4.1 (a), in the pre-midnight period the altitude is mostly above 100 km. However, on rare occasions the maximum electron density is centered at altitudes between 90 and 100 km after 2 MLT. Corresponding electron density magnitudes showed higher values until 6 MLT. After 6 MLT electron density values decrease, which is consistent with the previous reports.

The spatial coverage of PsA is restricted to the equatorward part of the main auroral oval, and covers between 58° and 75° magnetic latitude (*Grono and Donovan*, 2020; *Oguti et al.*, 1981). The latitude extent of PsA depends on geomagnetic conditions and magnetic local time. Based on 34 nights of all-sky TV data *Oguti et al.* (1981) showed that during active geomagnetic periods (KP > 4), PsA can be nearly seen at all local times below 68° geomagnetic latitude, while during KP < 3 it is restricted to the post-midnight sector at > 65° latitude. *Partamies et al.* (2017) also reported high latitude (over Svalbard) PsA after 6 MLT while an earlier PsA in the Lapland region disappeared poleward. In Paper III, HF radio attenuation in the Southern polar D region of the ionosphere was analysed to show that the PsA impact area can cover 4 to 12 degrees magnetic latitude and 7 hours of magnetic local time. We also found that the equatorial edge of the auroral oval the PsA covers a larger magnetic local time extent compared to the poleward edge.

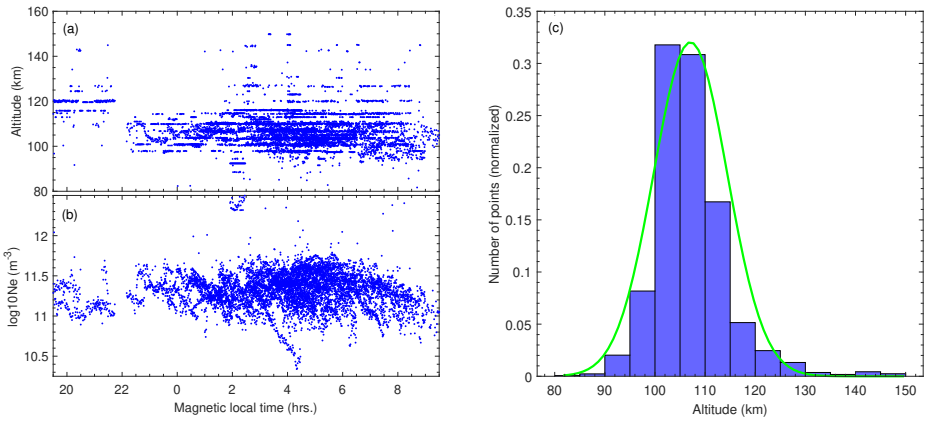

Figure 4.1: Altitude of maximum electron density (a) and magnitude of maximum electron density (b) as a function of MLT, and histogram of altitude of maximum electron density with normal distribution centered around 107 km altitude (green curve) (c), Alternative way of illustrating Figure 6 on Paper II.

Previous studies reported that PsA is a very thin structure compared to discrete aurora types. *Stenbaek-Nielsen and Hallinan* (1979) applied triangulation method on PsA patches observed by two nearby low-light level TV cameras in Alaska and found a thickness of 2 km or less. EISCAT radar electron density observations showed that pulsating patches thickness can range between 4.5 and 8 km (*Kaila et al.*, 1989; *Wahlund et al.*, 1989). Recently, similar incoherent scatter radar observations of four PsA events in the North-American sector by *Jones et al.* (2009) showed relatively thick pulsating

patches of 15–25 km. However, in Paper II, the full width at half maximum of individual EISCAT electron density profiles from 92 PsA events in the Fennoscandian region showed that the median PsA thickness can vary between 20 and 40 km depending on the morphological types of PsA.

PsA shows a wide variety of shapes. It can be observed as east-west elongated arc bands, arc segments or irregularly shaped patches (*Böinger et al.*, 1996; *Royrvik and Davis*, 1977; *Wahlund et al.*, 1989; *Yang et al.*, 2015). Pulsating arcs and arc segments tend to have similar width of 1–10 km. However, arcs can be as long as 1000 km with diffuse boundaries and arc segments 100 km with well-defined edges. Patches are generally 10–200 km across, mainly irregularly shaped, and can have various orientations. However, patches are the most common aurora forms of PsA. It is also reported that individual patches can pulsate out of phase with each other with slightly different periods (*Royrvik and Davis*, 1977). The longitudinal and latitudinal scale size of the pulsating patches can be nearly the same or evolve through time (*Partamies et al.*, 2019).

The drift of stable patches has been reported to follow the $\mathbf{E} \times \mathbf{B}$ plasma convection velocity, which is on the order of 1 km/s in the dawn sector (*Davis*, 1978; *Scourfield et al.*, 1983; *Yang et al.*, 2015, 2017). Westward drift patches are often observed in the pre-midnight and eastward drift in the post-midnight sector (*Oguti et al.*, 1981). However, there are also reports showing that the patch drift can be significantly different from the convection velocity. From four patches located at around 4 MLT *Humberset et al.* (2018) showed that the patches appear to drift differently from SuperDARN determined $\mathbf{E} \times \mathbf{B}$ convection velocity. However, in a non-rotating frame they found that patches drift in the north-eastward with the speed of 230–287 m/s, which is usually expected for the convection return flow. *Yang et al.* (2015) used time-gradients in ewograms and found the eastward patch drifts in the range of 156–550 m/s. This was slightly larger but in good agreement with the localized eastward convection velocities obtained from SuperDARN. In addition, *Yang et al.* (2017) used the same combination of measurements to identify patches with east-west velocities ranging from tens to several hundreds of m/s in the corotating frame of reference. They suggested that pulsating patches are predominantly governed by the convection mainly due to their eastward motion after midnight and westward before midnight.

Ground-based optical observations of aurora require dark season and clear skies, and this often limits the inter-hemispheric studies of aurora. However, significant number of inter-hemispheric PsA studies are documented (*Fujii et al.*, 1987; *Partamies et al.*, 2017; *Sato et al.*, 1998, 2004; *Watanabe et al.*, 2007). *Sato et al.* (1998) reported a similar overall dynamic variations of PsAs at both hemispheres. However, the pulsating period, and shape (type) of PsA can be different at different hemispheres at the same time (*Sato et al.*, 2004; *Watanabe et al.*, 2007). On the other hand, *Fujii et al.* (1987) reported a nearly simultaneous patchy PsA with topologically the same shape in both hemispheres. In general, precise conjugacy of PsAs is suggested to be very poor (*Watanabe et al.*, 2007).

As discussed previously most of the studies focused on patchy structures of PsA considering it as a single phenomena and showed mixed results about pulsating patch drift motion. However, PsA can appear in different structures which undergo different motion. Recently, *Grono and Donovan* (2018) categorized PsAs into three categories, Amorphous PsA (APA), Patchy PsA (PPA), and Patchy aurora (PA). The categorization is based on the stability and motion of the auroral patches in relation to the ionospheric

convection. APAs are unstable auroral patches that often pulsate over their entire area and evolve very rapidly. On the other hand, PPA includes stable patches that pulsate over most of their area with longer lived structures following the plasma convection. The third category, PA, consists of a large non-pulsating structures with infrequent small regions of pulsations near the edges. These patches can persist for tens of minutes and their motion is consistent with convection (*Grono et al.*, 2017).

Single ASC image cannot provide the information to categorize PsA in to these three types, however, a quick look at the ewogram or a series of consecutive ASC images they can be identified, for example, as shown in Figure 4.2 and 4.3. Figure 4.2 (a) shows the PPA type, which covers the entire field of view of the camera. Figure 4.2 (b) shows the APA type, in this case the PsA is seen equatorward of diffuse aurora and restricted to a limited latitude coverage. The PA type is shown in Figure 4.2 (c), where large patches are visible. In terms of order of occurrence, generally, APA tends to appear first and PPA and PA follows (*Grono and Donovan*, 2020). However, in this particular case the order of PPA and APA is reversed. In Paper II and IV, we also found the same order of occurrence as *Grono and Donovan* (2020) reported.

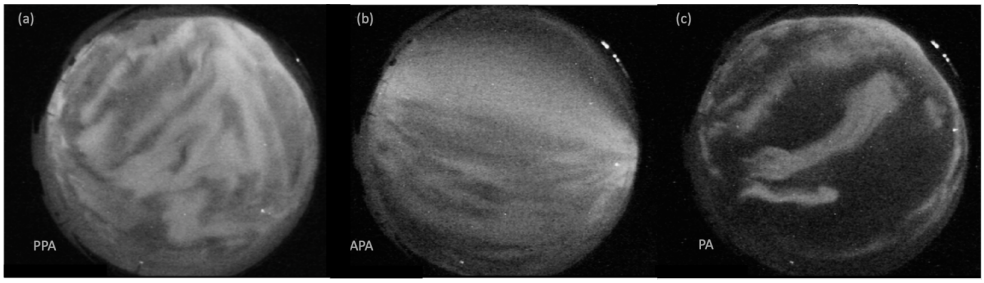

Figure 4.2: PsA types observed on January 09, 2014 at Tromsø. (a) PPA at 01:23:00:12 UT, (b) APA at 03:18:00:13 UT, and (c) PA at 04:27:00:15 UT.

In Paper II, we used *Grono and Donovan* (2018) approach to identify the PsA types. During APA type the keogram and ewogram showed a similar vertical stripes, during the PPA there are clear patchlines that have vertical striations (black, blue and red arrows) and during PA the patchlines have no striations (black arrow on Figure 4.3). It is interesting to see the change in the motion of patches as indicated by the arrows on the ewogram. The patchlines carry the patch speed information in different slopes of the ewogram. The blue arrows show that that PPA is moving eastward, the red arrow is also showing a patch moving eastward but with a slower speed and the black arrows show PPA and PA are moving westward. Such patchlines are completely absent during the APA type.

4.2 Electron precipitation associated with pulsating aurora

As is the case for most of the auroral emissions, the PsA is also caused by precipitating magnetospheric electrons. The source regions of electrons in the magnetosphere have been reported to be either earthward far from the equatorial plane of the magnetosphere or around the magnetospheric equator (*Miyoshi et al.*, 2010; *Sato et al.*, 2004). The

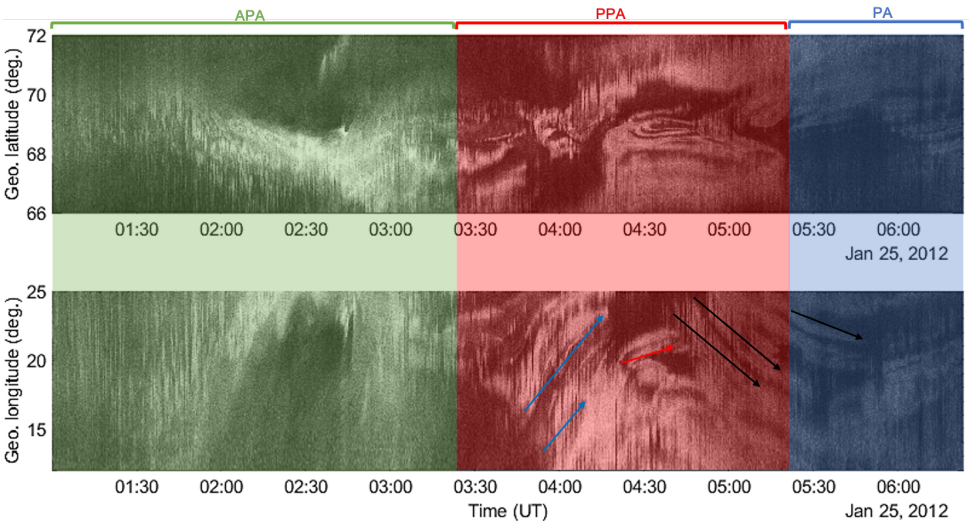

Figure 4.3: Keogram (top) and ewogram (bottom) and different types of PsA. APA (green), PPA (red), and PA (blue). Blue, red, and black arrows in the bottom panel are PPA or PA rapidly drifting eastward, slowly eastward, and westward directions, respectively.

measured electron energies associated with PsA cover a wide range of magnitudes. Observations from many rocket, satellite, and ground-based studies showed that PsA electrons' energy could be as low as 1 keV and as high as 200 keV (*Davidson*, 1990; *McEwen et al.*, 1981; *Miyoshi et al.*, 2010; *Reinard et al.*, 1997; *Sandahl*, 1984). The characteristic energy of electrons varies from one case to the next. For example, a direct measurement from rocket observations by *McEwen et al.* (1981) showed evidence that morning side PsA can be caused by electrons with 1.5 keV to 2.1 keV. However, rocket and satellite measurements by *Davidson* (1990) showed that PsA is mainly caused by electrons with energies between 50 and 100 keV and negligible pulsation is observed in the 2 to 4 keV energy range. *Jaynes et al.* (2013) found a high correlation between ground-based panchromatic THEMIS all-sky imager observations of PsA and electron flux modulation in energies ranging from 30–100 keV. From observations of four PsA events by ground-based optical observations and REIMEI satellite overpasses *Samara and Michell* (2010) showed that the typical energy of PsA lies between 8 and 12 keV. The lower end of the spectrum (< 30 keV) of PsA overlaps with electron energies that can produce diffuse aurora (*Ni et al.*, 2008).

Considerable electron density enhancements in the D region of the ionosphere, down to 68 km further suggested that electrons in the relativistic range also cause PsA (*Miyoshi et al.*, 2015a). In Paper II, we also found significant electron density enhancements from EISCAT radars below 100 km. The enhancement sometimes reaches down to 70 km. These altitudes correspond to an energy range between 20 and 200 keV. *Grandin et al.* (2017) showed a one to one correspondence between KAIRA CNA and optical PsA intensity and suggested that PsA covers energies > 30 keV. Recently, from simulation results, it has also been recommended that PsA electrons' energy consists of relativistic range and can be used as a proxy of the outer radiation belt flux variations

(*Miyoshi et al.*, 2020).

Most studies of PsA electron energy are limited to either case studies using directly in situ measurements, such as rockets (*Sandahl*, 1984; *Sandahl et al.*, 1980), or indirect methods as inverting electron densities from radar measurements (*Miyoshi et al.*, 2015a). Satellite measurements of precipitating electrons during PsA are also limited to case studies. This indicates a need for characterizing the actual variations and range of precipitating electrons further to study their effects on the Earth's atmosphere. In Paper I, we used a combination of low altitude satellites to construct a statistical and representative spectrum of PsA electrons. This is shown in Figure 4.4. These spectra is derived from DMSP, POES, and FAST satellites overpassing 253 PsA events over the Fennoscandian region. It consists of a non-relativistic and relativistic electron energy range between 30 eV and 1000 keV. From this Figure, it can be seen that fluxes of electrons between 10 and 200 keV energy range showed large variations. The spectra from these three satellites showed much smaller variations in the electrons flux with energies between 3 and 10 keV. Large variations in the softer precipitation (< 3 keV), especially from POES, is also evident.

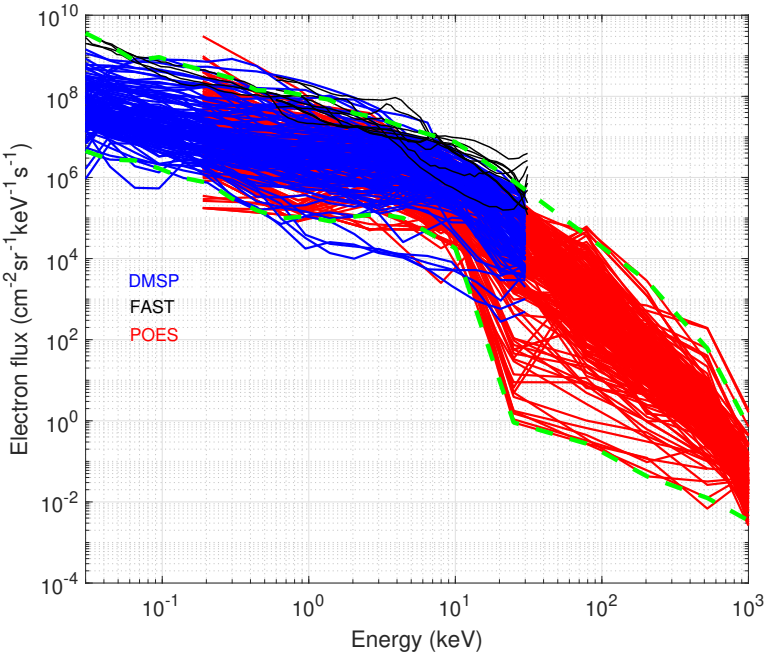

Figure 4.4: Statistical spectrum of PsA constructed from 376 overpasses of DMSP (blue), FAST (black), and POES (red) satellites over 253 PsA events. Lower and upper boundary of the spectra are marked with dashed green lines.

Precipitation energies of PsA electrons also showed MLT dependence from observations of POES and DMSP satellites (see Figure 5 on Paper I). We found a systematic increase in fluxes of energetic electrons after 7 MLT while the softer precipitation (< 10 keV) decayed. This is consistent with EISCAT observations of deeper ionization

(decrease in the altitude of maximum electron density shown in see Figure 4.1(a)) after 6 MLT. It is also evident from Figure 4.1(b) that the magnitude of electron density is decreasing during the deeper ionization period suggesting that the flux of the electrons at these higher energies is decreasing.

The large variations of PsA electron energies discussed above indicate that there are likely many different types of PsA associated with various generation mechanisms and ionospheric effects. It is also discussed in section 4.1 that PsA can appear in three types: APA, PPA, and PA. In Paper I, the large variations in the energy range above 10 keV (Figure 4.4) was suggested to be due to mixing these different types of PsA. In Paper II, we further study the precipitation energy of the different types of PsA using EISCAT electron density and KAIRA CNA. To illustrate this comparison, we present Figure 4.5 as an example. Figure 4.5 shows the cosmic noise absorption from KAIRA riometry, ionization level and height of maximum electron density from EISCAT radar for different categories of the PsA as identified in the keogram and ewogram in the top panels (see Paper II for details). From the first two panels, the APA marked by green shading coincided with a significant decrease in electron density magnitudes compared to PPA and PA marked by red and blue shading, respectively. The differences mainly lie below 100 km, as the harder precipitation is minimal during APA, especially compared to PPA in this particular case. Strong CNA from KAIRA also indicates that PPA and PA consist of deeper precipitating electrons. Above 100 km, the magnitude of electron density between PPA and PA show no significant differences, implying that the flux of the electrons stopped at this altitude range is the same for the two types. In this region, PA showed a decrease in the magnitude of electron density.

In Paper II, we analyzed the difference in ionization similar to that seen in Figure 4.5 for 92 PsA events to study the differences in precipitating electrons between the types. Differences are clearly seen in Figure 5(f) of Paper II. For example, in Figure 4.5, the differences cannot be captured by considering the altitude of maximum electron density. The electron density peak height does not give enough information about the energy and flux of the precipitating PsA electrons below 100 km. In a search for more detailed information from the electron density, we averaged the electron density in the altitude steps of 10 km dividing the D and E regions into five regions (see Figure 5(a-e) on Paper II). Below 100 km, a higher electron density during the PPA and PA was observed compared to APA. The region above 100 km showed no significant differences in electron densities between PPA and APA, while the PA showed smaller values. In addition, individual EISCAT electron density profiles from the PsA types showed that the layer thickness is different. PPA tends to be the thickest, followed by APA and PA. This suggests that not only energetic electrons are precipitating during PPA, it also consists of a wider energy range of precipitating electrons with higher fluxes. In Paper IV, we compare electron densities from EISCAT radars with auroral ion chemistry and the energetics model using PsA energy spectra derived from POES satellites as an energy input for the model. We found that the electron densities showed significant differences during a mix of PsA types (APA and PPA). However, when PPA filled the FOV of the ASC in the late morning sector, the model and EISCAT electron densities showed a very good agreement suggesting that the overpassing average spectra are a very good estimate for energy deposition with out considering patchiness of PsA.

The difference in precipitating energies during different types of PsA is also re-

ported by *Yang et al.* (2019). They used CNA observations to show a good correlation between the intensity of seven APA events and CNA compared to five PPA events, which showed no correlation. In addition, from observations of a single PsA event by the FAST satellite, they reported a higher energy range during APA compared to PPA. The sources and mechanisms behind the different PsA types are still open questions. *Grono and Donovan* (2019) used the location of proton aurora and indicated that PsA is entirely confined equatorward of the proton aurora. In their study, they also found that the PPA and PA types predominantly occur equatorward of the optical b2i boundary. In addition, *Grono and Donovan* (2020) used the spatio-temporal occurrence distributions of 564 hours of PsA from 280 days of observations and mapped them to the magnetospheric equatorial plane to study the location of the source. They found that both PPA and PA are dominantly located in the inner magnetosphere ($< 9\,R_E$), but APA sources can extend to the outer magnetosphere (up to $15\,R_E$). The order of occurrence of PsA types observed in their study as well as in Paper II is that APA tends to precede PPA and PA types. As mentioned in *Grono and Donovan* (2020), structuring of PsA types and whether the occurrence of PPA and PA is dependent on APA or not are still open questions.

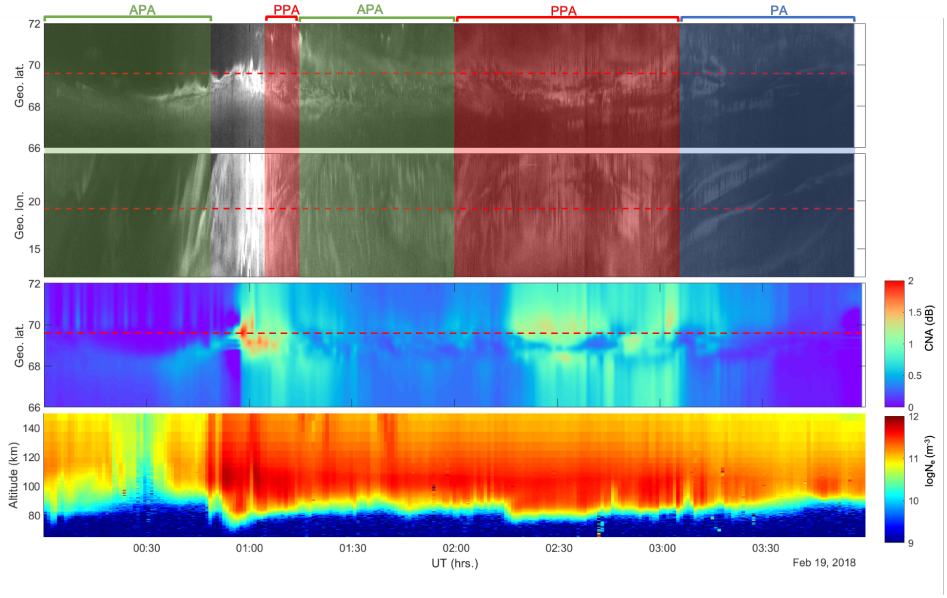

Figure 4.5: Keogram, ewogram, KAIRA riometry and EISCAT electron density (N_e) measurements during different types of PsA, APA (green), PPA (red), and PA (blue), on February 19 2018. The dashed red lines are the latitude and longitude of the EISCAT radar FOV. (The same as Figure 4 on Paper-II).

It is now widely believed that the sources of PsA electrons are originated from the plasma sheet and outer radiation belts. The electrons are accelerated and pitch angle scattered through wave-particle interactions at the equatorial region of the magnetosphere (*Kasahara et al.*, 2018; *Nishimura et al.*, 2010). The large range of energies discussed above suggested that the PsA electrons are subjected to cyclotron resonance with various magnetospheric plasma waves. Among numerous magnetospheric waves,

whistler-mode chorus waves stand out in pitch angle scattering and acceleration of the electrons, causing PsA. Chorus waves exist into two bands in the magnetosphere, lower band chorus (LBC) that has frequencies $f < 0.5 f_{ce}$, and upper band chorus (UBC) at frequencies $f > 0.5 f_{ce}$, where f_{ce} is the electron cyclotron frequency. *Nishimura et al.* (2010, 2011b) presented direct evidence on LBC waves being the primary driver for PsA. *Miyoshi et al.* (2015b) used computer simulation of the wave-particle interaction between electrons and chorus waves and reported that the main modulation of the energetic electrons (> 2 keV) is driven by LBC. They also found that stable precipitation at $\sim$ 1 keV is caused by UBC. The other possible candidate causing PsA is the electron cyclotron harmonic (ECH) waves. ECH waves can also scatter electrons and is mainly responsible for the lower energy precipitating electrons (*Ni et al.*, 2008). Thus, both ECH and UBC waves can cause scattering of lower energy electrons; however, the rate of scattering is reported to be smaller for ECH waves (*Ni et al.*, 2016). *Kasahara et al.* (2018) and *Fukizawa et al.* (2018) used a combination of Arase satellite and ground-based optical observations and showed that both LBC and ECH waves could scatter electrons responsible for PsA.

Different wave sources during PsA might be associated with the different categories of PsA. Looking at the keogram provided in Figure 1 of *Fukizawa et al.* (2018) it is highly likely that the Arase satellite passed over two categories of PsA: APA, followed by PPA. In the *Kasahara et al.* (2018) case study, both categories of PsA were also observed by the Arase satellite in the same order. During the time that presumably was dominated by PPA in both of these case studies, a combination of waves was present, but for the remaining period (i.e., during APA type), only one wave type was present. After 11:10 UT on Figure 3 of *Kasahara et al.* (2018) and after 01:52 UT of Figure 1 of *Fukizawa et al.* (2018), either a combination of UBC and LBC waves or LBC and ECH were present. However, during the rest of their observations (likely be APA type), and either ECH or LBC alone was present. This, of course, need a detailed investigation, but based on the results in Paper II, a thicker electron density region associated with PPA compared to APA is consistent with multiple sources scattering electrons over a wide energy band.

4.3 Atmospheric effects during pulsating aurora

Energetic particles from the magnetosphere can penetrate into the upper atmosphere and deposit their energy through ionization, dissociation, and excitation of atmospheric constituents. This results in auroral optical emission and electron density enhancement, cosmic noise absorption, and backscattered radar echoes in ionospheric altitudes. As discussed in the last two sections, PsA consists of energetic electrons that can impact the Earth's atmosphere in a wide range of altitudes. They can reach down to the mesospheric and lower thermospheric regions, including the D and E regions of the ionosphere. This indicates that PsA electrons can modify the ionospheric parameters and the neutral chemistry of the D region. Thus, the atmospheric effects of PsA electrons can be viewed in two ways as ionizing the neutrals and contributing to the mesospheric chemistry.

The ionizing effect of PsA electrons contributes to the ionospheric electrodynamics by modifying the electron density, and thus, the ionospheric parameters such as the

electric field and conductivity (*Oguti and Hayashi*, 1984). *Hosokawa et al.* (2008) found a possible ionospheric electric field modulation associated with PsA. They found a correlation between an oscillating electric field and optical pulsation of the aurora. They related the oscillation with modulation of the ionospheric conductance due to the quasi-periodic appearance of a polarized electric field generated by PsA electrons. Using EISCAT electron density and electric field measurements *Hosokawa et al.* (2010) further confirmed that a Hall conductance enhancement within the pulsating patches is a potential factor in modulating the ionospheric conductivity and current system. They also suggested that such a modification can affect the morphology of the pulsating patches. Similar studies about the effect of PsA electrons on the ionospheric current system strongly suggested the development of field-aligned currents near the edges of the patches (*Gillies et al.*, 2015, and references therein).

In addition to ionization of neutrals and modification of the current system, the energetic PsA electrons can also contribute to the chemistry of the atmosphere (*Turunen et al.*, 2016). They can produce an excess amount of NO_x and HO_x gases that can trigger catalytic reactions resulting in significant ozone loss. Sets of reactions in the stratospheric and mesospheric regions that lead to ozone loss due to HO_x and NO_x gases are discussed in section 2.6.4. HO_x gases are short-lived and induced a localized effect; however, NO_x gases can persist for months, during the winter season. Inside the polar vortex, NO_x can be transported to the stratosphere through a combination of diffusion and advection by the residual circulation. Once in the stratosphere, catalytic ozone depletion can start. Such direct and indirect effects of HO_x and NO_x gases in the chemistry of the middle atmosphere during energetic particles is now well documented (*Sinnhuber et al.*, 2012). Due to the frequent occurrence of the energetic electron precipitation, their long-term impacts on the neutral chemistry can dominate over other sources, such as solar proton events.

Most investigations carried out regarding the atmospheric effects of energetic particle precipitation have focused on substorm related precipitations and solar proton events (*Seppälä*, 2004; *Seppälä et al.*, 2007a, 2009; *Sinnhuber et al.*, 2012, 2016; *Turunen et al.*, 2009). PsA is often related to the substorm recovery phases and recognized as an integral part of substorms. As discussed in the previous section, PsA electrons energy span mainly between 20 and 200 keV, which is also in the range of substorm precipitation energies (*Beharrell et al.*, 2015; *Partamies et al.*, 2021; *Seppälä et al.*, 2015). It is then possible that substorm studies include the effect of PsA electrons implicitly; but, separate studies about chemical effects due to the PsA electrons have been very limited. The only result documented previously is a case study by *Turunen et al.* (2016). In addition, substorm related energy deposition in the atmosphere can be captured using magnetic indices; however, this is not the case for PsA (*Partamies et al.*, 2017). PsA occurrence in the substorm recovery phase or even in a relatively quiet periods in the post-midnight to morning sector makes it difficult to capture the energy deposition of PsA electrons using geomagnetic indices.

To investigate the effect of PsA electrons in the chemistry of the atmosphere, we used the SIC model as in *Turunen et al.* (2016). We ran the model for a location that is the center of the common field of view of the cameras used to identify the PsA events at the Muonio (MUO) station (see Figure 3.1). To account for the minimum and median durations of PsA, 30 minutes and 120 minutes long forcings were implemented for the upper, average, and lower boundary of the spectrum constructed from the satellite

measurements shown in Figure 4.4. Figure 4.6 displays the electron density, odd nitrogen, odd hydrogen, and percentage difference in odd oxygen for two days following the PsA forcing. Interestingly, the lower boundary spectrum, which was implemented for 30 minutes, did not induce any O_x change (bottom panel on the left of Figure 4.6). During this forcing, the NO_x increase resided dominantly above 100 km on the electron forcing day and started to descent the following day. There was no observable HO_x change during this forcing. The absence of ozone loss for this forcing implies that not every PsA can significantly affect the chemistry. However, there are not many spectra in the lower fluxes of electrons above 10 keV seen in Figure 4.4. The majority of spectra in this Figure showed a significant magnitude of flux compared to the lower boundary. But, the threshold sensitivity of the atmosphere is not known. For upper boundary forcing with 120 minutes duration shown on the right panels of Figure 4.6, the NO_x change increases significantly in magnitude and dominantly below 100 km. HO_x showed a sharp increase around 80 km and remained at elevated level the following day. The corresponding O_x depletion was about 79% which continued until sunrise.

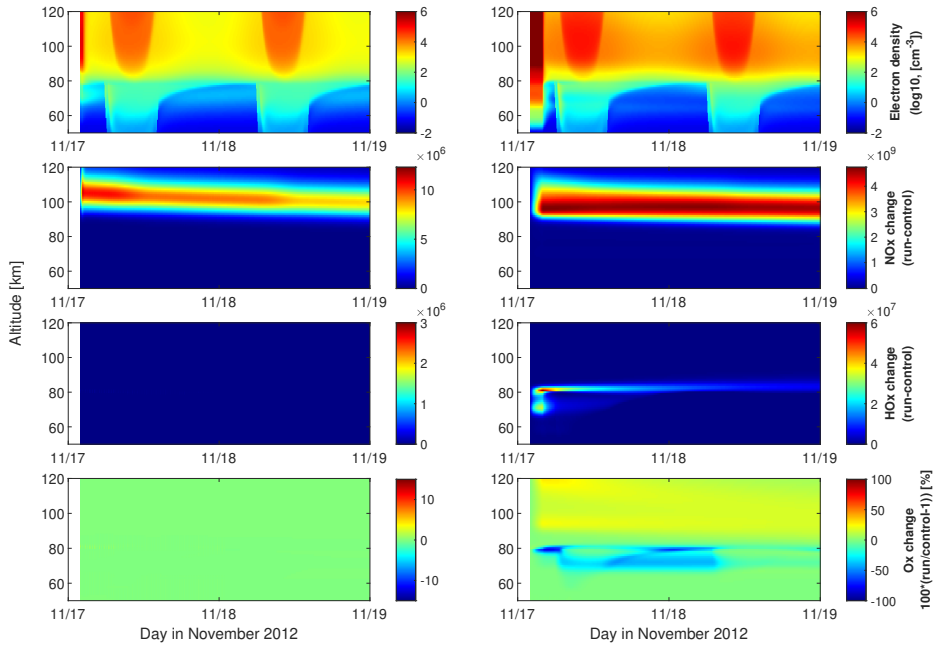

Figure 4.6: Modeled (from top), electron density (Ne), odd hydrogen (HO_x), odd nitrogen (NO_x), and odd oxygen (O_x). The left panels are forced with lower envelope from Figure 4.4 for 30 min, and the right panels are forced with the upper energy spectrum for 120 min. All model results are displayed for a 2-day time period.

A zoomed-in version of O_x percentage loss for average and upper boundary spectra for 30 and 120 minutes forcing is shown in Figure 4.7. For the longer duration forcing, below 75 km ozone loss persisted for the entire day. However, above 75 km, the ozone depletion slowed down during the day, and the loss continue the next night. The average

spectrum from Figure 4.4 well agrees with the Monte Carlo Markov chain (MCMC) median spectrum on Figure 2(a) from *Turunen et al.* (2016). In Paper I, the percentage change in O_x for the average spectrum forcing for 30 minutes was found to be -44%, which is of the same magnitude as their 30 minutes MCMC median forcing. Further comparison between *Turunen et al.* (2016) results on their Table 2 and our results in Figure 4.7 indicates that the range of percentage loss in O_x lies in the same magnitude. However, it should be noted that there is a difference in the time of the forcing. In Paper I, we started the forcing at 2 UT, but *Turunen et al.* (2016) started the forcing at 4:40 UT on the same day and nearly the same location. The earlier production of HO_x in Paper I induced a substantial ozone depletion during the day of forcing and less in the next day compared to the later forcing in the *Turunen et al.* (2016). This is, of course, due to the HO_x in the earlier run being consumed in the chemistry before the production of ozone by solar UV took place. However, during the earlier and longer duration forcing, more HO_x was produced before sunrise, and that survived until the following day to deplete ozone.

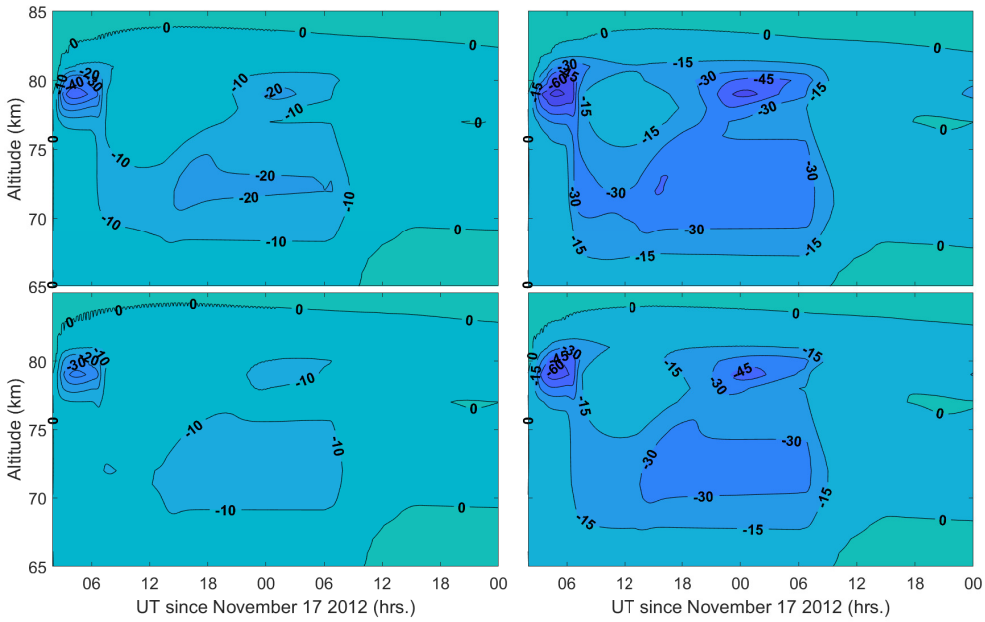

Figure 4.7: Percentage change in O_x using upper boundary spectrum for 30 and 120 minutes (top panels), and using average spectrum electron forcing for 30 and 120 minutes (bottom panels).

The atmospheric chemistry effect of PsA related precipitation is significant as reported by Paper I and by *Turunen et al.* (2016). In Paper I, the high ozone loss in the 1D chemistry model results indicated that the dynamical models, such as WACCM, need to include the PsA-related energetic electron precipitation (EEP). In addition to the occurrence rates, duration, and energy spectra, estimating the geographical location of EEP during PsA is crucial to use the chemistry-climate models and further study the impacts in the atmospheric system on a larger scale. As ground-based ASCs are the primary data source for detecting PsA, the spatio-temporal coverage can also be deter-

mined from ASCs that cover a wide range of latitudes and longitudes, like the THEMIS ASC network. *Grono and Donovan* (2019, 2020) reported the occurrence probability of APA, PPA, and PA categories from the THEMIS ASC network in Canada. This ASC network covers a wide range of latitudes and longitudes to study the spatial coverage of PsA. However, optical observations are often restricted by the sunlight and clear skies. This makes statistical studies on spatial coverage very challenging. The area impacted by PsA-related EEP could then be difficult to entirely determined from ASC observations. In Paper III, however, we used the HF radio attenuation from sets of SuperDARN radars to determine the EEP impact area during PsA. We used 10 SuperDARN radars in the Southern Hemisphere to study the EEP impact area of 74 PsA events. We found that the extent of magnetic local time at the equatorial edge for 44% of the events cover 7 hours, and at the poleward edge, this percentage reduces to 17%. The latitude coverage of the PsA impact area is also found to range from 4° to 12°. The average impact coverage area is between 62° and 70° magnetic latitudes. The instantaneous PsA impact area estimated from SuperDARN in Paper III agrees well with the statistical results by *Grono and Donovan* (2020). Similar latitude coverage during substorm precipitation has been reported by (*Cresswell-Moorcock et al.*, 2013).

The magnitude of ozone loss due to PsA discussed in this section is comparable to ozone loss related to the substorms, geomagnetic storms, solar proton events, and short-duration particle precipitations such as relativistic microburst events (*Jackman et al.*, 2007; *Seppälä et al.*, 2015, 2018). *Seppälä et al.* (2015) used the same ion chemistry model and substorm electron precipitation forcing for five days to show an ozone loss of 30–60% at 80 km. *Andersson et al.* (2014) further studied substorm related ozone loss using satellite measurements and found up to 34% at 70–80 km in solar cycle timescales. They also reported an extremely large (90%) short-term (1–5 days) ozone depletion at altitudes between 75 and 80 km. These model and observation-based studies of ozone depletion further suggest that the PsA ozone depletion we found in the 1D SIC model might also be significant in global models or could be observed in satellite measurements.

Chapter 5

Summary of papers

As discussed in Chapter 4, a significant number of studies have recently advanced the understanding of the characteristics and morphology of the PsA as well as the general source and energy range of PsA electrons. However, studies regarding its spatial occurrence, structure driving mechanisms, and middle atmospheric effects are very limited. In this thesis, we used a wide combination of measurements to also understand PsA electrons' energy and their impact on the middle atmosphere. The results presented in this study provide vital information about PsA electrons' energy spectrum, PsA spatial coverage, electrons' energy associated with different structures of PsA, and their effect on the middle atmospheric chemistry. The main findings are presented in four separate papers and are summarized in this chapter.

5.1 Paper I: Observations of Electron Precipitation During Pulsating Aurora and Its Chemical Impact

This study used optical observations from the MIRACLE all-sky cameras in the Fennoscandian sector to identify more than 800 PsA events in the years between 1997 and 2019. From these events, we found that pulsating aurora dominantly occurs during the post-midnight to morning sector with an average duration of 2 hours. The majority of PsA events were observed in the declining phase of the solar cycle. We found 253 events where DMSP, FAST, or POES satellites overpassed the region. By combining precipitating electron measurements from these satellites, an overpass averaged spectrum that consisted of electrons with energies between 30 eV and 1 MeV was constructed. Considerable variations of the flux of electrons with energy between 10 and 200 keV were clearly evident. The softer precipitation (< 10 keV) showed smaller variations. The MLT evolution of the precipitating electron energy spectra did not show any significant trend at any specific energy. However, a systematic increase in higher energies (> 30 keV) in the late MLT hours (after 7 MLT) was observed, while the softer precipitation decays after 6:30 MLT.

From the collection of energy spectra an average, lower and upper boundary spectra were defined and used in the 1D SIC model as an electron forcing to study the chemical change in the middle atmosphere. A 30 and 120 minutes of precipitation forcing was implemented using the boundary spectra electron forcing. It is found that the ozone destruction by the energetic PsA electrons can be as large as 78% and as low as 0%.

The average spectrum forcing for 120 minutes resulted in 69% ozone depletion at the time of forcing and 54% during the following night. The lower boundary forcing, which resulted in no ozone depletion, is suggested to be a rare case, as most of the spectra showed higher values than the lower end of the spectra. A significant ozone depletion (20 %) during the longer and upper boundary forcing persisted for two days, suggesting that the ozone depletion observed in the 1D model could be significant in the global models, such as WACCM and might also be detectable by atmospheric satellites.

5.2 Paper II: Observations of precipitation energies during different types of pulsating aurora

No ozone depletion at the lower boundary of the PsA spectra forcing found in Paper I implied different types of PsA. In this Paper, we further studied PsA by categorizing them to three as introduced by *Grono and Donovan* (2018). We used 10 years of ASC data (2010–2020) over Lapland region to identify PsA. Keograms and ewograms were constructed from ASC images to identify the different categories of pulsating aurora. We classified 92 PsA events into 39 APA, 35 PPA, and 18 PA. Corresponding electron density measurements from EISCAT radar at the Tromsø site were used to study the variations in ionization level. The KAIRA CNA was also used to infer electron precipitation impact during the three categories.

The altitude of the maximum electron density showed a considerable difference between the categories. PPA and PA ionization centered at 105 km and APA at 110 km. However, large differences in the electron density were observed below 100 km. To further investigate the ionization differences, we divided the region below 120 km into five height ranges with steps of 10 km altitude, and electron densities in these regions were averaged. Below 100 km PPA showed high electron density compared to APA, but no significant difference between 100 and 120 km. PA showed the smallest magnitude of electron density above 100 km and intermediate values below 100 km. During PPA and PA, an elevated ionization level down to 70 km was observed, which corresponds to 200 keV energy of electrons. The KAIRA CNA associated with D region electron density enhancement showed higher values during PPA (> 0.5 dB) compared to APA and PA (< 0.5 dB).

From the FWHM of individual electron density profiles, PPA ionization were the thickest PsA (about 40 km), followed by APA (30 km) and PA (20 km). The MLT occurrence of the three categories showed that PPA started to dominate after 4 MLT and continued in the late morning sector. APA was mainly observed between 1 and 5 MLT. However, PA is exclusively observed after 2 MLT. Higher KAIRA CNA values (> 0.5 dB) during PPA were observed after 3 MLT while APA showed low absorption < 0.5 dB after 5 MLT.

5.3 Paper III: D-region impact area of energetic electron precipitation during pulsating aurora

In this paper, we used a combination of 10 SuperDARN radars and one ASC data in the Southern Hemisphere to determine the impact area of the energetic PsA electrons.

From the Syowa ASC station in Antarctica, 74 pulsating aurora were identified. SuperDARN HF radio and noise attenuation due to the ionization increase in the D region ionosphere was used to characterize the EEP's impact area during pulsating aurora. It was found that the latitude coverage of PsA can range between 4 and 12 degrees. We showed that 36% of the events extended 12 degrees of magnetic latitude and about 60–75% of them extended over 4 degrees. The MLT extent was found to be wider at lower latitudes compared to higher latitudes. At 65° of magnetic latitude, we found an instantaneous MLT coverage of 2–3 hrs which became much narrower towards 75°. In general, MLT coverage of 7 hrs was observed at the equatorial edge for 44% of the events and at the poleward edge for 17% of the events. The average impact area of PsA-related EEP is found to reside between 62° and 70° magnetic latitudes covering 4–5 hours of MLT. A possible impact area differences between categories of PsA (APA, PPA, and PA) were checked. However, due to the limited events, the results were inconclusive.

5.4 Paper IV: Types of pulsating aurora: Comparison of model and EISCAT electron density observations

In this paper, we used EISCAT electron density, electron precipitation measurements from POES satellites, and electron density outputs from an auroral model to study three PsA events identified in Tromsø high-resolution Watec Monochromatic Imager (WMI) data. Different types of PsA were observed in all three cases. PsA energy spectra constructed from POES satellites were used as an input in the auroral model and the electron density output from the model was compared to the EISCAT electron density measurements. The near midnight PsA, which includes a mix of APA and PPA types showed large differences between EISCAT and model electron densities. However, the two PsA events which occurred in the morning sector and consisted mainly of PPA type over the entire POES observation period showed a very good agreement between the model and the EISCAT electron density measurements. The large electron density differences during a mix of PsA types indicated that the overpass averaged spectrum from POES could give a wrong estimate of the energy depostion. But, the agreement during the period of dominant PPA in the morning sector suggested that the average spectrum could be a very good estimate without considering patchiness of PsA.

Chapter 6

Conclusion and Future prospects

6.1 Conclusions

This thesis used a combination of measurements from different instruments and ion chemistry model results to provide a vital information about PsA electrons' energy and their middle atmospheric chemistry effects. Two solar cycles of optical data from the Fennoscandian region and significant number of optical observations of PsA in the southern hemisphere from Syowa station were used to identify more than 840 PsA events. For 253 PsA events precipitating electrons were observed by three satellites, DMSP, POES and FAST. From the satellite measurements representative PsA electron spectra were constructed and used as electron forcing in the 1D SIC model to study the change in the mesospheric chemistry. The electron precipitation associated with different types of PsA was studied using EISCAT electron density measurements as well as the southampton electron transport and ion chemistry model. The southern hemispheric PsA events were used to determine the PsA-related EEP impact area based on SuperDARN HF radio wave and noise attenuation. The most important findings of the thesis have been discussed in Chapter 4 and summarized in Chapter 5. The main conclusions are the following:

PsA characterstics and morphology

PsA is predominantly a post-midnight phenomenon occurring between 2 and 7 MLT with a median duration of about 2 hours as seen in the optical data. A high occurrence rate of PsA is observed in the declining phase of the solar cycle. The peak altitude of PsA ionization is centered around 105 km. In the morning sector (after 6 MLT) the altitude of PsA tends to decrease. PsA typically covers 4 degrees and 12 degrees magnetic latitude and 7 hours of MLT at any given time. The equatorial edge of PsA covers a larger MLT extent compared to the poleward side of the PsA.

Energy spectrum of PsA

The thesis presents the first statistical spectrum of PsA electrons constructed from low altitude satellite measurements. Large variation of flux of electrons in the range between 10 and 200 keV is observed. The spectrum is constructed from 253 PsA events and could be considered as a representative spectrum that provide the statistical varia-

tions and range of PsA electrons' fluxes. In the late MLT sector, the softer precipitation decay while the harder precipitation show a systematic increase.

Middle atmospheric chemistry during PsA

This thesis provide a very good starting point for considering the contribution of PsA electrons in changing the atmospheric chemistry. The 1D SIC model show as low as 0% and as high as 78% ozone depletion induced by the PsA electron forcing. There are not many low flux spectra and the average ozone depletion during PsA is about 44% for the 30-minute forcing and 69% for the 120 minutes forcing. The significant ozone depletion (above 20%), which persisted nearly two days further suggest the importance of considering PsA electrons energy deposition in the global atmospheric models.

Types of PsA

The three categories of PsA (APA, PPA, and PA) show significant difference in the magnitude of electron density (ionization level) below 100 km. PPA show the highest probability of causing largest electron density values in the lower E and D regions of the ionosphere, while APA show the smallest magnitude of electron density in these regions. The FWHM thickness of the ionization layer for the different categories show that PPA tends to be the thickest PsA followed by APA and PA. The MLT occurrence of the types of PsA show that PA is entirely confined after 2MLT, while PPA mostly occur in the late morning sector.

6.2 Future prospects

During the recent years, there has been significant progress in understanding the characteristics and morphology of PsA. The results presented in this thesis have in addition provided knowledge on the associated energy spectrum, the chemical impact, and characteristics for different types of PsA. New knowledge, however, also unravel new outstanding questions. Some of the possible research questions are discussed below:

PsA forcing in climate models and chemistry

As the results of this thesis provide a vital information to construct a realistic input for atmospheric models, the next step will be implementing this into global atmospheric models such as WACCM. Such modelling results will give us a good insight to further understand the energy deposition imposed into the Earth's atmosphere during PsA events. The significant and long lasting ozone depletion observed in this study implies that observation of ozone depletion from atmospheric satellites, such as GOMOS, SCIAMACHY, MIPAS, and Aura should also be possible.

Mechanisms structuring of PsA

It is now widely accepted that the sources of PsA electrons in the magnetosphere originate mainly in modulation of electrons by lower band chorus waves as well as upper band chorus and ECH waves. LBC is mainly responsible for the harder precipitation

while UBC and ECH scatter the lower energy electrons. However, which one is dominant in the scattering process during PsA is still an open question. What are the source of electrons during the three categories, why PPA and PA tends to follow the convection, but not APA? Is there any relation and mechanisms responsible of the order of occurrence of the three categories? Which type of wave or combination of waves is responsible for the different types of PsA? These all are open questions to be addressed. The answers for such questions can be approached by using a combination of satellites in the magnetosphere, such as Arase satellite or Van Allen probes data together with ground-based observations by high resolution ASC images from the MIRACLE, THEMIS, and NIPR networks.

Radar observations

SuperDARN radars can provide information that can further quantify the spatial coverage of PsA. The large coverage of SuperDARN radars in the Northern Hemisphere can be exploited to draw a statistical conclusion of the spatio-temporal coverage of PsA. Detail investigation of spatial coverage of different categories of PsA can also be achieved. EISCAT-3D is planned to be operational in late 2022 for superusers and early 2023 for the community. This huge advancement in the incoherent scatter radar observations will also provide high resolution three dimensional electron density data to study the ionization level and electrodynamical effects of PsA electrons in the scale of pulsation "on" and "off" periods.

Bibliography

Abbo, L., L. Ofman, S. K. Antiochos, V. H. Hansteen, L. Harra, Y. K. Ko, G. Lapenta, B. Li, P. Riley, L. Strachan, R. von Steiger, and Y. M. Wang (2016), Slow Solar Wind: Observations and Modeling, *Space Science Reviews*, *201*(1-4), 55–108, doi:10.1007/s11214-016-0264-1. 2.1

Akasofu, S. I. (1964), The development of the auroral substorm, *Planetary and Space Science*, *12*(4), 273–282, doi:10.1016/0032-0633(64)90151-5. 2.6.2

Akasofu, S.-I., and S. Chapman (1961), The ring current, geomagnetic disturbance, and the Van Allen radiation belts, *Journal of Geophysical Research: Space Physics*, *66*(5), 1321–1350, doi:10.1029/jz066i005p01321. 2.3

Alfvén, H. (1942), Existence of electromagnetic-hydrodynamic waves, *Nature*, *150*(3805), 405–406, doi:10.1038/150405d0. 2.1

Andersson, M. E., P. T. Verronen, C. J. Rodger, M. A. Clilverd, and A. Seppälä (2014), Missing driver in the Sun–Earth connection from energetic electron precipitation impacts mesospheric ozone, *Nature Communications*, *5*(1), 5197, doi:10.1038/ncomms6197. 4.3

Angelopoulos, V., W. Baumjohann, C. F. Kennel, F. V. Coroniti, M. G. Kivelson, R. Pellat, R. J. Walker, H. Lühr, and G. Paschmann (1992), Bursty bulk flows in the inner central plasma sheet, *Journal of Geophysical Research: Space Physics*, *97*(A4), 4027, doi:10.1029/91ja02701. 2.3

Angelopoulos, V., J. P. McFadden, D. Larson, C. W. Carlson, S. B. Mende, H. Frey, T. Phan, D. G. Sibeck, K. H. Glassmeier, U. Auster, E. Donovan, I. R. Mann, I. J. Rae, C. T. Russell, A. Runov, X. Z. Zhou, and L. Kepko (2008), Tail reconnection triggering substorm onset, *Science*, *321*(5891), 931–935, doi:10.1126/science.1160495. 2.3

Babcock, H. W. (1961), The Topology of the Sun's Magnetic Field and the 22-Year Cycle., *The Astrophysical Journal*, *133*, 572, doi:10.1086/147060. 2.1

Baker, D. N., A. N. Jaynes, X. Li, M. G. Henderson, S. G. Kanekal, G. D. Reeves, H. E. Spence, S. G. Claudepierre, J. F. Fennell, M. K. Hudson, R. M. Thorne, J. C. Foster, P. J. Erickson, D. M. Malaspina, J. R. Wygant, A. Boyd, C. A. Kletzing, A. Drozdov, and Y. Y. Shprits (2014), Gradual diffusion and punctuated phase space density enhancements of highly relativistic electrons: Van Allen Probes observations, *Geophysical Research Letters*, *41*(5), 1351–1358, doi:10.1002/2013GL058942. 2.5

Baker, D. N., A. N. Jaynes, S. G. Kanekal, J. C. Foster, P. J. Erickson, J. F. Fennell, J. B. Blake, H. Zhao, X. Li, S. R. Elkington, M. G. Henderson, G. D. Reeves, H. E. Spence, C. A. Kletzing, and J. R. Wygant (2016), Highly relativistic radiation belt electron acceleration, transport, and loss: Large solar storm events of March and June 2015, *Journal of Geophysical Research: Space Physics*, *121*(7), 6647–6660, doi:10.1002/2016JA022502. 2.5

Baker, D. N., P. J. Erickson, J. F. Fennell, J. C. Foster, A. N. Jaynes, and P. T. Verronen (2018), Space Weather Effects in the Earth's Radiation Belts, *Space Science Reviews*, *214*(1), 17, doi:10.1007/s11214-017-0452-7. 2.4, 2.5

Baumjohann, W., and R. A. Treumann (1996), *Basic Space Plasma Physics*, Imperial College Press, doi:10.1142/p015. 2.4

Beharrell, M. J., F. Honary, C. J. Rodger, and M. A. Clilverd (2015), Substorm-induced energetic electron precipitation: Morphology and prediction, *Journal of Geophysical Research: Space Physics*, *120*(4), 2993–3008, doi:10.1002/2014JA020632. 4.3

Berkey, F. (1978), Observations of pulsating aurora in the day sector auroral zone, *Planetary and Space Science*, *26*(7), 635–650, doi:10.1016/0032-0633(78)90097-1. 4.1

Bland, E. C., E. Heino, M. J. Kosch, and N. Partamies (2018), SuperDARN Radar-Derived HF Radio Attenuation During the September 2017 Solar Proton Events, *Space Weather*, *16*(10), 1455–1469, doi:10.1029/2018SW001916. 3.4.2

Bland, E. C., N. Partamies, E. Heino, A. S. Yukimatu, and H. Miyaoka (2019), Energetic Electron Precipitation Occurrence Rates Determined Using the Syowa East SuperDARN Radar, *Journal of Geophysical Research: Space Physics*, *124*(7), 6253–6265, doi:10.1029/2018ja026437. 3.3, 4.1

Böinger, T., K. Kaila, R. Rasinkangas, P. Pollari, J. Kangas, V. Trakhtengerts, A. Demekhov, and T. Turunen (1996), An EISCAT study of a pulsating auroral arc: simultaneous ionospheric electron density, auroral luminosity and magnetic field pulsations, *Journal of Atmospheric and Terrestrial Physics*, *58*(1), 23–35, doi:10.1016/0021-9169(95)00017-8. 4.1

Borovsky, J. E., J. Birn, M. M. Echim, S. Fujita, R. L. Lysak, D. J. Knudsen, O. Marghitu, A. Otto, T. H. Watanabe, and T. Tanaka (2020), Quiescent Discrete Auroral Arcs: A Review of Magnetospheric Generator Mechanisms, doi:10.1007/s11214-019-0619-5. 2.6.2

Brasseur, G. P., and S. Solomon (2005), *Aeronomy of the Middle Atmosphere*, *Atmospheric and Oceanographic Sciences Library*, vol. 32, Springer Netherlands, Dordrecht, doi:10.1007/1-4020-3824-0. 2.6.1, 2.6.3, 2.6.4, 2.6.4

Brekke, A. (2015), *Physics of the Upper Polar Atmosphere*, Springer Atmospheric Sciences, Springer Berlin Heidelberg. 2.6.2

Burns, C. J., E. Turunen, H. Matveinen, H. Ranta, and J. K. Hargreaves (1991), Chemical modelling of the quiet summer D- and E-regions using EISCAT electron density profiles, *Journal of Atmospheric and Terrestrial Physics*, *53*(1-2), 115–134, doi:10.1016/0021-9169(91)90026-4. 3.3

Carlson, C. W., R. F. Pfaff, and J. G. Watzin (1998), The Fast Auroral SnapshoT (FAST) Mission, *Geophysical Research Letters*, *25*(12), 2013–2016, doi:10.1029/98GL01592. 3.2

Carlson, C. W., J. P. Mcfadden, P. Turin, D. W. Curtis, and A. Magoncelli (2001), The electron and ion plasma experiment for FAST, *Space Science Reviews*, *98*(1-2), 33–66, doi:10.1023/A:1013139910140. 3.2

Cranmer, S. R. (2009), Coronal holes, *Living Reviews in Solar Physics*, *6*(1), 3, doi:10.12942/lrsp-2009-3. 2.1

Cresswell-Moorcock, K., C. J. Rodger, A. Kero, A. B. Collier, M. A. Clilverd, I. Häggström, and T. Pitkänen (2013), A reexamination of latitudinal limits of substorm-produced energetic electron precipitation, *Journal of Geophysical Research: Space Physics*, *118*(10), 6694–6705, doi:10.1002/jgra.50598. 4.3

Dai, L., J. R. Wygant, C. A. Cattell, S. Thaller, K. Kersten, A. Breneman, X. Tang, R. H. Friedel, S. G. Claudepierre, and X. Tao (2014), Evidence for injection of relativistic electrons into the Earth's outer radiation belt via intense substorm electric fields, *Geophysical Research Letters*, *41*(4), 1133–1141, doi:10.1002/2014GL059228. 2.3

Davidson, G. T. (1990), Pitch-angle diffusion and the origin of temporal and spatial structures in morningside aurorae, *Space Science Reviews*, *53*(1-2), 45–82, doi:10.1007/BF00217428. 4.2

Davis, T. N. (1978), Observed characteristics of auroral forms, *Space Science Reviews*, *22*(1), 77–113, doi:10.1007/BF00215814. 4.1, 4.1

Dungey, J. W. (1961), Interplanetary magnetic field and the auroral zones, *Physical Review Letters*, *6*(2), 47–48, doi:10.1103/PhysRevLett.6.47. 2.2, 2.3

Eastwood, J. P., H. Hietala, G. Toth, T. D. Phan, and M. Fujimoto (2015), What Controls the Structure and Dynamics of Earth's Magnetosphere?, *Space Science Reviews*, *188*(1-4), 251–286, doi:10.1007/s11214-014-0050-x. 2.2

Elsasser, W. M. (1939), On the origin of the Earth's magnetic field, *Physical Review*, *55*(5), 489–498, doi:10.1103/PhysRev.55.489. 2.2

Evans, D. S., and M. S. Greer (2000), Polar Orbiting Environmental Satellite Space Environment Monitor-2 Instrument Descriptions and Archive Data Documentation, *Oar Sec-93, Noaa*. 3.2

Feldman, U., E. Landi, and N. A. Schwadron (2005), On the sources of fast and slow solar wind, *Journal of Geophysical Research: Space Physics*, *110*(A7), A07,109, doi:10.1029/2004JA010918. 2.1

Frey, H. U., D. Han, R. Kataoka, M. R. Lessard, S. E. Milan, Y. Nishimura, R. J. Strangeway, and Y. Zou (2019), Dayside Aurora, *Space Science Reviews*, *215*(8), 1–32, doi:10.1007/s11214-019-0617-7. 2.6.2

Fujii, R., N. Sato, T. Ono, H. Fukunishi, T. Hirasawa, S. Kokubun, T. Araki, and T. Saemundsson (1987), Conjugacies of pulsating auroras by all-sky TV observations, *Geophysical Research Letters*, *14*(2), 115–118, doi:10.1029/GL014i002p00115. 4.1

Fukizawa, M., T. Sakanoi, Y. Miyoshi, K. Hosokawa, K. Shiokawa, Y. Katoh, Y. Kazama, A. Kumamoto, F. Tsuchiya, Y. Miyashita, Y. anaka, Y. Kasahara, M. Ozaki, A. Matsuoka, S. Matsuda, M. Hikishima, S. Oyama, Y. Ogawa, S. Kurita, and R. Fujii (2018), Electrostatic Electron Cyclotron Harmonic Waves as a Candidate to Cause Pulsating Auroras, *Geophysical Research Letters*, *45*(23), 661–12, doi:10.1029/2018GL080145. 4.2

Gillies, D. M., D. Knudsen, E. Spanswick, E. Donovan, J. Burchill, and M. Patrick (2015), Swarm observations of field-aligned currents associated with pulsating auroral patches, *Journal of Geophysical Research A: Space Physics*, *120*(11), 9484–9499, doi:10.1002/2015JA021416. 4.3

Gold, T. (1959), Motions in the magnetosphere of the Earth, *Journal of Geophysical Research: Space Physics*, *64*(9), 1219–1224, doi:10.1029/jz064i009p01219. 2.2

Grandin, M., A. Kero, N. Partamies, D. McKay, D. Whiter, A. Kozlovsky, and Y. Miyoshi (2017), Observation of pulsating aurora signatures in cosmic noise absorption data, *Geophysical Research Letters*, *44*(11), 5292–5300, doi:10.1002/2017GL073901. 3.5, 4.2

Green, J. C. (2013), NOAA NESDIS-NGDC MEPED Telescope Data Processing Algorithm Theoretical Basis document Version 1.0. 3.4

Greenwald, R. A., K. B. Baker, R. A. Hutchins, and C. Hanuise (1985), An HF phased-array radar for studying small-scale structure in the high-latitude ionosphere, *Radio Science*, *20*(1), 63–79, doi:10.1029/RS020i001p00063. 3.4.2

Greenwald, R. A., K. B. Baker, J. R. Dudeney, M. Pinnock, T. B. Jones, E. C. Thomas, J. P. Villain, J. C. Cerisier, C. Senior, C. Hanuise, R. D. Hunsucker, G. Sofko, J. Koehler, E. Nielsen, R. Pellinen, A. D. Walker, N. Sato, and H. Yamagishi (1995), DARN/SuperDARN-A global view of the dynamics of high-latitude convection, *Space Science Reviews*, *71*(1-4), 761–796, doi:10.1007/BF00751350. 3.4.2

Grono, E., and E. Donovan (2018), Differentiating diffuse auroras based on phenomenology, *Annales Geophysicae*, *36*(3), 891–898, doi:10.5194/angeo-36-891-2018. 4.1, 4.1, 5.2

Grono, E., and E. Donovan (2019), Constraining the Source Regions of Pulsating Auroras, *Geophysical Research Letters*, *46*(17-18), 10,267–10,273, doi:10.1029/2019GL084611. 4.2, 4.3

Grono, E., and E. Donovan (2020), Surveying pulsating auroras, *Annales Geophysicae*, *38*(1), 1–8, doi:10.5194/angeo-38-1-2020. 4.1, 4.1, 4.2, 4.3

Grono, E., E. Donovan, and K. R. Murphy (2017), Tracking patchy pulsating aurora through all-sky images, *Annales Geophysicae*, *35*(4), 777–784, doi:10.5194/angeo-35-777-2017. 4.1

Haaland, S., B. Lybekk, L. Maes, K. Laundal, A. Pedersen, P. Tenfjord, A. Ohma, N. Østgaard, J. Reistad, and K. Snekvik (2017), North-south asymmetries in cold plasma density in the magnetotail lobes: Cluster observations, *Journal of Geophysical Research: Space Physics*, *122*(1), 136–149, doi:10.1002/2016JA023404. 2.2

Hardy, A., E. G. Holeman, W. J. Burke, L. C. Gentile, and K. H. Bounar (2008), Probability distributions of electron precipitation at high magnetic latitudes, *Journal of Geophysical Research: Space Physics*, *113*(6), 1–19, doi:10.1029/2007JA012746. 3.2

Hardy, D. A., L. K. Schmitt, M. S. Gussenhoven, F. J. Marshall, and H. C. Yeh (1984), Precipitating electron and ion detectors (SSJ/4) for the block 5D/Flights 6-10 DMSP (Defense Meteorological Satellite Program) satellites: Calibration and data presentation, *Rep AFGL-TR-84-0317*. 3.2

Hardy, D. A., M. S. Gussenhoven, and D. Brautigam (1989), A statistical model of auroral ion precipitation, *Journal of Geophysical Research*, *94*(A1), 370, doi:10.1029/JA094iA01p00370. 3.2

He, H., C. Shen, H. Wang, X. Zhang, B. Chen, J. Yan, Y. Zou, A. M. Jorgensen, F. He, Y. Yan, X. Zhu, Y. Huang, and R. Xu (2016), Response of plasmaspheric configuration to substorms revealed by Chang'e 3, *Scientific Reports*, *6*(1), 1–11, doi:10.1038/srep32362. 2.3

Heelis, R. A. (1982), The polar ionosphere, *Reviews of Geophysics*, *20*(3), 567, doi:10.1029/RG020i003p00567. 2.6.1

Horne, R. B. (2003), Diffuse auroral electron scattering by electron cyclotron harmonic and whistler mode waves during an isolated substorm, *Journal of Geophysical Research: Space Physics*, *108*(A7), 1290, doi:10.1029/2002JA009736. 2.4

Horne, R. B., S. A. Glauert, N. P. Meredith, D. Boscher, V. Maget, D. Heynderickx, and D. Pitchford (2013), Space weather impacts on satellites and forecasting the Earth's electron radiation belts with SPACECAST, *Space Weather*, *11*(4), 169–186, doi:10.1002/swe.20023. 2.4

Hosokawa, K., and P. Ogawa (2015), Ionospheric variation during pulsating aurora :, *Journal of Geophysical Research: Space Physics*, *120*(7), 5943– 5957, doi:10.1002/2015JA021401.Received. 4.1

Hosokawa, K., T. Ogawa, N. F. Arnold, M. Lester, N. Sato, and A. S. Yukimatu (2005), Extraction of polar mesosphere summer echoes from SuperDARN data, *Geophysical Research Letters*, *32*(12), L12,801, doi:10.1029/2005GL022788. 3.4.2

Hosokawa, K., A. Kadokura, N. Sato, S. E. Milan, M. Lester, G. Bjornsson, and T. Saemundsson (2008), Electric field modulation behind pulsating aurora, *Journal of Geophysical Research: Space Physics*, *113*(11), doi:10.1029/2008JA013601. 4.3

Hosokawa, K., Y. Ogawa, A. Kadokura, H. Miyaoka, and N. Sato (2010), Modulation of ionospheric conductance and electric field associated with pulsating aurora, *Journal of Geophysical Research: Space Physics*, *115*(A3), doi:10.1029/2009JA014683. 4.3

Humberset, B. K., J. W. Gjerloev, I. R. Mann, R. G. Michell, and M. Samara (2018), On the Persistent Shape and Coherence of Pulsating Auroral Patches, *Journal of Geophysical Research: Space Physics*, *123*(5), 4272–4289, doi:10.1029/2017JA024405. 4.1

Hunsucker, R. D., and J. K. Hargreaves (2002), *The High-Latitude Ionosphere and its Effects on Radio Propagation*, Cambridge University Press, doi:10.1017/cbo9780511535758. 2.6.1

Hussey, G. C., C. E. Meek, D. André, A. H. Manson, G. J. Sofko, and C. M. Hall (2000), A comparison of northern hemisphere winds using SuperDARN meteor trail and MF radar wind measurements, *Journal of Geophysical Research: Atmospheres*, *105*(D14), 18,053–18,066, doi:10.1029/2000JD900272. 3.4.2

Jackel, B. J., T. Cameron, and J. M. Weygand (2013), Orientation of solar wind dynamic pressure phase fronts, *Journal of Geophysical Research: Space Physics*, *118*(4), 1379–1388, doi:10.1002/jgra.50183. 2.1

Jackman, C. H., R. G. Roble, and E. L. Fleming (2007), Mesospheric dynamical changes induced by the solar proton events in October–November 2003, *Geophysical Research Letters*, *34*(4), L04,812, doi:10.1029/2006GL028328. 4.3

Jaynes, A. N., M. R. Lessard, J. V. Rodriguez, E. Donovan, T. M. Loto'Aniu, and K. Rychert (2013), Pulsating auroral electron flux modulations in the equatorial magnetosphere, *Journal of Geophysical Research: Space Physics*, *118*(8), 4884–4894, doi:10.1002/jgra.50434. 4.2

Johnstone, A. D. (1978), Pulsating aurora, *Nature*, *274*(5667), 119–126, doi:10.1038/274119a0. 4.1

Jones, S. L., M. R. Lessard, P. A. Fernandes, D. Lummerzheim, J. L. Semeter, C. J. Heinselman, K. A. Lynch, R. G. Michell, P. M. Kintner, H. C. Stenbaek-Nielsen, and K. Asamura (2009), PFISR and ROPA observations of pulsating aurora, *Journal of Atmospheric and Solar-Terrestrial Physics*, *71*(6-7), 708–716, doi:10.1016/j.jastp.2008.10.004. 4.1

Jones, S. L., M. R. Lessard, K. Rychert, E. Spanswick, and E. Donovan (2011), Large-scale aspects and temporal evolution of pulsating aurora, *Journal of Geophysical Research: Space Physics*, *116*(3), 1–7, doi:10.1029/2010JA015840. 4.1

Jones, S. L., M. R. Lessard, K. Rychert, E. Spanswick, E. Donovan, and A. N. Jaynes (2013), Persistent, widespread pulsating aurora: A case study, *Journal of Geophysical Research: Space Physics*, *118*(6), 2998–3006, doi:10.1002/jgra.50301. 4.1

Kaila, K., R. Rasinkangas, P. Pollari, R. Kuula, J. Kangas, T. Turunen, and T. Bösinger (1989), High resolution measurements of pulsating aurora by EISCAT, optical instruments and pulsation magnetometers, *Advances in Space Research*, *9*(5), 53–56, doi:10.1016/0273-1177(89)90340-2. 4.1

Kanekal, S. G., D. N. Baker, M. G. Henderson, W. Li, J. F. Fennell, Y. Zheng, I. G. Richardson, A. Jones, A. F. Ali, S. R. Elkington, A. Jaynes, X. Li, J. B. Blake, G. D. Reeves, H. E. Spence, and C. A. Kletzing (2015), Relativistic electron response to the combined magnetospheric impact of a coronal mass ejection overlapping with a high-speed stream: Van Allen Probes observations, *Journal of Geophysical Research: Space Physics*, *120*(9), 7629–7641, doi:10.1002/2015JA021395. 2.5

Kasahara, S., Y. Miyoshi, S. Yokota, T. Mitani, Y. Kasahara, S. Matsuda, A. Kumamoto, A. Matsuoka, Y. Kazama, H. U. Frey, V. Angelopoulos, S. Kurita, K. Keika, K. Seki, and I. Shinohara (2018), Pulsating aurora from electron scattering by chorus waves, *Nature*, *554*(7692), 337–340, doi:10.1038/nature25505. 1, 4.2

Kataoka, R., Y. Miyoshi, D. Hampton, T. Ishii, and H. Kozako (2012), Pulsating aurora beyond the ultra-low-frequency range, *Journal of Geophysical Research: Space Physics*, *117*(A8), A08,336, doi:10.1029/2012JA017987. 4.1

Kataoka, R., Y. Fukuda, H. A. Uchida, H. Yamada, Y. Miyoshi, Y. Ebihara, H. Dahlgren, and D. Hampton (2016), High-speed stereoscopy of aurora, *Annales Geophysicae*, *34*(1), 41–44, doi:10.5194/angeo-34-41-2016. 4.1

Kawamura, Y., K. Hosokawa, S. Nozawa, Y. Ogawa, T. Kawabata, S. I. Oyama, Y. Miyoshi, S. Kurita, and R. Fujii (2020), Estimation of the emission altitude of pulsating aurora using the five-wavelength photometer, *Earth, Planets and Space*, *72*(1), 96, doi:10.1186/s40623-020-01229-8. 4.1

Kelley, M. C. (2009), *The Earth's ionosphere: plasma physics and electrodynamics*, Academic press. 2.5

Kessel, M. (2016), Things we do not yet understand about solar driving of the radiation belts, *Journal of Geophysical Research: Space Physics*, *121*(6), 5549–5552, doi:10.1002/2016JA022472. 2.5

Kidston, J., A. A. Scaife, S. C. Hardiman, D. M. Mitchell, N. Butchart, M. P. Baldwin, and L. J. Gray (2015), Stratospheric influence on tropospheric jet streams, storm tracks and surface weather, *Nature Geoscience*, *8*(6), 433–440, doi:10.1038/NGEO2424. 2.6.3

Lanchester, B. S., M. H. Rees, D. Lummerzheim, A. Otto, K. J. F. Sedgemore-Schulthess, H. Zhu, and I. W. McCrea (2001), Ohmic heating as evidence for strong field-aligned currents in filamentary aurora, *Journal of Geophysical Research: Space Physics*, *106*(A2), 1785, doi:10.1029/1999JA000292. 3.3

Lessard, M. R. (2012), A Review of Pulsating Aurora, *Auroral Phenomenology and Magnetospheric Processes: Earth and Other Planets*, pp. 55–68, doi:10.1029/2011GM001187. 4

Li, W., and M. K. Hudson (2019), Earth's Van Allen Radiation Belts: From Discovery to the Van Allen Probes Era, *Journal of Geophysical Research: Space Physics*, *124*(11), 8319–8351, doi:10.1029/2018JA025940. 2.5

Li, W., R. M. Thorne, V. Angelopoulos, J. Bortnik, C. M. Cully, B. Ni, O. LeContel, A. Roux, U. Auster, and W. Magnes (2009), Global distribution of whistler-mode chorus waves observed on the THEMIS spacecraft, *Geophysical Research Letters*, *36*(9), L09,104, doi:10.1029/2009GL037595. 2.4

Li, W., J. Bortnik, R. M. Thorne, and V. Angelopoulos (2011), Global distribution of wave amplitudes and wave normal angles of chorus waves using THEMIS wave observations, *Journal of Geophysical Research: Space Physics*, *116*(A12), A12,205, doi:10.1029/2011JA017035. 2.4

Lummerzheim, D., and J. Lilensten (1994), Electron transport and energy degradation in the ionosphere: Evaluation of the numerical solution, comparison with laboratory experiments and auroral observations, *Annales Geophysicae*, *12*(10-11), 1039–1051, doi:10.1007/s00585-994-1039-7. 3.3

McEwen, D. J., E. Yee, B. A. Whalen, and A. W. Yau (1981), Electron energy measurements in pulsating auroras, *Canadian Journal of Physics*, *59*(8), 1106–1115, doi:10.1139/p81-146. 4.1, 4.2

McKay, D., N. Partamies, and J. Vierinen (2018), Pulsating aurora and cosmic noise absorption associated with growth-phase arcs, *Annales Geophysicae*, *36*(1), 59–69, doi:10.5194/angeo-36-59-2018. 3.5, 4.1

McKay-Bukowski, D., J. Vierinen, I. I. Virtanen, R. Fallows, M. Postila, T. Ulich, O. Wucknitz, M. Brentjens, N. Ebbendorf, C. F. Enell, M. Gerbers, T. Grit, P. Gruppen, A. Kero, T. Iinatti, M. Lehtinen, H. Meulman, M. Norden, M. Orispaa, T. Raita, J. P. De Reijer, L. Roininen, A. Schoenmakers, K. Stuurwold, and E. Turunen (2015), KAIRA: The Kilpisjärvi atmospheric imaging receiver array-System overview and first results, *IEEE Transactions on Geoscience and Remote Sensing*, *53*(3), 1440–1451, doi:10.1109/TGRS.2014.2342252. 3.5, 3.6

McPherron, R. L. (1970), Growth phase of magnetospheric substorms, *Journal of Geophysical Research*, *75*(28), 5592–5599, doi:10.1029/ja075i028p05592. 2.3

McPherron, R. L. (1972), Substorm related changes in the geomagnetic tail: the growth phase, *Planetary and Space Science*, *20*(9), 1521–1539, doi:10.1016/0032-0633(72)90054-2. 2.3

McPherron, R. L., C. T. Russell, and M. P. Aubry (1973), Satellite studies of magnetospheric substorms on August 15, 1968: 9. Phenomenological model for substorms, *Journal of Geophysical Research*, *78*(16), 3131–3149, doi:10.1029/ja078i016p03131. 2.3

Millan, R. M., and D. N. Baker (2012), Acceleration of particles to high energies in earth's radiation belts, *Space Science Reviews*, *173*(1-4), 103–131, doi:10.1007/s11214-012-9941-x. 2.3, 2.4, 2.5

Miyoshi, Y., Y. Katoh, T. Nishiyama, T. Sakanoi, K. Asamura, and M. Hirahara (2010), Time of flight analysis of pulsating aurora electrons, considering wave-particle interactions with propagating whistler mode waves, *Journal of Geophysical Research: Space Physics*, *115*(10), 1–7, doi:10.1029/2009JA015127. 4.2

Miyoshi, Y., S. Oyama, S. Saito, S. Kurita, H. Fujiwara, R. Kataoka, Y. Ebihara, C. Kletzing, G. Reeves, O. Santolik, M. Clilverd, C. J. Rodger, E. Turunen, and F. Tsuchiya (2015a), Energetic electron precipitation associated with pulsating aurora: EISCAT and Van Allen Probe observations, *Journal of Geophysical Research: Space Physics*, *120*(4), 2754–2766, doi:10.1002/2014JA020690. 4.2

Miyoshi, Y., S. Saito, K. Seki, T. Nishiyama, R. Kataoka, K. Asamura, Y. Katoh, Y. Ebihara, T. Sakanoi, M. Hirahara, S. Oyama, S. Kurita, and O. Santolik (2015b), Relation between fine structure of energy spectra for pulsating aurora electrons and frequency spectra of whistler mode chorus waves, *Journal of Geophysical Research: Space Physics*, *120*(9), 7728–7736, doi:10.1002/2015JA021562. 4.2

Miyoshi, Y., S. Saito, S. Kurita, K. Asamura, K. Hosokawa, T. Sakanoi, T. Mitani, Y. Ogawa, S. Oyama, F. Tsuchiya, S. L. Jones, A. N. Jaynes, and J. B. Blake (2020), Relativistic electron microbursts as high energy tail of pulsating aurora electrons, *Geophysical Research Letters*, *47*(21), doi:10.1029/2020gl090360. 4.2

Nakamura, R., W. Baumjohann, A. Runov, M. Volwerk, T. L. Zhang, B. Klecker, Y. Bogdanova, A. Roux, A. Balogh, H. Rème, J. A. Sauvaud, and H. U. Frey (2002), Fast flow during current sheet thinning, *Geophysical Research Letters*, *29*(23), 55–1, doi:10.1029/2002GL016200. 2.3

Nesse Tyssøy, H., M. I. Sandanger, L.-K. G. Ødegaard, J. Stadsnes, A. Aasnes, and A. E. Zawedde (2016), Energetic electron precipitation into the middle atmosphere-Constructing the loss cone fluxes from MEPED POES, *Journal of Geophysical Research: Space Physics*, *121*(6), 5693–5707, doi:10.1002/2016JA022752. 3.4, 3.2

Newell, P. T., K. Liou, T. Sotirelis, and C.-I. Meng (2001), Auroral precipitation power during substorms: A Polar UV Imager-based superposed epoch analysis, *Journal of Geophysical Research: Space Physics*, *106*(A12), 28,885–28,896, doi:10.1029/2000JA000428. 2.6.2

Newell, P. T., T. Sotirelis, and S. Wing (2009), Diffuse, monoenergetic, and broadband aurora: The global precipitation budget, *Journal of Geophysical Research: Space Physics*, *114*(9), 1–20, doi:10.1029/2009JA014326. 2.6.2, 2.6.2

Ni, B., R. M. Thorne, Y. Y. Shprits, and J. Bortnik (2008), Resonant scattering of plasma sheet electrons by whistler-mode chorus: Contribution to diffuse auroral precipitation, *Geophysical Research Letters*, *35*(11), L11,106, doi:10.1029/2008GL034032. 2.6.2, 4.2, 4.2

Ni, B., R. Thorne, J. Liang, V. Angelopoulos, C. Cully, W. Li, X. Zhang, M. Hartinger, O. Le Contel, and A. Roux (2011), Global distribution of electrostatic electron cyclotron harmonic waves observed on THEMIS, *Geophysical Research Letters*, *38*(17), n/a–n/a, doi:10.1029/2011GL048793. 2.4

Ni, B., R. M. Thorne, X. Zhang, J. Bortnik, Z. Pu, L. Xie, Z. j. Hu, D. Han, R. Shi, C. Zhou, and X. Gu (2016), Origins of the Earth's Diffuse Auroral Precipitation, *Space Science Reviews*, *200*(1-4), 205–259, doi:10.1007/s11214-016-0234-7. 2.6.2, 4.2

Nishimura, Y., J. Bortnik, W. Li, R. M. Thorne, L. R. Lyons, V. Angelopoulos, S. B. Mende, J. W. Bonnell, O. Le Contel, C. Cully, R. Ergun, and U. Auster (2010), Identifying the driver of pulsating aurora, *Science*, *330*(6000), 81–84, doi:10.1126/science.1193186. 1, 4.2

Nishimura, Y., J. Bortnik, W. Li, R. M. Thorne, L. Chen, L. R. Lyons, V. Angelopoulos, S. B. Mende, J. Bonnell, O. Le Contel, C. Cully, R. Ergun, and U. Auster (2011a), Multievent study of the correlation between pulsating aurora and whistler mode chorus emissions, *Journal of Geophysical Research: Space Physics*, *116*(11), 1–11, doi:10.1029/2011JA016876. 1

Nishimura, Y., J. Bortnik, W. Li, R. M. Thorne, L. R. Lyons, V. Angelopoulos, S. B. Mende, J. Bonnell, O. Le Contel, C. Cully, R. Ergun, and U. Auster (2011b), Estimation of magnetic field mapping accuracy using the pulsating aurora-chorus connection, *Geophysical Research Letters*, *38*(14), 3–7, doi:10.1029/2011GL048281. 4.2

Nishimura, Y., J. Bortnik, W. Li, R. M. Thorne, B. Ni, L. R. Lyons, V. Angelopoulos, Y. Ebihara, J. W. Bonnell, O. Le Contel, and U. Auster (2013), Structures of dayside whistler-mode waves deduced from conjugate diffuse aurora, *Journal of Geophysical Research: Space Physics*, *118*(2), 664–673, doi:10.1029/2012JA018242. 2.6.2

Nishimura, Y., M. R. Lessard, Y. Katoh, Y. Miyoshi, E. Grono, N. Partamies, N. Sivadas, K. Hosokawa, M. Fukizawa, M. Samara, R. G. Michell, R. Kataoka, T. Sakanoi, D. K. Whiter, S. i. Oyama, Y. Ogawa, and S. Kurita (2020), Diffuse and Pulsating Aurora, *Space Science Reviews*, *216*(1), doi:10.1007/s11214-019-0629-3. 2.6.2, 4

Nishitani, N., J. M. Ruohoniemi, M. Lester, J. B. H. Baker, A. V. Koustov, S. G. Shepherd, G. Chisham, T. Hori, E. G. Thomas, R. A. Makarevich, A. Marchaudon, P. Ponomarenko, J. A. Wild, S. E. Milan, W. A. Bristow, J. Devlin, E. Miller, R. A. Greenwald, T. Ogawa, and T. Kikuchi (2019), Review of the accomplishments of mid-latitude Super Dual Auroral Radar Network (SuperDARN) HF radars, *Progress in Earth and Planetary Science*, *6*(1), 1–57, doi:10.1186/s40645-019-0270-5. 3.4.2

Nishiyama, T., T. Sakanoi, Y. Miyoshi, R. Kataoka, D. Hampton, Y. Katoh, K. Asamura, and S. Okano (2012), Fine scale structures of pulsating auroras in the early recovery phase of substorm using ground-based EMCCD camera, *Journal of Geophysical Research: Space Physics*, *117*(A10), A10,229, doi:10.1029/2012JA017921. 4.1

Nishiyama, T., T. Sakanoi, Y. Miyoshi, D. L. Hampton, Y. Katoh, R. Kataoka, and S. Okano (2014), Multiscale temporal variations of pulsating auroras: On-off pulsation and a few Hz modulation, *Journal of Geophysical Research: Space Physics*, *119*(5), 3514–3527, doi:10.1002/2014JA019818. 4.1

Ødegaard, L. K. G., H. N. Tyssøy, F. Søraas, J. Stadsnes, and M. I. Sandanger (2017), Energetic electron precipitation in weak to moderate corotating interaction region-driven storms, *Journal of Geophysical Research: Space Physics*, *122*(3), 2900–2921, doi:10.1002/2016JA023096. 3.2

Ogawa, Y., Y. Tanaka, A. Kadokura, K. Hosokawa, Y. Ebihara, T. Motoba, B. Gustavsson, U. Brändström, Y. Sato, S. Oyama, M. Ozaki, T. Raita, F. Sigernes, S. Nozawa, K. Shiokawa, M. Kosch, K. Kauristie, C. Hall, S. Suzuki, Y. Miyoshi, A. Gerrard, H. Miyaoka, and R. Fujii (2020), Development of low-cost multi-wavelength imager system for studies of aurora and airglow, *Polar Science*, *23*, 100,501, doi:10.1016/j.polar.2019.100501. 3.1

Oguti, T., and K. Hayashi (1984), Multiple correlation between auroral and magnetic pulsations: 2. Determination of electric currents and electric fields around a pulsating auroral patch, *Journal of Geophysical Research: Space Physics*, *89*(A9), 7467–7481, doi:10.1029/JA089iA09p07467. 4.3

Oguti, T., S. Kokubun, K. Hayashi, K. Tsuruda, S. Machida, T. Kitamura, O. Saka, and T. Watanabe (1981), Statistics of pulsating auroras on the basis of all-sky TV data from five stations. I. Occurrence frequency, *Canadian Journal of Physics*, *59*(8), 1150–1157, doi:10.1139/p81-152. 4.1, 4.1

Palmer, J. (1995), Plasma density variations in the aurora, Ph.D. thesis. 3.3

Parker, E. (1959), Extension of the solar corona into interplanetary space, *Journal of Geophysical Research: Space Physics*, *64*(11), 1675–1681, doi:10.1029/jz064i011p01675. 2.1

Parker, E. N. (1958a), Suprathermal Particle Generation in the Solar Corona, *The Astrophysical Journal*, *128*, 677, doi:10.1086/146580. 2.1

Parker, E. N. (1958b), Dynamics of the Interplanetary Gas and Magnetic Fields, *The Astrophysical Journal*, *128*, 664, doi:10.1086/146579. 2.1

Partamies, N., D. Whiter, A. Kadokura, K. Kauristie, H. Nesse Tyssøy, S. Massetti, P. Stauning, and T. Raita (2017), Occurrence and average behavior of pulsating aurora, *Journal of Geophysical Research: Space Physics*, *122*(5), 5606–5618, doi:10.1002/2017JA024039. 1, 4.1, 4.1, 4.3

Partamies, N., K. Bolmgren, E. Heino, N. Ivchenko, J. E. Borovsky, and H. Sundberg (2019), Patch size evolution during pulsating aurora, *Journal of Geophysical Research: Space Physics*, *124*(6), 4725–4738, doi:10.1029/2018JA026423. 4.1

Partamies, N., F. Tesema, E. Bland, E. Heino, H. Nesse Tyssøy, and E. Kallelid (2021), Electron precipitation characteristics during isolated, compound, and multi-night substorm events, *Annales Geophysicae*, *39*(1), 69–83, doi:10.5194/angeo-39-69-2021. 4.3

Pfaff, R., C. Carlson, J. Watzin, D. Everett, and T. Gruner (2001), An overview of the Fast Auroral Snapshot (FAST) satellite, *Space Science Reviews*, *98*(1-2), 1–32, doi:10.1023/A:1013187826070. 3.2

Pierrard, V., and J. Cabrera (2006), Dynamical simulations of plasmapause deformations, *Space Science Reviews*, *122*(1-4), 119–126, doi:10.1007/s11214-006-5670-3. 2.3

Pinto, V. A., J. Bortnik, P. S. Moya, L. R. Lyons, D. G. Sibeck, S. G. Kanekal, H. E. Spence, and D. N. Baker (2018), Characteristics, Occurrence, and Decay Rates of Remnant Belts Associated With Three-Belt Events in the Earth's Radiation Belts, *Geophysical Research Letters*, *45*(22), 099–12, doi:10.1029/2018GL080274. 2.5

Redmon, R. J., W. F. Denig, L. M. Kilcommons, and D. J. Knipp (2017), New DMSP database of precipitating auroral electrons and ions, *Journal of Geophysical Research: Space Physics*, *122*(8), 9056–9067, doi:10.1002/2016JA023339. 3.2

Reeves, G. D., K. L. McAdams, R. H. W. Friedel, and T. P. O'Brien (2003), Acceleration and loss of relativistic electrons during geomagnetic storms, *Geophysical Research Letters*, *30*(10), n/a–n/a, doi:10.1029/2002gl016513. 2.5

Reinard, A. A., R. M. Skoug, S. Datta, and G. K. Parks (1997), Energy spectral characteristics of auroral electron microburst precipitation, *Geophysical Research Letters*, *24*(5), 611–614, doi:10.1029/97GL00377. 4.2

Retinò, A., D. Sundkvist, A. Vaivads, F. Mozer, M. André, and C. J. Owen (2007), In situ evidence of magnetic reconnection in turbulent plasma, *Nature Physics*, *3*(4), 235–238, doi:10.1038/nphys574. 2.2

Ripoll, J., S. G. Claudepierre, A. Y. Ukhorskiy, C. Colpitts, X. Li, J. F. Fennell, and C. Crabtree (2020), Particle Dynamics in the Earth's Radiation Belts: Review of Current Research and Open Questions, *Journal of Geophysical Research: Space Physics*, *125*(5), doi:10.1029/2019JA026735. 2.5

Royrvik, O., and T. N. Davis (1977), Pulsating aurora: Local and global morphology, *Journal of Geophysical Research: Space Physics*, *82*(29), 4720–4740, doi:10.1029/ja082i029p04720. 4.1, 4.1

Rozanov, E., M. Calisto, T. Egorova, T. Peter, and W. Schmutz (2012), Influence of the Precipitating Energetic Particles on Atmospheric Chemistry and Climate, *Surveys in Geophysics*, *33*(3-4), 483–501, doi:10.1007/s10712-012-9192-0. 1

Rusch, D. W., J. C. Gérard, S. Solomon, P. J. Crutzen, and G. C. Reid (1981), The effect of particle precipitation events on the neutral and ion chemistry of the middle atmosphere–I. Odd nitrogen, *Planetary and Space Science*, *29*(7), 767–774, doi:10.1016/0032-0633(81)90048-9. 2.6.4

Samara, M., and R. G. Michell (2010), Ground-based observations of diffuse auroral frequencies in the context of whistler mode chorus, *Journal of Geophysical Research: Space Physics*, *115*(A9), A00F18, doi:10.1029/2009JA014852. 4.1, 4.2

Sandahl, I. (1984), Pitch Angle Scattering and Particle Precipitation in a Pulsating Aurora-an Experimental Study, *Tech. Rep. October*, Kiruna, Sweden: Kiruna Geophysical Institute. 4.2

Sandahl, I., L. Eliasson, and R. Lundin (1980), Rocket observations of precipitating electrons over a pulsating aurora, *Geophysical Research Letters*, *7*(5), 309–312, doi: 10.1029/GL007i005p00309. 4.1, 4.2

Sandanger, M. I., L.-K. G. Ødegaard, H. N. Tyssøy, J. Stadsnes, F. Søraas, K. Oksavik, and K. Aarsnes (2015), In flight calibration of NOAA POES proton detectors-derivation of the MEPED correction factors, *Journal of Geophysical Research: Space Physics*, *120*, 9578–9593, doi:10.1002/2015JA021388. 3.2

Sandhu, J. K., I. J. Rae, M. P. Freeman, C. Forsyth, M. Gkioulidou, G. D. Reeves, H. E. Spence, C. M. Jackman, and M. M. Lam (2018), Energization of the Ring Current by Substorms, *Journal of Geophysical Research: Space Physics*, *123*(10), 8131–8148, doi:10.1029/2018JA025766. 2.3

Sangalli, L., N. Partamies, M. Syrjäsuo, C. F. Enell, K. Kauristie, and S. Mäkinen (2011), Performance study of the new EMCCD-based all-sky cameras for auroral imaging, *International Journal of Remote Sensing*, *32*(11), 2987–3003, doi:10.1080/01431161.2010.541505. 3.1, 4.1

Sato, N., M. Morooka, K. Minatoya, and T. Saemundsson (1998), Nonconjugacy of pulsating auroral patches near L=6, *Geophysical Research Letters*, *25*(20), 3755–3758, doi:10.1029/1998GL900002. 4.1

Sato, N., D. M. Wright, C. W. Carlson, Y. Ebihara, M. Sato, T. Saemundsson, S. E. Milan, and M. Lester (2004), Generation region of pulsating aurora obtained simultaneously by the FAST satellite and a Syowa-Iceland conjugate pair of observatories, *Journal of Geophysical Research: Space Physics*, *109*(A10), 1–15, doi: 10.1029/2004JA010419. 4.1, 4.2

Schwadron, N. A., D. J. McComas, H. A. Elliott, G. Gloeckler, J. Geiss, and R. von Steiger (2005), Solar wind from the coronal hole boundaries, *Journal of Geophysical Research: Space Physics*, *110*(A4), doi:10.1029/2004JA010896. 2.1

Scourfield, M. W., J. G. Keys, E. Nielsen, C. K. Goertz, and H. Collin (1983), Evidence for the E×B drift of pulsating auroras, *Journal of Geophysical Research: Space Physics*, *88*(A10), 7983–7988, doi:10.1029/JA088iA10p07983. 4.1

Seppälä, A. (2004), Solar proton events of October–November 2003: Ozone depletion in the Northern Hemisphere polar winter as seen by GOMOS/Envisat, *Geophysical Research Letters*, *31*(19), L19,107, doi:10.1029/2004GL021042. 1, 4.3

Seppälä, A., M. A. Clilverd, and C. J. Rodger (2007a), NOx enhancements in the middle atmosphere during 2003–2004 polar winter: Relative significance of solar proton events and the aurora as a source, *Journal of Geophysical Research: Atmospheres*, *112*(23), doi:10.1029/2006JD008326. 1, 4.3

Seppälä, A., P. T. Verronen, M. A. Clilverd, C. E. Randall, J. Tamminen, V. Sofieva, L. Backman, and E. Kyrölä (2007b), Arctic and Antarctic polar winter NOx and energetic particle precipitation in 2002–2006, *Geophysical Research Letters*, *34*(12), L12,810, doi:10.1029/2007GL029733. 2.6.4

Seppälä, A., C. E. Randall, M. A. Clilverd, E. Rozanov, and C. J. Rodger (2009), Geomagnetic activity and polar surface air temperature variability, *Journal of Geophysical Research: Space Physics*, *114*(10), doi:10.1029/2008JA014029. 1, 2.6.3, 4.3

Seppälä, A., M. A. Clilverd, M. J. Beharrell, C. J. Rodger, P. T. Verronen, M. E. Andersson, and D. A. Newnham (2015), Substorm-induced energetic electron precipitation: Impact on atmospheric chemistry, *Geophysical Research Letters*, *42*(19), 8172–8176, doi:10.1002/2015GL065523. 4.3, 4.3

Seppälä, A., E. Douma, C. J. Rodger, P. T. Verronen, M. A. Clilverd, and J. Bortnik (2018), Relativistic Electron Microburst Events: Modeling the Atmospheric Impact, *Geophysical Research Letters*, *45*(2), 1141–1147, doi:10.1002/2017GL075949. 4.3

Shklyar, D. R. (2017), Energy transfer from lower energy to higher-energy electrons mediated by whistler waves in the radiation belts, *Journal of Geophysical Research: Space Physics*, *122*(1), 640–655, doi:10.1002/2016JA023263. 2.5

Shprits, Y. Y., R. M. Thorne, R. Friedel, G. D. Reeves, J. Fennell, D. N. Baker, and S. G. Kanekal (2006), Outward radial diffusion driven by losses at magnetopause, *Journal of Geophysical Research: Space Physics*, *111*(11), doi:10.1029/2006JA011657. 2.5

Sinnhuber, M., H. Nieder, and N. Wieters (2012), Energetic Particle Precipitation and the Chemistry of the Mesosphere/Lower Thermosphere, *Surveys in Geophysics*, *33*(6), 1281–1334, doi:10.1007/s10712-012-9201-3. 1, 4.3

Sinnhuber, M., F. Friederich, S. Bender, and J. P. Burrows (2016), The response of mesospheric NO to geomagnetic forcing in 2002–2012 as seen by SCIAMACHY, *Journal of Geophysical Research: Space Physics*, *121*(4), 3603–3620, doi:10.1002/2015JA022284. 1, 4.3

Stenbaek-Nielsen, H. C., and T. J. Hallinan (1979), Pulsating auroras: Evidence for non collisional thermalization of precipitating electrons, *Journal of Geophysical Research: Space Physics*, *84*(A7), 3257, doi:10.1029/ja084ia07p03257. 4.1

Syrjäsuo, M. T. (2001), FMI All-Sky Camera Network, *Tech. Rep. Nr. 52, ISBN 951-697-543-7*, Finnish Meteorological Institute. 3.1

Thomas, E. G., K. T. Sterne, P. V. Ponomarenko, J. B. H. Baker, and J. Michael Ruohoniemi (2014), Remote sensing of sea ice cover using SuperDARN HF radars, pp. 1–1, Institute of Electrical and Electronics Engineers, doi:10.1109/usnc-ursi-nrsm.2014.6928034. 3.4.2

Thorne, R. M., B. Ni, X. Tao, R. B. Horne, and N. P. Meredith (2010), Scattering by chorus waves as the dominant cause of diffuse auroral precipitation, *Nature*, *467*(7318), 943–946, doi:10.1038/nature09467. 2.6.2

Tu, W., W. Li, J. M. Albert, and S. K. Morley (2019), Quantitative Assessment of Radiation Belt Modeling, *Journal of Geophysical Research: Space Physics*, *124*(2), 898–904, doi:10.1029/2018JA026414. 2.5

Turner, D. L., Y. Shprits, M. Hartinger, and V. Angelopoulos (2012), Explaining sudden losses of outer radiation belt electrons during geomagnetic storms, *Nature Physics*, *8*(3), 208–212, doi:10.1038/nphys2185. 2.4, 2.5

Turner, D. L., J. F. Fennell, J. B. Blake, S. G. Claudepierre, J. H. Clemmons, A. N. Jaynes, T. Leonard, D. N. Baker, I. J. Cohen, M. Gkioulidou, A. Y. Ukhorskiy, B. H. Mauk, C. Gabrielse, V. Angelopoulos, R. J. Strangeway, C. A. Kletzing, O. Le Contel, H. E. Spence, R. B. Torbert, J. L. Burch, and G. D. Reeves (2017), Multipoint Observations of Energetic Particle Injections and Substorm Activity During a Conjunction Between Magnetospheric Multiscale (MMS) and Van Allen Probes, *Journal of Geophysical Research: Space Physics*, *122*(11), 481–11, doi:10.1002/2017JA024554. 2.3

Turunen, E., H. Matveinen, J. Tolvanen, and H. Ranta (1996), D-region ion chemistry model, STEP Handbook of Ionospheric Models, (Ed) Schunk, R. W., *SCOSTEP Secretariat, Boulder, Colorado, USA,*, pp. 1–25. 3.3

Turunen, E., P. T. Verronen, A. Seppälä, C. J. Rodger, M. A. Clilverd, J. Tamminen, C. F. Enell, and T. Ulich (2009), Impact of different energies of precipitating particles on NOx generation in the middle and upper atmosphere during geomagnetic storms, *Journal of Atmospheric and Solar-Terrestrial Physics*, *71*(10-11), 1176–1189, doi:10.1016/j.jastp.2008.07.005. 1, 4.3

Turunen, E., A. Kero, P. T. Verronen, Y. Miyoshi, S. I. Oyama, and S. Saito (2016), Mesospheric ozone destruction by high-energy electron precipitation associated with pulsating aurora, *Journal of Geophysical Research: Space Physics*, *121*(19), 11,852–11,861, doi:10.1002/2016JD025015. 4.3, 4.3, 4.3

Tyssøy, H. N., A. Haderlein, M. I. Sandanger, and J. Stadsnes (2019), Intercomparison of the POES/MEPED Loss Cone Electron Fluxes With the CMIP6 Parametrization, *Journal of Geophysical Research: Space Physics*, *124*(1), 628–642, doi:10.1029/2018JA025745. 1

Ukhorskiy, A. Y., and M. I. Sitnov (2013), Dynamics of radiation belt particles, *Space Science Reviews*, *179*(1-4), 545–578, doi:10.1007/s11214-012-9938-5. 2.5

Ukhorskiy, A. Y., B. J. Anderson, P. C. Brandt, and N. A. Tsyganenko (2006), Storm time evolution of the outer radiation belt: Transport and losses, *Journal of Geophysical Research: Space Physics*, *111*. 2.5

Van Allen, J. A. (1959), The geomagnetically trapped corpuscular radiation, *Journal of Geophysical Research: Space Physics*, *64*(11), 1683–1689, doi:10.1029/jz064i011p01683. 2.5

Van Allen, J. A., and L. A. Frank (1959), Radiation around the earth to a radial distance of 107,400 km., *Nature*, *183*(4659), 430–434, doi:10.1038/183430a0. 2.5

Van Allen, J. A., G. H. Ludwig, E. C. Ray, and C. E. McIlwain (1958), Observation of High Intensity Radiation by Satellites 1958 Alpha and Gamma, *Journal of Jet Propulsion*, *28*(9), 588–592, doi:10.2514/8.7396. 2.5

Verronen, P. T., E. Turunen, T. Ulich, and E. Kyrölä (2002), Modelling the effects of the October 1989 solar proton event on mesospheric odd nitrogen using a detailed ion and neutral chemistry model, *Annales Geophysicae*, *20*(12), 1967–1976, doi: 10.5194/angeo-20-1967-2002. 3.3

Verronen, P. T., A. Seppälä, M. A. Clilverd, C. J. Rodger, E. Kyrölä, C.-F. Enell, T. Ulich, and E. Turunen (2005), Diurnal variation of ozone depletion during the October–November 2003 solar proton events, *Journal of Geophysical Research: Space Physics*, *110*(A9), 1–12, doi:10.1029/2004JA010932. 3.3

Verronen, P. T., M. E. Andersson, D. R. Marsh, T. Kovács, and J. M. C. Plane (2016), WACCM-D –Whole Atmosphere Community Climate Model with D-region ion chemistry, *Journal of Advances in Modeling Earth Systems*, *8*(2), 954–975, doi: 10.1002/2015MS000592. 3.3

Wahlund, J. E., H. J. Opgenoorth, and P. Rothwell (1989), Observations of thin auroral ionization layers by EISCAT in connection with pulsating aurora, *Journal of Geophysical Research: Space Physics*, *94*(A12), 17,223–17,233, doi:10.1029/JA094iA12p17223. 4.1

Watanabe, M., A. Kadokura, N. Sato, and T. Saemundsson (2007), Absence of geomagnetic conjugacy in pulsating auroras, *Geophysical Research Letters*, *34*(15), doi:10.1029/2007GL030469. 4.1

Yamamoto, T. (1988), On the temporal fluctuations of pulsating auroral luminosity, *Journal of Geophysical Research: Space Physics*, *93*(A2), 897, doi:10.1029/JA093iA02p00897. 4.1

Yang, B., E. Donovan, J. Liang, J. M. Ruohoniemi, and E. Spanswick (2015), Using patchy pulsating aurora to remote sense magnetospheric convection, *Geophysical Research Letters*, *42*(13), 5083–5089, doi:10.1002/2015GL064700. 4.1

Yang, B., E. Donovan, J. Liang, and E. Spanswick (2017), A statistical study of the motion of pulsating aurora patches: using the THEMIS All-Sky Imager, *Annales Geophysicae*, *35*(2), 217–225, doi:10.5194/angeo-35-217-2017. 4.1

Yang, B., E. Spanswick, J. Liang, E. Grono, and E. Donovan (2019), Responses of Different Types of Pulsating Aurora in Cosmic Noise Absorption, *Geophysical Research Letters*, *46*(11), 5717–5724, doi:10.1029/2019GL083289. 4.2

Zhang, X., V. Angelopoulos, B. Ni, R. M. Thorne, and R. B. Horne (2014), Extent of ECH wave emissions in the Earth's magnetotail, *Journal of Geophysical Research: Space Physics*, *119*(7), 5561–5574, doi:10.1002/2014JA019931. 2.4

Zhang, X., F. He, B. Chen, C. Shen, and H. Wang (2017), Correlations between plasmapause evolutions and auroral signatures during substorms observed by Chang'e-3 EUV Camera, *Earth and Planetary Physics*, *1*(1), 35–43, doi:10.26464/epp2017005. 2.3

Papers

Paper I

Observations of Electron Precipitation During Pulsating Aurora and Its Chemical Impact

Fasil Tesema, Noora Partamies, H. Nesse Tyssøy, Antti Kero, and C. Smith Johnsen
Geophysical Research: Space Physics, **125**, e2019JA027713.
https://doi.org/10.1029/2019JA027713, 2020.

JGR Space Physics

RESEARCH ARTICLE
10.1029/2019JA027713

Observations of Electron Precipitation During Pulsating Aurora and Its Chemical Impact

Fasil Tesema[1,2], **Noora Partamies**[1,2], **H. Nesse Tyssøy**[2], **Antti Kero**[3], and **C. Smith-Johnsen**[2]

[1]Department of Arctic Geophysics, The University Centre in Svalbard, Longyearbyen, Norway, [2]Birkeland Centre for Space Science, University of Bergen, Bergen, Norway, [3]Sodankylä Geophysical Observatory, University of Oulu, Oulu, Finland

Key Points:

- Spacecraft particle measurements were used to construct a statistical precipitation spectrum for 253 pulsating aurora events
- Large flux variations of energetic electron precipitation associated with pulsating aurora between the energies of 10 and 200 keV
- Model results showed mesospheric O_x destruction up to 78% for the median duration of pulsating aurora

Correspondence to:
F. Tesema,
fasil.tesema@unis.no

Citation:
Tesema, F., Partamies, N., Nesse Tyssøy, H., Kero, A., & Smith-Johnsen, C. (2020). Observations of electron precipitation during pulsating aurora and its chemical impact. *Journal of Geophysical Research: Space Physics*, *125*, e2019JA027713. https://doi.org/10.1029/2019JA027713

Received 11 DEC 2019
Accepted 24 APR 2020
Accepted article online 13 MAY 2020

Abstract Pulsating auroras (PsAs) are low-intensity diffuse aurora, which switch on and off with a quasiperiodic oscillation period from a few seconds to ~10 s. They are predominantly observed after magnetic midnight, during the recovery phase of substorms and at the equatorward boundary of the auroral oval. PsAs are caused by precipitating energetic electrons, which span a wide range of energies between tens and hundreds of keV. Such energetic PsA electrons will deposit their energy at mesospheric altitudes and induce atmospheric chemical changes. To examine the effects of energetic PsA electrons on the atmosphere, we first collect electron flux and energy measurements from low-latitude spacecraft to construct a typical energy spectrum of precipitating electrons during PsA. Among the 840 PsA events identified using ground-based auroral all-sky camera (ASC) network over the Fennoscandian region, 253 events were observed by DMSP, POES, and FAST spacecraft over the common field of view of five ASCs. The combined measurements from these spacecraft enable us to obtain an energy spectrum consisting of nonrelativistic and relativistic (30 eV to 1,000 keV) electrons during PsA. The median spectrum was found to be in good agreement with earlier estimates of the PsA spectra. We then use the Sodankylä Ion-neutral Chemistry (SIC) model to assess the chemical effect of PsA electrons. The observed extreme and median spectra of PsA produce a significant depletion in the mesospheric odd oxygen concentration up to 78%.

1. Introduction

Pulsating auroras (PsAs) are characterized by their quasiperiodic low-intensity (few kilo Rayleigh at the green and blue line emissions) variations centered around 100 km altitude (McEwen et al., 1981; Stenbaek-Nielsen & Hallinan, 1979). The emission patches have a horizontal scale size ranging from 10 to 200 km, and they switch on and off with periods from a few to tens of seconds (Lessard, 2012; Royrvik & Davis, 1977; Yamamoto, 1988). The on-time period is shorter with higher energy precipitation (Dahlgren et al., 2017; McEwen et al., 1981) and shows relatively small variations from pulse to pulse compared to the off-time periods (Yamamoto, 1988). PsAs are composed of separate east-west elongated or irregularly shaped patches, which are usually pulsating out of phase from each other with a slightly different period (Sato et al., 2004; Yamamoto, 1988). They are frequently observed at the equatorward boundary of nightside auroral oval and during substorm recovery phases (Lessard, 2012; Nishimura et al., 2020). PsAs are also reported to occur before a substorm onset (McKay et al., 2018), in the premidnight sector during active times (Bland et al., 2019; Partamies et al., 2017), and can persist for up to 15 hr (Jones et al., 2013). They may appear simultaneously in both hemispheres with different shapes and pulsation periods (Sato et al., 2004).

Grono and Donovan (2018) reported three subcategories of PsA based on stability and spatial extent: patchy, amorphous, and patchy PsA. Patchy aurora consists of stable emission structures with pulsations of limited spatial area, patchy PsA is made of steady emission structure with pulsations over much of their spatial extent, and the amorphous type is unstable and rapidly varying PsA. Both patchy and patchy PsA follow magnetospheric convection and were suggested to be a convenient and accurate method to remote sense convection (Yang et al., 2015, 2017). However, amorphous PsA type is more dynamic and has no relation to the convection. Among the three categories the most dominant type is amorphous PsA followed by patchy and pulsating patchy aurora (Grono & Donovan, 2020). Patchy and patchy PsA are suggested to originate from inner magnetosphere, while the source of amorphous PsA can extend radially farthest out from the inner magnetosphere (Grono & Donovan, 2020).

Despite different structures, the mechanism behind the PsA is the precipitation of energetic electrons that originate from the modulation of magnetospheric electrons by wave-particle interactions (Fukizawa et al., 2018; Kasahara et al., 2018; Nishimura et al., 2010, 2011). The energy of the particles is on the order of keV to several tens of keV (Johnstone, 1978; Miyoshi, Oyama, et al., 2015; Sandahl et al., 1980; Sandahl, 1984). The dominant mechanism responsible for scattering magnetospheric electrons associated with precipitating PsA electrons is of much debate (Dahlgren et al., 2017; Mozer et al., 2018; Miyoshi, Saito, et al., 2015; Nishimura et al., 2018; Sato et al., 2004). Nishimura et al. (2010, 2011) provided direct evidence that lower-band chorus waves play a primary role in driving PsA. They further indicated that PsA can exist without upper-band chorus and electron cyclotron harmonic (ECH) waves. Recently, Kasahara et al. (2018) and Fukizawa et al. (2018) implemented the same combinations of measurements to show correlations between brightness fluctuations of the auroral patches with chorus and ECH waves, respectively.

A large range of precipitating electron energies have been measured during PsA. Sato et al. (2002) showed a one-to-one correspondence between optical PsA and the spatiotemporal variations of the downgoing electron fluxes >5 keV measured by Fast Auroral SnapshoT (FAST) spacecraft. Evans et al. (1987) reported a significant amplitude of fluctuation in the electron flux above 20 keV and smaller variations in those below 5 keV measured by National Oceanic and Atmospheric Administration (NOAA) 6 spacecraft overpassing PsA. Miyoshi, Saito, et al. (2015) discussed the energy spectrum of the precipitating PsA electrons generated by different magnetospheric wave sources. They showed that a stable electron precipitation at 1 keV is due to upper band chorus waves, while the lower band chorus waves control the electron precipitation with energies above 2 keV. Jaynes et al. (2013) also reported significant electron flux modulations between electron energies of 30 and 100 keV measured by Geostationary Operational Environmental spacecraft (GOES) 13 spacecraft. They further showed a high correlation between GOES 13 electron flux and PsA optical intensity. Samara et al. (2015) studied the energies of PsA electrons using overpasses of Reimei and Defense Meteorological spacecraft Program (DMSP) spacecraft during six PsA events. Their results showed that the energies causing PsA could range from 3 keV to 30 keV. Earlier rocket measurements of PsA showed that precipitating electrons have energies between 2 and 140 keV (McEwen et al., 1981; Sandahl, 1984; Whalen et al., 1971). A more recent study by Tsuchiya et al. (2018) found that PsA is associated with relativistic electron precipitation with energy range >100 keV using very low frequency (VLF) subionospheric radio wave propagation.

The electrons during PsAs can ionize neutral particles below 100 km (Miyoshi, Oyama, et al., 2015; Turunen et al., 2009, 2016). Electron density observations from the European incoherent scatter (EISCAT) radar have shown a D region (80–95 km) electron density enhancement during PsA events (Hosokawa & Ogawa, 2015). They reported electron density maximum altitude to be 10 km lower during the on-period compared to the off-period of PsA. Electron density enhancements below 70 km measured by EISCAT radar further suggest that the electron precipitation associated with PsA have energies up to hundreds of keV (Hosokawa & Ogawa, 2015; Miyoshi, Oyama, et al., 2015; Oyama et al., 2016; Turunen et al., 2016). Precipitation of PsA electrons can lead to significant production of odd hydrogen ($HO_x = H + OH + HO_2$) and odd nitrogen ($NO_x = N + NO + NO_2$) followed by catalytic reactions that destroy ozone in the polar mesosphere (Turunen et al., 2016).

However, the actual variation and range of the precipitation energy and flux related to PsA are not known. There is also no observational evidence of chemical changes during this type of precipitation. To fully understand the impact of energetic PsA electrons in the atmosphere, it is crucial to characterize the electrons spectra. Atmospheric models, such as Whole Atmosphere Community Climate Model (WACCM), use Kp and Ap indices to parameterize the energy input during energetic electrons precipitation (EEP) (Smith-Johnsen et al., 2018, and references therein); however, EEP associated with PsA often occurs during the recovery phase of a substorm, where magnetic deflection has already recovered. Thus, the use of magnetic indices may lead to an underestimation of the higher energy precipitation in to the atmosphere. In this paper, we will use an extensive data set from auroral all-sky cameras (ASCs) to detect PsA events together with in situ particle energy measurements to construct a typical precipitation energy spectrum with realistic variation. This is followed by investigation of chemical effects of the precipitating electrons by using the Sodankylä Ion-neutral Chemistry (SIC) model (Turunen et al., 2009; Verronen et al., 2005).

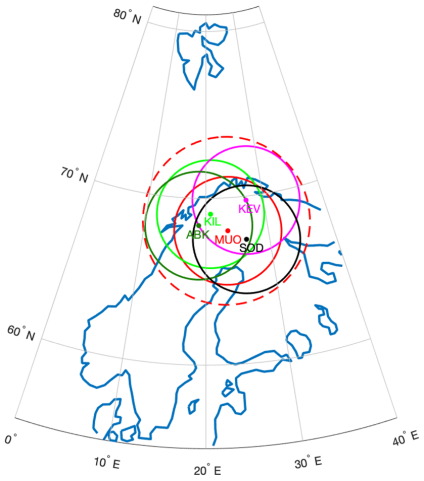

Figure 1. Geographic locations of ground based ASC stations in the Fennoscandian region from FMI-MIRACLE network. Color-coded circles around the stations show the full fields of view of the cameras. The red dashed circle, which comprises of all the ASC FOV, is the region where spacecraft overpasses are considered in the data analysis.

2. Data and Methods

The PsA events were identified by visual inspection of ASC keograms (Eather et al., 1976) from the MIRACLE network operated by the Finnish Meteorological Institute (FMI) (Sangalli et al., 2011). A keogram is a plot of north-south slices of individual ASC images, which are displayed as a function of time. We used data from Abisko (ABK, 68.36°N, 18.82°E), Kevo (KEV, 69.76°N, 27.01°E), Kilpisjärvi (KIL, 69.02°N, 20.87°E), Muonio (MUO, 68.02°N, 23.53°E), and Sodankylä (SOD, 67.42°N, 26.39°E) stations. For this study we extended the list by Partamies et al. (2017) to cover the years between 1997 and 2019. After all keograms were viewed, we searched for overpassing spacecraft that can measure precipitating electron energies. The region where the overpassing spacecraft are taken into consideration in the data analysis is the common field of view (FOV) of all the ASCs, which is indicated by the red dashed circle in Figure 1. A typical example of particle data from Polar Orbiting Environmental Spacecraft (POES) (from 0.189 keV to 1,000 keV) and DMSP (from 30 eV to 30 keV) is depicted in Figure 2c. From the 840 PsA events over the 23-year period of study, 253 events coincided with overpasses by DMSP (137), POES (240), and FAST (9) spacecraft with a total of 376 overpasses.

The electron and ion spectrometer analyzers on board FAST spacecraft are designed to measure energies of auroral particles with high pitch angle, temporal resolution, and sensitivity. They are used to obtain distributions of 48 energies at different angles with 1 s time resolution. The standard electron energy range measured by one of the analyzers is between 4 eV and 30 keV (Carlson et al., 1998). We analyze these data where the particles' pitch angle are below 3° to capture the precipitating population.

The special sensor for precipitating particles, Version 4 (SSJ4) and Version 5 (SSJ5) on board DMSP spacecraft is a particle spectrometer looking upward and designed to measure the flux of auroral electrons and ions with energies between 30 eV and 30 keV. Details about DMSP spacecraft SSJ measurements and data availability can be found in Redmon et al. (2017). We used the DMSP SSJ data archived in the Coupling Energetics and Dynamics of Atmospheric Regions (CEDAR) madrigal database.

The two sets of electron telescopes in the Medium Energy Proton and Electron Detector (MEPED) on board NOAA-POES spacecraft measure the flux of electrons which are pointing 0° and 90° with respect to local normal (Evans & Greer, 2000). At middle and high latitudes, the 0° telescope measures particle fluxes that will be lost to the atmosphere, whereas the 90° telescope might detect precipitating particle fluxes and/or trapped particles in the radiation belts (Rodger et al., 2010). As the level of pitch angle anisotropy varies significantly with particle energy, location, and geomagnetic activity, the 0° detector will underestimate,

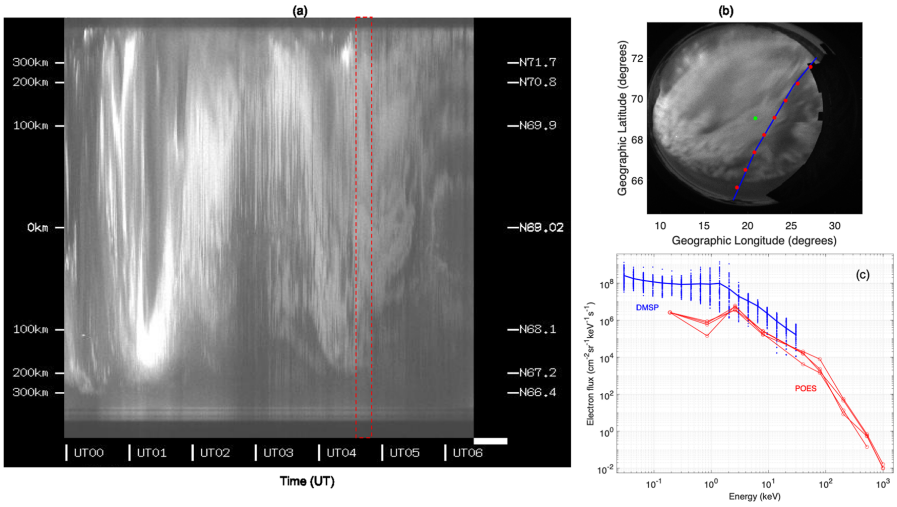

Figure 2. (a) Keogram generated from a series of KIL ASC camera images of green emission at 557.7 nm. (b) Overpasses of DMSP f16 (blue line, from 4:34 to 4:36 UT) with a time resolution of 1 s and NOAA-18 POES (red dots, 4:47 to 4:49 UT) with a time resolution of 16 s over Kilpisjärvi ASC image taken at 04:40 UT. The green dot shows the zenith of the ASC. (c) Spectrum constructed from the two spacecraft overpasses, on 22 January 2015. The red dashed box depicted on the keogram is the time between 4:34 and 4:49 UT, when both spacecraft were passing over KIL.

while the 90° detector will overestimate the flux of precipitating electrons. A more realistic estimate of the precipitating fluxes in the bounce loss cone can, however, be achieved by fitting the 0° and 90° fluxes onto the solution of the Fokker-Planck equation for particles (Nesse Tyssøy et al., 2016). The electron spectra are further corrected for low energy proton contamination, taking into account the degradation of the proton detectors. Cross contamination of relativistic electrons in the proton detector provides an extra electron energy channel. Finally, new optimized energy limits and associated geometric factors give the following four integral channels (>43, >114, >292, and >756 keV). Further details about the correction procedures and construction of optimized energy channels can be found in Nesse Tyssøy et al. (2016), Ødegaard et al. (2017), and Sandanger et al. (2015).

Total Electron Detector (TED) is another type of detector on board POES, which can measure low energy particle fluxes between 0.05 and 20 keV (Evans & Greer, 2000). POES-TED data are available as differential flux at four electron channels on both 0° and 30° telescopes with energy bands of 0.15–0.22, 0.69–1, 2.12–3.08, and 6.50–9.46 keV. In this study we use the 0° telescope measurement to account for the lower limit of electron precipitation. To construct the POES-MEPED differential flux from the integral flux measurements, we calculate the difference between consecutive energy channels. The centers of the channels are assumed to be the central energy. The data points obtained from this difference were fitted by a power law function (Whittaker et al., 2013), to derive the differential flux. This power law function was also used to extrapolate further points in both ends of the channels at 25 and 1,000 keV energies. With this approach we get nine data points at 0.19, 0.84, 2.60, 7.98, 25, 78.5, 203, 524, and 1,000 keV energies. To connect these data points, we use linear interpolation in a logarithmic scale.

To study the chemical effect of precipitating PsA electrons, we run the 1-D SIC model (Verronen et al., 2005) for the maximum, minimum, and average spectrum constructed from all overpasses. The SIC model is a coupled middle atmospheric ion and neutral chemistry model, which can be run in either steady state or time-dependent mode between 20 and 150 km altitudes with 1 km resolution. The model is known to capture ion and neutral changes in the atmosphere due to energetic particle precipitation (EPP) forcing (Verronen et al., 2016, and references therein). It includes hundreds of reactions consisting of 41 positive and 29 negative ions and 34 neutral species. It includes molecular and eddy diffusion but not atmospheric transport processes. The time-dependent mode is suitable for studying diurnal variations of atmospheric response due to external forcing such as electron and proton precipitations. We investigate effects due to

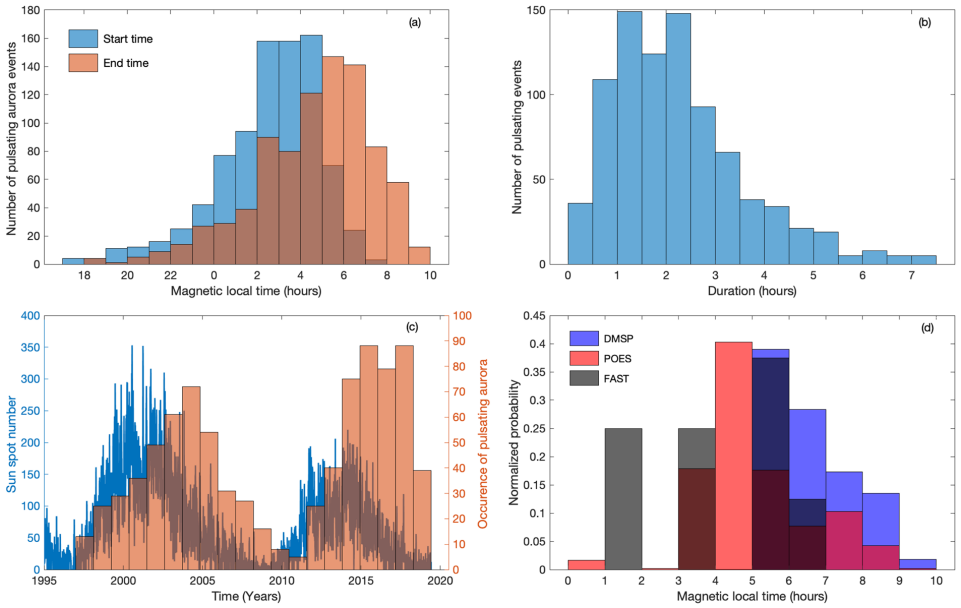

Figure 3. (a) A distribution of start and end times of all PsA events in MLT, (b) durations of the PsA events, (c) occurrence of PsA with respect to the sunspot number, and (d) self-normalized histogram of the MLT occurrence of spacecraft overpasses over the combined FOV of ASCs.

different durations and spectra of the PsA electrons forcing. More detailed explanation about the SIC model implementations is provided in Verronen et al. (2005) and Turunen et al. (2009).

3. Results

3.1. PsA Precipitation Energies

An analysis of precipitating electron measurements was undertaken using data from different spacecraft which are passing over PsA. Figure 2 shows an example of PsA ASC observation and electron spectra on 22 January 2015, during a moderate geomagnetic activity ($Kp = 3$). As it is shown in the keogram (Figure 2a), an active PsA that started just before 2 UT in the southern part of the FOV soon moved over the zenith. The PsA in the keogram is observed as consecutive bright and dark vertical stripes. The pulsation remains the dominant aurora type between 3:00 and 3:54 UT. It expanded southward and pulsated for nearly 20 min before retreating northward. The POES-NOAA18 spacecraft and DMSP-f16 spacecraft passed over the FOV at 4:47–4:49 and at 4:34–4:36 UT, respectively. The overpasses are shown in Figure 2b on the ASC image taken at 04:40 UT. The electron spectra during the overpasses are shown in Figure 2c. The solid blue line is the overpass average flux from DMSP, and the dots show the flux in one second time resolution during the overpass. The red curve shows the integrated measurements from POES-TED and MEPED instruments. From this figure, it can be seen that the electron flux between 700 eV and 2 keV, and between 10 keV and 30 keV show high variations. The softer precipitation of the energies between 3 and 10 keV undergo relatively small variations. POES TED and DMSP measurements show a large difference in the energy range below 2 keV. POES-MEPED measurements produce a smooth curve as a continuation of DMSP measurements toward higher energies.

As we used ASC data from five FMI-MIRACLE cameras, we could investigate some general characteristics of PsA events. In Figure 3a the distribution of the start and end times of the PsA events shows that these events are dominant during postmidnight to morning hours. The start time of the events peaks between 2:30 and 4:30 magnetic local time (MLT). The end time is a conservative estimate as many of the events were cut short due to the sunrise and the termination of imaging. The PsA events mostly end between 6 and 8 MLT.

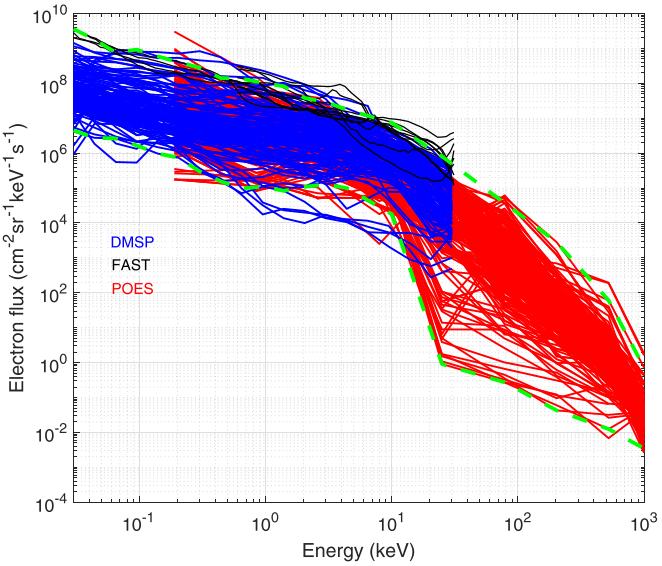

Figure 4. Constructed energy spectrum for pulsating aurora from a combination of 137 overpasses DMSP (blue), FAST 9 overpasses (black), and POES 240 overpasses (red), spacecraft measurements. The green dashed curves are the upper and lower boundaries of the spectra used in the SIC model run.

The duration of the events varies between 1 and 3 hr with a median value of 2 hr as shown in Figure 3b. There are also some events that persist longer than 4 hr. Figure 3c shows the annual number of PsA events with the sunspot number (SSN). The figure clearly shows a time shift of 1–3 years between the solar activity and the number of PsA events. Most of the events were observed during the declining phase of the solar activity. Comparing the two decline phases, the higher number of PsA events were found in the second one, where relatively low values of SSN in the whole solar cycle (2010–2019) were recorded.

Figure 4 shows all electron precipitation flux spectra from a combination of spacecraft overpasses over the common FOV illustrated in Figure 1. The electron fluxes are averaged over an overpass, while a spacecraft takes at most 4 min to cross the common ASC FOV. The spectra from different spacecraft (black, blue, and red colors for FAST, DMSP and POES, respectively) behave coherently at ~3 keV energy with small variation up to 10 keV. A considerable range of electron flux values with more than 2 orders of magnitude is evident with

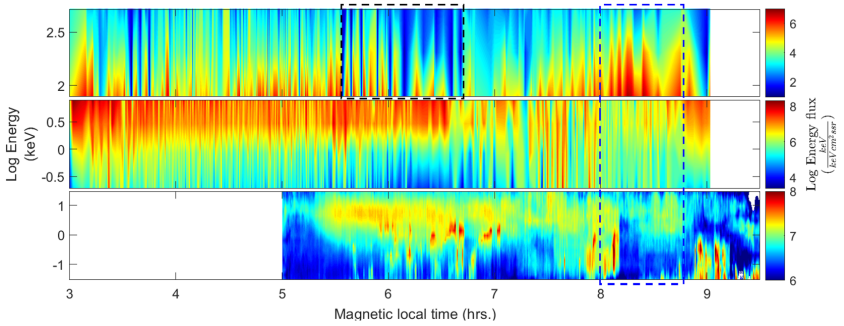

Figure 5. MLT evolution of PsA electrons energy spectra from MEPED and TED on board POES (upper two panels) and from DMSP (lowest panel) spacecraft.

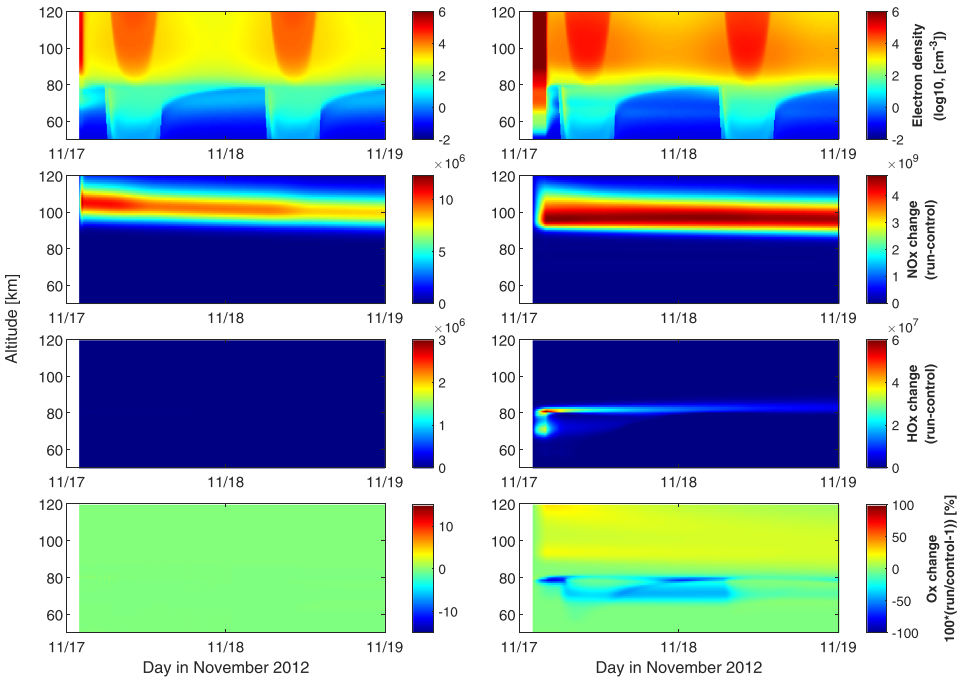

Figure 6. Modeled (from top), electron density (N_e), odd hydrogen (HO_x), odd nitrogen (NO_x), and odd oxygen (O_x). The left panels are forced with lower energy spectrum envelope from Figure 4 for 30 min, and the right panels are forced with the upper energy spectrum for 120 min. All model results are displayed for a 2-day time period.

the energies of <2 and >10 keV. Energies between 20 and 200 keV show the largest flux range. The overall spectrum shape is a smooth curve with significant variation in electron flux values in the high energy tail. For example, the flux at 30 and 100 keV ranges from 10^0 to 10^6 and 10^{-1} to $10^4 cm^{-2} keV^{-1} sr^{-1} s^{-1}$, respectively. The lowest spectra show a relatively sharp decrease at 10 keV. At the lower energy end of the spectrum, DMSP observations are coherent as compared to POES-TED measurements (red) at higher energies. Some of the differences seen can be due to the difference in MLT overpasses between the two spacecraft shown in Figure 3d. POES has a number of overpasses before 5 MLT, while all DMSP overpasses are after 5 MLT. The spectrum obtained from FAST spacecraft (black) lies at the upper boundary of all spectra and show sharp changes at energies higher than 20 keV. However, a large number of passes from DMSP and POES measurements together reflect smooth behavior.

By sorting all measurements from DMSP and POES spacecraft overpasses in time, we generate MLT evolution of the precipitating electrons energy flux spectra. We binned the energy flux of the precipitating electrons in 36 s time slots, which roughly accounts for on and off phases of PsA together (e.g., see Hosokawa & Ogawa, 2015), as shown in Figure 5. The first and second panels of Figure 5 are generated from POES-MEPED and POES-TED measurements, while the bottom panel consists of DMSP data. Generally, the MLT evolution of energetic particles from MEPED does not show any trend. However, there are abrupt decreases in flux around 5:30–6:30 MLT (dashed rectangle). Particles from TED with energies above 2 keV show high flux values until 6:30 MLT and a more systematic decrease in the morning hours passed 8 MLT. The third panel of Figure 5 shows relatively persistent fluxes at the electron energies between 1 and 10 keV over the entire period of observations. The prominent feature in this energy range is observed between 5:30 and 6:30 MLT, when the flux of ~10 keV electrons is nearly constant. Energy flux dropouts start to appear after 6:30 MLT. After 9 MLT, the harder precipitation starts to decay. The harder precipitation of electrons (>10 keV) shows a persistent value between 5:30 to 6:30 MLT followed by higher energy flux with dropouts,

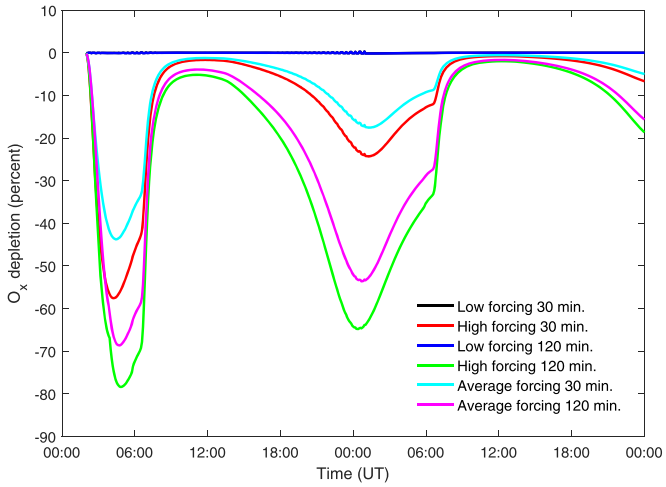

Figure 7. Relative differences in odd oxygen concentration at the maximum depletion altitude (79 km) with the different forcing durations for high, low, and average spectra. The modeled time span in 2 days.

particularly between 7 and 8:45 MLT. After 8:45, the flux at 10 keV energies are significantly reduced. The softer precipitation (<1 keV) shows a high variability throughout the whole observation period, with minima at 5 to 6, 7 to 7:30, and 8:10 to 8:50 and maxima values in the rest of the time period. The higher values of the softer precipitation are dominantly observed in the morning sector (after 7:30 MLT). Comparing the three panels of Figure 5, the precipitation lower than 10 keV decreases significantly after 6:30 MLT, while the higher energies either persist or show a tendency to increase in the morning sectors.

3.2. Atmospheric Effects of PsA

After initializing the SIC model at 68.02°N and 23.53°E (MUO station), the model run was performed for a randomly selected two day period on 17–19 November 2012 with and without the PsA forcing. The model temporal resolution was 5 min. We implemented the electron forcing for 30 and 120 min with the upper and lower boundaries of the spectrum, which are smooth curves identified by eye, as shown in Figure 4 (green dashed lines). By considering the median MLT of the spacecraft overpasses of to be at 4.5 MLT as shown in Figure 3d, the electron forcing was started at 2 UT (4.5 MLT in Fennoscandian sector) on 17 November 2012. The absolute and relative examined magnitudes of HO_x, NO_x, and O_x obtained from this model run are used to characterize the response of the atmosphere to the forcing. Figure 6 shows the model outputs of electron density, change in NO_x, change in HO_x, and percentage change in O_x with respect to the model run without forcing. The left panel shows a 30 min forcing with the lower boundary spectrum, and the right-hand side contains a 120 min forcing with the upper boundary spectrum. During the case of the shorter forcing, a significant enhancement of electron density reaches an altitude of 80 km. The NO_x response, in this case, was observed mainly between 100 and 120 km with the highest values at ~105 km at the time of forcing. The NO_x enhancement was centered around 100 km after 2 days with a value nearly half of the maximum. However, there were no observable HO_x and O_x changes. The case of the long time forcing with a harder spectrum showed an electron density enhancement at significantly lower altitudes reaching below 60 km. The NO_x change during this forcing was observed to be centered between 93 and 110 km with the maximum at 96 km. The change in HO_x shows a double maxima separated by ~10 km at the time of forcing. The largest HO_x change was observed at 81 km altitude with a value of 5.9×10^7 cm^{-3}, and the secondary maximum of 3.4×10^7 cm^{-3} occurred at 72 km. The primary increase in HO_x continued for more than 24 hr after the forcing. Consequently, the change in O_x showed the highest percentage depletion in a very narrow vertical extent at around 79 km until sunrise. After sunrise, a significant depletion persists as a double layer with the minimum values of −18% and −31% at altitudes of 81 and 71 km, respectively. The double structures observed during the daytime almost merged to create a vertically broader and more intense depletion during

the night. During the next day, the double layer depletion persisted but the magnitudes decreased to 7% and 17% at 72 and 79 km, respectively.

To study the temporal evolution of the change in O_x for the two days of the model run in more detail, we take the altitude of the maximum depletion observed during the entire model run time (79 km). In addition to the lower and upper boundary energy spectrum, we also calculated the average spectrum for the 30 and 120 min forcing as included in Figure 7. As mentioned above the atmosphere does not respond to the softer forcing scenarios. The four scenarios that showed significant depletions are from the averaged and upper boundary spectra. The maximum O_x depletion of these scenarios occurred 2.5 to 3 hr after the start of forcing. The average spectrum induced a maximum O_x depletion of 44% and 69%, and the upper boundary spectrum induce a depletion of 58% and 78% for 30 and 120 min forcing, respectively. The depletions in all these scenarios before sunrise showed a similar shape: a sharp decrease at the time forcing and a quick recovery before sunrise. However, the next day the change in O_x from these cases behaved differently. The O_x depletion during the longer forcing decreased quickly after sunset. The shorter forcing led to the maximum O_x depletion 25 min earlier on the forcing day and 40 min later in the following day compared to the longer forcing. The longer forcing induced almost the whole night of O_x depletion (>10%) even 24 hr after the forcing. The mesospheric O_x recovered during the next day, but the depletion continues during the night after. Comparing the maximum depletion between the day of forcing and the next day, the difference is smaller for the longer forcing. The O_x depletion is still significant (up to 20%) for the longer forcing after nearly 48 hr.

4. Discussions

We used an extensive data set of images and keograms from FMI-MIRACLE ASC network to identify 840 PsA events. In this study, the occurrence of PsA is highest from the local midnight until the end of the imaging in the morning sector. Our events have a median duration of 2 hr. The occurrence time is in a very good agreement with results from Grono and Donovan (2020). The PsA duration is also in agreement with previous statistical studies of PsA, which reported a duration between 1.4 and 2.25 hr (Bland et al., 2019; Jones et al., 2011; Partamies et al., 2017). PsA occurrence peaks toward the declining phase of the solar cycle. The declining phase of solar cycle is often associated with a high probability of high-speed solar wind streams and high occurrence frequency of EPP (Asikainen & Ruopsa, 2016), which is favorable for PsA.

Previous studies have indicated that the PsA electrons have energies between 2 and 200 keV. However, most of the studies have either been case studies or used an indirect method to obtain information about the precipitating PsA electrons energy (Miyoshi, Oyama, et al., 2015; McEwen et al., 1981; Sandahl, 1984; Sandahl et al., 1980; Whalen et al., 1971). This makes the results of such studies difficult to consider as representative for the typical energy range of precipitating PsA electrons. In this study, we used overpassing spacecraft to measure the PsA electrons during 253 events. We constructed PsA electrons energy flux spectra from different spacecraft measurements, which span energies between 30 eV and 1,000 keV with variable resolution. In Figure 4, it can be clearly seen that not all the spectra are smooth, but there are abrupt changes especially in connecting POES-TED and MEPED at energies from 20 to 80 keV, sudden increases in FAST observations above ~20 keV and sudden decreases in DMSP spectra above 10 keV. Keeping in mind that the MLT distribution shows fewer spacecraft overpasses in the morning sector (Figure 3d), Figure 5 (blue dashed rectangle) shows higher flux at higher energy range, while the softer precipitation decreases. Such increase in high energy flux in the late MLT sector was reported by Hosokawa and Ogawa (2015) and can be associated with a tendency to observe PsA in this sector. Furthermore, Hosokawa and Ogawa (2015) showed a higher electron density in late MLT PsA and the increase in the resonance energy of the pitch angle scattering in late MLT sector was suggested to be the cause for this increase in energy. Recently, Grono and Donovan (2018) categorized PsA into patchy, patchy pulsating, and amorphous PsA, Yang et al. (2019) further studied the energies of these categories and showed that one amorphous PsA case was related to energies centred around 20 keV, while a patchy PsA event had energies around 9 keV. The abrupt flux changes in the spectra could be related to a PsA subcategory change, which should be examined further in the future. It has been reported that different categories of PsA, patchy, patchy pulsating, and amorphous types, differ in time of occurrence, energy, and location (Grono & Donovan, 2020; Yang et al., 2019). Lacking harder precipitation between 5:30 and 6:30 MLT (Figure 5) but observing significant precipitation below 10 keV suggests that we are predominantly observing patchy PsA, which is associated with lower energy compared to amorphous

PsA. After 7 MLT softer precipitation decreases while harder precipitation tends to increase, which supports the dominance of the amorphous type PsA in the morning sector as reported by Grono and Donovan (2020).

As it is shown in the collection of spectra (Figure 4), the flux of PsA electrons in the medium energy (>30 keV) range is significant. Such energetic particles will strongly ionize the mesosphere and consequently destroy ozone through catalytic reactions involving HO_x (and NO_x) species (Sinnhuber et al., 2012, and references therein). This may further alter the thermal balance and the middle atmospheric dynamics. During winter this effect can propagate to lower altitudes and affect the lower stratospheric dynamics and regional climate over large timescales (Rozanov et al., 2012; Seppälä et al., 2013). Thus, the evaluation of the atmospheric response to PsA electron forcing was approached by using the SIC model with statistically characterized spectra. The absence of the atmospheric response to the forcing with a lower boundary spectrum raises the question on the threshold flux of energetic particles that can induce odd oxygen depletion. Forcing with the upper boundary spectrum indicated that the PsA electrons are capable of destroying a large amount of O_x species within a broad vertical extent (~10 km). A similar study by Turunen et al. (2016) showed strongest O_x depletion in the following day compared to the time of forcing. They reported mesospheric O_x depletion due to the electron forcing during a single PsA event to be between 14% and 82%. They discussed the possibility of an overestimation of the particle flux from the VanAllen probes' measurements and concluded the 25% depletion of odd oxygen to be realistic. The number of PsA events overpassed by the spacecraft represent 30% of all the events identified in this study. By taking the median duration of PsA (2 hr) as the duration of the forcing, together with the average spectrum, resulted in 69% depletion of O_x at the time of forcing and 54% during the following night. This is double the previously proposed ozone depletion.

Miyoshi, Oyama, et al. (2015) estimated the spectrum of a PsA event from EISCAT measurements. In their study, the spectra information from EISCAT electron density inversion was limited to energies below 100 keV. A reduced pitch angle scattering at relativistic energy range is suggested to lead to a high discrepancy between the estimated spectrum and spectrum measured by Van Allen Probes. Turunen et al. (2016) further investigate the uncertainity in the hard end of the spectrum using Metropolis-Hastings Markov chain Monte Carlo (MCMC) method. They conclude that the MCMC median spectrum, which lies between the estimated spectrum and Van Allen measurements spectrum is a reasonable one. This spectrum is in a very good agreement with our average spectrum, which further strengthens the significance of pitch angle scattering at relativistic energy range.

The O_x depletion of 44% we obtained soon after the forcing is significantly higher: (shown in Figure 6) compared to the 15% reported in Turunen et al. (2016). Because the highest energy end of the spectrum that predominantly affects the middle atmosphere was obtained from the POES spacecraft and the dominant overpassing time was between 4 and 5 MLT (1.5 to 2.5 UT, see Figure 3), we started the forcing at 2 UT. This is 2 hr earlier than in Turunen et al. (2016). Our results show that the magnitude of the depletion soon after the forcing is comparable to the depletion during the following night. This is not the case reported by the Turunen et al. (2016). They found a smaller depletion at the time of the forcing as compared to the following night for all the scenarios considered. The large O_x depletion shortly after the forcing suggests that a detectable mesospheric O_3 change could be measured in the future. Here, the average spectrum applied to the 30 min forcing resulted in 44% odd oxygen depletion, which is of the same magnitude as that during substrom electron precipitation (Seppälä et al., 2015). The short-term extremely large odd oxygen depletion obtained in this study, is also comparable with the EEP effect reported by Andersson et al. (2014). Using multiple spacecraft measurements, Andersson et al. (2014) showed that the direct HO_x production due to EEP lead to 90% depletion for a shorter time and 34% depletion for more extended time scales. The effects of the precipitating electrons are also comparable to large but less frequent ozone destruction due to solar proton events (Seppälä, 2004; Verronen et al., 2005).

The SIC model results presented in this study open a way to further study ozone destruction due to PsA electrons using coupled models including transport, such as the WACCM (which includes ion chemistry in the *D* region Verronen et al., 2016) model. By considering the magnitude and the spatial coverage of O_x depletion reported in this study, we anticipate that the atmospheric response to the PsA electron forcing will be significant in the dynamical models as well. As it is also known that PsAs are frequent events with nearly 50% occurrence (Bland et al., 2019), and the HO_x, NO_x, and O_x responses reported in this study did not fully recover within almost 48 hr, there may also be a cumulative atmospheric effect by the precipitating particles.

5. Conclusions

By combining measurements from three spacecraft, we presented statistical PsA electron energy spectrum that includes relativistic and nonrelativistic energies between 30 eV and 1,000 keV. The highest variations of the flux of electrons were observed between 10 and 200 keV, typical for PsA events. The MLT evolution of PsA electrons energy flux does not show any significant trend at any specific energy. However, PsA electrons with higher energies (>30 keV) persisted in the morning hours, while the softer precipitation decayed earlier. The ion chemistry model implemented here showed a wide range of magnitude of O_x depletion between 0% and 78% for short (30 min) to median (120 min) duration of PsA precipitation. The lowest measured fluxes during PsA neither produced HO_x nor depleted ozone, while the highest measured fluxes caused significant ozone depletions both during the forcing and the following night due to the persistent enhancement in the odd hydrogen. The results of this 1-D model raise a number of questions, such as the sensitivity of the atmosphere for the particle forcing, the significance of this depletion in the dynamical model runs, and if observations of change in ozone and associated species during PsA events can be achieved.

Data Availability Statement

MIRACLE ASC quicklook data are available at the website (https://space.fmi.fi/MIRACLE/ASC/?page=keograms), and full-resolution image data can be requested from FMI (kirsti.kauristie@fmi.fi). The entire FAST mission data can be found online (http://sprg.ssl.berkeley.edu/fast/). DMSP particle data are available at CEDAR madrigal database (http://cedar.openmadrigal.org). Event lists, precipitating electrons energy from DMSP, POES, and FAST spacecraft, and SIC model outputs used in this study are available in Tesema et al. (2019).

Acknowledgments
The funding support for F. Tesema and H. Nesse Tyssøy work is provided by the Norwegain Research Council (NRC) under CoE Contract 223252. In addition, the work of N. Partamies is supported by NRC project 287427. The work of C. Smith-Johnsen is supported by the NRC project 263008. The work of Antti Kero is funded by the Tenure Track Project in Radio Science at Sodankylä Geophysical Observatory/University of Oulu. We thank K. Kauristie, S. Mäkinen, J. Mattanen, A. Ketola, and C.-F. Enell for maintaining MIRACLE camera network and data flow. We thank NOAA's SWPC and NCEI (formerly NGDC) for the availability of NOAA POES data.

References

Andersson, M. E., Verronen, P. T., Rodger, C. J., Clilverd, M. A., & Seppälä, A. (2014). Missing driver in the Sun-Earth connection from energetic electron precipitation impacts mesospheric ozone. *Nature Communications*, *5*(1), 5197. https://doi.org/10.1038/ncomms6197

Asikainen, T., & Ruopsa, M. (2016). Solar wind drivers of energetic electron precipitation. *Journal of Geophysical Research: Space Physics*, *121*(3), 2209–2225. https://doi.org/10.1002/2015JA022215

Bland, E. C., Partamies, N., Heino, E., Yukimatu, A. S., & Miyaoka, H. (2019). Energetic electron precipitation occurrence rates determined using the Syowa East SuperDARN radar. *Journal of Geophysical Research: Space Physics*, *124*, 6253–6265. https://doi.org/10.1029/2018JA026437

Carlson, C. W., Pfaff, R. F., & Watzin, J. G. (1998). The Fast Auroral SnapshoT (FAST) Mission. *Geophysical Research Letters*, *25*(12), 2013–2016. https://doi.org/10.1029/98GL01592

Dahlgren, H., Lanchester, B. S., Ivchenko, N., & Whiter, D. K. (2017). Variations in energy, flux, and brightness of pulsating aurora measured at high time resolution. *Annales Geophysicae*, *35*(3), 493–503. https://doi.org/10.5194/angeo-35-493-2017

Eather, R. H., Mende, S. B., & Judge, R. J. R. (1976). Plasma injection at synchronous orbit and spatial and temporal auroral morphology. *Journal of Geophysical Research*, *81*(16), 2805–2824. https://doi.org/10.1029/JA081i016p02805

Evans, D. S., Davidson, G. T., Voss, H. D., Imhof, W. L., Mobilia, J., & Chiu, Y. T. (1987). Interpretation of electron spectra in morningside pulsating aurorae. *Journal of Geophysical Research*, *92*(A11), 12,295. https://doi.org/10.1029/JA092iA11p12295

Evans, D. S., & Greer, M. S. (2000). Polar orbiting environmental satellite space environment monitor—2: Instrument descriptions and archive data documentation. NOAA Tech. Memo., OAR SEC 93, 93, version 1.4, Boulder, Colo., 2004 Jan.

Fukizawa, M., Sakanoi, T., Miyoshi, Y., Hosokawa, K., Shiokawa, K., Katoh, Y., et al. (2018). Electrostatic electron cyclotron harmonic waves as a candidate to cause pulsating auroras. *Geophysical Research Letters*, *45*, 12,661–12,668. https://doi.org/10.1029/2018GL080145

Grono, E., & Donovan, E. (2018). Differentiating diffuse auroras based on phenomenology. *Annales Geophysicae*, *36*(3), 891–898. https://doi.org/10.5194/angeo-36-891-2018

Grono, E., & Donovan, E. (2020). Surveying pulsating auroras. *Annales Geophysicae*, *38*(1), 1–8. https://doi.org/10.5194/angeo-38-1-2020

Hosokawa, K., & Ogawa, P. (2015). Ionospheric variation during pulsating aurora. *Journal of Geophysical Research: Space Physics*, *120*, 5943–5957. https://doi.org/10.1002/2015JA021401

Jaynes, A. N., Lessard, M. R., Rodriguez, J. V., Donovan, E., Loto'Aniu, T. M., & Rychert, K. (2013). Pulsating auroral electron flux modulations in the equatorial magnetosphere. *Journal of Geophysical Research: Space Physics*, *118*, 4884–4894. https://doi.org/10.1002/jgra.50434

Johnstone, A. D. (1978). Pulsating aurora. *Nature*, *274*(5667), 119–126. https://doi.org/10.1038/274119a0

Jones, S. L., Lessard, M. R., Rychert, K., Spanswick, E., & Donovan, E. (2011). Large-scale aspects and temporal evolution of pulsating aurora. *Journal of Geophysical Research*, *116*, A03214. https://doi.org/10.1029/2010JA015840

Jones, S. L., Lessard, M. R., Rychert, K., Spanswick, E., Donovan, E., & Jaynes, A. N. (2013). Persistent, widespread pulsating aurora: A case study. *Journal of Geophysical Research: Space Physics*, *118*, 2998–3006. https://doi.org/10.1002/jgra.50301

Kasahara, S., Miyoshi, Y., Yokota, S., Mitani, T., Kasahara, Y., Matsuda, S., et al. (2018). Pulsating aurora from electron scattering by chorus waves. *Nature*, *554*(7692), 337–340. https://doi.org/10.1038/nature25505

Lessard, M. R. (2012). A review of pulsating aurora. *Aurora Phenomenology Magnetospheric Processes Earth Other Planets*, 55–68. https://doi.org/10.1029/2011GM001187

McEwen, D. J., Yee, E., Whalen, B. A., & Yau, A. W. (1981). Electron energy measurements in pulsating auroras. *Canadian Journal of Physics*, *59*(8), 1106–1115. https://doi.org/10.1139/p81-146

McKay, D., Partamies, N., & Vierinen, J. (2018). Pulsating aurora and cosmic noise absorption associated with growth-phase arcs. *Annales Geophysicae*, *36*(1), 59–69. https://doi.org/10.5194/angeo-36-59-2018

Miyoshi, Y., Oyama, S., Saito, S., Kurita, S., Fujiwara, H., Kataoka, R., et al. (2015). Energetic electron precipitation associated with pulsating aurora: EISCAT and Van Allen Probe observations. *Journal of Geophysical Research: Space Physics*, *120*, 2754–2766. https://doi.org/10.1002/2014JA020690

Miyoshi, Y., Saito, S., Seki, K., Nishiyama, T., Kataoka, R., Asamura, K., et al. (2015). Relation between fine structure of energy spectra for pulsating aurora electrons and frequency spectra of whistler mode chorus waves. *Journal of Geophysical Research: A Space Physics*, *120*, 7728–7736. https://doi.org/10.1002/2015JA021562

Mozer, F. S., Hull, A., Lejosne, S., & Vasko, I. Y. (2018). Reply to Comment by Nishimura Et Al. *Journal of Geophysical Research: Space Physics*, *123*, 2071–2077. https://doi.org/10.1002/2018JA025218

Nesse Tyssøy, H., Sandanger, M. I., Ødegaard, L.-K. G., Stadsnes, J., Aasnes, A., & Zawedde, A. E. (2016). Energetic electron precipitation into the middle atmosphere—Constructing the loss cone fluxes from MEPED POES. *Journal of Geophysical Research: Space Physics*, *121*, 5693–5707. https://doi.org/10.1002/2016JA022752

Nishimura, Y., Bortnik, J., Li, W., Angelopoulos, V., Donovan, E. F., & Spanswick, E. L. (2018). Comment on Pulsating auroras produced by interactions of electrons and time domain structures by Mozer Et Al. *Journal of Geophysical Research: Space Physics*, *123*, 2064–2070. https://doi.org/10.1002/2017JA024844

Nishimura, Y., Bortnik, J., Li, W., Thorne, R. M., Chen, L., Lyons, L. R., et al. (2011). Multievent study of the correlation between pulsating aurora and whistler mode chorus emissions. *Journal of Geophysical Research*, *116*, A11221. https://doi.org/10.1029/2011JA016876

Nishimura, Y., Bortnik, J., Li, W., Thorne, R. M., Lyons, L. R., Angelopoulos, V., et al. (2010). Identifying the driver of pulsating aurora. *Science (80-.)*, *330*(6000), 81–84. https://doi.org/10.1126/science.1193186

Nishimura, Y., Lessard M. R., Katoh Y., Miyoshi Y., Grono E., Partamies N., et al. (2020). Diffuse and Pulsating Aurora. *Space Science Reviews*, *216*(1). https://doi.org/10.1007/s11214-019-0629-3

Ødegaard, L. K. G., Tyssøy, H. N., Søraas, F., Stadsnes, J., & Sandanger, M. I. (2017). Energetic electron precipitation in weak to moderate corotating interaction region-driven storms. *Journal of Geophysical Research: Space Physics*, *122*, 2900–2921. https://doi.org/10.1002/2016JA023096

Oyama, S., Kero A., Rodger C. J., Clilverd M. A., Miyoshi Y., Partamies N., et al. (2017). Energetic electron precipitation and auroral morphology at the substorm recovery phase. *Journal of Geophysical Research: Space Physics*, *122*(6), 6508–6527. https://doi.org/10.1002/2016JA023484

Partamies, N., Whiter, D., Kadokura, A., Kauristie, K., Nesse Tyssøy, H., Massetti, S., et al. (2017). Occurrence and average behavior of pulsating aurora. *Journal of Geophysical Research: Space Physics*, *122*, 5606–5618. https://doi.org/10.1002/2017JA024039

Redmon, R. J., Denig, W. F., Kilcommons, L. M., & Knipp, D. J. (2017). New DMSP database of precipitating auroral electrons and ions. *Journal of Geophysical Research: Space Physics*, *122*, 9056–9067. https://doi.org/10.1002/2016JA023339

Rodger, C. J., Clilverd, M. A., Green, J. C., & Lam, M. M. (2010). Use of POES SEM-2 observations to examine radiation belt dynamics and energetic electron precipitation into the atmosphere. *Journal of Geophysical Research*, *115*, A04202. https://doi.org/10.1029/2008JA014023

Royrvik, O., & Davis, T. N. (1977). Pulsating aurora: Local and global morphology. *Journal of Geophysical Research*, *82*(29), 4720–4740. https://doi.org/10.1029/JA082i029p04720

Rozanov, E., Calisto, M., Egorova, T., Peter, T., & Schmutz, W. (2012). Influence of the precipitating energetic particles on atmospheric chemistry and climate. *Survey of Geophysics*, *33*(3-4), 483–501. https://doi.org/10.1007/s10712-012-9192-0

Samara, M., Michell, R. G., & Redmon, R. J. (2015). Low-altitude satellite measurements of pulsating auroral electrons. *Journal of Geophysical Research: Space Physics*, *120*, 8111–8124. https://doi.org/10.1002/2015JA021292

Sandahl, I. (1984). Pitch angle scattering and particle precipitation in a pulsating aurora—An experimental study. KGI Rept. no. 185. Kiruna, Sweden: Kiruna Geophysical Institute.

Sandahl, I., Eliasson, L., & Lundin, R. (1980). Rocket observations of precipitating electrons over a pulsating aurora. *Geophysical Research Letters*, *7*(5), 309–312. https://doi.org/10.1029/GL007i005p00309

Sandanger, M. I., Ødegaard, L.-K. G., Tyssøy, H. N., Stadsnes, J., Søraas, F., Oksavik, K., & Aarsnes, K. (2015). In flight calibration of NOAA POES proton detectors—Derivation of the MEPED correction factors. *Journal of Geophysical Research: Space Physics*, *120*, 9578–9593. https://doi.org/10.1002/2015JA021388

Sangalli, L., Partamies, N., Syrjäsuo, M., Enell, C. F., Kauristie, K., & Mäkinen, S. (2011). Performance study of the new EMCCD-based all-sky cameras for auroral imaging. *International Journal of Remote Sensing*, *32*(11), 2987–3003. https://doi.org/10.1080/01431161.2010.541505

Sato, N., Wright, D. M., Carlson, C. W., Ebihara, Y., Sato, M., Saemundsson, T., et al. (2004). Generation region of pulsating aurora obtained simultaneously by the FAST satellite and a Syowa-Iceland conjugate pair of observatories. *Journal of Geophysical Research*, *109*, A10201. https://doi.org/10.1029/2004JA010419

Sato, N., Wright, D. M., Ebihara, Y., Sato, M., Murata, Y., Doi, H., et al. (2002). Direct comparison of pulsating aurora observed simultaneously by the FAST satellite and from the ground at Syowa. *Geophysical Research Letters*, *29*(21), 2041. https://doi.org/10.1029/2002GL015615

Seppälä, A., Clilverd, M. A., Beharrell, M. J., Rodger, C. J., Verronen, P. T., Andersson, M. E., & Newnham, D. A. (2015). Substorm induced energetic electron precipitation: Impact on atmospheric chemistry. *Geophysical Research Letters*, *42*, 8172–8176. https://doi.org/10.1002/2015GL065523

Seppälä, A., Lu, H., Clilverd, M. A., & Rodger, C. J. (2013). Geomagnetic activity signatures in wintertime stratosphere wind, temperature, and wave response. *Journal of Geophysical Research: Atmospheres*, *118*, 2169–2183. https://doi.org/10.1002/jgrd.50236

Seppälä, A. (2004). Solar proton events of October November 2003: Ozone depletion in the Northern Hemisphere polar winter as seen by GOMOS/Envisat. *Geophysical Research Letters*, *31*, L19107. https://doi.org/10.1029/2004GL021042

Sinnhuber, M., Nieder, H., & Wieters, N. (2012). Energetic particle precipitation and the chemistry of the mesosphere/lower thermosphere. *Survey of Geophysical*, *33*(6), 1281–1334. https://doi.org/10.1007/s10712-012-9201-3

Smith-Johnsen, C., Marsh, D. R., Orsolini, Y., Nesse Tyssøy, H., Hendrickx, K., Sandanger, M. I., et al. (2018). Nitric oxide response to the April 2010 electron precipitation event: Using WACCM and WACCM-D with and without medium-energy electrons. *Journal of Geophysical Research: Space Physics*, *123*, 5232–5245. https://doi.org/10.1029/2018JA025418

Stenbaek-Nielsen, H. C., & Hallinan, T. J. (1979). Pulsating auroras: Evidence for non collisional thermalization of precipitating electrons. *Journal of Geophysical Research*, *84*(A7), 3257. https://doi.org/10.1029/JA084ia07p03257

Tesema, F., Partamies, N., Tyssøy, H. N., Kero, A., & Johnsen, C. S. (2019). Precipitating electrons energy and SIC model run during pulsating aurora over fennoscandian region. Dataset. https://doi.org/10.6084/m9.figshare.11352065.v1

Tsuchiya, F., Hirai, A., Obara, T., Misawa, H., Kurita, S., Miyoshi, Y., et al. (2018). Energetic electron precipitation associated with pulsating aurora observed by VLF radio propagation during the recovery phase of a substorm on 27 March 2017. *Geophysical Research Letters*, 651–660. https://doi.org/10.1029/2018GL080222

Turunen, E., Kero, A., Verronen, P. T., Miyoshi, Y., Oyama, S. I., & Saito, S. (2016). Mesospheric ozone destruction by high-energy electron precipitation associated with pulsating aurora. *Journal of Geophysical Research: Space Physics*, *121*, 11,852–11,861. https://doi.org/10.1002/2016JD025015

Turunen, E., Verronen, P. T., Seppälä, A., Rodger, C. J., Clilverd, M. A., Tamminen, J., et al. (2009). Impact of different energies of precipitating particles on NOx generation in the middle and upper atmosphere during geomagnetic storms. *Journal of Atmospheric and Solar-Terrestrial Physics*, *71*(10-11), 1176–1189. https://doi.org/10.1016/j.jastp.2008.07.005

Verronen, P. T., Andersson, M. E., Marsh, D. R., Kovács, T., & Plane, J. M. C. (2016). WACCM-D—Whole Atmosphere Community Climate Model with D-region ion chemistry. *Journal Advance Modeling Earth System*, *8*, 954–975. https://doi.org/10.1002/2015MS000592

Verronen, P. T., Seppälä, A., Clilverd, M. A., Rodger, C. J., Kyrölä, E., Enell, C. F., et al. (2005). Diurnal variation of ozone depletion during the October-November 2003 solar proton events. *Journal of Geophysical Research*, *110*, A09S32. https://doi.org/10.1029/2004JA010932

Whalen, B. A., Miller, J. R., & McDiarmid, I. B. (1971). Energetic particle measurements in a pulsating aurora. *Journal of Geophysical Research*, *76*(4), 978–986. https://doi.org/10.1029/JA076i004p00978

Whittaker, I. C., Gamble, R. J., Rodger, C. J., Clilverd, M. A., & Sauvaud, J.-A. (2013). Determining the spectra of radiation belt electron losses: Fitting DEMETER electron flux observations for typical and storm times. *Journal of Geophysical Research: Space Physics*, *118*, 7611–7623. https://doi.org/10.1002/2013JA019228

Yamamoto, T. (1988). On the temporal fluctuations of pulsating auroral luminosity. *Journal of Geophysical Research*, *93*(A2), 897. https://doi.org/10.1029/JA093iA02p00897

Yang, B., Donovan, E., Liang, J., Ruohoniemi, J. M., & Spanswick, E. (2015). Using patchy pulsating aurora to remote sense magnetospheric convection. *Geophysical Research Letters*, *42*, 5083–5089. https://doi.org/10.1002/2015GL064700

Yang, B., Donovan, E., Liang, J., & Spanswick, E. (2017). A statistical study of the motion of pulsating aurora patches: using the THEMIS All-Sky Imager. *Annales Geophysicae*, *35*(2), 217–225. https://doi.org/10.5194/angeo-35-217-2017

Yang, B., Spanswick, E., Liang, J., Grono, E., & Donovan, E. (2019). Responses of different types of pulsating aurora in cosmic noise absorption. *Geophysical Research Letters*, *46*, 5717–5724. https://doi.org/10.1029/2019GL083289

Paper II

Observations of precipitation energies during different types of pulsating aurora

Fasil Tesema, Noora Partamies, H. Nesse Tyssøy, and Derek McKay
Ann. Geophys., **38, 1191–1202**, https://doi.org/10.5194/angeo-38-1191-2020, 2020.

Ann. Geophys., 38, 1191–1202, 2020
https://doi.org/10.5194/angeo-38-1191-2020

Annales Geophysicae
Open Access
EGU

Observations of precipitation energies during different types of pulsating aurora

Fasil Tesema[1,2], **Noora Partamies**[1,2], **Hilde Nesse Tyssøy**[2], **and Derek McKay**[3,4]

[1]The University Centre in Svalbard (UNIS), Longyearbyen, Norway
[2]Birkeland Centre for Space Science, University of Bergen, Bergen, Norway
[3]Finnish Centre for Astronomy with ESO, FINCA, University of Turku, Turku, Finland
[4]Sodankylä Geophysical Observatory, University of Oulu, Sodankylä, Finland

Correspondence: Fasil Tesema (fasil.tesema@unis.no)

Received: 30 June 2020 – Discussion started: 7 July 2020
Revised: 21 September 2020 – Accepted: 29 September 2020 – Published: 13 November 2020

Abstract. Pulsating aurora (PsA) is a diffuse type of aurora with different structures switching on and off with a period of a few seconds. It is often associated with energetic electron precipitation (> 10 keV) resulting in the interaction between magnetospheric electrons and electromagnetic waves in the magnetosphere. Recent studies categorize pulsating aurora into three different types – amorphous pulsating aurora (APA), patchy pulsating aurora (PPA), and patchy aurora (PA) – based on the spatial extent of pulsations and structural stability. Differences in precipitation energies of electrons associated with these types of pulsating aurora have been suggested. In this study, we further examine these three types of pulsating aurora using electron density measurements from the European Incoherent Scatter (EISCAT) VHF/UHF radar experiments and Kilpisjärvi Atmospheric Imaging Receiver Array (KAIRA) cosmic noise absorption (CNA) measurements. Based on ground-based all-sky camera images over the Fennoscandian region, we identified a total of 92 PsA events in the years between 2010 and 2020 with simultaneous EISCAT experiments. Among these events, 39, 35, and 18 were APA, PPA, and PA types with a collective duration of 58, 43, and 21 h, respectively. We found that, below 100 km, electron density enhancements during PPAs and PAs are significantly higher than during APA. However, there are no appreciable electron density differences between PPA and APA above 100 km, while PA showed weaker ionization. The altitude of the maximum electron density also showed considerable differences among the three types, centered around 110, 105, and 105 km for APA, PPA, and PA, respectively. The KAIRA CNA values also showed higher values on average during PPA (0.33 dB) compared to PA (0.23 dB) and especially APA (0.17 dB). In general, this suggests that the precipitating electrons responsible for APA have a lower energy range compared to PPA and PA types. Among the three categories, the magnitude of the maximum electron density shows higher values at lower altitudes and in the late magnetic local time (MLT) sector (after 5 MLT) during PPA than during PA or APA. We also found significant ionization down to 70 km during PPA and PA, which corresponds to ∼ 200 keV of precipitating electrons.

1 Introduction

The interaction between solar wind and the magnetosphere results in particle precipitation into the Earth's atmosphere through many different processes. Particles from the plasma sheet and radiation belts are accelerated and scattered into a loss cone to eventually collide with the species in the Earth's polar atmosphere. These collisions cause the atmospheric gas to glow in different shimmering bands of color in the sky, called aurora. The most common colors of the aurora are blue, green, and red at wavelengths of 427.8, 557.7, and 630.0 nm, respectively. However, an auroral spectrum ranges from ultraviolet to infrared wavelengths depending on the type of atmospheric gas that undergoes emission. In general, the electrons generating aurora have energies ranging from 100 eV to 100 keV, which affects the atmosphere by ionizing and changing the chemistry (Rees, 1969). The auroras are varied in appearance due to different magnetospheric pro-

cesses; most are visible as discrete auroras with ribbons, arcs, and spirals, and some are visible as blinking patches of light called pulsating auroras (PsAs).

Pulsating auroras are mostly characterized as quasi-periodic low-intensity (a few kilo rayleigh) diffuse emission, which switches on and off with periods of a few seconds to a few tens of seconds (Royrvik and Davis, 1977; Yamamoto, 1988). The structures of PsA can be irregularly shaped patches or thin arcs elongated in an east–west direction (Wahlund et al., 1989; Böinger et al., 1996) and constantly evolving (Partamies et al., 2019). They usually occur at 100 km altitude and have a horizontal scale size ranging from 10 to 200 km (McEwen et al., 1981; Hosokawa and Ogawa, 2015; Nishimura et al., 2020). The average duration of PsA is around 2 h (Jones et al., 2011; Partamies et al., 2017; Bland et al., 2019; Tesema et al., 2020); however, some very long durations (15 h) have also been reported (Jones et al., 2013). Pulsating auroras are frequently observed in the nightside equatorward boundary of the auroral oval and during substorm recovery phases in the morning sector. Depending on the level of geomagnetic activity, the time and location of PsA may vary. This variation ranges from observing at all local times during intense geomagnetic activity to being localized to midnight to the morning sector around 68° magnetic latitude during weak geomagnetic activity.

Most of the investigations related to pulsating aurora have been multi-measurement case studies using, for instance, all-sky cameras (ASCs), radars, rockets, riometers, and satellite measurements (Jones et al., 2009; Lessard et al., 2012; McKay et al., 2018; Yang et al., 2019; Nishimura et al., 2020). However, recently a considerable number of statistical findings have been documented, specifically using optical, satellite, incoherent scatter radars, and Super Dual Auroral Radar Network (SuperDARN) measurements (Jones et al., 2011; Hosokawa and Ogawa, 2015; Partamies et al., 2017; Grono and Donovan, 2018; Bland et al., 2019; Grono and Donovan, 2020; Tesema et al., 2020). It is now well documented that the energies associated with PsA span a wide range from tens to hundreds of kiloelectron volts (Miyoshi et al., 2010, 2015). Pulsating aurora electrons are generally accepted to originate from the magnetosphere near the equatorial plane through pitch angle scattering of energetic electrons into the loss cone by plasma waves (Nishimura et al., 2010, 2011). A source in the magnetospheric equatorial plane implies that pulsating aurora is observed in both hemispheres. However, different shapes and pulsating periods of PsA between hemispheres have also been reported (Watanabe et al., 2007; Sato et al., 2004).

A significant number of studies have used incoherent scatter radars to study the ionization, structure, and energies of precipitating electrons associated with PsA (Wahlund et al., 1989; Böinger et al., 1996; Jones et al., 2009; Hosokawa and Ogawa, 2015; Miyoshi et al., 2015). A recent study by Hosokawa and Ogawa (2015) showed a higher European Incoherent Scatter (EISCAT) electron density at lower altitudes during PsA, which is more pronounced in the morning sector. Similarly, Oyama et al. (2016) showed a maximum electron density below 100 km during a pulsating aurora. Jones et al. (2009) utilized ionization from incoherent scatter radar in Poker Flat, Alaska, to estimate the energy distribution of PsA electrons and compared it with rocket measurements. They showed that the layer of maximum electron density associated with pulsating patches has a thickness (full width at half maximum) of $\sim$ 15–25 km. Miyoshi et al. (2015) used EISCAT electron density, Van Allen Probes, and optical data to study the source and the energy of precipitating electrons during PsA. They identified electron density enhancement at altitudes above 68 km associated with the pulsating aurora. Hosokawa and Ogawa (2010) showed a significant ionization in the E region and upper part of the D region (80–95 km) due to energetic precipitation during PsA. This ionization in the D region leads to the appearance of the Pedersen current layer exactly at the altitudes where pulsating ionization occurs and plays a vital role in modifying the current system in the ionosphere. Hosokawa et al. (2010) used high-time-resolution electron density data during PsA and identified enhanced electron density in the E region (95–115 km). They further indicated that the intense ionization could lead to a significant effect on the ionospheric conductivity and current system and, in turn, affect the motion and shapes of PsA patches. Hard precipitation of PsA electrons is known to reach below 70 km and can ionize and change the chemistry of the mesosphere (Turunen et al., 2009, 2016; Tesema et al., 2020). It has also been shown by model results that not all PsA electrons cause strong ionization and chemical changes (Tesema et al., 2020).

Ionospheric absorption of cosmic radio noise at the D region altitudes has been observed during energetic particle precipitation ($>$ 10 keV) associated with PsA (Milan et al., 2008; Grandin et al., 2017; McKay et al., 2018; Bland et al., 2019). Riometric absorption in the ionosphere covers a range of altitudes in the D and E regions that contribute to the observed absorption (Wild et al., 2010; Rodger et al., 2012). Thus, observing a one-to-one correspondence between PsA and ionospheric absorption (Grandin et al., 2017; McKay et al., 2018) further suggests that PsA electrons' energy also covers large ranges. However, the cosmic noise absorption (CNA) values are reported to be low during PsA (below $\sim$ 0.5 dB), compared to substorm values (above $\sim$ 1 dB). These low values suggest that the flux of energetic electrons during substorms is significantly larger than during PsA. High-frequency radio attenuations in the D region from the SuperDARN radars can also be used to detect energetic electron precipitation associated with PsA (Bland et al., 2019).

Based on pulsation, lifetime, and spatial extent, a recent study by Grono and Donovan (2018) categorized pulsating aurora into three groups: patchy, amorphous, and patchy pulsating aurora. Patchy aurora (PA) consists of stable emission structures with pulsations over a limited area of the

spatial extent. A patchy pulsating aurora (PPA) is made up of steady emission structures with pulsations over a large fraction of their spatial extent, and the amorphous pulsating aurora (APA) is unstable and rapidly varying pulsating aurora. PPA and PA follow the magnetospheric convection, while APA is more dynamic and does not follow the magnetospheric convection. The occurrence probability of the different types of PsA is reported by Grono and Donovan (2020). The most dominant type is APA, followed by PA and PPA. They concluded that before midnight the typical PsA type is APA, while PPA and PA are more common in the late morning. They also estimated the average location of the source regions using T89 model mapping. Before midnight, the source of all types of PsA is constrained in the same area, while after midnight APA extends further out in the magnetosphere.

An investigation of a few PsA events by Yang et al. (2019) showed a high correlation between CNA absorption and emission intensity of the APA type, but no correlation with PPA emission intensity. They also reported the possibility of an extended higher energy range during APA compared to PPA using satellite measurements of a single event. Recently, Tesema et al. (2020) suggested that the abrupt changes in the statistical energy spectrum curve of PsA might be associated with mixing different types of PsA. PsA structure change between patch-like and arc-like, and having a characteristic of changing patch size through time in general, is suggested to be related to the change in precipitation energy (Partamies et al., 2017, 2019). The question of what are the sources and mechanisms driving different PsAs is still unanswered. A key step to answering this question is to quantify the associated electron fluxes and spectra. In this study, we therefore investigate the altitude and level of ionization, which are related to energies and flux of precipitating electrons, during different PsAs. We use electron density measurements from EISCAT VHF/UHF radars and CNA measurements from the Kilpisjärvi Atmospheric Imaging Receiver Array (KAIRA) riometer. The EISCAT radars and KAIRA measure the impact from electrons that is truly lost in the atmosphere, compared to incomplete loss cone observations from, for instance, satellite observations. Thus, the height and magnitude of maximum electron density are an indirect measure of energies and flux of precipitating electrons, respectively.

2 Materials and methods

The optical data used in this study are from ground-based ASCs operated by the Finnish Meteorological Institute (FMI). The FMI Magnetometers–Ionospheric Radars–Allsky Cameras Large Experiment (MIRACLE) network consists of nine ASCs located in the Fennoscandian region. The database has been a huge data source in auroral studies for more than 40 years. As technological advancements were growing and the ASC quality was degrading in time, two of the digital ASCs with intensified charge-coupled devices (ICCDs) were replaced with the newer technology of electron-multiplying CCDs (EMCCDs) in 2007. Such cameras are more suitable for studying very faint auroral structures (Sangalli et al., 2011), like pulsating aurora, in detail. For event identification, the entire data set in this study is from these newer cameras. We use images filtered for the green emission at 557.7 nm in addition to a few events with images of the blue emission at 427.8 nm. From the nine ASCs, we used Kilpisjärvi (KIL, 69.02° N, 20.87° E, geographic) as our primary data source. However, when there were no data at KIL, a nearby site, Abisko (ABK, 68.36° N, 18.82° E, geographic), was used as a substitute. The fields of view (FOVs) of both sites cover a large area around the FOV of EISCAT radars located in Tromsø, as shown in Fig. 1.

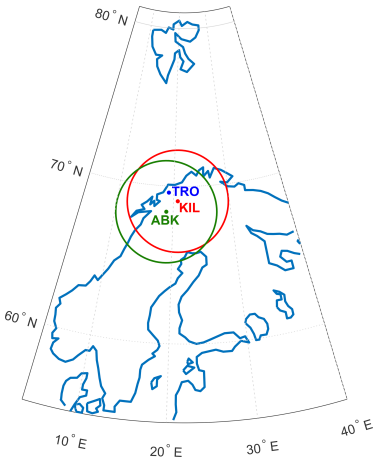

Figure 1. Geographic locations of ground-based ASC stations (KIL and ABK) from the MIRACLE network and locations of EISCAT radars (TRO). KAIRA FOV is the same as KIL ASC.

To study the ionization associated with PsA, we examined electron density measurements from the EISCAT radar located at Tromsø, Norway (69.58° N, 19.21° E, geographic). The EISCAT radar system consists of UHF and VHF radars, which operate at frequencies of 931 and 224 MHz, respectively (Rishbeth and Williams, 1985). We used Common Programme One (CP1), Common Programme Two (CP2) radar modes for UHF, and Common Programme Six (CP6) radar mode VHF radars. These modes are suitable for observing ionization in the D and E regions with a range resolution of < 6 km during particle precipitation events. Details about the radar modes can be found at https://eiscat.se/scientist/document/experiments/ (last access: 4 November 2020). During the pulsating auroras, either the UHF or VHF radar was operative, and electron density was obtained in either the field-aligned or zenith measurements. We then

used the magnitude and altitude of electron densities during different types of PsA to understand the flux and energy of electrons associated with them.

We identified 92 pulsating aurora events observed simultaneously by ASC at KIL or ABK and the EISCAT radars at Tromsø (see Fig. 1). The temporal resolutions of optical data was ≤ 10 s, and that of the radar data was 1 min. This period is significantly longer than the typical period of PsA, which does not allow separation of the on and off phases of PsA. Thus, all the results presented in this study are average statistics over on and off periods of PsA. Types of PsA are identified using keograms and ewograms generated at the location of the ASC, as described by Grono and Donovan (2018). As these quick-look data formats are not always sufficient and accurate for detecting types of PsA, especially during the transition between types, we used individual all-sky camera images to confirm the detection. APA can be distinguished from the other PsA types by looking at the ewograms and identifying periods where there are no apparent speed line tracings (i.e., similar structures shown by a blue arrow on the second panel of Fig. 2). PPA and PA have more persistent structures, which enables us to identify them quickly. Since PPA has a pulsating nature over a wider spatial extent of otherwise stable patches, striations (alternating bright and dim states of PsA) in the speed line on ewograms are used to differentiate them from PA. During PA, the speed lines have no vertical striations. Once all PsA with at least a few minutes (> 10 min) duration were divided into the three subcategories, we then investigated the altitude profile of PsA ionization. The altitude of the maximum electron density and the magnitude of the electron density provide indirect information about the energy and flux of the precipitating PsA electrons, respectively.

Because PsAs cover a wide range of altitudes and electron energies, comparing the altitude and magnitude of maximum electron density does not always provide the full information on the precipitating electrons. For a detailed investigation of electron density between different PsA types, we average the electron density into five groups with altitude steps of 10 km between 70 and 120 km. Two of them, between 110 and 120 km and between 100 and 110 km, are groups in the E region, and the other three – between 90 and 100 km, between 80 and 90 km, and between 70 and 80 km – are groups in the D region of the ionosphere.

We also used measurements of CNA made using KAIRA: a radio-receiving system located at Kilpisjärvi in northern Finland (McKay et al., 2015). An observing frequency of 38.086 ± 0.098 MHz was used. Signals from the 48 low-band antennas of KAIRA were cross-correlated with a sample integration of 1 s to form antenna covariance matrices. All-sky radio images can be formed from these using 2D Fourier transforms, which have a zenith spatial resolution of approximately 24 km at 90 km altitude. However, to achieve the same effect as an optical keogram, only a 1D Fourier transform of the meridian pixels is made for each time sample, thus forming a "riometric keogram" – or *riogram*. CNA is determined as $A = 10\log_{10}(P_q/P)$, where A is absorption in decibels, P is the observed power, and P_q is the quiet-sky power derived from a median of meridian slices from equivalent sidereal times over a period of 14 d prior to the observation.

The separation between the locations of the FMI camera and KAIRA array is ~ 2.27 km. This proximity means that for observations of ionospheric phenomena in the D region they have nearly coincident sky coverage. Since the field of view of EISCAT lies within the all-sky absorption image, comparing results obtained from EISCAT and KAIRA is also possible. The KAIRA facility has previously been used to study pulsating aurora (Grandin et al., 2017; McKay et al., 2018). The riometry data corpus from KAIRA spans from 2014 to 2020 and includes 50 events out of the 92 events identified using optical data.

3 Results

By inspecting 11 years (between 2010 and 2020) of ASC images from the FMI-MIRACLE network in combination with EISCAT electron density measurements, we identified PsA events based on classification implemented in Grono and Donovan (2018) and Yang et al. (2019). In the process, we produced high-time-resolution keograms and ewograms (~ 10 s cadence instead of 1 min, as in quick-look data) from ASC images at KIL and ABK. Examples of events that consist of all the three types of PsAs within a single event are shown in Figs. 2, 3, and 4. The panels in these figures from top to bottom show the keogram, ewogram, EISCAT electron density, and altitude of maximum electron density, and an additional panel with KAIRA CNA riogram in Fig. 4. The dashed red line overlaid in the keograms (ewograms) is the latitude (longitude) of the EISCAT radar. In Fig. 2, the APA type is observed between 00:30 and 01:06 UT (green shading), PPA between 01:06 and 01:26 UT (red shading), and PA between 01:26 and 02:00 UT (purple shading). During these intervals, a single type was dominant over the FOV of the ASC and/or EISCAT. However, after 02:00 UT, the APA type starts to be apparent in the northwestward direction and lasts until 03:10 UT. After that, the APA type fills the FOV of the camera. For this event, the PsA type between 02:00 and 03:10 UT is labeled as PA, because the EISCAT radar beam lies within this type of PsA as indicated by dashed red lines. The third panel in Fig. 2 shows the electron density profiles. During APA, the electron density (N_e) enhancement shows significant values above 100 km, which is apparent at the beginning and end of this event. In between, we observe PPA and PA types, for which the N_e shows higher values, mostly below 100 km. A corresponding substantial N_e enhancement is observed when the patchy aurora lies in the FOV of the radar after 01:30 UT. The N_e enhancements during these PsA types reach down to 70 km. The last panel in Fig. 2 shows the altitude of the maximum N_e, illustrating a gradual decrease

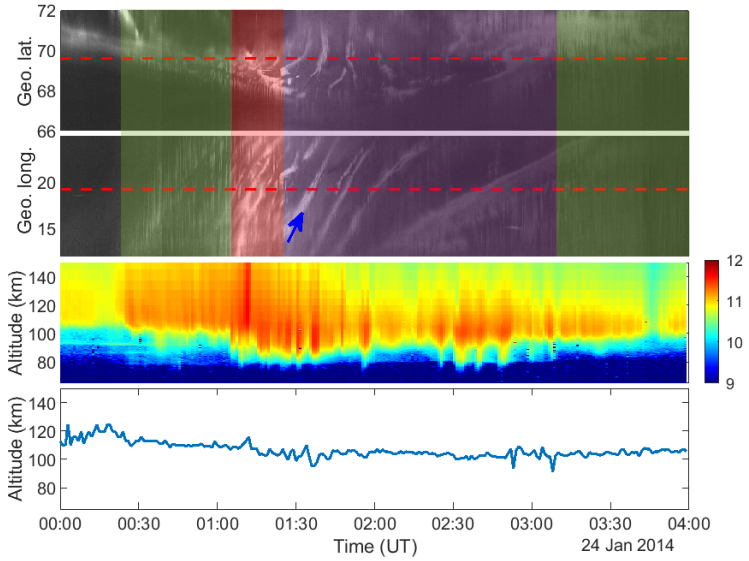

Figure 2. Keogram, ewogram, EISCAT electron density, and altitude of maximum electron density on 24 January 2014. The dashed red lines are the latitude and longitude of the EISCAT radar's FOV. PsA types – APA (green), PPA (red), and PA (purple) – are marked with rectangles in the keograms and ewograms.

in height at the beginning and a slight increase at the end of the event. However, equivalent substantial differences in N_e observed below 105 km between APA and the other two are not captured by the height of maximum electron density.

Figure 3 shows the three types of PsA in a single event on 25 January 2012, which lasts more than 6 h. The panels displayed in the figure are the same as in Fig. 2. Inspection of this figure shows that different types of PsA are observed in different regions of the sky. Before 02:00 UT APA is dominant below 70° latitude followed by a combination of faint unstructured and very low emission up until 03:00 UT. After that, PPA becomes dominant below 68° latitude; however, over the EISCAT FOV APA is dominant until 04:00 UT. After 04:00 UT, almost the entire sky is filled with PPA, and then, after 05:30 UT, PA starts to appear. The N_e and its maximum altitude in the EISCAT FOV (dashed red lines in keograms and ewograms) are displayed on the lower two panels of the figure. There is a clear difference in the magnitude of electron density and the altitude of maximum N_e during the different types of PsA. The interesting big difference is observed around 04:00 UT, where there was a transition between APA and PPA. This transition is also apparent at the altitude of the maximum N_e. During APA, the maximum N_e altitude lies at 110 km; however, during PPA, it is below 100 km. The PA electron density magnitudes and the altitude of the maximum N_e show high variations corresponding to the patch-on and patch-off periods over the EISCAT FOV.

Figure 4 shows similar panels to those displayed in Figs. 2 and 3 with an additional panel of KAIRA CNA riogram with the EISCAT FOV marked by the dashed red line. In this figure, before 01:00 UT, the APA type of PsA on the top panel is far away from the EISCAT FOV. However, just before 01:00 UT, a different non-pulsating type of auroral activity becomes visible over EISCAT. This is followed by PPA for a very short duration; then up until 02:00 UT, APA is dominant. Between 02:00 and 03:00 UT, PPA followed by PA was observed. The N_e also shows considerable differences during the different PsA types. A significant N_e magnitude enhancement below 80 km around 02:15 UT is seen during PPA. But such a transition is not apparent at the altitude of the maximum electron density. Furthermore, the close correspondence between the CNA values and the emission in the keogram is evident. The CNA values, along with the EISCAT FOV and how deep the ionization occurred, have a nearly one-to-one correspondence. The CNA values during PPA are above 1 dB, while during APA CNA is below 1 dB.

The thickness (full width at half maximum) of PsA ionization during these three types of PsA showed large differences. Individual electron density profiles illustrated that PA ionization has a layer thickness of about 20 km, followed by APA with 30 km and PPA with 40 km thickness. This is consistently the same in all the three examples displayed in Figs. 2, 3, and 4, and from all the electron density profiles in the study (not shown here). A deeper and higher ioniza-

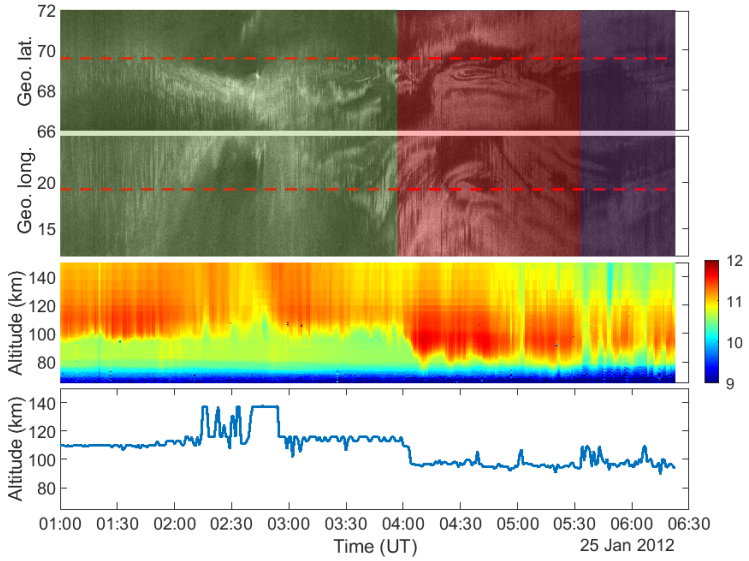

Figure 3. Keogram, ewogram, EISCAT electron density, and altitude of maximum electron density on 25 January 2012. Color-coded rectangles and dashed red lines are PsA types and EISCAT FOV respectively, the same as in Fig. 2.

tion was observed when the patchy aurora was passing over the FOV of EISCAT. This is also apparent in the height of the maximum electron density plots with high variations in altitude during the patch-on and patch-off periods.

As the altitude of the maximum N_e is a single point, it does not reflect the differences in N_e we observe along with the height profile. For example, in Fig. 4, the maximum electron density altitude barely changes, while electron densities during different PsA types at different altitudes show significant transitions. To include this information in the comparison, we average electron densities in height bins during different types of PsA. Figure 5 shows a histogram of these averages in 10 km intervals between 70 and 120 km (panels a–e), as well as a histogram of the maximum altitude electron density (f) for the entire data set (APA $\sim$ 58 h, PPA $\sim$ 43 h, PA $\sim$ 21 h). As shown in Fig. 5a and b, there is not much difference in N_e between APA and PPA types at heights above 100 km. However, PA ionization shows a significant reduction in the 110–120 km region but similar distributions to those of APA and PPA in the 100–110 km region. In panels (c), (d), and (e) – which correspond to average N_e between 90 and 100, 80 and 90, and 70 and 80 km, respectively – a substantial shift to the higher N_e is observed during PPA compared to APA and PA. In the three groups of the D region (70–80, 80–90, and 90–100 km altitude ranges), PPA $\log 10(N_e)$ values are centered around 9.9, 10.7, and 11.3 m^{-3}, respectively. However, during APA these values are 9.3, 10.1, and 10.8 m^{-3}. According to Fig. 5f, precipitation during PPA and PA penetrates deeper on average as compared to APA. The maximum N_e during PPA and PA primarily lies below 105 km, while during APA it is above 105 km.

To further understand the differences between types of PsA, we statistically analyzed the peak electron density and altitude, as shown in Fig. 6. Figure 6 is a two-dimensional histogram, in which the number of points are color-coded, and shows the time evolution of the altitude and magnitude of the maximum electron density. Most of the events were observed between midnight and 9 MLT (magnetic local time; 07:30 UT), where PPA is more dominant after 5 MLT and there is no PA before magnetic midnight. The PsA altitude tends to be lower in the morning sector, especially for PPA and PA. The altitude decrease in the morning sector is significant in the PPA type, reaching down to 95 km, while the magnitude of the maximum $\log 10(N_e)$ stays above 11.3 m^{-3}. The magnitude of the maximum N_e is higher and more persistent during PPA. However, during PA and APA, the maximum N_e varies a lot with smaller amplitudes (below 11.5 m^{-3}). Generally, it is seen that the height of the peak electron density reaches below 100 km during PPA and PA, while during APA it stays predominantly above 100 km.

The cosmic noise absorption from KAIRA during the three types of PsA is shown in Fig. 7. During PPA, the CNA is relatively high compared to the other two types. Based on this figure, the absorption during PPA after 2 MLT shows high values, while the absorption due to APA starts to decline. CNA values during APA are predominantly below 0.5 dB;

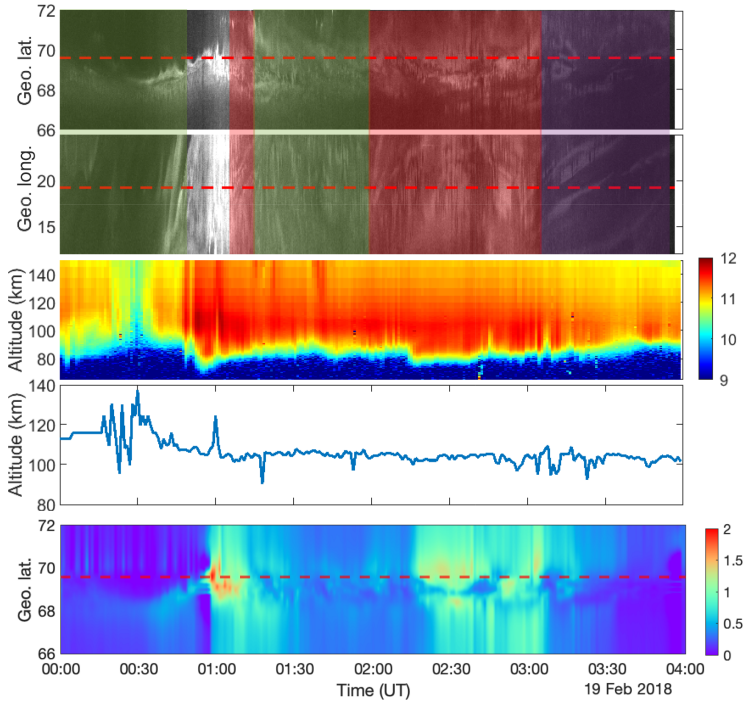

Figure 4. Similar to Figs. 2 and 3 but on 19 February 2018 with an additional panel of KAIRA CNA riogram (in dB). The dashed red line overlaid in the riogram is the EISCAT FOV.

however, during PPA a substantial number of data points have values above 0.5 dB and reach values greater than 1 dB. Most of the high CNA values are observed during the late MLT period (after 3 MLT), which is consistent with the period of high ionization at lower altitudes observed by the EISCAT radars (see Fig. 6). On average, CNA index values during PPA are also higher, at 0.33 dB, compared to PA (0.23 dB) and APA (0.17 dB) as shown by the color-coded lines in Fig. 7.

4 Discussions

The primary purpose of this study is to investigate the differences in fluxes and energies of electrons during different types of pulsating aurora using EISCAT radar electron measurements and KAIRA riometric observations as proxies. Based on keograms generated from high-resolution ($\sim$ 10 s) KIL and ABK ASC images, we identified 39 APA, 35 PPA, and 18 PA types, with a total of 92 events, also observed by EISCAT radar. From the collective duration of time, APA was observed for a substantial period of time of 58 h, followed by PPA for 43 h and PA for 21 h. Grono and Donovan (2020) reported the highest probability occurrence of APA and lowest occurrence of PPA using 10 years of ASC data from North America. In our study, PPA was more dominant than PA. The location and precipitation energy of the magnetospheric electrons responsible for the different types of PsA have been reported to be different (Yang et al., 2019; Grono and Donovan, 2020). The change in the patch sizes during PsAs is also suggested to be an indication of energy deposition in the atmosphere (Partamies et al., 2017, 2019). However, detailed studies about the precipitation energies and the mechanisms behind different structures of PsA are still required. The magnitude of the maximum electron density and its altitude provide both the flux and the energy information about the precipitating PsA electrons. From the electron density measurements, the differences in the magnitude of the electron density and the height of the maximum electron density among the three types of PsA were significant. The statistical findings presented in this study suggested that PPA has a higher energy range compared to PA and APA types, on average. This is contrary to the results from Yang et al. (2019), which reported that APA has a higher energy range compared to PPA. We used KAIRA CNA data to further show the differences in energy deposition during

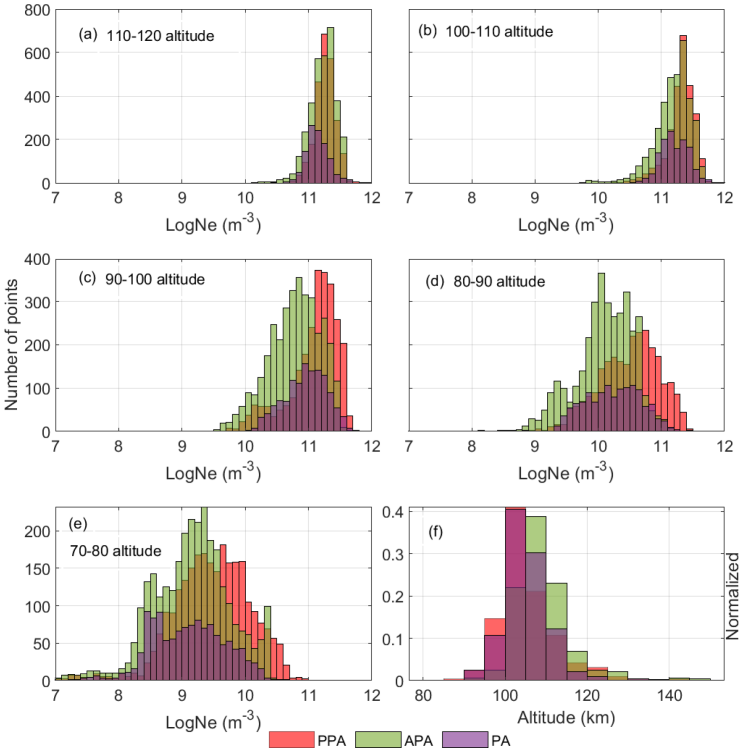

Figure 5. Histogram of EISCAT electron density measurements averaged between **(a)** 110 and 120 km, **(b)** 100 and 110 km, **(c)** 90 and 100 km, **(d)** 80 and 90 km, **(e)** 70 and 80 km, and **(f)** altitude of maximum electron density during different types of pulsating aurora.

the different PsAs. Yang et al. (2019) analyzed CNA from a riometer in Canada to study 12 PsA events (7 APA and 6 PPA) and showed that CNA is systematically higher during APA than during PPA. They suggested that APA has a higher energy range than PPA by further providing evidence from a single event of FAST satellite measurements of electron energy. However, in this statistical study, which has a significant number of events for each PsA type, we found that PPA electron energies often have a higher energy range than APA, and PA energies lie in between the two. It has been established that both CNA (Wild et al., 2010; Rodger et al., 2012) and pulsating aurora (Jones et al., 2009; Partamies et al., 2017) extend over a range of altitudes. Thus, such a contradiction might depend on which altitude the pulsating aurora and CNA were observed at. It is also possible to find cases where energies of APA electrons are higher than those of PPA electrons, specifically in the energy range below the energy limit (30 keV) measured by FAST. The stopping altitude of these electrons is above 95 km (Turunen et al., 2009). However, in this study, most of the energy (ionization) differences between the types were observed below 100 km. This suggests that in a higher energy range ($\sim>$ 30 keV) PPA electrons' energy is typically higher than that of APA electrons. Riometers also respond to precipitating electrons below 30 keV; such particles deposit their energy above 90 km, which is the D region in Fig. 6. To further explore the energy difference between PsA types, we use the KAIRA CNA. The CNA values from KAIRA suggest that the PPA electrons have higher energies to ionize at lower altitudes as compared to APA. The KAIRA CNA observations showed that the values could reach 1 dB, specifically during PPA types. Such high absorption values are comparable to values during auroral substorms. However, the average CNA values during APA, PPA, and PA were 0.17, 0.33, and 0.23 dB, respectively (Fig. 7).

In the late MLT sector (after 5 MLT), PPA and PA are more common with higher electron density at a lower altitude (see Fig. 6). In this study, the occurrence of PA was entirely confined to after 2 MLT. The non-existence of PA before magnetic midnight is also reported by Grono and Donovan (2020). APA is dominant between 2 and 5 MLT, which is also consistent with their study. In terms of the order of

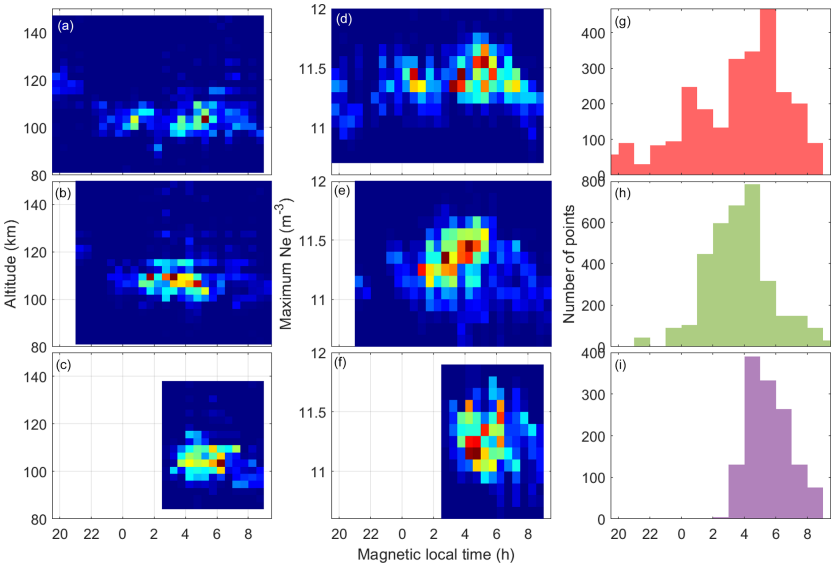

Figure 6. Two-dimensional histogram of altitude of maximum electron density **(a–c)**, magnitude of maximum electron density **(d–f)**, and distribution of the occurrence of data points **(g–i)** during different types of pulsating aurora: PPA, APA, and PA from top to bottom.

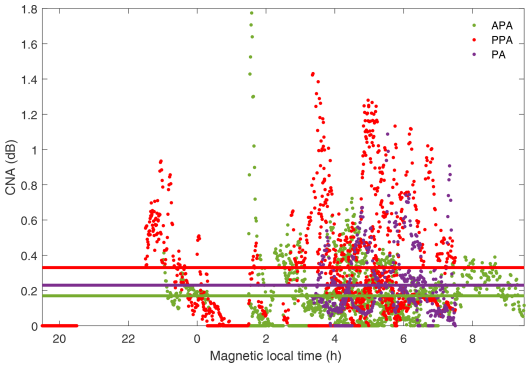

Figure 7. KAIRA cosmic noise absorption (CNA) during different types of pulsating aurora. Color-coded horizontal lines are the average CNA for respective PsA types.

occurrence, APA tends to be more dominant first, and then PPA or PA follows. Such an order of occurrence is also reported in Grono and Donovan (2020). As pointed out in their study, it is still unclear if APA is the onset of the two PsA types. However, this order of occurrence is also an indication that PPA and PA might be associated with higher energies as compared to APA. In the radiation belt, both the distribution of energetic electrons and chorus wave activity are dependent on MLT (Aryan et al., 2014; Allison et al., 2017). Allison et al. (2017) showed the persistence of a high flux of electrons with energy > 30 keV throughout the dawn sector. On the other hand, Aryan et al. (2014) showed that chorus wave activity is dominant in the morning-to-noon period. Thus, the higher electron density observed late in the morning in this study could be the result of the combination of the two, which include the source and mechanisms for energetic electron precipitation (see, e.g., Lam et al., 2010). Oyama et al. (2017) also suggested that the auroral patch formation in the post-midnight-to-dawn sector is associated with the development of energetic electron precipitation, despite the low level of geomagnetic activity. Hosokawa and Ogawa (2015) also reported the descent of the peak electron density associated with an increase in precipitation energy in the later MLT sector. Their statistical study of 21 PsA events showed that the peak height of PsA moves below 100 km after 6 MLT. The layer thickness of the categories is also observed to be different. PPA is the thickest structure, at 40 km, while PA is the thinnest structure, at 20 km. Thus, the thick ionization layer during PPA is also associated with precipitating electrons with a broader energy spectrum. This further indicates that the PPA is the most important PsA type in the D region.

In this study, we found a significant ionization of around 70 km during PPA and PA, which corresponds to 200 keV energy. Such hard precipitation at this altitude is capable of changing the chemistry of the atmosphere by destroying mesospheric ozone (Turunen et al., 2016; Tesema et al., 2020). The type of PsA most likely to contribute largely to

such destruction of ozone is PPA (Fig. 6). Most of the low fluxes in the higher-energy end of PsA spectra observed by Tesema et al. (2020) might account for APA types. This probable energy spectra difference from satellite measurements among the categories should be investigated in the future. If exclusively associated with APA, the low-flux scenario with no chemical changes in their study also suggests that it could be possible to visually differentiate which type causes chemical changes and which does not.

5 Conclusions

By combining ASC images and EISCAT radar experiments, we identified 39 APA, 35 PPA, and 18 PA types. We used the ionization level to investigate the electron flux and energy range difference between them. The CNA measured by the KAIRA riometer is also used to support the observations. The ionization level during PPA was considerably larger than APA in the region below 100 km. However, the ionization level above 100 km has no significant difference between the two PsA types, while PA showed a low ionization level. Lower altitudes of the maximum electron density during PPA in the late MLT sector were observed. This suggests that the flux and energy of electrons during PPA are relatively higher than during APA. The CNA from KAIRA was also consistent with the EISCAT electron density results: higher CNA values during PPA ($\sim >$ 0.5 dB) after 3 MLT and lower CNA values during APA ($\sim <$ 0.5 dB) after 5 MLT. We also observed a high ionization level down to 70 km in EISCAT measurements, which corresponds to precipitation of relativistic electrons. The mechanisms responsible for the different types of PsA are still unclear, but on average this study showed that the precipitating electron spectra during the three types of PsA have significant differences, specifically in the higher-energy tail. To understand the sources of electrons during different types of pulsating auroras, an ideal combination of measurements would be satellite measurements in the magnetosphere, ground-based optical and radar measurements, and precipitation measurements from a low-latitude satellite. Such combinations will be sought in the future.

Data availability. The quick-look keograms for event selection are available at https://space.fmi.fi/MIRACLE/ASC/?page=keograms (Finnish Metrological Institute (FMI), 2020, last access: 28 June 2020). All-sky camera data are obtainable from the FMI-MIRACLE network database, which can be requested from FMI (kirsti.kauristie@fmi.fi). High-resolution keograms generated from ASC images and the PsA category event list are available at https://doi.org/10.6084/m9.figshare.12559127 (Tesema, 2020). The 1 min resolution of EISCAT data used in this analysis is available at http://portal.eiscat.se/schedule/schedule.cgi (EISCAT Scientific Association, 2020, last access: 28 June 2020). The interferometric riometry images and keograms are based on cross-correlation statistics data, which are available on request from the KAIRA PI, Sodankylä Geophysical Observatory, http://www.sgo.fi/KAIRA (Sodankylä Geophysical Observatory, 2020).

Supplement. The supplement related to this article is available online at: https://doi.org/10.5194/angeo-38-1191-2020-supplement.

Author contributions. All authors contributed by providing necessary data, participating in discussions, and writing the paper.

Competing interests. The authors declare that they have no conflict of interest.

Special issue statement. This article is part of the "Special Issue on the joint 19th International EISCAT Symposium and 46th Annual European Meeting on Atmospheric Studies by Optical Methods". It is a result of the 19th International EISCAT Symposium 2019 and 46th Annual European Meeting on Atmospheric Studies by Optical Methods, Oulu, Finland, 19–23 August 2019.

Acknowledgements. The funding support for the work of Fasil Tesema and Hilde Nesse Tyssøy is provided by the Norwegian Research Council (NRC) under CoE contract 223252. In addition, the work of Noora Partamies is supported by NRC project 287427. The work of Derek McKay is partly supported by Academy of Finland project 322535. We thank Kirsti Kauristie, S. Mäkinen, J. Mattanen, A. Ketola, and C.-F. Enell for maintaining the MIRACLE camera network and data flow. KAIRA was funded by the University of Oulu and the FP7 European Regional Development Fund and is operated by Sodankylä Geophysical Observatory with support from the University of Tromsø and volunteer effort.

Financial support. This research has been supported by the Norwegian Research Council (grant nos. 223252 and 287427), and the Academy of Finland (grant no. 322535).

Review statement. This paper was edited by Daniel Whiter and reviewed by two anonymous referees.

References

Allison, H. J., Horne, R. B., Glauert, S. A., and Del Zanna, G.: The magnetic local time distribution of energetic electrons in the radiation belt region, J. Geophys. Res.-Space, 122, 8108–8123, https://doi.org/10.1002/2017JA024084, 2017.

Aryan, H., Yearby, K., Balikhin, M., Agapitov, O., Krasnoselskikh, V., and Boynton, R.: Statistical study of chorus wave distributions in the inner magnetosphere using *Ae* and solar wind parameters, J. Geophys. Res.-Space, 119, 6131–6144, https://doi.org/10.1002/2014JA019939, 2014.

Bland, E. C., Partamies, N., Heino, E., Yukimatu, A. S., and Miyaoka, H.: Energetic Electron Precipitation Occurrence Rates Determined Using the Syowa East SuperDARN Radar, J. Geophys. Res.-Space, 124, 6253–6265, https://doi.org/10.1029/2018ja026437, 2019.

Böinger, T., Kaila, K., Rasinkangas, R., Pollari, P., Kangas, J., Trakhtengerts, V., Demekhov, A., and Turunen, T.: An EISCAT study of a pulsating auroral arc: simultaneous ionospheric electron density, auroral luminosity and magnetic field pulsations, J. Atmos. Terr. Phys., 58, 23–35, https://doi.org/10.1016/0021-9169(95)00017-8, 1996.

EISCAT Scientific Association: VHF and UHF radar analysed data, available at: http://portal.eiscat.se/schedule/schedule.cgi, last access: 4 November 2020.

Finnish Metrological Institute (FMI): Magnetometers-Ionospheric Radars-All-Sky Cameras Large Experiment (MIRACLE) project, FMI All-sky camera quicklook data, available at: https://space.fmi.fi/MIRACLE/ASC/?page=keograms, last access: 4 Novemeber 2020.

Grandin, M., Kero, A., Partamies, N., McKay, D., Whiter, D., Kozlovsky, A., and Miyoshi, Y.: Observation of pulsating aurora signatures in cosmic noise absorption data, Geophys. Res. Lett., 44, 5292–5300, https://doi.org/10.1002/2017GL073901, 2017.

Grono, E. and Donovan, E.: Differentiating diffuse auroras based on phenomenology, Ann. Geophys., 36, 891–898, https://doi.org/10.5194/angeo-36-891-2018, 2018.

Grono, E. and Donovan, E.: Surveying pulsating auroras, Ann. Geophys., 38, 1–8, https://doi.org/10.5194/angeo-38-1-2020, 2020.

Hosokawa, K. and Ogawa, Y.: Pedersen current carried by electrons in auroral D-region, Geophys. Res. Lett., 37, L18103, https://doi.org/10.1029/2010GL044746, 2010.

Hosokawa, K. and Ogawa, Y.: Ionospheric variation during pulsating aurora, J. Geophys. Res.-Space, 120, 5943–5957, https://doi.org/10.1002/2015JA021401, 2015.

Hosokawa, K., Ogawa, Y., Kadokura, A., Miyaoka, H., and Sato, N.: Modulation of ionospheric conductance and electric field associated with pulsating aurora, J. Geophys. Res.-Space, 115, A03201, https://doi.org/10.1029/2009JA014683, 2010.

Jones, S. L., Lessard, M. R., Fernandes, P. A., Lummerzheim, D., Semeter, J. L., Heinselman, C. J., Lynch, K. A., Michell, R. G., Kintner, P. M., Stenbaek-Nielsen, H. C., and Asamura, K.: PFISR and ROPA observations of pulsating aurora, J. Atmos. Sol.-Terr. Phy., 71, 708–716, https://doi.org/10.1016/j.jastp.2008.10.004, 2009.

Jones, S. L., Lessard, M. R., Rychert, K., Spanswick, E., and Donovan, E.: Large-scale aspects and temporal evolution of pulsating aurora, J. Geophys. Res.-Space, 116, 1–7, https://doi.org/10.1029/2010JA015840, 2011.

Jones, S. L., Lessard, M. R., Rychert, K., Spanswick, E., Donovan, E., and Jaynes, A. N.: Persistent, widespread pulsating aurora: A case study, J. Geophys. Res.-Space, 118, 2998–3006, https://doi.org/10.1002/jgra.50301, 2013.

Lam, M. M., Horne, R. B., Meredith, N. P., Glauert, S. A., Moffat-Griffin, T., and Green, J. C.: Origin of energetic electron precipitation $>$ 30 keV into the atmosphere, J. Geophys. Res., 115, A00F08, https://doi.org/10.1029/2009JA014619, 2010.

Lessard, M. R.: A Review of Pulsating Aurora, Auror. Phenomenol. Magnetos. Process. Earth Other Planets, 55–68, https://doi.org/10.1029/GM197, 2012.

McEwen, D. J., Yee, E., Whalen, B. A., and Yau, A. W.: Electron energy measurements in pulsating auroras, Can. J. Phys., 59, 1106–1115, https://doi.org/10.1139/p81-146, 1981.

McKay-Bukowski, D., Vierinen, J., Virtanen, I. I., Fallows, R., Postila, M., Ulich, T., Wucknitz, O., Brentjens, M., Ebbendorf, N., Enell, C., Gerbers, M., Grit, T., Gruppen, P., Kero, A., Iinatti, T., Lehtinen, M., Meulman, H., Norden, M., Orispää, M., Raita, T., de Reijer, J. P., Roininen, L., Schoenmakers, A., Stuurwold, K., and Turunen, E.: KAIRA: The Kilpisjärvi Atmospheric Imaging Receiver Array – System Overview and First Results, IEEE T. Geosci. Remote Sens., 53, 1440–1451, https://doi.org/10.1109/TGRS.2014.2342252, 2015.

McKay, D., Partamies, N., and Vierinen, J.: Pulsating aurora and cosmic noise absorption associated with growth-phase arcs, Ann. Geophys., 36, 59–69, https://doi.org/10.5194/angeo-36-59-2018, 2018.

Milan, S. E., Hosokawa, K., Lester, M., Sato, N., Yamagishi, H., and Honary, F.: D region HF radar echoes associated with energetic particle precipitation and pulsating aurora, Ann. Geophys., 26, 1897–1904, https://doi.org/10.5194/angeo-26-1897-2008, 2008.

Miyoshi, Y., Katoh, Y., Nishiyama, T., Sakanoi, T., Asamura, K., and Hirahara, M.: Time of flight analysis of pulsating aurora electrons, considering wave-particle interactions with propagating whistler mode waves, J. Geophys. Res.-Space, 115, 1–7, https://doi.org/10.1029/2009JA015127, 2010.

Miyoshi, Y., Oyama, S., Saito, S., Kurita, S., Fujiwara, H., Kataoka, R., Ebihara, Y., Kletzing, C., Reeves, G., Santolik, O., Clilverd, M., Rodger, C. J., Turunen, E., and Tsuchiya, F.: Energetic electron precipitation associated with pulsating aurora: EISCAT and Van Allen Probe observations, J. Geophys. Res.-Space, 120, 2754–2766, https://doi.org/10.1002/2014JA020690, 2015.

Nishimura, Y., Bortnik, J., Li, W., Thorne, R. M., Lyons, L. R., Angelopoulos, V., Mende, S. B., Bonnell, J. W., Le Contel, O., Cully, C., Ergun, R., and Auster, U.: Identifying the driver of pulsating aurora, Science, 330, 81–84, https://doi.org/10.1126/science.1193186, 2010.

Nishimura, Y., Bortnik, J., Li, W., Thorne, R. M., Chen, L., Lyons, L. R., Angelopoulos, V., Mende, S. B., Bonnell, J., Le Contel, O., Cully, C., Ergun, R., and Auster, U.: Multievent study of the correlation between pulsating aurora and whistler mode chorus emissions, J. Geophys. Res.-Space, 116, 1–11, https://doi.org/10.1029/2011JA016876, 2011.

Nishimura, Y., Lessard, M. R., Katoh, Y., Miyoshi, Y., Grono, E., Partamies, N., Sivadas, N., Hosokawa, K., Fukizawa, M., Samara, M., Michell, R. G., Kataoka, R., Sakanoi, T., Whiter, D. K., Oyama, S. ichiro, Ogawa, Y., and Kurita, S.: Diffuse and Pulsating Aurora, Space Sci. Rev., 216, 4, https://doi.org/10.1007/s11214-019-0629-3, 2020.

Oyama, S.-I., Shiokawa, K., Miyoshi, Y., Hosokawa, K., Watkins, B. J., Kurihara, J., Tsuda, T. T., and Fallen, C. T.: Lower thermospheric wind variations in auroral patches during the substorm recovery phase, J. Geophys. Res.-Space, 121, 3564–3577, https://doi.org/10.1002/2015JA022129, 2016.

Oyama, S., Kero, A., Rodger, C. J., Clilverd, M. A., Miyoshi, Y., Partamies, N., Turunen, E., Raita, T., Verronen, P. T., and Saito, S.: Energetic electron precipitation and auroral morphology at the substorm recovery phase, J. Geophys. Res.-Space, 122, 6508–6527, https://doi.org/10.1002/2016JA023484, 2017.

Partamies, N., Whiter, D., Kadokura, A., Kauristie, K., Nesse Tyssøy, H., Massetti, S., Stauning, P., and Raita, T.: Occurrence and average behavior of pulsating aurora, J. Geophys. Res.-Space, 122, 5606–5618, https://doi.org/10.1002/2017JA024039, 2017.

Partamies, N., Bolmgren, K., Heino, E., Ivchenko, N., Borovsky, J. E., and Sundberg, H.: Patch size evolution during pulsating aurora, J. Geophys. Res.-Space, 124, 4725–4738, https://doi.org/10.1029/2018JA026423, 2019.

Rees, M. H.: Auroral electrons, Space Sci. Rev., 10, 413–441, https://doi.org/10.1007/BF00203621, 1969.

Rishbeth, H. and Williams, P. J. S.: The EISCAT ionospheric radar: The system and its early results, Q. J. Roy. Astron. Soc., 26, 478–512, 1985.

Rodger, C. J., Clilverd, M. A., Kavanagh, A. J., Watt, C. E. J., Verronen, P. T., and Raita, T.: Contrasting the responses of three different ground-based instruments to energetic electron precipitation, Radio Sci., 47, RS2021, https://doi.org/10.1029/2011RS004971, 2012.

Royrvik, O. and Davis, T. N.: Pulsating aurora local and global morphology, J. Geophys. Res., 82, 4720–4740, 1977.

Sangalli, L., Partamies, N., Syrjäsuo, M., Enell, C. F., Kauristie, K., and Mäkinen, S.: Performance study of the new EMCCD-based all-sky cameras for auroral imaging, Int. J. Remote Sens., 32, 2987–3003, https://doi.org/10.1080/01431161.2010.541505, 2011.

Sato, N., Wright, D. M., Carlson, C. W., Ebihara, Y., Sato, M., Saemundsson, T., Milan, S. E., and Lester, M.: Generation region of pulsating aurora obtained simultaneously by the FAST satellite and a Syowa-Iceland conjugate pair of observatories, J. Geophys. Res.-Space, 109, 1–15, https://doi.org/10.1029/2004JA010419, 2004.

Sodankylä Geophysical Observatory: Kilpisjärvi Atmospheric Imaging Receiver Array (KAIRA) project, available at: https://www.sgo.fi/KAIRA/, last access: 4 Novemeber 2020.

Tesema, F.: Replication data for: Observations of precipitation energies during different types of pulsating aurora, Dataset, figshare, https://doi.org/10.6084/m9.figshare.12559127, 2020.

Tesema, F., Partamies, N., Tyssøy, H. N., Kero, A., and Smith-Johnsen, C.: Observations of electron precipitation during pulsating aurora and its chemical impact, J. Geophys. Res.-Space, 125, e2019JA027713, https://doi.org/10.1029/2019JA027713, 2020.

Turunen, E., Verronen, P. T., Seppälä, A., Rodger, C. J., Clilverd, M. A., Tamminen, J., Enell, C. F., and Ulich, T.: Impact of different energies of precipitating particles on NO_x generation in the middle and upper atmosphere during geomagnetic storms, J. Atmos. Sol.-Terr. Phys., 71, 1176–1189, https://doi.org/10.1016/j.jastp.2008.07.005, 2009.

Turunen, E., Kero, A., Verronen, P. T., Miyoshi, Y., Oyama, S. I., and Saito, S.: Mesospheric ozone destruction by high-energy electron precipitation associated with pulsating aurora, J. Geophys. Res., 121, 11852–11861, https://doi.org/10.1002/2016JD025015, 2016.

Wahlund, J. E., Opgenoorth, H. J., and Rothwell, P.: Observations of thin auroral ionization layers by EISCAT in connection with pulsating aurora, J. Geophys. Res.-Space, 94, 17223–17233, https://doi.org/10.1029/JA094iA12p17223, 1989.

Watanabe, M., Kadokura, A., Sato, N., and Saemundsson, T.: Absence of geomagnetic conjugacy in pulsating auroras, Geophys. Res. Lett., 34, L15107, https://doi.org/10.1029/2007GL030469, 2007.

Wild, P., Honary, F., Kavanagh, A. J., and Senior, A.: Triangulating the height of cosmic noise absorption: A method for estimating the characteristic energy of precipitating electrons, J. Geophys. Res., 115, A12326, https://doi.org/10.1029/2010JA015766, 2010.

Yamamoto, T.: On the temporal fluctuations of pulsating auroral luminosity, J. Geophys. Res., 93, 897, https://doi.org/10.1029/JA093iA02p00897, 1988.

Yang, B., Spanswick, E., Liang, J., Grono, E., and Donovan, E.: Responses of Different Types of Pulsating Aurora in Cosmic Noise Absorption, Geophys. Res. Lett., 46, 5717–5724, https://doi.org/10.1029/2019GL083289, 2019.

Paper III

D-region impact area of energetic electron precipitation during pulsating aurora

Emma Bland, Fasil Tesema, and Noora Partamies
Ann. Geophys., **39, 135–149**, https://doi.org/10.5194/angeo-39-135-2021, 2021.

Ann. Geophys., 39, 135–149, 2021
https://doi.org/10.5194/angeo-39-135-2021

Annales Geophysicae
Open Access
EGU

D-region impact area of energetic electron precipitation during pulsating aurora

Emma Bland[1], **Fasil Tesema**[1,2], **and Noora Partamies**[1,2]

[1]Department of Arctic Geophysics, University Centre in Svalbard, Longyearbyen, Norway
[2]Birkeland Centre for Space Science, University of Bergen, Bergen, Norway

Correspondence: Emma Bland (emma.bland@unis.no)

Received: 6 August 2020 – Discussion started: 18 August 2020
Revised: 14 December 2020 – Accepted: 17 December 2020 – Published: 10 February 2021

Abstract. A total of 10 radars from the Super Dual Auroral Radar Network (SuperDARN) in Antarctica were used to estimate the spatial area over which energetic electron precipitation (EEP) impacts the D-region ionosphere during pulsating aurora (PsA) events. We use an all-sky camera (ASC) located at Syowa Station to confirm the presence of optical PsAs, and then we use the SuperDARN radars to detect high frequency (HF) radio attenuation caused by enhanced ionisation in the D-region ionosphere. The HF radio attenuation was identified visually by examining quick-look plots of the background HF radio noise and backscatter power from each radar. The EEP impact area was determined for 74 PsA events. Approximately one-third of these events have an EEP impact area that covers at least 12° of magnetic latitude, and three-quarters cover at least 4° of magnetic latitude. At the equatorward edge of the auroral oval, 44 % of events have a magnetic local time extent of at least 7 h, but this reduces to 17 % at the poleward edge. We use these results to estimate the average size of the EEP impact area during PsAs, which could be used as a model input for determining the impact of PsA-related EEP on the atmospheric chemistry.

1 Introduction

Pulsating aurorae (PsAs) are diffuse auroral emissions which exhibit quasi-periodic brightness fluctuations of about 2–20 s (Lessard, 2012; Nishimura et al., 2020). They are commonly observed in the recovery phase of substorms, with the greatest occurrence rates in the early morning sector (Jones et al., 2011; Bland et al., 2019; Grono and Donovan, 2020). The energetic electron precipitation (EEP) that produces PsA is thought to arise from chorus wave activity, whereby electrons from the radiation belts are scattered into the atmospheric loss cone (Thorne et al., 2010; Kasahara et al., 2018). The precipitating electrons typically have energies up to the order of 10–100 keV, depositing their energy into the upper mesosphere/lower thermosphere region at approximately 70–120 km altitude (Fang et al., 2008; Turunen et al., 2009; Miyoshi et al., 2010; Tesema et al., 2020b). PsA-related electron density enhancements have been observed at altitudes as low as 68 km, corresponding to electron energies of at least 200 keV (Miyoshi et al., 2015; Turunen et al., 2016; Tesema et al., 2020a).

Due to their high occurrence rates, PsAs are thought to be a significant source of ionisation in the upper mesosphere/lower thermosphere region at high latitudes. Impact ionisation by EEP in this region leads to the production of odd-hydrogen ($HO_x = OH + HO_2$) and odd-nitrogen ($NO_x = N + NO + NO_2$) chemical species, which act as catalysts in ozone depletion reactions. Tesema et al. (2020a) used the 1D Sodankylä ion-neutral chemistry model (Verronen et al., 2005; Turunen et al., 2009) to show that a typical PsA energy spectrum applied for 120 min causes mesospheric odd-oxygen depletion of 69 %. This significant chemical response indicates that PsA-related EEP may also need to be included in atmospheric/climate models, such as the Whole Atmosphere Community Climate Model (WACCM) (Marsh et al., 2007), to properly capture the long-term impact of EEP on natural climate variability. Currently, the EEP forcing in WACCM is described using an Ap-index-based parameterisation of particle flux measurements (van de Kamp et al., 2016) from the Polar Orbiting Environmental Satellite (POES). Although the actual particle flux measurements

from POES would include the PsA-related EEP, the parameterisation is unlikely to capture the contribution from PsAs due to the poor correlation between PsA occurrence and geomagnetic indices (e.g. Partamies et al., 2017). Pulsating aurora may therefore represent a significant energy input to the atmosphere that is not currently captured in the forcing used for long-term modelling of natural climate variability.

To develop a more realistic EEP forcing for atmospheric/climate modelling applications that properly captures the contribution from PsAs, characteristics of PsAs, such as occurrence rates, durations, energy spectra and spatial coverage, need to be determined. PsA occurrence rates and event durations have been determined in several recent studies which used observations from all-sky cameras (ASCs). The median PsA event duration has been reported to be between 1.4 and 2.25 h (Jones et al., 2011; Partamies et al., 2017; Bland et al., 2019), and one event lasting 15 h was reported by Jones et al. (2013). Jones et al. (2011) and Grono and Donovan (2020) showed that PsAs are most common in the morning sector, with occurrence rates as high as 86 % at around 03:30–06:00 magnetic local time (MLT). Since these occurrence rates were determined using optical data, the authors noted that the results are unreliable after about 06:00 MLT when the observation time is restricted by sunlight. Bland et al. (2019) made novel use of the Super Dual Auroral Radar Network (SuperDARN) radar at Syowa Station, Antarctica, to show that D-region ionisation associated with PsAs may continue up to about 10:00 MLT, when optical observations are not possible due to daylight.

Our current knowledge of the spatial distribution of PsAs comes from a series of studies that used the Time History of Events and Macroscale Interactions during Substorms (THEMIS) all-sky camera network in Canada (Donovan et al., 2006). THEMIS is well suited to studying the PsA spatial coverage due to its large combined field of view. Grono and Donovan (2019) used three THEMIS cameras and two meridian-scanning photometers to determine the upper and lower latitude boundaries of PsAs relative to the proton aurora location to identify the source region of the precipitating particle populations. Grono and Donovan (2020) then determined the occurrence probability of PsAs as a function of magnetic latitude and MLT. These studies made a distinction between different types of PsAs – amorphous PsAs (APA), patchy PsAs (PPA), and patchy aurora (PA) (see also Grono and Donovan, 2018) – based mainly on the spatial extent and stability of the pulsations and their motion with the convection. These different PsA types were shown to have different source regions and occurrence distributions. APA was found to have the highest occurrence rate and the widest spatial distribution in both latitude and MLT. APA was the dominant PsA type observed in the pre-midnight sector, whereas all three types were detected in the early morning sector. Yang et al. (2019) reported that APA were associated with stronger cosmic noise absorption compared to PPA for a fixed auroral brightness. In a larger study using incoherent scatter radar and imaging riometer (relative ionospheric opacity meter) data, Tesema et al. (2020b) showed that the electron density enhancement below 100 km altitude was greatest for PPA- and PA-type events, indicating that these precipitating particle populations have higher energies on average compared to APA. Although these conclusions are not consistent, they show that it may be important to distinguish between the different types of PsAs when characterising the middle atmospheric response to EEP.

Grono and Donovan (2019, 2020) provided new information about the occurrence probability of APA, PPA, and PA at different latitudes and MLTs. These results, however, do not provide information about the latitudinal and MLT extent of individual events. This type of spatial coverage information is important for developing a realistic model input. A single PsA event reported by Jones et al. (2013) spanned more than 10 h of MLT at its maximum, but this is probably much wider than average. Since optical observations of PsAs are possible only during periods of dark, clear skies, it is very difficult to obtain a data set that is large enough to estimate the statistical spatial coverage of PsAs. Furthermore, cameras provide no information about the precipitating particle energy spectrum, or, at best, they provide very limited information, such as the peak emission height (e.g. Partamies et al., 2017). This type of information is important for determining whether a noticeable atmospheric chemical response will occur. Tesema et al. (2020a) developed statistical energy spectra for PsAs by combining satellite measurements from 253 events and then used these results to model the atmospheric chemical response to different levels of forcing. They showed that not all PsAs have sufficient energy to produce a measurable chemical response. Therefore, PsA occurrence rates and spatial coverage information determined from optical data alone may overestimate the forcing applied to the mesosphere–lower thermosphere region and the resulting chemical response.

The purpose of this study is to estimate the typical area over which PsA-related EEP has sufficient energy to reach mesosphere–lower thermosphere altitudes ($\sim$ 10–200 keV) and, hence, produce a chemical response. We shall refer to this area as the EEP impact area. To perform this estimate, we use the fact that this higher energy precipitation causes enhanced ionisation in the D-region ionosphere, which in turn attenuates high frequency (HF) radio waves. This attenuation can be detected using SuperDARN HF radars, as previously shown by Bland et al. (2019). In this study, we build upon this work by using 10 SuperDARN radars in Antarctica to estimate the EEP impact area for different types of PsAs.

2 Instrumentation

SuperDARN is a global network of 36 HF radars primarily designed for studying high-latitude plasma convection (Greenwald et al., 1995; Chisham et al., 2007; Nishitani

et al., 2019). Recently, the radars have also been used to detect HF radio attenuation during shortwave fadeout events (Watanabe and Nishitani, 2013; Berngardt et al., 2018; Chakraborty et al., 2018; Fiori et al., 2018), polar cap absorption events (Bland et al., 2018; Chakraborty et al., 2019), and auroral absorption events including PsAs (Bland et al., 2019). HF radio attenuation events are identified in the SuperDARN radar data as periods of reduced backscatter power combined with a reduction in the background radio noise. The reduced backscatter power is caused by the attenuation of the transmitted radio waves in the ionosphere, which often reduces the signal strength to below the detection threshold (e.g. Bland et al., 2018). The reduced background noise levels are caused by the attenuation of the background HF radio noise at the radar operating frequency. At the standard SuperDARN operating frequencies of 8–20 MHz, this background radio noise is produced mainly by lightning activity and propagates around the globe via ionospheric reflections. The noise measurements can be used to estimate the attenuation in decibels relative to a radar-specific quiet day curve, using an approach analogous to riometry (Bland et al., 2018; Berngardt, 2020). However, due to the high variability in the noise at the SuperDARN operating frequencies, producing quiet day curves is not straightforward, and the methodology is still being developed (Berngardt, 2020). Therefore, in this work, we adopt a more qualitative approach based on visual identification of HF attenuation events in quick-look plots.

In this study we have used 10 SuperDARN radars located in Antarctica and also an all-sky colour digital camera located at Syowa Station. The locations of the radars and the all-sky camera are shown in Fig. 1. The grey shading and magnetic local time (MLT) contours in Fig. 1 relate to the example event described Sect. 3. The red circle shows the ASC field of view projected to 100 km height. The radar fields of view are shown in black, and beam 5 for each radar is shaded yellow. For simplicity, we show only the near-range field of view of each radar (180–600 km in range), which is the approximate area in which the transmitted radio waves pass through the D-region ionosphere. This estimate is based on the vertical extent of the radars' antenna radiation patterns extending from roughly 10 to 50° from the horizontal (e.g. Milan et al., 1997). Each radar's total field of view extends to over 3500 km in range, creating significant overlap between the fields of view, which is useful for measuring the F-region ionospheric convection (e.g. Nishitani et al., 2019, Fig. 1b). Each SuperDARN radar consists of a linear array of log-periodic or twin-terminated folded dipole antennas which are phased electronically to produce a beam which can be steered in 16 different azimuthal directions. This beam is narrow in azimuth ($\sim 3.5°$) but has a wide vertical extent ($\sim 40°$). The 16 beams are scanned sequentially every minute, with a ~ 3 s integration time for each beam.

SuperDARN radars detect coherent backscatter from electron density structures in the E-region and F-region ionospheres and also from the ground, following reflection in the ionosphere. The Southern Hemisphere SuperDARN radars were chosen for this study because they generally detect larger amounts of backscatter on the nightside compared to the Northern Hemisphere radars. This is probably due to the favourable orientation of the geomagnetic field relative to the radar look directions and geographic latitudes. The near-continuous presence of backscatter on the nightside for most Antarctic radars makes it straightforward to identify periods of reduced backscatter power caused by HF radio attenuation. An example of this procedure is given in Sect. 3. Note that the three mid-latitude SuperDARN radars located in Australia/New Zealand were not included in this study, due to their very large spatial separation from the radars in Antarctica, so they are not shown in Fig. 1.

The camera located at Syowa Station is a colour digital camera fitted with a 8 mm f/2.8 fisheye lens. The imaging season lasts from April to October, and the camera is programmed to capture images automatically whenever the Sun is more than 12° below the horizon. Exposure times are a few seconds, and the image cadence varies from about 6 to 30 s. Daily keogram (quick-look) plots are constructed by taking a magnetic north–south slice through the all-sky image and then placing these slices on a time axis. Similarly, an ewogram (east–west keogram) can be constructed using a magnetic east–west slice. PsAs can be readily identified in these plots as patchy auroral displays (e.g. Jones et al., 2013; Partamies et al., 2017; Yang et al., 2017), but the original all-sky images are normally required to determine the PsA type (APA, PPA, and PA).

3 Example event – 14 June 2015

Our method for visually identifying signatures of HF radio attenuation is illustrated using Fig. 2. The 12 h time interval shown commenced at 18:00 universal time (UT) on 13 June 2015. This figure shows the magnetic north–south keogram plot for the all-sky camera at Syowa Station and the background noise and power measurements for each radar with available data. The panels are arranged in order of magnetic latitude, but it should be noted that the radars are located over a wide range of longitudes (see Fig. 1). The keograms are identical in both columns, with magnetic south at the top. The yellow vertical lines in the keogram plots indicate the onset and end times of a PsA event observed over Syowa Station on 14 June 2015. This is an APA event which occurred in the recovery phase of a substorm. There is a second APA event in this time interval which commences at 04:20 UT, but for the purposes of illustrating our event selection, we will focus on the first event at 00:40–02:20 UT. No data were available from either the Falkland Islands (FIR) radar or the South African National Antarctic Expedition (SAN) radar during this time interval, so they are not included in the figure.

The first column of Fig. 2 shows the background noise measurements from each beam of each radar. The noise data

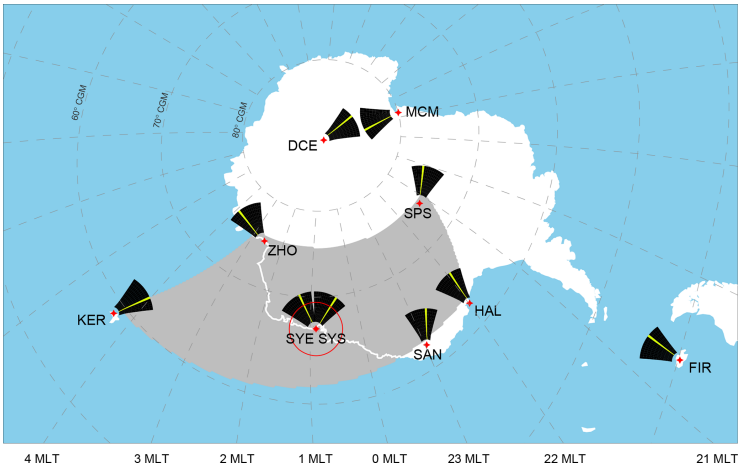

Figure 1. Locations and fields of view of the SuperDARN radars and all-sky camera used in this study. Instrument locations are shown by red symbols. The red circle indicates the camera field of view, and the black shading indicates the radar fields of view. The position of beam 5 for each radar is shaded yellow. Only the first 600 km of the radar fields of view are shown, which is the area in which the radio waves are expected to pass through the D-region ionosphere. The grey shading shows the spatial coverage of the energetic electron precipitation impact area for the example pulsating aurora event on 14 June 2015, 00:40–02:20 UT. Dashed grey lines indicate corrected geomagnetic (CGM) latitude and magnetic local time (MLT) contours.

have been binned into 10 min intervals and averaged separately in each bin to remove spikes. These data have arbitrary units, and the colour scales were chosen to best match the dynamic range of the noise measurements from each radar. The colour scales contain 256 colours and are saturated at the top end in order to emphasise the low-power features. For most radars there is some variation in the noise levels between different beams, which may arise from real spatial variations in the atmospheric noise production and ionospheric propagation conditions or differences in beamforming across the radar field of view. For this work, we are not interested in the absolute values of the background noise. Instead, we look for sudden changes in the background noise over the entire field of view which indicate that the HF radio noise has been attenuated in response to enhanced D-region ionisation. For the example event, reduced background noise levels during the PsA event are observed for six out of the eight radars shown, as indicated by the black vertical lines.

To justify that the reduced background noise measured at the six radar sites was indeed caused by enhanced D-region ionisation, we also study the backscatter power measured by each radar. These measurements are shown in the right column of Fig. 2. Each panel shows the raw power levels measured in each 45 km range gate along beam 5. The raw power measurements also have arbitrary units and are displayed on a logarithmic scale. High power values observed across several range gates, and lasting from several minutes to hours, indicate coherent backscatter returning to the radar from ionospheric electron density irregularities or from the ground. The yellow vertical lines on these plots indicate the time periods for which the background noise was attenuated (determined from the left panel). During these time periods, the backscatter returns from all six radars have reduced power or are completely suppressed. This indicates that the radio waves transmitted by the radar have been attenuated. This combination of reduced background noise and reduced backscatter power is strong evidence that the D-region electron density has been enhanced near the radar site (Bland et al., 2018), and we use these two signatures together in our event selection for this study.

For the example shown in Fig. 2, there are two radars that did not detect a clear attenuation signature during the PsA event. These are the McMurdo (MCM) and Dome C East (DCE) radars, located at 80 and 89° corrected geomagnetic (CGM) latitude, respectively. For these radars, there is neither a clear decrease in the background noise level nor a reduction in the backscatter power. Note that the background noise at MCM does decrease close to the event onset time. This, however, is accompanied by an increase in the echo power, which indicates that the transmitted radio waves were not strongly attenuated in the ionosphere. Therefore, the reduced noise at MCM is probably related to the normal diurnal variation in the background noise at the radar site rather than being a response to energetic particle precipitation.

Based on the information in Fig. 2, we can now make a rough estimate of the spatial coverage of the EEP impact

area for this PsA event. This area is shown by the grey shading in Fig. 1, which is the region bounded by the six radars that detected the event. This area actually represents the minimum EEP impact area for this event. The poleward edge of the EEP impact area extends to at least 75° CGM latitude, where both the South Pole Station (SPS) and Zhongshan (ZHO) radars detected attenuation, but it does not extend as far as the MCM radar at 80° CGM latitude. At the event onset, the SPS and ZHO fields of view were located at 20–21 and 03–04 MLT, respectively, indicating an instantaneous MLT extent of about 7 h. A similar MLT extent at the equatorward edge of the EEP impact area is inferred from the Halley (HAL) and Kerguelen (KER) radar pair, extending from ∼ 22–04 MLT at the event onset. Since the event was detected at the KER radar site, we can conclude that the equatorward edge of the EEP impact area extends at least as far as 60° CGM latitude in the morning sector. No data were available from the SAN or FIR radars for this event, so we cannot determine whether the EEP impact area extends to the locations of these radars.

It is worth commenting briefly on the nature of background radio noise measurements from SuperDARN radars. The background noise consists of (1) natural atmospheric radio noise, (2) anthropogenic noise produced by electrical and electronic equipment near the radar site, and (3) internal noise in the radar receiver system. The short- and long-term variability in the background noise depends on the relative contribution of these three sources to the total noise level. EEP-related attenuation signatures are easiest to identify when the background radio noise exhibits a smooth diurnal variation in the absence of any D-region enhancement. In Fig. 2, we observe this smooth noise variation in the DCE, MCM, ZHO, SPS, and Syowa East (SYE) data, and the sudden reduction in the background noise at the onset of PsAs stands out clearly against the slowly varying background. This diurnal variation in the noise is controlled by the global atmospheric noise production and ionospheric propagation conditions. In contrast, the noise measurements from the Halley (HAL) radar are highly variable from one 10 min time bin to the next and also between neighbouring beams, which might arise from either internal receiver noise or anthropogenic noise near the radar site. This variability in the noise measurements at Halley makes the visual identification of HF attenuation signatures more difficult. For this radar, the echo loss from 00:30–02:30 UT is clear (right column of Fig. 2), so we rely more heavily on this parameter to determine whether any HF attenuation has occurred. This type of variability in the background noise measurements for some radars is a key reason for adopting qualitative event selection criteria in this study, as some judgement regarding the usability of the data is required in each case.

4 Event identification for statistical study

To select PsA events for our statistical study of the EEP impact area, we began with a list of 102 optical PsA events identified visually in keogram plots from the all-sky camera at Syowa Station. This same event list was used by Bland et al. (2019) to determine PsA occurrence rates and durations using the SYE SuperDARN radar paired with the all-sky camera data. This event list excludes all solar proton events based on the threshold of $10\,\text{protons}\,\text{cm}^{-2}\,\text{sr}^{-1}\,\text{s}^{-1}$ with energies above 10 MeV. Excluding these events removes most of the effects of polar cap absorption from this study. The optical PsA events were classified as APA, PPA, or PA by visually studying the keogram and ewogram plots and also the 10 s cadence all-sky images for each event. The pulsating auroral structures that we used to distinguish between the different types are described in detail by Grono and Donovan (2018) and Yang et al. (2019). APA are identified as transient pulsating emissions with no persistent structure or sense of average motion. In contrast, PPA and PA consist of quasi-stable auroral patches that last for tens of minutes and can be tracked across the camera field of view. For PA, pulsations are observed only within a small portion of the emission, such as near the edges, whereas for PPA the pulsations are observed over a much larger area. For the 56 events in our list, one dominant type of PsA was observed throughout the whole event. For the remaining 18 events, the dominant type of PsA changed part-way through the event. For these events, we classified them based on the first type of PsA that was observed. There were only three events during which PA were observed, and in all cases, the PA were preceded by APA so they were classified as APA. Note that our PsA classifications apply only to Syowa Station as we cannot determine the PsA type from the radar data. Due to this limitation, this study is designed to detect periods of enhanced D-region ionisation that occur simultaneously with different types of optical PsAs observed at Syowa Station.

Quick-look plots similar to Fig. 2 were produced for each PsA event in the list. For each radar, we determined whether the background noise level and the echo power had been attenuated based on a visual inspection of the data. Often there was some uncertainty about whether a given radar had (or had not) detected an EEP signature. In particular, for some radars it was unclear whether the background noise had decreased (e.g. Fig. 2; HAL and KER radars). To capture this uncertainty, the attenuation for each radar was classified as clearly observed/not observed or probably observed/not observed. If we could not determine the presence or absence of an attenuation signature either way for a given event, then that radar was excluded from the analysis. For an event to be included in this study, we required that at least one radar in addition to the Syowa Station instrumentation had data available with sufficient quality to determine whether an attenuation signature was present. The final event list contained 74 events detected during the 2011, 2013, and 2015 Antarc-

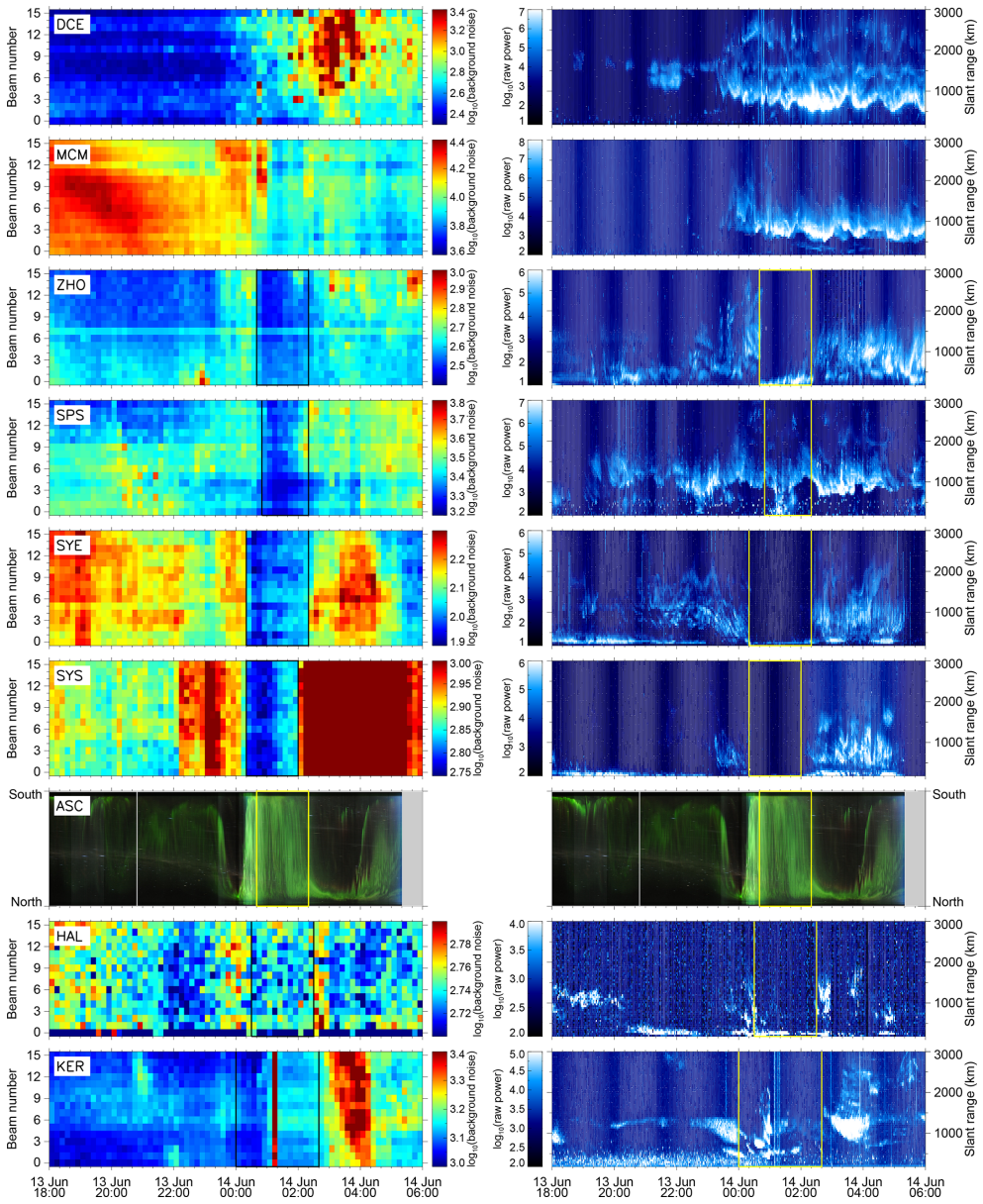

Figure 2. Quick-look plots showing the background radio noise (left) and raw echo power (right) parameters for eight SuperDARN radars from 13–14 June 2015. The magnetic north–south keogram from the all-sky camera (ASC) at Syowa Station is also shown in both columns. The event start and end times are marked using black/yellow vertical lines.

tic winter seasons. For each event we recorded the following information:

- The availability of data from each radar;
- The start time and end time of the attenuation at each radar site (if observed);
- A classification of our uncertainty regarding whether or not any HF attenuation had occurred at each radar site.

In most cases, the onset times for each radar that detected the event are within 30 min of the onset times recorded for the SYE radar. For a few events, the onset times at ZHO, KER, or SPS are delayed 1–3 h after the onset at SYE, but there is still considerable temporal overlap between the two sites. This might indicate a latitudinal expansion of the EEP impact area as the event evolves. Similarly, there are three events during which the HAL or KER radars detected attenuation more than 1 h before the onset at SYE, which might indicate that the particle precipitation began at lower latitudes and later expanded over Syowa Station.

In this study, we have used the all-sky camera at Syowa Station to determine the presence of optical PsAs. Since HF attenuation will occur in response to any process that enhances the D-region ionisation, we cannot confirm that the attenuation signatures observed by the radars were caused by PsAs specifically. For example, the attenuation observed by the SYE and Syowa South (SYS) radars in Fig. 2 commences at substorm onset at 00:20 UT, about 20 min before optical PsAs are visible in the keogram. This is very typical since PsAs are frequently observed in the substorm recovery phase, so the onset times determined from the radar data will often be 10–30 min earlier than the onset of optical PsAs (Bland et al., 2019). To increase the chances that the attenuation signatures at all radar sites are due to PsA-related EEP, we require that the attenuation observed by any individual radar lasts for at least 1 h to qualify as a positive event identification at that site. Since substorm expansion phases are relatively short (Juusola et al., 2011; Partamies et al., 2013), this criterion should eliminate brief attenuation enhancements during substorm expansion phases that are not accompanied by PsAs in the recovery phase.

5 Results

Figure 3 is a bar graph showing the number of events observed and not observed by each radar. Colour coding is used to represent our uncertainty in determining whether any HF attenuation had occurred. The ASC is also included in this plot, with all 74 events clearly present. The data presented in both panels are identical, but the radars/ASC are ordered by magnetic latitude in Fig. 3a and by magnetic longitude in Fig. 3b. The SYE and SYS radars detected attenuation during all events for which data were available (74 and 63 events, respectively). For the SYE radar, five of these events included

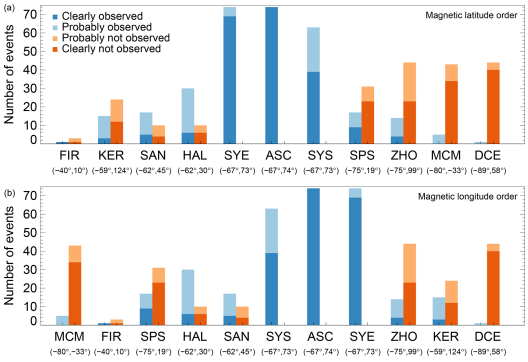

Figure 3. Number of events observed and not observed by each radar and the ASC. The instruments are sorted by magnetic latitude in **(a)** and by magnetic longitude in **(b)**, except for DCE. Corrected geomagnetic coordinates are given in parentheses.

some evidence of HF attenuation, but this signature was less clear compared to the other events. For the KER and HAL radars, most of the positive and negative identifications of HF attenuation were uncertain due to the variability in the background noise and lower backscatter occurrence for these radars, similar to Fig. 2. The MCM and DCE radars rarely detect any attenuation during the PsA events. These two radars had good data availability, high echo occurrence, and the background noise exhibits smooth diurnal variations, so we conclude that the EEP impact area rarely extends to these latitudes. The lowest latitude radar, FIR, had very limited data availability, so it is not possible to draw conclusions about the EEP response at that location.

To obtain a general overview of the spatial coverage of the PsA events, it is helpful to first consider only those events that had data available from most of the radars. Therefore, we now take the subset of events with data available from at least five of the following six radars: HAL, KER, SAN, SPS, SYE, and ZHO. These radars cover the spatial region extending from 59 to 75° magnetic latitude over a $\sim 100°$-wide magnetic longitudinal sector. The DCE and MCM radars are not included in this list because the event-detection rate at these sites was close to zero. The FIR radar was also excluded due to the low data availability.

In total, there were 17 APA and 10 PPA events with data available from at least five of the six radars listed above, and the EEP impact area for these events is shown in Figs. 4 and 5, respectively. For events where the PsA type changed during the event, we grouped the events according to the PsA type observed at the event onset. The events have been sorted and numbered according to the magnetic local time of the event onset at SYE. The red symbols are used to indicate our uncertainty in whether attenuation occurred or did not occur at each radar site. The light grey shading shows the region

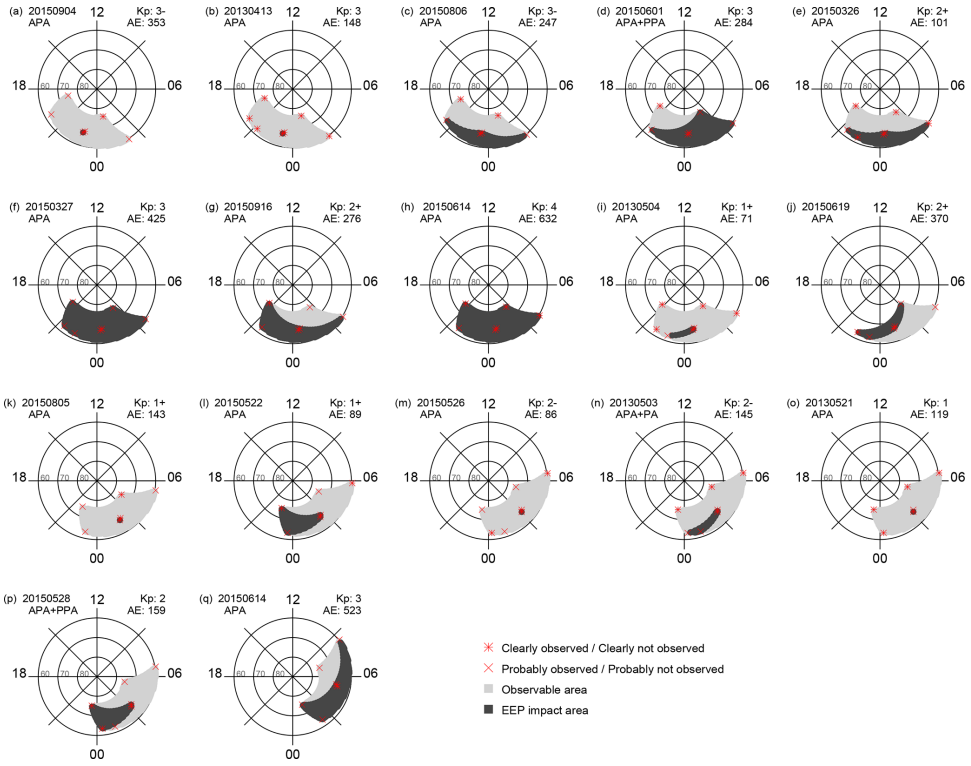

Figure 4. EEP impact area for amorphous pulsating aurora (APA) events with data available from at least five radars. The dark grey shading shows the EEP impact area, defined as the latitude/MLT region bounded by all radars that detected attenuation during that event (see text for details). The light grey shading shows the region bounded by the radars that did not detect any attenuation. Red symbols are used to indicate our uncertainty in determining whether any attenuation had occurred.

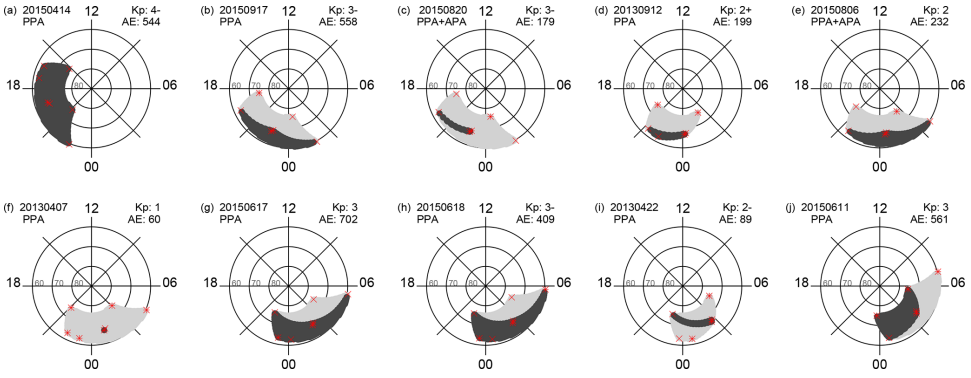

Figure 5. Same as Fig. 4 but for patchy pulsating aurora (PPA).

bounded by all radars with available data, and then a portion of this area is shaded dark grey to show the region in which the attenuation was detected. To determine the perimeter of each region, we performed a linear interpolation between the magnetic latitude and MLT coordinates of adjacent stations, which produces the curved lines in the polar plots. The event onset times are slightly different for each radar. To focus on the presence/absence of attenuation events, we use the dark grey shading to represent the total area in which attenuation was observed during the event. The auroral electrojet (AE) index and the planetary K-index (Kp) at the event onset time are also shown, and we note that there is no obvious correlation between geomagnetic activity and the size of the EEP impact area. This highlights the need to move beyond the geomagnetic-index-based descriptions of EEP forcing used for long-term climate modelling, since it does not adequately capture the contribution from PsA-related EEP.

A total of two APA events and one PPA event were detected by all radars simultaneously (dark grey shading only). For these events, the EEP impact area extended over a minimum of 7 h of MLT and 16° of magnetic latitude. For the remaining events, the latitude or MLT boundary of the EEP impact area can be identified. For example, APA events nos. 3 and 5 are confined to the ∼ 60–70° CGM latitude range. There are also many events that do not extend over the entire observable MLT range, such as APA event no. 9 and PPA event no. 3. A total of five APA events and one PPA event were observed only at Syowa Station. For these events, we conclude that the EEP impact area is narrow in both latitudinal and longitudinal extent. Since the radar coverage is very sparse, we checked ASC data from Syowa Station to determine the spatial coverage of the optical PsAs for these events. For all events detected only by the Syowa Station radars, the latitudinal extent of the optical PsA was narrower than the camera field of view. We show an example of this in Fig. 6 for APA event no. 2, where the optical PsA covers about half of the north–south field of view. We found no examples in which the east–west extent of the optical PsA was smaller than the camera field of view.

The results presented in Figs. 4 and 5 show that the EEP impact area associated with PsA events can vary significantly. However, due to the limited number of events that met our data availability criteria, it is difficult to draw conclusions about the average EEP impact area based on these results. Therefore, we now use the observations from all 74 events to build a statistical description of the EEP impact area. These results are presented in Fig. 7 using a format similar to a correlation matrix. Each cell shows the percentage of optical PsA events that were accompanied by an attenuation signature from both radars corresponding to that cell. For example, 36 % of the optical PsA events were accompanied by an attenuation signature from both the HAL and SPS radars simultaneously. The percentage occurrence for the ASC paired with each individual radar is also included in Fig. 7. The cells are colour coded according to these percentages, and the numerical value is provided in each cell. The total number of events used to calculate the percentage is given in parentheses. The total number of events varies widely between radar pairs because there were many events for which data were not available from both radars simultaneously. The radars/ASC are sorted by magnetic longitude on the horizontal axis and magnetic latitude on the vertical axis, except for DCE which is placed to the far right/top of the plot. The geomagnetic coordinates for each instrument are shown below each three-letter radar/camera code. Cells with a dark blue outline identify instrument pairs that are separated by less than 5° of magnetic latitude, which are useful for estimating the longitudinal extent of the EEP impact area at a particular latitude. Similarly, cells with a light blue outline identify radar pairs that are separated by less than 15° of magnetic longitude and can be used to estimate the latitudinal extent of the EEP impact area.

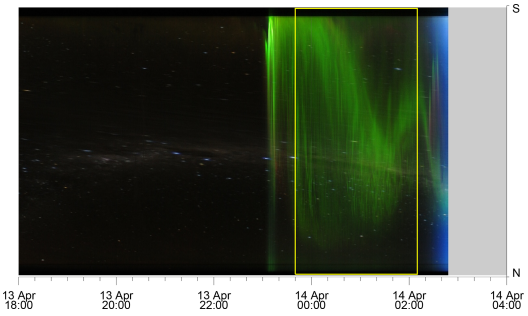

Figure 6. Magnetic north–south (N–S) keogram from the ASC at Syowa Station for the period 13–14 April 2013. The yellow rectangle indicates the time period during which the pulsating aurora was observed.

We will first discuss the probability that each radar detects HF attenuation simultaneously with optical PsAs at Syowa Station. A total of 100 % of the optical PsA events at Syowa Station were accompanied by HF attenuation at SYE and SYS. This is expected because these instruments have similar fields of view. The HAL radar, which is located at a similar magnetic latitude to Syowa Station, but 44° to the west, detected HF attenuation with 75 % probability. For radars near the poleward edge of the auroral oval, we see that 24 % of the optical PsA events were accompanied by attenuation at ZHO (75° latitude), and this drops to just 10 % at 80° latitude (MCM radar). For the lowest magnetic latitude station, FIR, data were available for just four events, and the radar detected attenuation for only one of these events, so the 25 % occurrence rate for this radar is unreliable.

The KER–HAL and SPS–ZHO radar pairs provide information about the MLT extent of the EEP impact area near the equatorward and poleward edges of the auroral oval, respectively. The KER and HAL radars, located at 59–62° latitude,

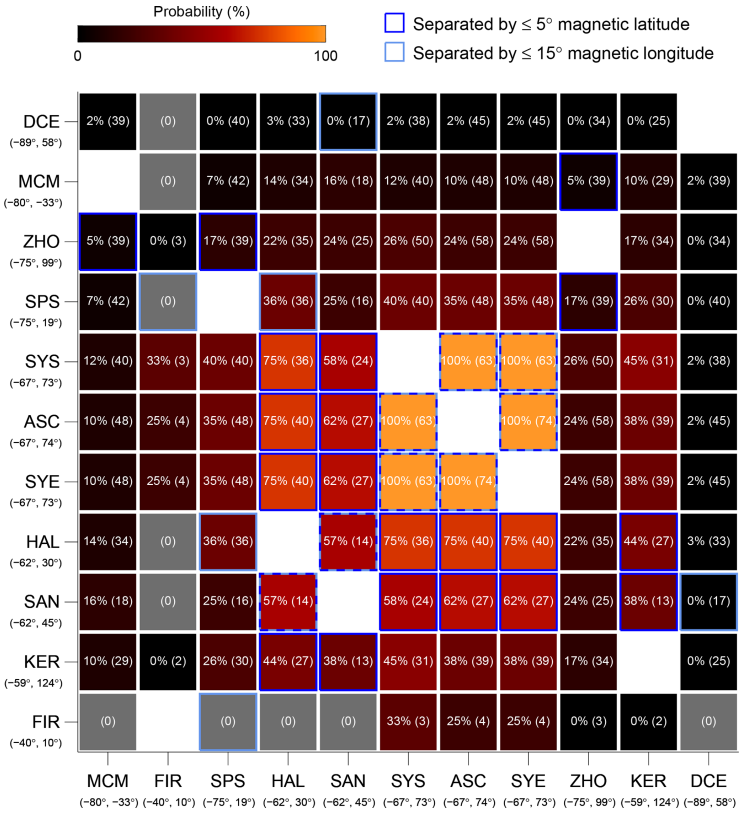

Figure 7. Probability of detecting HF radio attenuation for each pair of SuperDARN radars. In all cases, optical PsAs were also detected simultaneously by the ASC at Syowa Station. The white text shows the probabilities for each radar pair, and the number of events used to calculate these probabilities is given in parentheses. The probabilities for the ASC paired with each radar are also shown. The box shading is used to represent these probabilities visually. The corrected geomagnetic coordinates for each radar are given in parentheses below each three-letter station ID. The radars/ASC are sorted by magnetic longitude on the horizontal axis (except DCE) and by magnetic latitude on the vertical axis. Dark and light blue box outlines indicate radars with a similar magnetic latitude and magnetic longitude, respectively.

both detected attenuation for 44 % of the PsA events. This radar pair is separated by ∼ 6 h of MLT. At the poleward edge of the auroral oval (∼ 75°), 17 % of events were detected by both the SPS and ZHO radars, which have a 7 h MLT separation. We conclude from these results that the MLT extent of the EEP impact area is, on average, larger at the equatorward edge of the auroral oval.

The HAL–SPS radar pair provides information about the latitudinal extent of the EEP impact area to the west of our reference location at Syowa Station. This pair detected HF attenuation simultaneously with a probability of 36 %. East of the reference location, the ZHO–KER radar pair detected HF attenuation simultaneously with a probability of 17 %. The SPS–HAL and ZHO–KER pairs do not have the same latitudinal spacing, so it is not appropriate to compare the probabilities between these pairs. However, both results indicate that the latitudinal extent of the EEP impact area is less than 12° for the majority of events.

6 Discussion

The results presented in this study provide some basic estimates of the EEP impact area during pulsating aurora events. This type of information is necessary for developing realistic inputs to atmospheric models that are used to study the impact of EEP on the middle atmospheric chemistry and the contribution of EEP forcing to natural climate variability. Our results show that 36 % of PsA events extend over at least 12° of magnetic latitude (SPS–HAL pair), and ∼ 60 %–75 % extend over at least 4° of magnetic latitude (SYE–SAN

and SYE–HAL pairs). At the equatorward edge of the auroral oval, 44 % of events have a magnetic local time extent greater than 7 h (KER–HAL pair). At the poleward edge, 17 % of events cover this MLT range (ZHO–SPS pair).

Our study has demonstrated a novel application of the SuperDARN HF radars for estimating the spatial extent of the EEP impact area during pulsating aurora events. The use of SuperDARN radars for this purpose provides an advantage over optical instruments because the radar observations are not restricted by daylight or cloud cover. This significantly increases the availability of multi-point observations for our statistical study. However, the number of events used to determine the occurrence probabilities for each radar pair are still relatively low (see Fig. 7). For validation purposes, we used the ASC data from Syowa Station as a starting point for identifying PsA-related HF attenuation in the SuperDARN data, which limits the observation time to periods of dark, clear skies at Syowa Station. The four most important radars for estimating the EEP impact area in our study are KER, ZHO, SPS, and HAL. These radars provide observations from the equatorward and poleward edges of the Southern Hemisphere auroral oval over a wide longitudinal area. Unfortunately, the HAL radar ceased operations in 2015, so it was not possible to extend the data set to include more recent events from that location. Although the data set for the other radars could potentially be expanded to include more events, it may be more fruitful to repeat this analysis using the North American SuperDARN radars. This would provide additional coverage from a larger number of radars and allow comparisons with optical PsA observations from the THEMIS ASCs and with riometer observations of cosmic noise absorption.

The Southern Hemisphere data were used in this study because they generally detect large amounts of backscatter on the nightside, which makes it straightforward to identify periods of reduced backscatter power. We speculate that the high echo occurrence for the Southern Hemisphere radars is due to the low operating frequencies used and more favourable geometry with the magnetic field for satisfying the aspect angle condition for ionospheric scatter detection. Also, the Southern Hemisphere radars generally operate at just one or two frequencies, making it easier to identify attenuation signatures in the background radio noise, which is frequency dependent. With an improved understanding of the background radio noise measured by SuperDARN radars, it may be possible to reliably identify HF attenuation events using only the background noise parameter. This would improve the suitability of the North American SuperDARN radars for estimating the EEP impact area.

Due to the limited number of events in our statistical study, some caution is required when interpreting the occurrence probabilities presented in Fig. 7. For most radar pairs, the occurrence probabilities were calculated based on 30–40 events, so each event represents 2–4 percentage points. For the FIR and SAN radars, the uncertainties in the probabilities are much higher due to the low data availability. Based on the information presented in Fig. 3, we can determine which radars provide the most reliable information about PsA occurrence. These are the radars for which the large majority of events were either clearly observed or clearly not observed. This is the case for the two highest-latitude radars, MCM and DCE, so we conclude that the very low occurrence rates observed at 80 and 89° are reliable. In contrast, there was significant uncertainty in identifying events for the KER, SAN, and HAL radars. The SAN radar in particular has a low total number of events and high uncertainties with respect to whether any attenuation occurred. Despite these uncertainties, it is apparent from Fig. 7 that the occurrence rates exhibit a smooth variation with the distance from Syowa Station, both in latitude and longitude.

To determine whether our results are realistic, we can make some simple comparisons to an earlier work. At the equatorward edge of the auroral oval, we found that 44 % of events have a MLT extent greater than 7 h (KER–HAL pair). At the poleward edge, 17 % of events cover this MLT range (ZHO–SPS pair). Optical observations by Grono and Donovan (2020) showed that APA occur over a wider MLT range at $\sim 65°$ latitude compared to $\sim 75°$ latitude. Although their study did not provide information about the instantaneous spatial coverage of optical PsAs, it is likely that the wider MLT range of APA observed at lower latitudes is due to a wider instantaneous spatial coverage of the events in their study and is therefore consistent with our results. It is also important to recognise that the latitudinal separation between Syowa Station and the ZHO–SPS and KER–HAL radar pairs might contribute to the different MLT extents observed at ~ 60 and $\sim 75°$ latitude. The ZHO–SPS pair is located about 8° poleward of Syowa Station, whereas the HAL and KER radars are about 5 and 8° equatorward of Syowa Station, respectively. Therefore, with this study design it is difficult to decouple the effects of latitude and distance to the reference location when determining the MLT extent of PsAs.

Whatever the cause of these latitudinal differences in the EEP impact area, we can conclude from our results that the optical PsA event reported by Jones et al. (2013) is probably quite rare. For that event, optical PsAs were observed over 10 h of MLT, but our results indicate that a large majority of PsA events have an impact area covering less than 7 h of MLT. It is possible, however, that the EEP impact area is smaller than the spatial area over which optical PsAs are observed. This could be investigated further using the SuperDARN radars and riometers in North America combined with simultaneous observations from the THEMIS all-sky cameras.

A key difference in our results compared to earlier work is the location of the poleward boundary of PsAs. Our results show that PsA-related attenuation frequently extends beyond $\sim 75°$ latitude. This was determined using the SPS–SYE and ZHO–SYE radar pairs, which detected PsA-related attenuation with 35 % and 24 % probability, respectively. The MCM

radar (80° latitude) also detected attenuation with about 10 % probability. This upper latitude boundary for PsAs is significantly poleward of the optical PsA boundary reported in earlier work. For example, Oguti et al. (1981) reported that optical PsAs are restricted to $\leq 70°$ magnetic latitude, but that discrete aurora may occur up to 75° latitude. However, optical PsAs have been reported over Svalbard at 75° latitude (Kvifte and Pettersen, 1969), and Grono and Donovan (2020) reported PsAs up to about 74–75° but the occurrence was very low.

Grono and Donovan (2020) also showed that the magnetic latitude range of PsAs depends on the PsA type, with APA occurring over the magnetic latitude range 56–75° and PPA and PA restricted to slightly narrower ranges of 57–73 and 59–74°, respectively. They reported that the APA occurrence probability above about 74° was $\lesssim 15$ % and zero for PPA and PA. In our data set, there are several PPA events for which HF attenuation was detected by the ZHO or SPS radars. This is particularly so for event nos. 1, 7, 8, 9, and 10 in Fig. 5, which is half of the events shown in that figure. Kp and AE indices for these PPA events are higher than for the other PPA events, which might play a role in determining the size and location of the EEP impact area. Differences in the auroral oval location between the Northern and Southern hemispheres may contribute to the different latitudinal coverage results in this study compared to Grono and Donovan (2020). We also note that the PsA type classification was determined only at Syowa Station, and it is likely that other PsA types, and non-pulsating auroral emissions, were present elsewhere for many events. Although we have excluded polar cap absorption (PCA) from our event list, it is possible that very weak PCA caused by proton fluxes below the $10\,\mathrm{cm^{-2}\,sr^{-1}\,s^{-1}}$ threshold may cause some detectable HF attenuation at above $\sim 75°$ magnetic latitude. However, the timing of the absorption detected at these polar latitude radars matches well with the optical PsAs observed at Syowa Station. It therefore seems more likely that the polar latitude attenuation is caused by energetic electron precipitation that is related to the PsA activity occurring equatorward.

Since PsAs are often observed in the recovery phase of substorms, it is worth comparing our results with earlier studies of the spatial extent of substorm precipitation. For example, riometer observations by Berkey et al. (1974) showed that substorm precipitation extends over the magnetic latitude range ~ 60–$74°$. This magnetic latitude range is similar to the optical results described above, except that PsAs tend to remain further equatorward until the morning MLT sector. Regarding the HF attenuation observed at latitudes above 75°, Cresswell-Moorcock et al. (2013) reported that there is an enhancement in the > 30 keV electron fluxes at $L > 15$ in the morning sector about 1–2 h after the substorm onset. This is likely to correspond to the substorm recovery phase when PsAs are commonly observed. Therefore, some of the very high-latitude EEP fluxes reported by Cresswell-Moorcock et al. (2013) are probably related to PsAs. The latitude extent of these morning sector substorm-related EEP fluxes matches well with our observations of HF attenuation at magnetic latitudes above 75° in connection with PsAs at Syowa Station.

Based on the results described above, we can make a rough estimate of the average EEP impact area that could be used as input to an atmospheric model such as WACCM (Marsh et al., 2007; Verronen et al., 2016). As described above, the majority of events cover less than 7 h of MLT. From the SYE, SYS, KER, SAN, and HAL pair combinations shown in Fig. 7, we determine that roughly half of the PsA events have an instantaneous MLT coverage of at least 2–3 h at $\sim 65°$ magnetic latitude. Therefore, the average MLT extent at this latitude is probably around 4–5 h. The average MLT extent is much narrower at $\sim 75°$ magnetic latitude, with the large majority (65 %–76 %) of events covering less than 2–4 h simultaneously (SYE–SPS and SYE–ZHO pairs). PsA occurrence rates reach a maximum in the early morning sector, at about 04:00 MLT (Jones et al., 2011; Bland et al., 2019; Grono and Donovan, 2020), and this result could be used to centre the EEP impact area in a model PsA forcing. The average latitudinal extent of the EEP impact area is difficult to estimate due to the very sparse latitudinal coverage of the SuperDARN radars and the latitude dependence of PsA occurrence. We have determined that approximately one-third of the events cover 12° of latitude to the west of Syowa Station (SPS–HAL pair), so the median latitudinal extent would be a few degrees narrower. By combining this result with the latitude-dependent optical PsA occurrence rates (Grono and Donovan, 2020, Fig. 5), one could reasonably assume that the average EEP impact area covers the magnetic latitude range of about 62–70°.

Since our event detection procedure is qualitative, we cannot draw conclusions about the magnitude of the D-region electron density enhancements. This may be possible in the future with improved baselining of the background noise parameter (e.g. Berngardt, 2020) and a better understanding of the sensitivity of SuperDARN radars to PsA-related EEP. For the purposes of atmospheric modelling, however, statistical EEP energy spectra from satellite observations (e.g. Tesema et al., 2020b) would probably provide a more accurate estimate the relative impact of different types of PsAs than what is possible with the SuperDARN radars.

7 Conclusions

The spatial extent of the EEP impact area during 74 pulsating aurora events has been estimated using observations of HF radio attenuation from 10 SuperDARN radars in Antarctica. We defined the EEP impact area as the horizontal region over which PsA-related EEP has sufficient energy to cause a detectable amount of HF attenuation in the D-region ionosphere. This represents the area over which PsA-related EEP may cause an atmospheric chemical response. For 75 % of

the events studied, the EEP impact area extended over at least 4° of magnetic latitude, and 36 % of events extended over at least 12° of magnetic latitude. The MLT extent was found to be larger, on average, at lower latitudes compared to higher latitudes. Based on our results, and earlier work using optical data, we estimated the average EEP impact area for PsAs that could be used as input to an atmospheric model such as WACCM. This average EEP impact area extends from about 62–70° magnetic latitude and covers about 4–5 h of MLT. We emphasise that the SuperDARN radars have sparse spatial coverage, and that the sample size used in our statistical study was relatively small, so these results provide only a rough estimate of the average EEP impact area.

Code availability. Software for reading and analysing SuperDARN data is available at https://doi.org/10.5281/zenodo.801458 (SuperDARN Data Analysis Working Group et al., 2021).

Data availability. The SuperDARN data were obtained from the British Antarctic Survey data mirror (https://www.bas.ac.uk/project/superdarn; British Antarctic Survey, 2020). The all-sky camera data were provided by the National Institute of Polar Research, Japan (http://polaris.nipr.ac.jp/~acaurora/syowa_CDC_QL/; National Institute of Polar Research, Japan, 2020). Geomagnetic activity indices were obtained from the GSFC/SPDF OMNIWeb interface (https://omniweb.gsfc.nasa.gov; NASA, 2020).

Author contributions. The SuperDARN data analysis was done by EB. NP provided the original PsA event list from Syowa Station, and FT performed the classification. All authors contributed to the discussion of the results and the writing of the paper.

Competing interests. The authors declare that they have no conflict of interest.

Special issue statement. This article is part of "Special Issue on the joint 19th International EISCAT Symposium and 46th Annual European Meeting on Atmospheric Studies by Optical Methods". It is a result of the 19th International EISCAT Symposium 2019 and 46th Annual European Meeting on Atmospheric Studies by Optical Methods, Oulu, Finland, 19–23 August 2019.

Acknowledgements. Emma Bland has been supported by the Research Council of Norway (NRC; grant no. 287427). Noora Partamies and Fasil Tesema have been supported by the NRC under CoE (grant no. 223252). The authors acknowledge the use of SuperDARN data. SuperDARN is a collection of radars funded by the national scientific funding agencies of Australia, Canada, China, France, Italy, Japan, Norway, South Africa, the United Kingdom, and the United States of America. We thank Hiroshi Miyaoka of the National Institute of Polar Research (NIPR), Japan, for providing the data from the all-sky colour digital camera at Syowa Station. This camera is part of the science programme of the Japanese Antarctic Research Expedition and NIPR.

Financial support. This research has been supported by the Norges Forskningsråd (grant nos. 287427 and 223252).

Review statement. This paper was edited by Andrew J. Kavanagh and reviewed by two anonymous referees.

References

Berkey, F. T., Driatskiy, V. M., Henriksen, K., Hultqvist, B., Jelly, D. H., Shchuka, T. I., Theander, A., and Ylindemi, J.: A synoptic investigation of particle precipitation dynamics for 60 substorms in IQSY (1964–1965) and IASY (1969), Planet. Space Sci., 22, 255–307, https://doi.org/10.1016/0032-0633(74)90028-2, 1974.

Berngardt, O. I.: Noise level forecasts at 8–20 MHz and their use for morphological studies of ionospheric absorption variations at EKB ISTP SB RAS radar, Adv. Space Res., 66, 278–291, https://doi.org/10.1016/j.asr.2020.04.005, 2020.

Berngardt, O. I., Ruohoniemi, J. M., Nishitani, N., Shepherd, S. G., Bristow, W. A., and Miller, E. S.: Attenuation of decameter wavelength sky noise during x-ray solar flares in 2013–2017 based on the observations of midlatitude HF radars, J. Atmos. Sol.-Terr. Phy., 173, 1–13, https://doi.org/10.1016/j.jastp.2018.03.022, 2018.

Bland, E. C., Heino, E., Kosch, M. J., and Partamies, N.: SuperDARN Radar-Derived HF Radio Attenuation During the September 2017 Solar Proton Events, Space Weather, 16, 1455–1469, https://doi.org/10.1029/2018SW001916, 2018.

Bland, E. C., Partamies, N., Heino, E., Yukimatu, A. S., and Miyaoka, H.: Energetic Electron Precipitation Occurrence Rates Determined Using the Syowa East SuperDARN Radar, J. Geophys. Res.-Space, 124, 6253–6265, https://doi.org/10.1029/2018JA026437, 2019.

British Antarctic Survey: Super Dual Auroral Radar Network, available at: https://www.bas.ac.uk/project/superdarn, last access: 1 June 2020.

Chakraborty, S., Ruohoniemi, J. M., Baker, J. B. H., and Nishitani, N.: Characterization of Short-Wave Fadeout seen in Daytime SuperDARN Ground Scatter Observations, Radio Sci., 53, 472–484, https://doi.org/10.1002/2017RS006488, 2018.

Chakraborty, S., Baker, J. B. H., Ruohoniemi, J. M., Kunduri, B., Nishitani, N., and Shepherd, S. G.: A Study of SuperDARN Response to Co-occurring Space Weather Phenomena, Space Weather, 17, 1351–1363, https://doi.org/10.1029/2019SW002179, 2019.

Chisham, G., Lester, M., Milan, S. E., Freeman, M. P., Bristow, W. A., Grocott, A., McWilliams, K. A., Ruohoniemi, J. M., Yeoman, T. K., Dyson, P. L., Greenwald, R. A., Kikuchi, T., Pinnock, M., Rash, J. P. S., Sato, N., Sofko, G. J., Villain, J. P., and Walker, A. D. M.: A decade of the Super Dual Auroral Radar Network (SuperDARN): Scientific achievements, new techniques and future directions, Surv. Geophys., 28, 33–109, https://doi.org/10.1007/s10712-007-9017-8, 2007.

Cresswell-Moorcock, K., Rodger, C. J., Kero, A., Collier, A. B., Clilverd, M. A., Häggström, I., and Pitkänen, T.: A reexamination of latitudinal limits of substorm-produced energetic electron precipitation, J. Geophys. Res.-Space, 118, 6694–6705, https://doi.org/10.1002/jgra.50598, 2013.

Donovan, E., Mende, S., Jackel, B., Frey, H., Syrjäsuo, M., Voronkov, I. Trondsen, T., Peticolas, L., Angelopoulos, V., Harris, S., Greffen, M., and Connors, M.: The THEMIS all-sky imaging array – System design and initial results from the prototype imager, J. Atmos. Sol.-Terr. Phy., 68, 1472–1487, 2006.

Fang, X., Randall, C. E., Lummerzheim, D., Solomon, S. C., Mills, M. J., Marsh, D. R., Jackman, C. H., Wang, W., and Lu, G.: Electron impact ionization: A new parameterization for 100 eV to 1 MeV electrons, J. Geophys. Res.-Space, 113, A09311, https://doi.org/10.1029/2008JA013384, 2008.

Fiori, R. A. D., Koustov, A. V., Chakraborty, S., Ruohoniemi, J. M., Danskin, D. W., Boteler, D. H., and Shepherd, S. G.: Examining the potential of the Super Dual Auroral Radar Network for monitoring the space weather impact of solar X-ray flares, Space Weather, 16, 1348–1362, https://doi.org/10.1029/2018SW001905, 2018.

Greenwald, R. A., Baker, K. B., Dudeney, J. R., Pinnock, M., Jones, T. B., Thomas, E. C., Villain, J. P., Cerisier, J. C., Senior, C., Hanuise, C., Hunsucker, R. D., Sofko, G. J., Koehler, J., Nielsen, E., Pellinen, R., Walker, A. D. M., Sato, N., and Yamagishi, H.: DARN/SuperDARN: A Global View of the Dynamics of High-Latitude Convection, Space Sci. Rev., 71, 761–796, https://doi.org/10.1007/BF00751350, 1995.

Grono, E. and Donovan, E.: Differentiating diffuse auroras based on phenomenology, Ann. Geophys., 36, 891–898, https://doi.org/10.5194/angeo-36-891-2018, 2018.

Grono, E. and Donovan, E.: Constraining the Source Regions of Pulsating Auroras, Geophys. Res. Lett., 46, 10267–10273, https://doi.org/10.1029/2019GL084611, 2019.

Grono, E. and Donovan, E.: Surveying pulsating auroras, Ann. Geophys., 38, 1–8, https://doi.org/10.5194/angeo-38-1-2020, 2020.

Jones, S. L., Lessard, M. R., Rychert, K., Spanswick, E., and Donovan, E.: Large-scale aspects and temporal evolution of pulsating aurora, J. Geophys. Res.-Space, 116, A03214, https://doi.org/10.1029/2010JA015840, 2011.

Jones, S. L., Lessard, M. R., Rychert, K., Spanswick, E., Donovan, E., and Jaynes, A. N.: Persistent, widespread pulsating aurora: A case study, J. Geophys. Res.-Space, 118, 2998–3006, https://doi.org/10.1002/jgra.50301, 2013.

Juusola, L., Østgaard, N., Tanskanen, E., Partamies, N., and Snekvik, K.: Earthward plasma sheet flows during substorm phases, J. Geophys. Res.-Space, 116, A10228, https://doi.org/10.1029/2011JA016852, 2011.

Kasahara, S., Miyoshi, Y., Yokota, S., Mitani, T., Kasahara, Y., Matsuda, S., Kumamoto, A., Matsuoka, A., Kazama, Y., Frey, H. U., Angelopoulos, V., Kurita, S., Keika, K., Seki, K., and Shinohara, I.: Pulsating aurora from electron scattering by chorus waves, Nature, 554, 337–340, https://doi.org/10.1038/nature25505, 2018.

Kvifte, G. J. and Pettersen, H.: Morphology of the pulsating aurora, Planet. Space Sci., 17, 1599–1607, https://doi.org/10.1016/0032-0633(69)90148-2, 1969.

Lessard, M. R.: A review of pulsating aurora, Auroral phenomenology and magnetospheric processes: Earth and Other Planets, 197, 55–68, https://agupubs.onlinelibrary.wiley.com/doi/abs/10.1029/2011GM001187 (last access: 8 February 2021), 2012.

Marsh, D., Garcia, R., Kinnison, D., Boville, B., Sassi, F., Solomon, S., and Matthes, K.: Modeling the whole atmosphere response to solar cycle changes in radiative and geomagnetic forcing, J. Geophys. Res.-Atmos., 112, D23306, https://doi.org/10.1029/2006JD008306, 2007.

Milan, S. E., Jones, T. B., Robinson, T. R., Thomas, E. C., and Yeoman, T. K.: Interferometric evidence for the observation of ground backscatter originating behind the CUTLASS coherent HF radars, Ann. Geophys., 15, 29–39, https://doi.org/10.1007/s00585-997-0029-y, 1997.

Miyoshi, Y., Katoh, Y., Nishiyama, T., Sakanoi, T., Asamura, K., and Hirahara, M.: Time of flight analysis of pulsating aurora electrons, considering wave-particle interactions with propagating whistler mode waves, J. Geophys. Res.-Space, 115, A10312, https://doi.org/10.1029/2009JA015127, 2010.

Miyoshi, Y., Oyama, S., Saito, S., Kurita, S., Fujiwara, H., Kataoka, R., Ebihara, Y., Kletzing, C., Reeves, G., Santolik, O., Clilverd, M., Rodger, C. J., Turunen, E., and Tsuchiya, F.: Energetic electron precipitation associated with pulsating aurora: EISCAT and Van Allen Probe observations, J. Geophys. Res.-Space, 120, 2754–2766, https://doi.org/10.1002/2014JA020690, 2015.

NASA: GSFC/SPDF OMNIWeb interface, available at: https://omniweb.gsfc.nasa.gov, last access: 1 June 2020.

National Institute of Polar Research, Japan: Syowa Color Digital Camera (CDC), available at: http://polaris.nipr.ac.jp/~acaurora/syowa_CDC_QL/, last access: 1 June 2020.

Nishimura, Y., Lessard, M. R., Katoh, Y., Miyoshi, Y., Grono, E., Partamies, N., Sivadas, N., Hosokawa, K., Fukizawa, M., Samara, M., Michell, R. G., Kataoka, R., Sakanoi, T., Whiter, D. K., Oyama, S., Ogawa, Y., and Kurita, S.: Diffuse and pulsating aurora, Space Sci. Rev., 216, 1–38, https://doi.org/10.1007/s11214-019-0629-3, 2020.

Nishitani, N., Ruohoniemi, J. M., Lester, M., Baker, J. B. H., Koustov, A. V., Shepherd, S. G., Chisham, G., Hori, T., Thomas, E. G., Makarevich, R. A., Marchaudon, A., Ponomarenko, P., Wild, J. A., Milan, S. E., Bristow, W. A., Devlin, J., Miller, E., Greenwald, R. A., Ogawa, T., and Kikuchi, T.: Review of the accomplishments of mid-latitude Super Dual Auroral Radar Network (SuperDARN) HF radars, Prog. Earth Planet. Sc., 6, 1–57, https://doi.org/10.1186/s40645-019-0270-5, 2019.

Oguti, T., Kokubun, S., Hayashi, K., Tsuruda, K., Machida, S., Kitamura, T., Saka, O., and Watanabe, T.: Statistics of pulsating auroras on the basis of all-sky TV data from five stations. I. Occurrence frequency, Can. J. Phys., 59, 1150–1157, https://doi.org/10.1139/p81-152, 1981.

Partamies, N., Juusola, L., Tanskanen, E., and Kauristie, K.: Statistical properties of substorms during different storm and solar cycle phases, Ann. Geophys., 31, 349–358, https://doi.org/10.5194/angeo-31-349-2013, 2013.

Partamies, N., Whiter, D., Kadokura, A., Kauristie, K., Nesse Tyssøy, H., Massetti, S., Stauning, P., and Raita, T.: Occurrence and average behavior of pulsating aurora, J. Geophys. Res.-Space, 122, 5606–5618, https://doi.org/10.1002/2017JA024039, 2017.

SuperDARN Data Analysis Working Group, Thomas, E. G., Schmidt, M. T., Bland, E. C., Burrell, A. G., Ponomarenko, P. V., Reimer, A. S., Sterne, K. T., and Walach, M.-T.:

SuperDARN Radar Software Toolkit (RST) 4.5, Zenodo, https://doi.org/10.5281/zenodo.801458, 2021.

Tesema, F., Partamies, N., Nesse Tyssøy, H., Kero, A., and Smith-Johnsen, C.: Observations of electron precipitation during pulsating aurora and its chemical impact, J. Geophys. Res.-Space, 125, e2019JA027713, https://doi.org/10.1029/2019JA027713, 2020a.

Tesema, F., Partamies, N., Nesse Tyssøy, H., and McKay, D.: Observations of precipitation energies during different types of pulsating aurora, Ann. Geophys., 38, 1191–1202, https://doi.org/10.5194/angeo-38-1191-2020, 2020b.

Thorne, R. M., Ni, B., Tao, X., Horne, R. B., and Meredith, N. P.: Scattering by chorus waves as the dominant cause of diffuse auroral precipitation, Nature, 467, 943–946, https://doi.org/10.1038/nature09467, 2010.

Turunen, E., Verronen, P. T., Seppälä, A., Rodger, C. J., Clilverd, M. A., Tamminen, J., Enell, C.-F., and Ulich, T.: Impact of different energies of precipitating particles on NO_x generation in the middle and upper atmosphere during geomagnetic storms, J. Atmos. Sol.-Terr. Phy., 71, 1176–1189, https://doi.org/10.1016/j.jastp.2008.07.005, 2009.

Turunen, E., Kero, A., Verronen, P. T., Miyoshi, Y., Oyama, S.-I., and Saito, S.: Mesospheric ozone destruction by high-energy electron precipitation associated with pulsating aurora, J. Geophys. Res.-Atmos., 121, 11852–11861, https://doi.org/10.1002/2016JD025015, 2016.

van de Kamp, M., Seppälä, A., Clilverd, M. A., Rodger, C. J., Verronen, P. T., and Whittaker, I. C.: A model providing long-term data sets of energetic electron precipitation during geomagnetic storms, J. Geophys. Res.-Atmos., 121, 12520–12540, https://doi.org/10.1002/2015JD024212, 2016.

Verronen, P. T., Seppälä, A., Clilverd, M. A., Rodger, C. J., Kyrölä, E., Enell, C.-F., Ulich, T., and Turunen, E.: Diurnal variation of ozone depletion during the October–November 2003 solar proton events, J. Geophys. Res.-Space, 110, A09S32, https://doi.org/10.1029/2004JA010932, 2005.

Verronen, P. T., Andersson, M. E., Marsh, D. R., Kovács, T., and Plane, J. M. C.: WACCM-D – Whole Atmosphere Community Climate Model with D-region ion chemistry, J. Adv. Model. Earth Sy., 8, 954–975, https://doi.org/10.1002/2015MS000592, 2016.

Watanabe, D. and Nishitani, N.: Study of ionospheric disturbances during solar flare events using the SuperDARN Hokkaido radar, Advances in Polar Science, 24, 12–18, https://doi.org/10.3724/SP.J.1085.2013.00012, 2013.

Yang, B., Donovan, E., Liang, J., and Spanswick, E.: A statistical study of the motion of pulsating aurora patches: using the THEMIS All-Sky Imager, Ann. Geophys., 35, 217–225, https://doi.org/10.5194/angeo-35-217-2017, 2017.

Yang, B., Spanswick, E., Liang, J., Grono, E., and Donovan, E.: Responses of Different Types of Pulsating Aurora in Cosmic Noise Absorption, Geophys. Res. Lett., 46, 5717–5724, https://doi.org/10.1029/2019GL083289, 2019.

Paper IV

Types of pulsating aurora: Comparison of model and EISCAT electron density observations

Fasil Tesema, Noora Partamies, Daniel K. Whiter, and Yasunobu Ogawa
Ann. Geophys., **Submitted**, 2021.

https://doi.org/10.5194/angeo-2021-16
Preprint. Discussion started: 29 March 2021

Annales Geophysicae Discussions

Types of pulsating aurora: Comparison of model and EISCAT electron density observations

Fasil Tesema[1,2], Noora Partamies[1,2], Daniel K. Whiter[3], and Yasunobu Ogawa[4]

[1]The University Centre in Svalbard (UNIS), Norway
[2]Birkeland Centre for Space Science, University of Bergen, Norway
[3]School of Physics and Astronomy, University of Southampton, Southampton, UK
[4]National Institute of Polar Research, Japan

Correspondence: Fasil Tesema (fasil.tesema@unis.no)

Abstract. Energetic particle precipitation associated with pulsating aurora (PsA) can reach down to lower mesospheric altitude and deplete ozone. It is well documented that pulsating aurora is a common phenomenon during substorm recovery phases. This indicates that using magnetic indices to model the chemistry induced by PsA electrons could underestimate the energy deposition in the atmosphere. Integrating satellite measurements of precipitating electrons in models is considered to be an alternative way to account for such underestimation. One way to do this is to test and validate existing ion chemistry models using integrated measurements from satellite and ground-based observations. By using satellite measurements, an average/typical spectrum of PsA electrons can be constructed and used as an input in models to study the effects of the energetic electrons in the atmosphere. In this study, we compare electron densities from EISCAT radars with auroral ion chemistry and the energetics model by using pulsating aurora spectra derived from POES satellites as an energy input for the model. We found a good agreement between the model and EISCAT electron densities in the region dominated by patchy pulsating aurora. However, the magnitude of the observed electron densities suggests a significant difference in the flux of precipitating electrons for different pulsating aurora types (structures) observed.

1 Introduction

Pulsating aurora is a diffuse type of aurora with distinctive structures as arcs, bands, arc segments, and patches that are blinking on and off independently with a period of few seconds (Royrvik and Davis, 1977; Yamamoto, 1988). The sizes of pulsating aurora range from 10 to 200 km horizontally, and 10 to 40 km vertically and usually occur at around 100 km altitude (McEwen et al., 1981; Jones et al., 2009; Hosokawa and Ogawa, 2015; Nishimura et al., 2020; Tesema et al., 2020b). Pulsating aurora is often observed after midnight, during the recovery phase of a substorm, and at the equatorward part of the auroral oval, (Lessard, 2012; Nishimura et al., 2020) and it can persist for more than 2 hours (Jones et al., 2011; Partamies et al., 2017; Bland et al., 2019; Tesema et al., 2020a). However, substorm growth and expansion phase PsA (McKay et al., 2018) as well as afternoon PsA (Berkey, 1978) have also been reported.

The latitude of pulsating aurora can span a wide range, which depends on geomagentic activity and local time. In general, PsA often observed between 56° and 77° degrees of magnetic latitude (Grono and Donovan, 2020; Oguti et al., 1981). During

https://doi.org/10.5194/angeo-2021-16
Preprint. Discussion started: 29 March 2021

Annales Geophysicae Discussions
Open Access
EGU

the post-midnight period it is restricted between 60° and 70° magnetic latitude and in the morning sector it moves to higher latitudes, between 65° and 75°. The source location of these regions maps to the magnetosphere between 4 R_E and 15 R_E (Grono and Donovan, 2020). PsA is very common with an occurrence rate of about 30% around magnetic midnight (Oguti et al., 1981) and above 60% in the morning sector (Oguti et al., 1981; Bland et al., 2019)

The precipitating electrons' energy during pulsating aurora spans a wide range of magnitudes, predominantly between 10 and 200 keV (Miyoshi et al., 2015; Tesema et al., 2020a). However, electron energies as low as 1 keV have also been reported (McEwen et al., 1981). PsA can consist of microbursts of relativistic electrons in the high energy tail of the precipitation, which makes PsA an important magnetosphere–ionosphere (MI) coupling process in studying radiation belt dynamics (Miyoshi et al., 2020). A significant number of studies have shown that the precipitation of PsA electrons is driven by wave-particle interactions (Miyoshi et al., 2010; Nishimura et al., 2010, 2020; Kasahara et al., 2018). Recent studies further show that chorus waves play an important role in pitch angle scattering of electrons over a wide range of energy during pulsating aurora (Nishimura et al., 2010; Miyoshi et al., 2020). Electron cyclotron harmonic (ECH) waves are also a possible candidate in causing pulsating aurora, especially at the lower end of the PsA energy spectrum (Fukizawa et al., 2018; Nishimura et al., 2020).

A recent study by Grono and Donovan (2018) categorize pulsating aurora into three different types in relation to their structural stability and motion along the ionospheric convection. Salient and persistent structures moving along the ionospheric convection belong to patchy pulsating aurora (PPA), and transient structures with no definite motion characterize amorphous pulsating aurora (APA), which are the dominant PsA types. In addition, the third category, patchy aurora (PA), consists of very persistent structure with limited pulsation at the patch edges. The energy of electrons associated with the pulsating aurora types are different (Yang et al., 2019; Tesema et al., 2020b). From a total of 92 PsA events Tesema et al. (2020b) compared the D region ionization level obtained by EISCAT radars for different types of PsA and suggested that PPA is the dominant type of aurora affecting the D region atmosphere. The different categories of PsA reported in Grono and Donovan (2018) originated from different source regions of the magnetosphere, where PPA and PA mapped entirely to the inner magnetosphere while the APA source region spanned both inner and outer magnetosphere (Grono and Donovan, 2020). This indicates that PsA can contribute to our understanding of the radiation belt dynamics as well, despite the challenges imposed by the large spatio-temporal variation of the PsA structures.

Energetic PsA electrons can affect the chemistry of the mesosphere by strong production of odd hydrogen, which depletes ozone in catalytic reactions (Turunen et al., 2016; Tesema et al., 2020a). As demonstrated by Tesema et al. (2020a) the softest PsA precipitation does not have chemical consequences. It was further suggested in their study that it is mainly PA and PPA that can most effectively ionize the atmosphere below 100 km.

In this study we test an ion chemistry and energetics model using measurements of precipitating electrons from low altitude satellite as an energy input. We compared the EISCAT electron density measurements with the model output electron density to investigate the ionization level during different types of pulsating aurora. This will enable us to understand the ionization rates and energy spectra as they are measured at very different spatial and temporal resolutions, as well as the ionization changes in the transitions between different PsA types.

https://doi.org/10.5194/angeo-2021-16
Preprint. Discussion started: 29 March 2021

Annales Geophysicae Discussions
Open Access
EGU

2 Materials and methods

The optical data used in this study is from an all-sky camera (ASC) located in Tromsø (69.58°N, 19.21°E) in Norway, at the same site with the EISCAT radars. It belongs to the network of Watec monochromatic Imagers (WMI) owned and is operated by the National Institute of Polar Research (NIPR). The WMI consists of a highly sensitive Watec camera, a fish eye lens, and band-pass filter at 428 nm, 558 nm, and 630 nm with bandwidth of 10 nm. The imaging system is capable of taking images with 1 sec time resolution. In this study, we used images from the 558 nm filter. Technical details of the ASC can be found in Ogawa et al. (2020).

POES satellite measurements are used to construct the spectrum of precipitating PsA electrons. The spectrum is used as an input to the model. We approached the same procedure as explained in Tesema et al. (2020a) to construct the spectrum and extrapolate the softer precipitation end using a power law function. This includes the energy range from 50 eV to 1 MeV.

Field aligned and vertical electron density measurements are obtained from VHF/UHF EISCAT radars located in Tromsø. Instead of the standard 1 minute resolution data available for public on EISCAT database, we use a 5 seconds resolution electron density processed using Grand Unified incoherent scatter design and analysis package (GUISDAP) software to match with the high-resolution auroral imaging. The electron density measurements of the EISCAT radars are used to compare the ionization level during pulsating aurora with the electron density from the model described below.

The auroral model used in this study is the combination of an electron transport code (Lummerzheim and Lilensten, 1994) and a time-dependent ion chemistry and energetics model (Palmer, 1995; Lanchester et al., 2001), which solves the coupled continuity equations for positive ions and minor neutrals above 80 km altitude.

In this study, we used a directly measured energy of precipitating electrons by POES satellite to construct the spectrum for the input. We start the model run with an empty ionosphere, since prompt precipitation below 120 km does not respond to the softer precipitation that is usually used to warm up the ionosphere for upper atmospheric studies. The run time and time step for the model was about 3.5 seconds and 0.2 seconds, respectively. The minimum and maximum altitude of the model run is 80 and 500 km, respectively. Thus, the model does not reproduce ionization below 80 km, which corresponds to 100 keV (Turunen et al., 2009).

The electron density output from the model is compared with the EISCAT-measured electron density. This will enable us to answer the question of whether the overpass-averaged spectrum is a good representative as model input or if the patchiness of the aurora should be considered in atmospheric models. Requiring the availability of EISCAT data, POES satellites overpass and PsA from ASC images resulted in three events. Keograms (North–South overview) and ewograms (East–West overview) of ASC images are constructed to further classify and study the pulsating aurora structures and the associated precipitation.

3 Results

Pulsating aurora can easily be identified from ASC keograms (e.g. Partamies et al., 2017), and categorized into different types using ewograms (Grono and Donovan, 2018). A keogram is created by extracting north-south pixel columns of consecutive individual all-sky images and stacking them in time and an ewogram is an east-west counterpart of a keogram. The energy

https://doi.org/10.5194/angeo-2021-16
Preprint. Discussion started: 29 March 2021


Annales Geophysicae Discussions
Open Access
EGU

and flux of the precipitating electrons can be inferred indirectly from altitude and magnitude of the maximum electron density measured by ground-based incoherent scatter radars. Combining ASC data, EISCAT electron density measurements, electron density output from auroral model, and PsA energy spectra from POES measurements, we investigate the characteristics of precipitating PsA electrons and their ionization effects during three PsA events as follows:

3.1 Event 1: November 17, 2012

Figure 2 shows a keogram, ewogram, and EISCAT electron density measurements on November 17, 2012 between 4 and 5 UT. The keogram and ewogram are generated from one second time resolution ASC images taken at the Tromsø EISCAT site. Before 4:27 UT there was no electron density enhancement in the D and E regions, as there is no electron density enhancement nor auroral activity during this period. After 4:27 UT significant electron density enhancement (more than one order of magnitude) is seen below 110 km. Correspondingly, the ASC data showed PsA drifting into the EISCAT field of view (FOV) where it stayed until 4:43 UT. The PsA seen during this period is dominantly APA type. There is PPA type in the poleward region of the ASC FOV. After 4:43 UT this PPA drifted from north to east and became visible in the EISCAT radar FOV. The APA coverage started to diminish and the PPA took over most of the camera FOV. A clear transition in the EISCAT electron density is apparent at 4:43 UT. The electron density showed a thicker layer and precipitation reaching deeper, below 90 km, especially, after 4:49 UT. The thicker layer and more energetic precipitation corresponds to the PPA seen over the EISCAT radar.

Figure 3 shows the ASC images in 16 second intervals (a-f), the PsA spectrum constructed from POES measurements at the blue dots on the ASC images (g), electron density measured by EISCAT and modelled using the POES spectra (h-m), and green line emission intensity at the EISCAT (red) and POES (blue) measurement locations (n). From the ASC images it is clearly seen that the PsA structures are slowly drifting to east with decreasing intensity in the south (see also Supplementary Video one). This drift can be seen as patch lines (pathlines appear with or without stirations for patchy pulsating or patchy aurora, respectively (Grono et al., 2017)) in the ewogram on Figure 2. The median intensity of 10 pixels around the location of EISCAT (red) and the POES measurements (blue) are plotted in Figure 3(n). The intensity at the location of EISCAT over the entire duration was high, while at the location of the POES satellite measurements in the last three ASC images the intensity is extremely low. Looking at the electron density comparison between the model and EISCAT radar measurements, there is a good agreement between the two (Figure 3(h–k)) except the last two panels (Figure 3(l–m)), where the POES and EISCAT observations are looking into an entirely different region of auroral intensity. The first four points of POES observation spectra show similar magnitudes; curves (a–d) plotted in Figure 3(g) corresponding to the ASC observations in Figure 3(a–f). During this period, the altitude of maximum electron density in the EISCAT measurements was 95 km and from the model output it was 105 km. There is no significant differences in the electron density profiles as the FOV of EISCAT is mostly looking into a patch. The POES data points were also measurements within the patch "on" period, except in Figure 3(d), where there was very low emission (Figure 3(n)). Even though the emission intensity was low right after the whole FOV of the camera was filled with patches (as seen in the keogram plot on Figure 2), the electron density agreement between the model and EISCAT stayed the same in Figure 3(k). From Figure 3(d) POES is looking into a low emission region, which has correspondingly low fluxes in the spectra, which is similar to the spectra as in Figure 3(e–f). It is also clearly evident that above 10 keV the flux of

https://doi.org/10.5194/angeo-2021-16
Preprint. Discussion started: 29 March 2021


Annales Geophysicae Discussions

electrons in Figure 3(d) stayed similar to the previous three ASCs observations. However, for the last two ASC observations (Figure 3(e–f)) the POES observations were probably outside the precipitation region as the precipitating electron energies in the spectrum plot showed a large decrease above 10 keV on Figure 3(g). This causes a huge discrepancy between the model and EISCAT electron densities, accordingly.

The spectra from POES (Figure 3(g)) does not show significant variations except for the last two spectra in time. Above 10 keV there is a significant drop in electron flux for the last two observations (Figure 3(e–f)). This corresponds to the low emission observed in those two points of the ASC images. The electron density comparison shows a good agreement between altitudes of 90 and 120 km in the first four panels. However, the last two panels show a big difference in the electron fluxes. The shape of the curves in these two panels are similar, and the gap between the curves below 80 km becomes narrower in these two panels.

The altitude of maximum electron density showed a significant difference between the model run and the EISCAT observations. However, the magnitude of electron density showed a good agreement between 85 and 120 km. The height of maximum electron density for the model output is about 105 km (corresponding to 10 keV electrons), and that of the EISCAT measurements 95 km (corresponding to 25 keV electrons) (Turunen et al., 2009). Note that the model can only reproduce electron density above 80 km, and thus, below 90 km the discrepancy between the two densities becomes large. The electron densities above 120 km are due to the softer precipitation and were approximated by a power law function, which may not reproduce realistic ionization in this region. In addition, we did not perform warming up the ionosphere since we are interested in the prompt precipitation effects below 120 km. However, comparing the region between 85 and 120 km, the agreement between the model and EISCAT electron densities is good.

The last two panels in the electron density (Figure 3(l–m)) comparison showed a kink-like structure at around 90 km, corresponding to 40 keV electrons. From the spectrum it is apparent that above 40 keV the spectra for these two cases (magenta and cyan colors) showed almost the same fluxes. The median intensity around the EISCAT and satellite observations showed a large difference in these two panels (Figure 3(l-m)). From the EISCAT electron density plots shown in Figure 3(h–m), the zenith (black curve) and field aligned measurements (red curve) are similar. This event was studied by (Miyoshi et al., 2015) using the same EISCAT data, however, we used different ASC data, additional satellite data and model outputs in this study.

3.2 Event 2: November 09, 2015

Figure 4 shows keogram, ewogram, and EISCAT electron density measurements on November 09, 2015 between 2 and 3 UT. The keogram and ewogram are generated from one second time resolution ASC images in Tromsø. For this event a mixture of PsA types is clearly seen. Before 2:24 UT the PsA type was APA, which was followed by both APA and PPA (see also Supplementary Video two). During this one hour period the PsA structure and the magnitude of the electron density over the ASC and EISCAT FOVs change significantly. After 2:24 UT the PPA starts to emerge from south and move northward to fill the FOV after 2:42 UT. The electron density significantly dropped between 2:04 and 2:28 UT (third panel of the Figure), when the EISCAT FOV was predominantly observing the APA type. After 2:44 UT the dominant PPA type corresponds to the increase

https://doi.org/10.5194/angeo-2021-16
Preprint. Discussion started: 29 March 2021


Annales Geophysicae Discussions

in electron density, and also deeper precipitation. It is also clearly seen that the width of the ionization layer starts to get thicker after 2:20 UT, when a mix of PsA types and later PPA is observed over the FOV of EISCAT.

Figure 5 shows the ASC observation, the POES spectra for the overpass data points (blue dots), electron density measurements at EISCAT (red dots in the ASC images) and electron density from the model output (blue curve) using the spectra obtained from POES (blue dots in the ASC images). The ASC images were dominated by two different auroral structures. The poleward portion of the ASC is filled with diffuse arc and the equatorward portion with patches. It is not clearly seen if the diffuse arc is pulsating or not. But displaying all images as a video (see supplementary material), the structure over the EISCAT FOV is seen pulsating and can be categorized as APA. However, the POES measurements encounter a different type of PsA, namely PPA.

The spectra measured by POES are shown in Figure 5(e). The peak flux of electrons was observed below 10 keV. Above 100 keV, data point 4 showed significantly higher fluxes as compared to others. The height difference of the maximum electron density between the model output and EISCAT observations is small. However, the fluxes show more than one order of magnitude difference. The emission intensity at data point 4 and at the EISCAT observation point showed a large difference. The POES data point 4 is entirely within the PPA precipitation region, while EISCAT is looking into the APA type. Note that this data point 4 showed higher fluxes in the energy range above 100 keV.

3.3 Event 3: January 13, 2016

Figure 6 shows the keogram, ewogram, and electron densities on January 13, 2016 between 5 and 6 UT. From the ASC, a very slowly drifting and persistently stable structure of pulsating aurora is seen over the whole ASC FOV including the EISCAT FOV after 5:10 UT. A clear increase in electron density is observed when the pulsating patch is on and drifting in and out of the EISCAT FOV. The pulsating aurora over the entire FOV of the ASC is predominantly PPA during the one hour period, however, there are also some APA components seen in the keogram and ewogram plots. For example, before 5:15 UT APA type is seen in most of the ASC FOV. The ionization layer thickness also varies when the patch is visible in the EISCAT FOV (see also Supplementary Video three). The thickness of the ionization around 5:25 UT is different from the thickness of the ionized layer seen just before 5:20 UT.

As shown in Figure 7(a-e) the POES satellite measurement is not co-located with the EISCAT location, however the structure of PsA is the same over the ASC FOV. As is shown in Figure 7(f), the POES energy spectra is very similar in magnitude and shape in all the overpassing data points. From the ASC images (Figure 7 (a-e)), the EISCAT is looking into the edge of a pulsating patch, while the POES satellite is looking in to patch and the edge of a patch as it overpasses the pulsating aurora.

This event occurred very late in the morning, around 8 MLT. A persistent structure was observed over the whole FOV of the camera for the time period where the satellite is overpassing the region. The EISCAT electron density showed constant values at 95–115 km, but agrees well with the model electron density around 90 km. In Figure 7 (h-k), the electron densities showed a good agreement below 105 km. However, the discrepancy between the electron densities started at an altitude of 90 km (panel g), and the electron densities below 87 km showed a significant difference (Figure 7(j-k)). There is no significant increase in the fluxes at any specific energy during this whole observation period, but the spectra rather showed a steep decrease at all the

https://doi.org/10.5194/angeo-2021-16
Preprint. Discussion started: 29 March 2021


Annales Geophysicae Discussions
Open Access
EGU

energy levels. The median auroral emission intensity showed a similar decreasing trend at both the EISCAT location and at the satellite observation point.

4 Discussion

In this study, three PsA events were analyzed for their ionization characteristics. Each event analysis included high-resolution electron density measurements from the EISCAT Tromsø radar, high-resolution ASC images from the same site, and in-situ particle precipitation measurements from an overpassing POES satellite. The in-situ particle spectra were used as an input to an ionospheric model, and the model results were compared to the measured electron densities. Despite the differences between the space-borne and ground-based measurements, the conjugate measurements reveal some valuable details about the different PsA types.

Event 1 on November 17 occurred very late in the morning sector, around 7:30 MLT, where harder precipitation is often reported to be present (Hosokawa and Ogawa, 2015). This is clearly seen in the EISCAT electron density measurements as a significant ionization below 80 km. Similar local time evolution of hardening precipitation was recently investigated by Tesema et al. (2020b) in a more statistical approach including EISCAT and optical data from the same geographical area. However, the cut-off altitude of the model is 80 km, which causes a large discrepancy between the model and the EISCAT electron density below 80 km. The January 13 event (Event 3), which occurred about 30 minutes later in local time as compared to Event 1, showed a very good agreement between measured and modelled electron densities in the altitude range below 95 km during a softer type of precipitation. This indicates that the model is capable of reproducing measured electron densities very well within the height region of the prompt ionization at 80–120 km and during precipitation that primarily includes particle energies which impact this height range (∼1–100 keV). Our conclusions are thus focused on interpreting the height range of 80–120 km.

In two of the three cases (both November events 1 & 2) presented in this work, the PsA category changed within the observed one hour time period. During both events APA that was observed first changed into more persistent PPA. An enhancement in the measured electron density was observed at the same time with the optical transition between the two categories. Furthermore, in the November 2015 event (Event 2) the POES satellite passed over the ASC station at the time of the transition between APA and PPA types. This resulted in a big difference, more than one order of magnitude difference between the electron densities and a difference in the altitude of the modelled and measured maximum electron density. In this Event 2, the satellite measured primarily the PPA type precipitation, while the EISCAT radar was looking mainly into the APA type precipitation. This suggests that a mixture of PsA types is the likely cause of the observed discrepancy.

As previously shown by a statistical analysis of PsA type Grono and Donovan (2020), APA has a tendency to occur at earlier local times than PPA and PA, i.e. around and even prior to midnight. A similar order of the PsA types was found in the two of our three case studies which included the transition between the different PsA types. This further suggests that the APA type may dominate the PsA events, which occur during (or in between) substorm activity and predominantly undergo increase patch sizes during the event evolution (Partamies et al., 2019). Because these PsA events are embedded into substorm aurora, and

https://doi.org/10.5194/angeo-2021-16
Preprint. Discussion started: 29 March 2021


Annales Geophysicae Discussions

thus would typically cover limited spatial regions as compared to PA and PPA, an overpassing spacecraft is likely to measure a mixture of different precipitation types and thus provide a false estimate for electron spectra at a near-conjugate ground location. However, deeper into the morning sector where the PsA is more often PA or PPA (Grono and Donovan, 2020) the regions covered by PsA are large. In this kind of case, our findings (clearest for Event 1) suggest that the overpass average of the in-situ particle spectra agrees well with the ground-based measurements of electron densities. As the overpass-averaged spacecraft spectrum would necessarily include precipitation information for patches both in their on and off phases, this finding indicates that the patchiness of PsA is not a key factor in the energy deposition to the atmosphere. More detailed analysis is needed for a large number of different PsA types to confirm this result, but nonetheless this finding may have important implications for PsA modelling studies for atmospheric chemistry impact.

5 Conclusions

By combining EISCAT electron density, electron precipitation measurements from POES, and model electron density outputs, we study three PsA events identified using Tromsø high-resolution ASC data. We observed different types of PsA in the three cases. We showed that the near midnight PsA event (Event 2), which includes a mix of PsA types (APA and PPA), showed a significant electron density magnitude difference between EISCAT and model outputs. The model and EISCAT electron density magnitude in the morning sector events (Events 1 and 3), which consisted of measurements when the POES satellite overpassed entirely over PPA types, showed a very good agreement. This suggests that the PsA spectra from POES used in modelling during a mix of PsA types could give an incorrect estimate if averaged spectra are used to model the energy deposition. However, the agreement during both the morning sector events indicated that overpassed averaged spectra are a very good estimate to model PsA energy deposition without considering the patchiness of the PsA. This also indicates that MLT dependence of PsA types might play an important role in future studies of atmospheric effects of PsA.

Data availability. The quicklook ASC images and keograms for event selection are available at Auroral Quicklook Viewer of NIPR ground-based network (http://pc115.seg20.nipr.ac.jp/www/AQVN/index.html) (last access: 26 February 2021). All-sky camera data are obtained by requesting the Principal Investigator of the auroral observation (uapdata@nipr.ac.jp) at National Institute of Polar Research (NIPR). Raw EISCAT data used in this analysis is available at http://portal.eiscat.se/schedule/schedule.cgi (last access: 26 January 2021) and GUISDAP software used to analyse the EISCAT raw data in high time resolution is available at https://eiscat.se/scientist/user-documentation/guisdap-9-0/ (last access: 26 January 2021).

Author contributions. All authors contribute by providing necessary data, discussions and writing the paper.

Competing interests. The authors declare that no competing interests are present.

https://doi.org/10.5194/angeo-2021-16
Preprint. Discussion started: 29 March 2021

Annales Geophysicae Discussions
Open Access
EGU

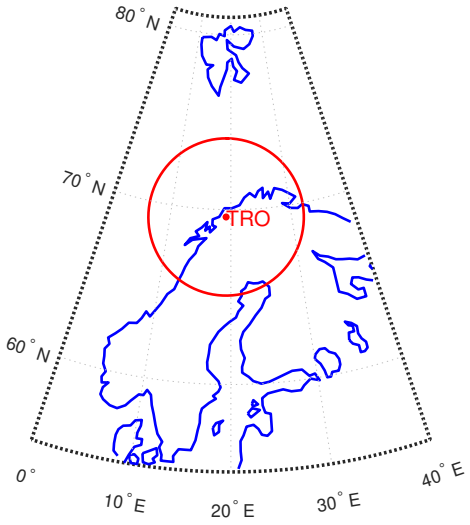

Figure 1. Geographic locations of ground-based ASC station and EISCAT radars in Tromsø (TRO) (red dot). The red circle marks the ASC FOV at about 110 km altitude. POES overpasses were selected so that their foot-points mapped to the ASC FOV.

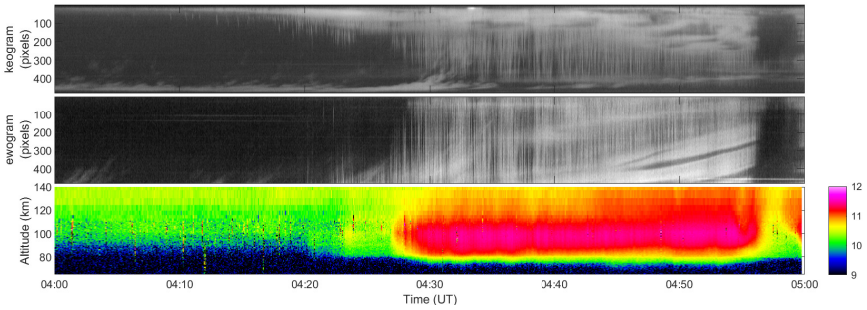

Figure 2. Keogram (top), ewogram (middle), and EISCAT electron density as a function of height (bottom) from UHF radar in Tromsø on November 17, 2012 between 4 and 5 UT. EISCAT beam points to the centre of the keogram at 235 pixel and in the ewogram at 245 pixel. The electron density is displayed in a logarithmic color scale.

Acknowledgements. The funding support for Fasil Tesema is provided by the Norwegian Research Council (NRC) under CoE contract 223252. In addition, the work of Noora Partamies is supported by NRC project 287427.

https://doi.org/10.5194/angeo-2021-16
Preprint. Discussion started: 29 March 2021

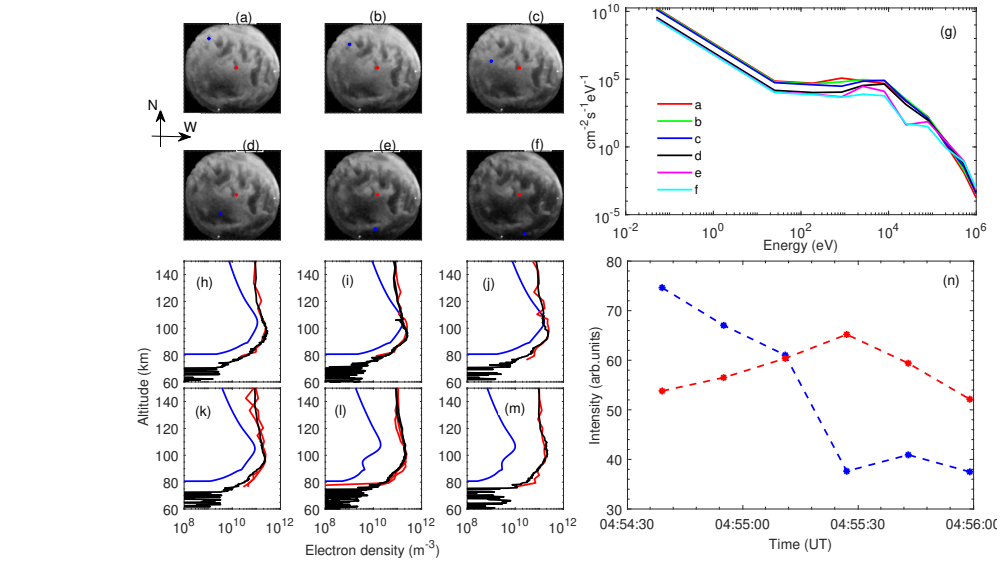

Figure 3. ASC images (a–f), spectra constructed from POES and power law extrapolation (g), curves labeled as a–f are corresponding spectra to the blue point on the ASC images, model and EISCAT electron densities (field aligned from UHF radar (red) and zenith measurements from VHF radar (black)) ((h–m) corresponding to the 6 ASC image times (a–f)), and relative auroral intensities at the location of satellite measurements as a function of time (n), blue dots at POES data points corresponding to (a–f) and red dots at EISCAT.

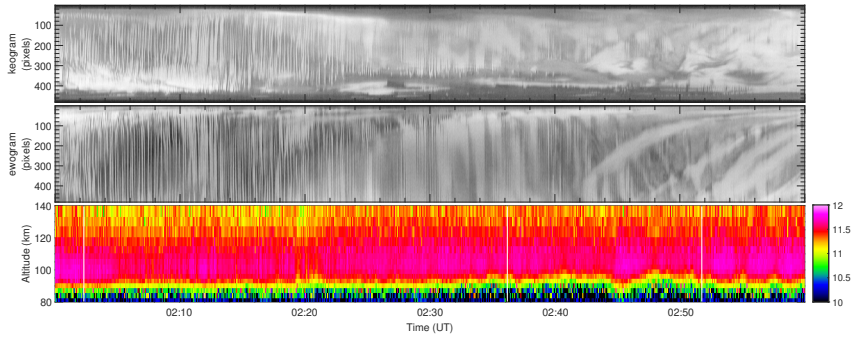

Figure 4. Keogram (top), ewogram (middle), and EISCAT electron density (bottom) from UHF radar at Tromsø on November 09, 2015 between 2 and 3 UT. EISCAT beam points to the centre of the keogram at 235 pixel and in the ewogram at 230 pixel. The electron density is displayed in a logarithmic color scale.

https://doi.org/10.5194/angeo-2021-16
Preprint. Discussion started: 29 March 2021

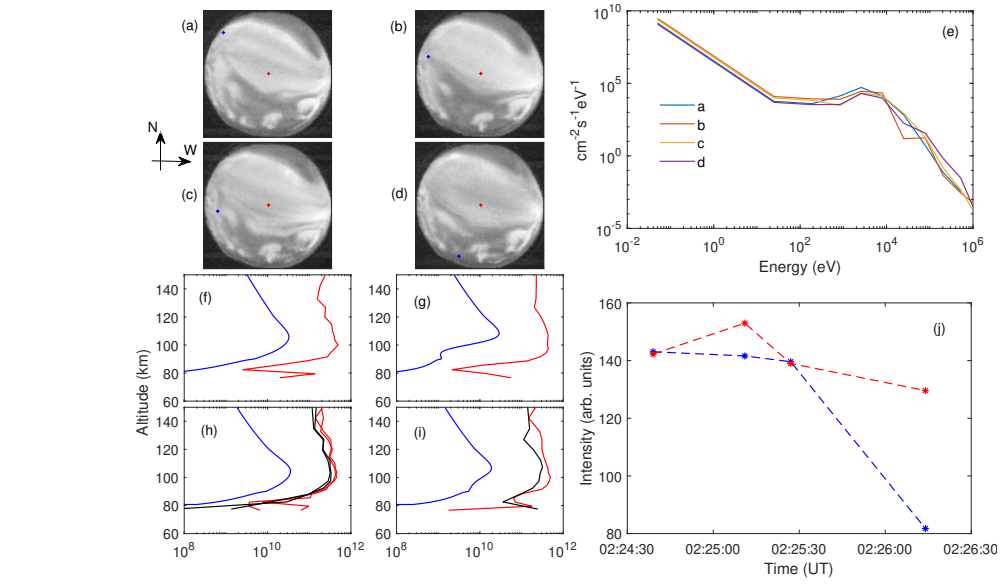

Figure 5. ASC images (a–d), spectra constructed from POES and power law extrapolation (e), curves labeled as a–d are corresponding spectra to the blue point on the ASC images, model and EISCAT electron densities ((f–i), colors as in Figure 3), and relative auroral intensities at the location of satellite measurements (blue dots) and at the EISCAT beam points (red dots).

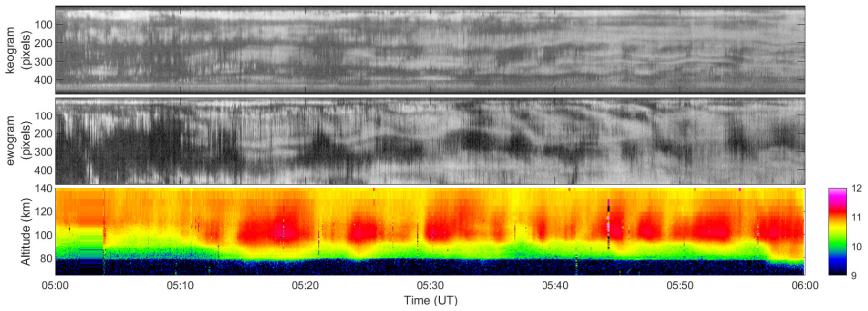

Figure 6. As in Figure 4 but for Event 3.

https://doi.org/10.5194/angeo-2021-16
Preprint. Discussion started: 29 March 2021

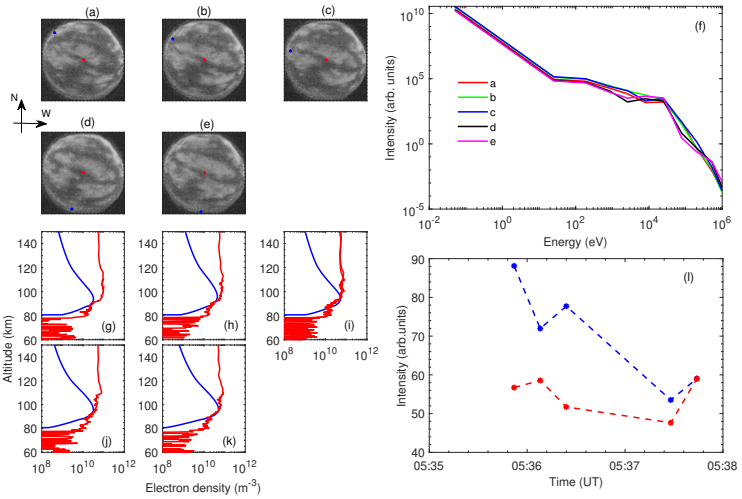

Figure 7. As in Figures 3 and 5 but for Event 3.

References

Berkey, F.: Observations of pulsating aurora in the day sector auroral zone, Planetary and Space Science, 26, 635–650, https://doi.org/10.1016/0032-0633(78)90097-1, 1978.

Bland, E. C., Partamies, N., Heino, E., Yukimatu, A. S., and Miyaoka, H.: Energetic Electron Precipitation Occurrence Rates Determined Using the Syowa East SuperDARN Radar, Journal of Geophysical Research: Space Physics, 124, 6253–6265, https://doi.org/10.1029/2018ja026437, 2019.

Fukizawa, M., Sakanoi, T., Miyoshi, Y., Hosokawa, K., Shiokawa, K., Katoh, Y., Kazama, Y., Kumamoto, A., Tsuchiya, F., Miyashita, Y., Tanaka, Y. Kasahara, Y., Ozaki, M., Matsuoka, A., Matsuda, S., Hikishima, M., Oyama, S., Ogawa, Y., Kurita, S., and Fujii, R.: Electrostatic Electron Cyclotron Harmonic Waves as a Candidate to Cause Pulsating Auroras, Geophysical Research Letters, 45, 661–12, https://doi.org/10.1029/2018GL080145, https://onlinelibrary.wiley.com/doi/abs/10.1029/2018GL080145, 2018.

Grono, E. and Donovan, E.: Differentiating diffuse auroras based on phenomenology, Annales Geophysicae, 36, 891–898, https://doi.org/10.5194/angeo-36-891-2018, 2018.

Grono, E. and Donovan, E.: Surveying pulsating auroras, Annales Geophysicae, 38, 1–8, https://doi.org/10.5194/angeo-38-1-2020, https://www.ann-geophys.net/38/1/2020/, 2020.

Grono, E., Donovan, E., and Murphy, K. R.: Tracking patchy pulsating aurora through all-sky images, Annales Geophysicae, 35, 777–784, https://doi.org/10.5194/angeo-35-777-2017, 2017.

Hosokawa, K. and Ogawa, P.: Journal of Geophysical Research : Ionospheric variation during pulsating aurora :, pp. 1–15, https://doi.org/10.1002/2015JA021401.Received, 2015.

https://doi.org/10.5194/angeo-2021-16
Preprint. Discussion started: 29 March 2021

Jones, S. L., Lessard, M. R., Fernandes, P. A., Lummerzheim, D., Semeter, J. L., Heinselman, C. J., Lynch, K. A., Michell, R. G., Kintner, P. M., Stenbaek-Nielsen, H. C., and Asamura, K.: PFISR and ROPA observations of pulsating aurora, Journal of Atmospheric and Solar-Terrestrial Physics, 71, 708–716, https://doi.org/10.1016/j.jastp.2008.10.004, 2009.

Jones, S. L., Lessard, M. R., Rychert, K., Spanswick, E., and Donovan, E.: Large-scale aspects and temporal evolution of pulsating aurora, Journal of Geophysical Research: Space Physics, 116, 1–7, https://doi.org/10.1029/2010JA015840, 2011.

Kasahara, S., Miyoshi, Y., Yokota, S., Mitani, T., Kasahara, Y., Matsuda, S., Kumamoto, A., Matsuoka, A., Kazama, Y., Frey, H. U., Angelopoulos, V., Kurita, S., Keika, K., Seki, K., and Shinohara, I.: Pulsating aurora from electron scattering by chorus waves, Nature, 554, 337–340, https://doi.org/10.1038/nature25505, 2018.

Lanchester, B. S., Rees, M. H., Lummerzheim, D., Otto, A., Sedgemore-Schulthess, K. J. F., Zhu, H., and McCrea, I. W.: Ohmic heating as evidence for strong field-aligned currents in filamentary aurora, Journal of Geophysical Research, 106, 1785, https://doi.org/10.1029/1999JA000292, http://doi.wiley.com/10.1029/1999JA000292, 2001.

Lessard, M. R.: A Review of Pulsating Aurora, Auroral Phenomenology and Magnetospheric Processes: Earth and Other Planets, pp. 55–68, https://doi.org/10.1029/2011GM001187, 2012.

Lummerzheim, D. and Lilensten, J.: Electron transport and energy degradation in the ionosphere: Evaluation of the numerical solution, comparison with laboratory experiments and auroral observations, Annales Geophysicae, 12, 1039–1051, https://doi.org/10.1007/s00585-994-1039-7, 1994.

McEwen, D. J., Yee, E., Whalen, B. A., and Yau, A. W.: Electron energy measurements in pulsating auroras, Canadian Journal of Physics, 59, 1106–1115, https://doi.org/10.1139/p81-146, 1981.

McKay, D., Partamies, N., and Vierinen, J.: Pulsating aurora and cosmic noise absorption associated with growth-phase arcs, Annales Geophysicae, 36, 59–69, https://doi.org/10.5194/angeo-36-59-2018, 2018.

Miyoshi, Y., Katoh, Y., Nishiyama, T., Sakanoi, T., Asamura, K., and Hirahara, M.: Time of flight analysis of pulsating aurora electrons, considering wave-particle interactions with propagating whistler mode waves, Journal of Geophysical Research: Space Physics, 115, 1–7, https://doi.org/10.1029/2009JA015127, 2010.

Miyoshi, Y., Oyama, S., Saito, S., Kurita, S., Fujiwara, H., Kataoka, R., Ebihara, Y., Kletzing, C., Reeves, G., Santolik, O., Clilverd, M., Rodger, C. J., Turunen, E., and Tsuchiya, F.: Energetic electron precipitation associated with pulsating aurora: EISCAT and Van Allen Probe observations, Journal of Geophysical Research: Space Physics, 120, 2754–2766, https://doi.org/10.1002/2014JA020690, 2015.

Miyoshi, Y., Saito, S., Kurita, S., Asamura, K., Hosokawa, K., Sakanoi, T., Mitani, T., Ogawa, Y., Oyama, S., Tsuchiya, F., Jones, S. L., Jaynes, A. N., and Blake, J. B.: Relativistic Electron Microbursts as High Energy Tail of Pulsating Aurora Electrons, Geophysical Research Letters, 47, https://doi.org/10.1029/2020gl090360, 2020.

Nishimura, Y., Bortnik, J., Li, W., Thorne, R. M., Lyons, L. R., Angelopoulos, V., Mende, S. B., Bonnell, J. W., Le Contel, O., Cully, C., Ergun, R., and Auster, U.: Identifying the driver of pulsating aurora, Science (80-.)., 330, 81–84, https://doi.org/10.1126/science.1193186, 2010.

Nishimura, Y., Lessard, M. R., Katoh, Y., Miyoshi, Y., Grono, E., Partamies, N., Sivadas, N., Hosokawa, K., Fukizawa, M., Samara, M., Michell, R. G., Kataoka, R., Sakanoi, T., Whiter, D. K., Oyama, S. i., Ogawa, Y., Kurita, S., ichiro Oyama, S., Ogawa, Y., and Kurita, S.: Diffuse and Pulsating Aurora, https://doi.org/10.1007/s11214-019-0629-3, 2020.

Ogawa, Y., Tanaka, Y., Kadokura, A., Hosokawa, K., Ebihara, Y., Motoba, T., Gustavsson, B., Brändström, U., Sato, Y., Oyama, S., Ozaki, M., Raita, T., Sigernes, F., Nozawa, S., Shiokawa, K., Kosch, M., Kauristie, K., Hall, C., Suzuki, S., Miyoshi, Y., Gerrard, A., Miyaoka,

https://doi.org/10.5194/angeo-2021-16
Preprint. Discussion started: 29 March 2021

H., and Fujii, R.: Development of low-cost multi-wavelength imager system for studies of aurora and airglow, Polar Science, 23, 100 501, https://doi.org/10.1016/j.polar.2019.100501, 2020.

Oguti, T., Kokubun, S., Hayashi, K., Tsuruda, K., Machida, S., Kitamura, T., Saka, O., and Watanabe, T.: Statistics of pulsating auroras on the basis of all-sky TV data from five stations. I. Occurrence frequency, Canadian Journal of Physics, 59, 1150–1157, https://doi.org/10.1139/p81-152, https://cdnsciencepub.com/doi/abs/10.1139/p81-152, 1981.

Palmer, J.: Plasma density variations in the aurora, Ph.D. thesis, 1995.

Partamies, N., Whiter, D., Kadokura, A., Kauristie, K., Nesse Tyssøy, H., Massetti, S., Stauning, P., and Raita, T.: Occurrence and average behavior of pulsating aurora, Journal of Geophysical Research: Space Physics, 122, 5606–5618, https://doi.org/10.1002/2017JA024039, 2017.

Partamies, N., Bolmgren, K., Heino, E., Ivchenko, N., Borovsky, J. E., and Sundberg, H.: Patch Size Evolution During Pulsating Aurora, Journal of Geophysical Research: Space Physics, 124, 4725–4738, https://doi.org/10.1029/2018JA026423, 2019.

Royrvik, O. and Davis, T. N.: Pulsating aurora: Local and global morphology, Journal of Geophysical Research, 82, 4720–4740, https://doi.org/10.1029/ja082i029p04720, https://agupubs.onlinelibrary.wiley.com/doi/full/10.1029/JA082i029p04720, 1977.

Tesema, F., Partamies, N., Tyssøy, H. N., Kero, A., and Smith-Johnsen, C.: Observations of electron precipitation during pulsating aurora and its chemical impact, Journal of Geophysical Research: Space Physics, n/a, e2019JA027 713, https://doi.org/10.1029/2019JA027713, 2020a.

Tesema, F., Partamies, N., Tyssøy, H. N., and McKay, D.: Observations of precipitation energies during different types of pulsating aurora, Annales Geophysicae, 38, 1191–1202, https://doi.org/10.5194/angeo-38-1191-2020, 2020b.

Turunen, E., Verronen, P. T., Seppälä, A., Rodger, C. J., Clilverd, M. A., Tamminen, J., Enell, C. F., and Ulich, T.: Impact of different energies of precipitating particles on NOx generation in the middle and upper atmosphere during geomagnetic storms, Journal of Atmospheric and Solar-Terrestrial Physics, 71, 1176–1189, https://doi.org/10.1016/j.jastp.2008.07.005, 2009.

Turunen, E., Kero, A., Verronen, P. T., Miyoshi, Y., Oyama, S. I., and Saito, S.: Mesospheric ozone destruction by high-energy electron precipitation associated with pulsating aurora, Journal of Geophysical Research, 121, 11 852–11 861, https://doi.org/10.1002/2016JD025015, 2016.

Yamamoto, T.: On the temporal fluctuations of pulsating auroral luminosity, J. Geophys. Res., 93, 897, https://doi.org/10.1029/JA093iA02p00897, 1988.

Yang, B., Spanswick, E., Liang, J., Grono, E., and Donovan, E.: Responses of Different Types of Pulsating Aurora in Cosmic Noise Absorption, Geophysical Research Letters, pp. 5717–5724, https://doi.org/10.1029/2019GL083289, 2019.

Graphic design: Communication Division, UiB / Print: Skipnes Kommunikasjon AS

uib.no

ISBN: 9788230855225 (print)
9788230853832 (PDF)